2009

Ocular Phenotyping in the harlequin Mouse Model of Retinal Degeneration: A Framework for Therapeutic Testing

Thomas C. MacPherson
Western University

Ocular Phenotyping in the *harlequin* Mouse Model of Retinal Degeneration: A Framework for Therapeutic Testing

(Spine title: Ocular phenotyping in the *harlequin* mouse model of retinal degeneration)

(Thesis format: Monograph)

By

Thomas C. MacPherson

Graduate Program in Biology

A thesis submitted in partial fulfilment
of the requirements for the degree of
Master of Science

School of Graduate and Postdoctoral Studies
The University *of* Western Ontario
London, Ontario, Canada

Abstract

Retinal degeneration, despite devastating effects, lacks therapy. Memantine has potential for preserving vision by reducing excitotoxicity associated with reactive oxygen species (ROS). A model for memantine delivery is the oxidative stress- and retinal degeneration in *harlequin* (*hq*) mice. Wild type (WT) and *hq* mice received untreated or memantine-treated (30 mg/kg/ day) drinking water at 1 out to 2, 4, 6, 8 and 10 months (mo) of age (5 males per cohort). Retinal integrity was assessed using electroretinography and ocular coherence tomography with ROS levels and apoptosis examined postmortem. Reduced *hq* vision was evident at 2 mo with a slight elevation in ROS at 2 mo, central retinal photoreceptor layer thinning at 4 mo and significant apoptosis at 4 mo. Excitotoxicity was not evident. Memantine had expected effects in WT mice but did not preserve *hq* vision. Ocular phenotyping of *hq* mice revealed dry age-related macular degeneration and a valid framework for testing appropriate drugs.

Keywords: *harlequin,* memantine, electroretinography, ocular coherence tomography, dry age-related macular degeneration, reactive oxygen species, excitotoxicity, mitochondrial dysfunction.

Co-Authorship

Thomas Clayton MacPherson performed the following work under the supervision and financial support of Dr. Kathleen Allen Hill. Thomas Clayton MacPherson performed the experimental research presented in this thesis and will be first author on resulting publications. This thesis is presented in monographical format. Dr. Kathleen Hill will be a senior author on all publications produced from this research due to role in project design, supervision, literature review, data analysis, and assistance with publication writing. Kevin Leonard will be a co-author on specialized papers produced from the following research due to his assistance in the experimental design, specifically for memantine-associated papers. Dr. Cindy Hutnik will be included as a co-author on publications resulting from this research due to assistance with experimental design and her integral role as a clinical ophthalmologist consultant associated with the research. Alex Laliberte will be included on specialized papers for his work with the heterozygous *harlequin* carrier mouse.

Acknowledgements

I would like to acknowledge the following people for their efforts throughout the duration of my Master's degree. I am extremely appreciative of the assistance and contributions that I have received from Dr. Kathleen Hill during the completion of my Master's degree. Her motivation and drive has pushed me and allowed me to realize the work I am capable of completing. Her positivity and questioning attitude have made for excellent experimental meetings which have led me to think outside of the "obvious" and to delve deep into scientific literature. My advisory Committee members, Dr Jack Miller and Dr. Sashko Damjanovski were valuable resource for advice when troubleshooting experimental protocols, as well as writing comments for my proposal and this thesis. I would also like to thank Alex Laliberte and Anita Pretenjaca for their assistance with laboratory work and constant support.

I would like to thank the following individuals for assistance vital to the research provided herein. Dr. Cindy Hutnik for her assistance as a clinical ophthalmologist consultant for human disease. Dr. Hutnik assisted greatly in the "bench-top to bedside" applications of my research. Kelly Galloway-Kay and Darcy O'Neil at the Molecular Pathology Core Facility were very helpful for their training in tissue processing and sectioning. Dr. Ian Welch assisted greatly with his expertise in histopathology in the mouse eye. Veterinary technician, Heather Cadieux provided assistance on multiple occasions including monitoring of unhealthy mice. Ben Rubin, who provided assistance with statistical analyses on multiple occasions. Dr. Stuart Coupland, from the University of Ottawa, for his assistance in electroretinography training, designing of the electroretinography program, and electroretinography protocol. I would also like to thank the animal care staff at western for their assistance with my animal colonies. I appreciate the time all of these individuals have put aside to assist me and teach me what they know. I have no doubt that it will benefit me in the future.

Finally, I would like to thank my friends and family for their constant support through the duration of my studies. My mother, Judy Henderson, provided moral support from the moment my studies began. All of the success that I have experienced to date is greatly due to her and I cannot thank her enough. I would like to thank my step father, John Henderson, and my brothers, Eric MacPherson and Dave Anspach, for always putting a smile on my face and reminding me that there is life after a Master's degree. I would also like to thank my girlfriend, Evie Mytka, for not disowning me as her boyfriend during the long days and nights of lab work and thesis writing, I couldn't have done this without her behind me. To the Mytka family, thank-you for all of the interest you showed in my research over the past two years. Also, thank-you for buying me a terabyte hard drive, I have made great use of it. Finally, to all of my friends in Bradford, Toronto and London, I apologize for being MIA over the past two years but I appreciate the fact that every time I see you we pick up right where we left off.

Funding from the Plunkett Foundation, Canadian Glaucoma Society, Lawson Health Research Institute - Internal Research Fund, Canadian Institutes of Health Research, Natural Sciences and Engineering Research Council of Canada, and to Dr. Kathleen Hill supported the research in this thesis. Thomas C. MacPherson was funded by the Early Researcher Award, awarded to Dr. Kathleen Hill.

Table of Contents

Certificate of Examination ii

Abstract iii

Co-Authorship iv

Acknowledgements v

Table of Contents vii

List of Figures xiii

List of Appendices xv

List of Abbreviations xvi

Chapter 1. Introduction 1

1.1 Visual Impairment in Canada 1

1.2 General Structures of the Human Eye 2

1.3 Imaging of Ocular Structures *In Vivo* Using Ocular Coherence Tomography 5

1.4 Retinal Structure and the Visual Pathway 6

1.5 Retinal Function Assessed *In Vivo* by Electroretinography 15

1.6 Age-Related Macular Degeneration 16

1.7 Glaucoma 18

1.8 The Use of Mice as Models of Eye Disease 20

1.9 Oxidative Stress and Retinal Disease 21

1.10 The *hq* Mouse as a Model of Oxidative-Stress Induced Retinal Degeneration 22

1.11 Glutamate-Mediated Excitotoxicity 24

1.12 Memantine Hydrochloride 25

1.13 Central Hypothesis and Research Aims 26

Table of Contents (Continued)

Chapter 2. Materials and Methods 28

2.1 Experimental Design 28

2.2 Breeding of *harlequin* Transgenic Mice 29

2.3 Genotyping of Wild Type and *harlequin* Mice 30

2.4 Animal Housing 31

2.5 Delivery of Memantine Hydrochloride 31

2.6 Euthanization of Mice and Tissue Harvest 33

2.7 Mouse Anesthesia and Anticholinergic Drug Delivery 33

2.8 Reversion of Mouse Anesthesia 35

2.9 Dark Adaptation of Mice In Preparation of Electroretinography Testing 36

2.10 Electroretinography Experimental Protocol 37

2.11 Electroretinography Data Analysis 39

2.12 Correlation Studies Using Electroretinography Data 40

2.13 Animal Preparation for Ocular Coherence Tomography Imaging 41

2.14 Ocular Coherence Tomography Image Capture 41

2.15 Ocular Coherence Tomography Data Analysis 42

2.16 Embedding of Left and Right Eyes Postmortem 44

2.17 Sectioning of the Left and Right Eyes 45

2.18 Hematoxylin and Eosin Staining Protocol 45

2.19 Data Analysis for Hematoxylin and Eosin Images 47

2.20 Trichrome and Modified Gram Staining 48

Table of Contents (Continued)

2.21 Dihydroethidium Staining Protocol 49

2.22 Dihydroethidium Data Analysis 50

2.23 Terminal Deoxynucleotidyl Transferase dUTP Nick End Labeling Protocol 51

2.24 Data Analysis of Cellular Apoptosis 52

2.25 Statistical Analyses of Experimental Data 53

Chapter 3. Results 55

3.1 Confirmation of Experimental Genotypes 55

3.2 Survivorship of Mice 55

3.3 Comparison of Body Mass Between Mouse Cohorts 60

3.4 Comparison of Water Consumption Between Mouse Cohorts 64

3.5 Comparison of Average Daily Drug Consumption Between Mouse Cohorts 67

3.6 Retinal Function Assessed By Electroretinography Between OS and OD *In Vivo* 67

3.7 Photoreceptor Response Time Assessed by Electroretinography a-wave Latency 70

3.8 Correlation Studies of Photoreceptor Response Time 74

3.9 Photoreceptor Health Assessed by Electroretinography a-wave Amplitude 75

3.10 Linear Regression Analysis of a-wave Amplitudes 79

3.11 Correlation Studies of Photoreceptor Health 79

3.12 Retinal Response Time Assessed by Electroretinography b-wave Latency 80

3.13 Correlation Studies of Retinal Response Time 84

3.14 Retinal Function Measured by Electroretinography b-wave Amplitude 85

Table of Contents (Continued)

3.15 Linear Regression Analysis of b-wave Amplitudes 89

3.16 Correlation Studies of Retinal Function 90

3.17 Comparison of Tissue Thickness Between OS and OD *In Vivo* 91

3.18 Assessment of Corneal Thickness Between Mouse Cohorts 92

3.19 Assessment of Anterior Chamber Width and Depth Between Mouse Cohorts 100

3.20 Assessment of Retinal Thickness Between Mouse Cohorts 104

3.21 Quantitation of the Structural Integrity of the Cornea 108

3.22 Quantitation of the Structural Integrity of the Ganglion Cell Layer 112

3.23 Quantitation of the Structural Integrity of the Inner Plexiform Layer 115

3.24 Quantitation of the Structural Integrity of the Inner Nuclear Layer 119

3.25 Quantitation of the Structural Integrity of the Outer Plexiform Layer 122

3.26 Quantitation of the Structural Integrity of the Outer Nuclear Layer 125

3.27 Quantitation of the Structural Integrity of the Photoreceptor Segments 129

3.28 Quantitation of the Structural Integrity of the Retina 132

3.29 Comparison of Reactive Oxygen Species Profiles in the Mouse Eye 137

3.30 Comparison of Reactive Oxygen Species in the Corneal Epithelium 142

3.31 Comparison of Reactive Oxygen Species in the Ganglion Cell Layer 147

3.32 Comparison of Reactive Oxygen Species in the Inner Nuclear Layer 147

3.33 Comparison of Reactive Oxygen Species in the Outer Nuclear Layer 148

3.34 Quantitation of Programmed Cell Death in the Mouse Retina 148

Table of Contents (Continued)

Chapter 4. Discussion 152

4.1 Summary 153

4.2 New Features of the *harlequin* Phenotype 154

4.3 Detailed Characterization of the *harlequin* Eye Anterior Segment 156

4.4 Detailed Characterization of Reduced Retinal Function in the *harlequin* Mouse 157

4.5 Detailed Characterization of the *harlequin* Retina 158

4.6 New Insights into *harlequin* Disease Mechanisms 160

4.7 Revised Hypothesis of Disease Mechanisms in the *harlequin* Mouse Model of Retinal Degeneration 162

4.8 The *harlequin* Retinal Disease Mimics Human Dry-AMD not Glaucoma 163

4.9 Memantine Treatment Reduces Body Mass in Wild Type but not *harlequin* Mice 165

4.10 Memantine Treatment Demonstrated Neurological Impairment in the Retina 166

4.11 Memantine Treatment did not Preserve Retinal Function 167

4.12 Memantine Treatment Induced Corneal Histopathology in *harlequin* Mice 167

4.13 Memantine Induced Predicted but Insufficient Protection of Ocular Structure 169

4.14 Evaluation of Memantine Delivery to Wild Type and *harlequin* Mice 169

4.15 Therapeutic Intervention in the *harlequin* Mouse Model of Retinal Degeneration 170

4.16 ERG is a Sensitive Measure of Ocular Function Capable of Early Disease Detection 172

Table of Contents (Continued)

4.17 OCT is Valuable in Detecting Retinal Degeneration and Anterior Structural Abnormalities 174

4.18 Framework of Therapeutic Intervention in the *harlequin* Mouse Model of Retinal Degeneration 177

4.19 Limitations 178

4.20 Conclusions 179

Chapter 5. References 183

***Vita* 268**

List of Figures

Chapter 3

Figure 3.1 Wild type and *harlequin* disease status was evaluated postmortem using PCR amplification 56

Figure 3.2 Kaplan-Meier curve of survivorship through the experimental timeline of ten months 58

Figure 3.3 Mean body mass of experimental cohorts of mice from weaning to ten months of age 61

Figure 3.4 Mean daily water consumption by experimental mice corrected for body mass 65

Figure 3.5 Mean daily memantine consumption by drug-treated mice from two to ten months of age 68

Figure 3.6 Photoreceptor response time measured by a-wave latency from two to ten months of age 71

Figure 3.7 Photoreceptor function assessed by a-wave amplitude from two to ten months of age 76

Figure 3.8 Retinal response assessed by b-wave latency from two to ten months of age 82

Figure 3.9 Retinal function assessed by b-wave amplitude from two to ten months of age 86

Figure 3.10 Corneal thickness assessed by ocular coherence tomography imaging 93

Figure 3.11 A fusion between the iris and cornea of a mouse led to the exclusion of a single data point from the untreated *hq* data set 95

Figure 3.12 Corneal thickening and opacity were observed using ocular coherence tomography imaging 98

Figure 3.13 Anterior chamber width and depth assessed using ocular coherence tomography 101

Figure 3.14 Retinal thickness assessed by ocular coherence tomography imaging 105

List of Figures (Continued)

Figure 3.15 Corneal histopathology assessed using the fixed right eye (OD) of mice postmortem 109

Figure 3.16 Ganglion cell counts of the retina assessed using the fixed right eye (OD) of mice postmortem 113

Figure 3.17 Inner plexiform layer thickness of the retina assessed using the fixed right eye (OD) of mice postmortem 117

Figure 3.18 Inner nuclear layer cell counts of the retina assessed using the fixed right eye (OD) of mice postmortem 120

Figure 3.19 Outer plexiform layer thickness of the retina assessed using the fixed right eye (OD) of mice postmortem 123

Figure 3.20 Photoreceptor cell counts of the retina assessed using the fixed right eye (OD) of mice postmortem 126

Figure 3.21 Photoreceptor segment thickness of the retina assessed using the fixed right eye (OD) of mice postmortem 130

Figure 3.22 Whole retinal thickness of the retina assessed using the fixed right eye (OD) of mice postmortem 133

Figure 3.23 Structural integrity of the central retina of experimental cohorts at ten months of age 135

Figure 3.24 Quantification of reactive oxygen species in the mouse eye of experimental cohorts 138

Figure 3.25 Quantification of reactive oxygen species in the mouse eye of experimental cohorts at specific ages 143

Figure 3.26 Quantification of apoptosis in the mouse eye of experimental cohorts 149

Chapter 4

Figure 4.1 Quantification of apoptosis in the mouse eye of experimental cohorts 180

List of Appendices

Appendix A *The* University *of* Western Ontario Ethics Approval for Animal Use in Research 204

Appendix B Supplementary Figures and Tables 206

Appendix C Comprehensive Tables of Statistically Determined Values 238

List of Abbreviations

•OOR	Lipid Peroxide
$•O_2^-$	Superoxide
ACD	Anterior Chamber Depth
ACW	Anterior Chamber Width
Aif	Apoptosis Inducing Factor Gene (*pdcd8*)
AIF	Apoptosis Inducing Factor Protein
AMD	Age-Related Macular Degeneration
AMPA	α-amino-3-hydroxy-5-methyl-isoxazole-4-propionate Receptor
ANOVA	Analysis of Variance
AR	Anterior Retina
ATP	Adenosine Triphosphate
au	Arbitrary Units
Ca^{2+}	Calcium Cation
CC	Central Corneal
CCAC	Canadian Council on Animal Care
CE	Corneal Epithelium
cGMP	Cyclic Guanosine Monophosphate
CR	Central Retina
CWR	Central Whole Retina
DCIP	2,6-dichloroindophenol
DHE	Dihydroethidium
DMSO	Dimethyl Sulfoxide

DR	Dorsal Peripheral Retina
ELOVL4	Elongation of Very Long Chain Fatty Acids Protein 4
ERG	Electroretinography
FDA	Food And Drug Administration
GABA	γ-aminobutyric acid Neurotransmitter
GCAP	Guanylate Cyclase Activator Protein
GDP	Guanosine Diphosphate
GMP	Guanosine Monophosphate
GTP	Guanosine Triphosphate
H_2O	Water
H_2O_2	Hydrogen Peroxide
H&E	Hematoxylin and Eosin
hq	*harlequin* Affected Phenotype
iGluR	Ionotropic Glutamate Receptor
KA	Kainate Receptor
Memantine	Memantine Hydrochloride
Mg^{2+}	Magnesium Cation
$MgCl_2$	Magnesium Chloride
mGluR	Metabotropic Glutamate Receptor
mo	Month
n	Sample Size
Na^+	Sodium Cation

NMDA	*N*-methyl-D-Aspartate Receptor
NPC	Nasal Peripheral Cornea
OCT	Ocular Coherence Tomography
OD	Right eye
OS	Left Eye
OXPHOS	Oxidative Phosphorylation
p	Correlation Coefficient
PBS	Phosphate Buffered Saline
PCR	Polymerase Chain Reaction
Pdcd8	Programmed Cell Death 8 Gene
PDE	Phosphodiesterase
PR	Posterior Retina
RGC	Retinal Ganglion Cell
ROS	Reactive Oxygen Species
RPE	Retinal Pigment Epithelium
SOD	Superoxide Dismutase
SPSS	Statistical Package for the Social Sciences
TE	Tris(hydroxymethyl)aminomethane and ethylenediaminetetraacetic buffer
TENS	50 mM Tris HCl [pH 8.0], 20 mM ethylenediaminetetraacetic acid, 100 mM NaCl, 1% sodium dodecyl sulfate: buffer
TPC	Temporal Peripheral Cornea
Tris-HCl	Tris(hydroxymethyl)aminomethane Hydrochloride

TUNEL	Terminal Deoxynucleotidyl Transferase dUTP Nick End Labeling
UV	Ultraviolet
VEGF	Vascular Endothelial Growth Factor
VR	Ventral Peripheral Retina
WT	Wild Type

Chapter 1 - Introduction

The ear tends to be lazy, craves the familiar and is shocked by the unexpected; the eye, on the other hand, tends to be impatient, craves the novel and is bored by repetition.

- W. H. Auden (1907-1973)

1.1 Visual Impairment in Canada

North America is currently heading into a growing crisis in visual health. The Canadian population over 60 years of age is projected to double within the next 25 years, soaring from 4.3 million in 2006 to an estimated 9.1 million in 2031 (Population Projections for Canada, Provinces and Territories, 2005). The rapid increase in aged population would elevate the proportion of senior citizens in Canada to ~ 25% of the total population (Population Projections for Canada, Provinces and Territories, 2005). With the increasingly aged population, a seemingly inevitable increase in age-related blindness is resulting.

Though not life threatening, vision loss causes an undeniable decrease in quality of life for many Canadians. Visual impairment has been shown to increase the difficulties in daily living and social interactions (West et al., 1997), while magnifying the risk of depression (Cruess et al., 2007) and accidental falls (Bramley et al., 2008). In 2006 it was estimated that over 610, 000 Canadians were visually disabled, with 108, 000 considered legally blind (Foundations for a Canadian Vision Health Strategy, 2007). This led to an estimated direct cost of $2.9 billion for medical diagnosis, treatment and scientific research (Economic Burden of Illness in Canada., 1998). A further $5 billion dollars was estimated for indirect cost in lost earnings, medical aids and cost of caregivers. The total cost of $7.9 billion places vision loss among the top 10 most costly disease groups in Canada, ahead of both digestive disease and diabetes (Foundations for a Canadian Vision Health Strategy, 2007). Over the next 15 years, the number of patients per ophthalmologist is projected to increase by as much as 76% making patient wait times even longer than the current 6-12 months (Bellan & Buske, 2007). Ophthalmologists currently diagnose and treat close to 4 million Canadian adults having one of the leading forms of age-related blindness.

1.2 General Structures of the Human Eye

Prior to the discussion of specific forms of visual impairment, a general knowledge of the eye's structure and function is necessary. The cornea (Appendix B: Figure 1.1 A) is the most anterior portion of the eye and is composed of four quadrants (Appendix B: Figure 1.1 B). The corneal tissue is made up of five layers: epithelium, Bowman's layer, stroma, Descemet's membrane and endothelium. The corneal epithelium is made up of densely packed keratinocytes with virtually no intercellular space important to its transparency (Dohlman, 1971). Mitosis is limited to the columnar basal cells of the corneal epithelium. As the keratinocytes approach the corneal surface they gradually flatten but typically are not cornified (Schermer et al., 1986). The Bowman's layer is found posterior to the corneal epithelium and is acellular consisting of a random network of type I collagen fibrils (Gordon et al., 1994). The Bowman's layer is succeeded by the corneal stroma which accounts for two thirds of the total corneal thickness. The corneal stroma contains fibroblastic cells known as keratocytes but is primarily made up of type I collagen fibrils. The collagen fibrils have a uniform diameter and are arranged in bundles which are regularly spaced and arranged in parallel to the corneal surface (Meek & Leonard, 1993). This highly structured organization of collagen along with a relatively dehydrated stroma creates a high level of transparency in the cornea. The posterior stroma is bordered with the

Descemet's membrane, a highly specialized basal lamina produced by the corneal endothelium. The interior corneal surface is covered by a layer of cells referred to as endothelial cells. However, they most closely resemble mesothelium cells (Beuerman & Pedroza, 1996). These 'endothelial' cells are mitochondrion rich and critical for corneal dehydration and transparency because endothelial cells transport fluid out of the corneal stroma (Bonanno, 2003). The normal human cornea is completely avascular which adds to corneal transparency but is innervated by axons from the trigeminal nerve (Beuerman & Pedroza, 1996). The corneal tissue merges with the sclera at the corneoscleral junction known as the limbus. The highly organized bundles of collagen give way to a random arrangement that results in a slightly thinner tissue at the limbus. Also, the highly uniform diameter of collagen fibrils is lost, producing an extremely tough opaque tissue (Young, 1985). Blood vessels are found posterior of the the limbus and encircle the cornea in the vertebrate eye (Morrison et al., 1995).

Light enters the eye through the cornea where it is refracted prior to reaching the iris. The iris separates the anterior and posterior chambers of the eye. The iris contains both dilator and sphincter muscles that work together to control pupillary diameter. Sphincter muscles constrict and dilator muscles relax in high levels of light and vice versa in low levels of light. Pupillary diameter controls the levels of light entering the eye protecting the photosensitive retina and optimizing the visual image.

After passing through the pupil, light reaches the lens. The anterior lens contains a monolayer of cuboidal cells creating the lens epithelium. These cells slowly migrate along the anterior edge of the lens until they reach the equator. Epithelial cells then differentiate to form a lens fiber by elongating anteriorly and posteriorly and migrating toward the center of the lens

(McAvoy, 1978). The bulk of the cytoplasmic structures are eliminated including the nucleus and mitochondria while the plasma membrane and cytoplasm experience complex morphological changes. While differentiating, the cells rapidly synthesize specialized lens crystallins which are water-soluble proteins that make up 90% of the proteins found in the lens. These crystallins form high-molecular-weight aggregates that pack densely in the lens fibers. These high-molecular weight aggregates increase the index of refraction in the tissue while maintaining its transparency (McAvoy, 1978; Lovicu & McAvoy, 2005).

The posterior segment of the eye contains three main tissues: sclera, choroid and retina. The sclera is an extension of the cornea that encompasses the eye creating an enclosed fluid-filled capsule. The sclera is vital for the containment of the semi-fluid vitreous humour and for the protection of the neural retinal tissue. The choroid is a highly vascular tissue that provides the blood supply for the external layers of the retina. The choroid is supplied by the ophthalmic artery via the anterior and posterior ciliary arteries (Hayreh, 1975). The retina is the inner most tissue of the posterior eye. The retina is composed of two main tissues: retinal pigment epithelium and neural retina. The retina is the most complex substructure of the eye and is one of the most vascularized and metabolic tissues per tissue weight in the body (Duong et al., 2002). The peripheral retina has a lower concentration of photoreceptors than the central retina and provides peripheral vision. Photoreceptors become more densely packaged and change function and morphology toward the center of the retina. The macula of the human retina has an extremely high density of photoreceptors and is the focal point of light directed by the cornea and lens. The macula is responsible for the high level of detail and visual acuity in central vision. Finally, a large optic nerve exits the back of the eye slightly off center. The optic nerve creates a small blind-spot in peripheral vision because no photosensitive cells are present at the exit point.

1.3 Imaging of Ocular Structures *In Vivo* Using Ocular Coherence Tomography

Clinical diagnosis of structural abnormalities in the eye can be made using ocular coherence tomography (OCT) (Sakata et al., 2008). The basic principle behind OCT is much like ultrasound technology but uses light waves in place of sound waves (Appendix B: Figure 1.2). A super-luminescent diode with emission between 800-850 nm (near-infrared) is typically used for imaging, but lasers can also be used (Grieve et al., 2004). The beam of light emitted from the diode is split into two components, the incident and reference beam. The incident beam is reflected off of tissues in the eye and back into the detector where the incident beam is compared against the initial reference beam. The OCT machine can then measure this 'echo' by comparing the coherence of waves and the interference the waves have experienced (Grieve et al., 2004). A thickness of a tissue can be calculated by multiplying the optical echo delay by the speed of light. In order to do this, the OCT machine relies on assuming an index of refraction for all tissues. OCT images are dependent on differences in optical reflection and backscatter, thus any two tissues may appear as one if they are similar in these properties. A two-dimensional image is produced by focusing the beam of light in successive axial scans in a transverse plane across the eye. The orientation of the transverse plane can be manipulated based on what quadrant of the eye is under investigation. OCT resolution can vary dependent on the machine used but may be as high as 2-3 μm (Sakata et al., 2008). In clinical use, separate machines are used to image the anterior and posterior segments of the eye.

1.4 Retinal Structure and the Visual Pathway

The neural retina is separated from the choroid by the retinal pigment epithelium (RPE) (Appendix B: Figure 1.3). The RPE is a cell layer derived from the neuroectoderm that also differentiates into the neural retina (Strauss, 2005). The RPE is a monolayer of highly pigmented epithelial cells that forms part of the blood/retinal barrier (Rizzolo et al., 2007). The high level of pigmentation in the RPE absorbs excess light that passes through the neural retina and reduces the back scatter of light (Strauss, 2005). This is essential in reducing noise in the visual pathway. The RPE is intimately associated with the adjacent photoreceptor cells of the neural retina and is vital to their survival. The RPE is necessary in the conversion of all-*trans*-retinaldehyde (all-*trans*-retinal) to 11-*cis*-retinaldehyde (11-*cis*-retinal). The chromophore 11-*cis*-retinal binds opsin in the photoreceptors and isomerizes to all-*trans*-retinal when stimulated by a photon of light, necessary for the initiation of phototransduction (Radu et al., 2008). The cells of the RPE are also highly metabolic and have abundant levels of mitochondria located in the basal region of the cell. A major function of the RPE is to phagocytose and recycle the outer segments of photoreceptors which are shed and restored daily (Young & Bok, 1969).

Photoreceptors have two main classifications: cones and rods. Under most light conditions vision is mediated by the cone photoreceptors. The cone photoreceptors are responsible for the detection of color and perform in high levels of background light (photopic conditions). Cones are extremely sensitive to small changes in light, being able to detect a contrast change of ~0.5% (Choi et al., 2005). Humans have three main subtypes of cone photoreceptors based on wavelength of light detected: short wavelength (blue light), medium wavelength (green light) and long wavelength (red light). Cone photoreceptor concentrations are highest in the macula of the human retina providing high levels of visual acuity. Cone photoreceptors become more sparse toward the periphery of eye lowering peripheral visual acuity. An estimated 4.5 million cone photoreceptors are present in the human eye (Curcio et al., 1990).

Evolutionarily speaking, rod photoreceptors have arisen more recently than cones and have superimposed themselves on the cone circuitry of the retina (Lamb et al., 2007). During daylight, rods are typically saturated by light and do not function. The role of rods is revealed in low levels of light (scotopic conditions) where they function in a 'photon counting' manner (Doan et al., 2006). Rods are specialized for the detection of individual photons of light and are much more sensitive than cone photoreceptors. Rods have elongated outer segments and though more recent in origin, are the dominant photoreceptors in the human eye, outnumbering cones approximately 20 fold (Curcio et al., 1990). The high levels of rod photoreceptors in the eye permit the detection of just about every photon that reaches the retina. When light reaches levels where hundreds of photons stimulate a single rod, the photoreceptor becomes saturated and cones become the primary source of visual detection (Williams et al., 1998).

All photoreceptors have three primary functional domains: outer segment, inner segment and synaptic ending. The inner segments of the photoreceptors contain the endoplasmic reticulum, Golgi apparatus and nucleus of the cell. The inner segment of the photoreceptors have high levels of protein synthesis and strict membrane trafficking demands. The plasma membrane also contains potassium channels that allow the efflux of potassium ions in the dark. This balances an influx of ions found in the outer segments of photoreceptors in the dark creating a "resting" dark circulating current (Pelucchi et al., 2008). The inner segment also contains high levels of mitochondria necessary for the metabolic demands of the photoreceptor cells. The mitochondria are densely packed at the distal end of the inner segment in a structure known as the ellipsoid. This provides adenosine triphosphate (ATP) to the outer segment via a narrow ciliary stalk. The ellipsoid also serves an optical purpose by increasing the refractive index of the cell focusing photons of light onto the light sensitive outer segments (Hoang et al., 2002).

The outer segments of the photoreceptors compose the most posterior layer of the neural retina. The outer segments contain hundreds to thousands of stacked lateral foldings of the plasma membrane. In cones, these lateral foldings are consistent with the plasma membrane of the outer segment. In rods, these foldings are pinched off from the outer plasma membrane creating intracellular organelles called disks. The lateral folds of the plasma membrane will be referred to as disks in both rod and cone photoreceptors for ease of understanding. Rhodopsin is the most abundant protein in the outer segment of all photoreceptors (Kwok et al., 2008). Rhodopsin is composed of the 11-*cis*-retinal chromophore bound to an opsin protein. Different forms of the 'rhodopsin' protein are found in the rods and subtypes of cones but will be considered collectively for ease of understanding. The rhodopsin molecule and many other components of the phototransduction cascade are anchored in the plasma membrane of the disks.

In the activation step of phototransduction, a photon of light is absorbed by the rhodopsin molecule. This absorption of light changes the rhodopsin molecule into an enzymatically active state. The absorption of light occurs in the 11-*cis*-retinal molecule with a high probability (~0.67) and converts the isomer into all-*trans*-retinal (Okada et al., 2001). The more linear structure of the all-*trans*-retinal molecule places stress on the rhodopsin molecule causing a series of molecular rearrangements that activate rhodopsin. The activated rhodopsin then binds to a G-protein called transducin via lateral diffusion in the cell membrane (Calvert et al., 2001). Coupling of the proteins activates the transducin molecule. Activation occurs when the Gα subunit of transducin molecule releases a bound guanosine diphosphate (GDP) and replaces it with a molecule of guanosine triphosphate (GTP) from the cytoplasm. The activation of transducin leaves the activated rhodopsin molecule unaltered and free to activate additional transducin molecules (Palczewski & Saari, 1997). A single rhodopsin molecule can activate 150 transducin molecules per second providing an excellent amplification in the phototransduction cascade (Leskov et al., 2000). After activation, the Gα subunit of the transducin molecules disassociate and interact with phosphodiesterase (PDE) via lateral diffusion (Calvert et al., 2001). A one to one ratio of activation is found between transducin and phosphodiesterase (Leskov et al., 2000). Phosphodiesterase is a dimeric structure containing α and β catalytic subunits. Inactivated phosphodiesterase is bound to two additional small γ subunits which inhibit the function of phosphodiesterase (Paglia et al., 2002). When the Gα subunit of the activated transducin molecule couples with the γ subunit of the phosphodiesterase molecule it relieves the inhibitory effects. The activated phosphodiesterase subunits then permit hydrolysis of cytoplasmic cyclic guanosine monophosphate (cGMP). In darkness, there is a resting concentration of cGMP of several micromolar. The cGMP binds to and opens cyclic nucleotide gated channels allowing for the inward flux of Na^+ and Ca^{2+}. The hydrolysis of cGMP by activated phosphodiesterase reduces levels of cGMP in the cell while increasing levels of guanosine monophosphate (GMP) (Zimmerman et al., 1985). This causes a closure of the nucleotide gated channels blocking the inward flux of cations reducing the circulating electrical current and hyperpolarizes the photoreceptor cell (Chen et al., 1994).

The closure of the nucleotide gated channels stops the influx of calcium while exchanger molecules continue to remove intracellular Ca^{2+}. The reduced level of intracellular Ca^{2+} begins the inactivation phase of phototransduction. At high Ca^{2+} concentrations, guanylate cyclase activator proteins (GCAP) are bound to Ca^{2+} inhibiting function. The Ca^{2+} molecules disassociate from the GCAP in low concentrations of intracellular Ca^{2+}. The GCAP can then activate guanylate cyclases. Guanylate cyclases convert intracellular GTP to cGMP opening the nucleotide gated channels, restoring the resting circulating current (Dizhoor & Hurley,1999). Additionally, phosphodiesterase needs to be inactivated in order to keep intracellular cGMP concentrations high. Phosphodiesterase cannot be inactivated until the Gα subunit of the transducin G-coupled protein disassociates from the inhibitory γ subunit of phosphodiesterase. It has been shown that regulators of G protein signaling are expressed in rods and cones promoting GTP hydrolysis (Arshavsky & Bownds, 1992). The regulators of G protein signaling inactivate the Gα subunit of transducin causing it to disassociate from phosphodiesterase and return to the α and β subunits of transducin via lateral diffusion. The first step in rhodopsin inactivation is the phosphorylation of the COOH-terminal residues of the rhodopsin molecule. This is achieved by rhodopsin kinase (Chen et al., 2001). Following phosphorylation, a protein known as arrestin binds with high affinity (Craft et al., 1994). Arrestin is typically inactivated by calcium-bound recoverin in dark conditions. The all-*trans*-retinal molecule is converted to all-*trans*-retinol and exits the photoreceptor cell and is recycled in the RPE.

The axons of the photoreceptor cells extend into the outer plexiform layer of the retina. The visual signal is transmitted to the second-order cells of the retina via cell synapses (Appendix B: Figure 1.4). This is achieved by two different kinds of synapses with second-order cells. The superficial synapses are relatively simple and similar to many synapses found elsewhere in the body. The second form of synapse is the invaginating synapse which is remarkably complex. The invaginating synapse is typically composed of three main components that are forced inside the synaptic terminal of the photoreceptor (Raviola & Gilula, 1975). The central element is typically the dendrite of a bipolar cell. The two other elements embedded deeper in the synaptic terminal and lateral to the bipolar cell are dendrites of horizontal cells.

A synaptic ribbon is located on the presynaptic side of the synapse and is a flat plate that has multiple vesicles attached in an orderly array and allows for a continuous release of neurotransmitters (Harlow et al., 2001). In mammals, cone photoreceptors can have 25 to 40 invaginating synapses whereas rods have only been shown to have a single invaginating synapse. This single synapse in rods has been shown to release 40 vesicles per second in the dark (Rao et al., 1994). The synaptic ribbon has 130 vesicles at docking sites on the presynaptic membrane while having ~640 vesicles on reserve (Harlow et al., 2001). These vesicles are filled with the neurotransmitter L-glutamate in both rods and cones (Kreft et al., 2003). Release of glutamate is continuous in darkness while photoreceptors experience a relatively depolarized membrane potential of about -40 mV. Light hyperpolarizes the photoreceptors and closes the voltage gated Ca^{2+} channels in the synaptic terminal diminishing transmitter release (Rea et al., 2004). The retina sorts information into categories that are kept separate for several more processing steps.

Initially, signals representing local increments or decrements in luminance are separated into two streams, ON and OFF. Within these two streams there is further splitting of signals into 'channels' in which luminance changes are represented with different temporal filtering. In the mammalian retina, ON bipolar cells are postsynaptic only at invaginating synapses, whereas OFF bipolar cells synapse only at superficial synapses (Haverkamp et al., 2001). ON bipolar cells depolarize to increments of light whereas OFF bipolar cells hyperpolarize to increments of light. In the ON bipolar cell pathway, glutamate is released from the photoreceptor in dark conditions where it binds to the metabotropic (G-protein linked) glutamate receptor mGluR6 on the ON bipolar cell dendrite (Snellman et al., 2008). This binding of glutamate to mGluR6 activates a G-protein and causes an enzymatic cascade resulting in the closure of cation channels through which Ca^{2+} enters the cell. This hyperpolarizes the ON bipolar cells in the dark. When a photoreceptor is stimulated by light, levels of glutamate decrease which opens the cation channels depolarizing the cells. As opposed to the unusual and seemingly reversed activation of the ON bipolar cells, OFF bipolar cells follow a more orthodox stimulation. The OFF bipolar cells use α-amino-3-hydroxy-5-methyl-isoxazole-4-propionate (AMPA) or kainate-preferring receptors for detecting glutamate levels. In dark conditions, high levels of glutamate bind to the ionotropic receptors opening non selective cationic channels depolarizing the cells (DeVries, 2000). When low levels of glutamate are present, nonselective cationic channels are closed and the cell hyperpolarizes. Photoreceptor cells also synapse with horizontal cells that contain ionotropic glutamate receptors (Blanco & de la Villa, 1999). Horizontal cells are lateral interneurons that provide both feedback to photoreceptor and feed forward to bipolar cells using the neurotransmitter gamma-aminobutyric acid (GABA; Kamermans & Spekreijse, 1999). This creates a complex neural network in the outer retina.

The cell bodies of the bipolar and horizontal cells are found in the inner nuclear layer. Axons of the bipolar and horizontal cells extend into the inner plexiform layer. Similar to the outer retina, the inner layers of the retina form a complex neural network (Appendix B: Figure 1.5). Bipolar cells can synapse directly with ganglion cells but also provide input to amacrine cells. Bipolar cells are responsible for ~30% of the input directly to ganglion cells whereas amacrine cells make up the majority ~70% input (Sterling, 2004). Amacrine cell bodies are found in the upper stratum of the inner nuclear layer and axons extend into the inner plexiform layer. Amacrine cells are lateral interneurons of the inner retina similar to horizontal cells of the outer retina. Amacrine cells provide feedback to bipolar cells and feedforward to the ganglion cells as well as having extensive connection between themselves. When bipolar cells directly interact with ganglion cells ON bipolar cells synapse chiefly with ON ganglion cells and OFF bipolar cells synapse with OFF ganglion cells. Although it has been shown that some ganglion cells combine ON and OFF inputs. Actually, 10 to 20 different ganglion cell types are found in the ganglion cell layer of the mammalian retina (Roska & Werblin, 2001).

Bipolar cell terminals typically have two components, one usually a ganglion cell dendrite and the other an amacrine cell. Once again, glutamate is the chief neurotransmitter used in these synapses (Tachibana & Okada, 1991). Bipolar cells contain synaptic ribbons with similar levels of vesicle docking sites compared to those found in photoreceptors (Harlow et al., 2001). Just beneath the ribbons are L-type Ca^{2+} channels which open with membrane depolarization. This increases Ca^{2+} in the immediate vicinity of the docked vesicles and allows them to be released very quickly (Mennerick & Matthews, 1996). Axons of OFF bipolar cells extend into the lower stratum of the inner plexiform layer. The axons of ON bipolar cells are limited to the upper stratum of the inner plexiform layer. The organization of ON and OFF synapses allow for ionotropic excitation of both cells. The ON-OFF ganglion cells extend dendrites into both strata of the inner plexiform layer but have very specific connections (Zhang et al., 2005). If the dendrites synapse with an ON bipolar cell receiving signals from a short wavelength photoreceptor, it will have dendrites synapsing with two OFF bipolar cells receiving signals from medium and long wavelength photoreceptors. This makes the cell extremely sensitive to a blue rich signal but less sensitive to green and red light. The cell delivers a blue minus yellow spectrally opponent signal.

N-methyl-D-Aspartate (NMDA) receptors are commonly found on ganglion cell dendrites and can also be seen on amacrine cell dendrites (Fletcher et al., 2000; Hartveit & Veruki, 1997). Both NMDA and AMPA/KA receptors mediate the excitatory input from bipolar cells to ganglion cells (Mittman et al., 1990). NMDA receptors contribute a significant fraction of excitatory input to ganglion cells, and this helps shape the ganglion cell response (Wenzel et al., 1997). The ganglion cell bodies are located in the ganglion cell layer and axons extend to the optic nerve via the nerve fiber layer. The ganglion cell axons then exit the eye and relay the visual signal to the brain. Müller cells are found throughout the retina and are important for the rapid removal of glutamate from the synaptic spaces (Derouiche, 1996).

1.5 Retinal Function Assessed *In Vivo* by Electroretinography

A combined response of the retina can be assessed *in vivo* using electroretinography (ERG). ERG measures the electrical response produced from the cells of the retina after light stimulation. An electrode is placed on the cornea after the eye has been anesthetized by a topical anesthetic. Further electrodes are placed around the eyes. The patient is exposed to a flash of light with fixed luminosity and the resulting signal is recorded. Different light stimuli can test various responses of the retina. For example, all cones and rods will be stimulated when a white flash of light is presented. However, if a blue flash of light is presented, the resulting recording will be from small wavelength cone photoreceptors that detect blue light. Similarly, the condition of the patient can also test certain responses. If a patient has been dark adapted prior to experimentation and a dim flash of light is presented, rod responses can be observed. If a patient has been dark adapted and a bright flash of light is presented, the combination of rod and cone photoreceptors are recorded. Finally, if the patient was not dark adapted prior to experimentation, the rods of the retina would be saturated and a cone response would be recorded.

An ERG trace can be broken down into components to measure specific responses in the retina (Appendix B: Figure 1.6). The a-wave is the first wave observed after stimulation by light. The a-wave latency is a measure of the time it takes the hyperpolarizing signal of the photoreceptors to reach the cornea. The a-wave amplitude is the first negative corneal potential observed and is the summation of photoreceptor responses in the retina (Barraco et al., 2009).

The b-wave latency is a measure of the time it takes the depolarizing signal of the retina to reach the cornea. The b-wave amplitude is a summation of light induced depolarizing cells in the retina (Heynen & van Norren, 1985).

1.6 Age-Related Macular Degeneration

Not surprisingly, three of the four leading forms of blindness are diseases of the retina: macular degeneration, glaucoma and diabetic retinopathy. The fourth leading cause of blindness is a clouding of the lens, known as cataracts. Retinal degeneration is defined as the deterioration of retinal function and structure caused by progressive cell death in the retina (LaVail, 1981). Age-Related Macular Degeneration (AMD) has been the leading cause of blindness in North America for many years. An estimated 965, 000 Canadians show signs of early manifestations of AMD while 253, 000 are in advanced stages of the disease (Foundations for a Canadian Vision Health Strategy, 2007). AMD is a progressive late-onset disease characterized by an initial degeneration in central vision creating a large central blindspot (Appendix B: Figure 1.7 A, 1.7 B). This blindspot can make it difficult to read and recognize faces. The deterioration of sharp central vision is due to degenerating photoreceptors in an area of the retina known as the macula. Like many retinal diseases leading to blindness it is the degeneration of photoreceptors causing an inability to detect light. In advanced stages, vision loss encroaches on peripheral vision.

Two main classifications of AMD exist. The choroidal neovascularization (exudative) or 'wet' form is the more severe form making up 80-90% of all advanced cases of blindness (Pauleikhoff, 2005). Wet AMD is typically due to abnormal blood vessel growth in the retina stemming from the choroid. The neovascularization leads to leakage of blood, fluid and proteins into the retina causing scarring and irreversible damage to the photoreceptors of the retina. The atrophic (nonexudative) or 'dry' form has an accumulation of cellular debris called drusen (yellow plaques) building up between the retina and choroid. These drusen are typically due to a malfunctioning RPE and a breakdown of the photoreceptors in the macula, increasing the risk of retinal detachment. The dry form of AMD makes up 85% of all diagnosed cases of AMD (Bourla & Young, 2006) beginning with slightly blurred vision often recovered by increasing environmental light. As the disease progresses, the blurring becomes more severe and can not be recovered leading to a central blind spot. Both forms of AMD can be detected early with visual acuity tests (Amsler grid) and eye exams. Early detection is necessary for any chance of a successful intervention strategy.

Currently, AMD is one of the most difficult eye diseases to treat and intervention strategies are often ineffective. Wet AMD has multiple modes of intervention including laser surgery, photodynamic therapy and intravitreal injections. Laser surgery introduced in the early 1990's uses a high energy beam focused directly on the new blood vessels destroying them to prevent further vision loss. This treatment is effective but can cause damage to healthy tissue surrounding these vessels and potentially increase vision loss (Kourlas & Abrams, 2007). This surgery is only optional for a small subset of wet AMD patients. Photodynamic therapy was introduced in 2000 as a rapid and painless treatment used to slow vision loss due to AMD. A pharmaceutical drug, verteporfin, is injected intravenously into the arm and travels throughout the body. The drug tends to stick to newly formed blood vessels in the body including those in the eye. Drug treatment is followed by exposure to a bright light focused into the eye activating the drug and destroying the newly formed blood vessels and leaving healthy tissue intact

(Parmeggiani et al., 2008). Patients are urged to avoid light exposure for five days and are typically treated multiple times. Vision loss is depressed but not eliminated or reversed. The most common treatment is intravitreal injections of an anti-vascular endothelial growth factor (anti-VEGF therapy). This blocks the effects of the VEGF proteins that are highly expressed and necessary in neovascularization (Ng & Adamis, 2005). Injections are typically repeated and have been shown to slow disease progression and even improve vision (Michalova et al., 2009). Unfortunately, once dry AMD reaches an advanced disease stage there is no treatment available. If detected in early or moderate stages, a dosage of specific antioxidant and zinc supplements may slow photoreceptor degeneration and progression of the disease, but has not been shown to reverse the disease. It is clear that an appropriate prevention strategy needs to be designed specifically for the more common atrophic form of AMD.

1.7 Glaucoma

Glaucoma refers to a group of diseases affecting the RGC layer and optic nerve. This is dramatically different from the more abundant photoreceptor-related diseases. Approximately 250,000 Canadians were affected by glaucoma in 2006 placing it as the second most common form of blindness in Canada (Foundations for a Canadian Vision Health Strategy, 2007). Glaucoma is considered a progressive late-onset disease of the eye characterized by optic nerve damage and peripheral vision loss (Appendix B: Figure 1.7 A, 1.7 C). There are two main forms of glaucoma: open-angle and closed-angle. Open-angle glaucoma is the most common form of the disease and affects approximately 95% of diseased individuals (Burr et al., 2005). An elevated intraocular pressure often accompanies the disease and is considered to be a major risk factor. However, glaucoma may still occur with normal pressure. A second major risk factor is vascular insufficiency (Joos et al., 1999). This initial loss of peripheral sight creates "tunnel" vision and visual degeneration slowly encroaches on central vision in a seemingly opposite manner of AMD. The mechanisms leading to ganglion cell death in glaucoma are still unknown. Data derived from clinical observation and animal studies show that ganglion cell death and death of the axons in the optic nerve do not occur simultaneously (Osborne et al., 1999). Closed-angle glaucoma may be acute or chronic. In closed-angle glaucoma the fluid found in the anterior chamber is suddenly blocked from proper drainage. Symptoms include severe pain, nausea, vomiting, blurred vision and seeing a rainbow halo around lights. Information regarding risk factors and disease progression remain elusive, but an increase in focused research is leading to potential breakthroughs.

Current treatments for glaucoma include: multiple medications, laser surgery or conventional filtration surgery. Medications are used to reduce fluid production in the anterior chamber and increase drainage. Multiple patients have allergic reactions to these medications and side effects are numerous. The side effects include increased heart rate, irregular heartbeat, depression, impotence, drowsiness, double vision, elevated blood pressure, headaches, blurry vision, fatigue, dry mouth, redness in or around the eye and more (Sharts-Hopko & Glynn-Milley, 2009). When medication does not work, or disease progression is rapid laser surgery is performed (Fink & Jordan, 1984). Laser surgery can be used for open-angle, closed-angle or neovascular glaucoma. A laser is directed toward the trabecular meshwork, iris, ciliary body or retina and is used to reduce eye pressure. A last resort is conventional filtration surgery. It is most often performed with the open-angle form of the disease. All treatments have risks and may not slow disease progression. Along with reducing intraocular pressure, a protective strategy is necessary to save the ganglion cells of the retina and prevent vision loss.

1.8 The Use of Mice as Models of Eye Disease

Mice have been used in many studies of visual impairment with a main focus on retinal degeneration. Mice can be used as a representative mammalian model of human disease due to similarities in genetic composition and physiology (Bogue, 2003; Sieck, 2003). Also, the power of transgenic and knockout mice as models for visual impairment make the laboratory mouse a prime candidate for vision research.

Substantial differences do exist between the visual systems of the nocturnal mouse and the diurnal human. The most notable difference is the size of the mouse eye (Appendix B: Figure 1.8). A mouse eye has a much smaller axial length from anterior cornea to anterior choroid (~ 3.4 mm), compared to the human eye (~ 23-24 mm; Zhou et al., 2008, Stone et al., 2004). A relatively large cornea and lens are also found in the mouse eye. The lens actually accounts for 60% of the axial length of the eye (Zhou et al., 2008). Rods account for 97% of all photoreceptors found in the mouse retina (Smith et al., 2002c), higher than found in humans (~ 95%; Curcio et al. 1990). The mouse retina also does not have a *fovea centralis* (location of the macula). However, the density of rods and cones peaks in the *area centrailis* (found in nonfoveate mammals) and decreases peripherally allowing for heightened central visual acuity (Leamey et al., 2008). There are two types of cone photoreceptors in the mouse compared to three in the human. The two types of photoreceptors differ in their photopigments and absorption spectra. One is maximally responsive to ultraviolet (UV) light (360 nm) and the other is responsive to medium wave length light (508 nm) (Nikonov et al., 2006). The basic functional organization of the mouse retina is largely similar to that of other mammalian species, including humans (Tsukamoto et al., 2001). Mice also have short generation times and large litter sizes. The laboratory mouse can be inbred through multiple generations reducing interanimal variation. The low interanimal variation allows for more precise testing with a smaller sample size and detection of subtle differences. The laboratory mouse has a short life span (~2 years; Jackson laboratories) allowing for the study of age-related disease in a relatively short time period. These features collectively, make the laboratory mouse an excellent model for the study of visual impairment.

1.9 Oxidative Stress and Retinal Disease

The free radical theory of aging hypothesizes that free radicals are generated as a byproduct of metabolism and cause oxidative damage, resulting in aging and death (Harman, 1956). The retina is particularly susceptible to oxidative stress because of its high levels of metabolic activity, oxygen consumption, polyunsaturated fatty acids, and its constant exposure to visible light. Oxidative stress has been implicated in retinal diseases including both AMD (Beatty et al., 2000) and glaucoma (Feilchenfeld et al., 2008; Izzotti et al., 2003). It has also been shown to affect additional ocular tissues (Ohia et al., 2005).

Three main forms of reactive oxygen species (ROS) exist within cells: lipid peroxide (•OOR), hydrogen peroxide (H_2O_2) and the superoxide anion (•O_2^-) (Mills, 1960). ROS may be produced endogenously as a natural byproduct of metabolism (St-Pierre et al., 2002), or induced by exogenous sources such as environmental mutagens (Drechsel & Patel, 2008). High ROS levels lead to cell death as a result of lipid peroxidation (Zitting et al., 1981), protein oxidation (Starke-Reed & Oliver, 1989), and DNA damage (Yamafuji & Uchida, 1966).

Oxidative stress occurs when ROS levels outweigh the cell's antioxidant defense mechanisms (Sayre et al., 2001). An imbalance can occur by increased environmental oxidative stress or a genetic disorder resulting in decreased endogenous antioxidant defenses (Sayre et al., 2001). The enzymes involved in endogenous antioxidant defense are typically superoxide dismutase, catalase, and glutathione peroxidase (Marklund et al., 1982). In addition, antioxidants obtained in the diet, such as zinc, iron, and vitamin E, act in combination with endogenous antioxidant defense mechanisms (Fang et al., 2002). The ability to counteract ROS is associated with a decreased likelihood of oxidative stress-associated disease and an increased life span (Fang et al., 2002).

1.10 The *hq* Mouse as a Model of Oxidative-Stress Induced Retinal Degeneration

The *harlequin* ($X^{hq}Y$; *hq)* mouse is a model of premature aging and ROS-associated neurodegeneration (Klein et al., 2002). The *hq* mouse has a spontaneous proviral insertion in the X-linked programmed cell death 8 gene (*Pdcd8*). This proviral insertion is located in the first intron of *Pdcd8* which is typically involved in transcriptional regulation. The interrupted intron 1 leads to a downregulation of *Pdcd8* expression in tissues of *hq* mice (Klein et al., 2002; van Empel et al., 2005; Zhu et al., 2007; Srivastava et al., 2007). The *Pdcd8* gene codes for the apoptosis-inducing factor (AIF) protein (Klein et al., 2002). Functional AIF has two main roles in cellular life and death; it is involved in the oxidative phosphorylation (OXPHOS) pathway and is an effector of cell death in apoptosis when released from the mitochondrion (Susin et al., 1999). AIF is typically found in the mitochondrial intermembrane space (Susin et al., 1999) or the inner mitochondrial membrane (Arnoult et al., 2002) where it interacts with complex I of the OXPHOS chain in an unknown fashion. However, in apoptotic conditions, AIF translocates to the nucleus and induces chromosomal condensation and large-scale DNA fragmentation (Susin et al., 1999). AIF has also been found to have a free-radical scavenging domain that sequesters ROS in neuronal cells (van Empel et al., 2005; van Empel et al., 2006). With lower AIF levels in the cells of *hq* mice, an increase in endogenous ROS ensues (Klein et al., 2002; van Empel et al., 2005).

The *hq* mouse exhibits ROS associated delayed development noticeable at birth, patchy or no hair growth, and many late-onset abnormalities (Klein et al., 2002). Decreased AIF production leads to increased peroxide sensitivity resulting in ROS-induced DNA mutations in neurons (Stringer et al., 2004). By three months of age, terminally differentiated ganglion cells and amacrine cells in the peripheral retinal begin to degenerate (Klein et al., 2002). By four months of age, retinal function was shown to be reduced through ERG testing and cerebellar granule neurons begin to degenerate. The *hq* mice were also observed to have cell loss in the ganglion cell layer, the inner nuclear layer and outer nuclear layers by four months of age (Klein et al., 2002). By 6 months of age, *hq* mice exhibit higher levels of oxidative stress and apoptosis in the olfactory epithelium (Vaishnav et al., 2008). By seven months, of age there is a significant decrease in the size of the cerebellum (Klein et al., 2002). ERG experiments have shown that *hq* mice are completely blind by ten months of age. At 11 months of age, most retinal cell layers exhibit cellular loss. The *hq* disease phenotype demonstrates the effects of elevated levels of

ROS thought to be associated with age-related disease. This makes the *hq* mouse an ideal candidate for the study of ROS-associated, age-related blindness, a common hypothesis in many retinal degenerative disorders.

1.11 Glutamate-Mediated Excitotoxicity

Glutamate-mediated neuronal death, known as excitotoxicity, was discovered forty years ago (Olney, 1969). Both cell culture studies and various *in vivo* models of neurodegeneration have shown that glutamate can kill many different types of mammalian neurons in a concentration-dependent and receptor-mediated manner (Mattson, 1997; Sonsalla et al., 1998). Activation of ionotropic glutamate receptors results in an increase in the concentration of cytoplasmic Ca^{2+} cations. Typically it is the AMPA/KA or NMDA ionotropic receptor channels that are stimulated. In addition to the increased levels of cytoplasmic Ca^{2+} due to ionotropic glutamate receptors, the binding of glutamate stimulates the release of Ca^{2+} from the endoplasmic reticulum (Jaffe & Brown, 1994). It has been demonstrated that this release of Ca^{2+} from the endoplasmic reticulum aids in excitotoxic conditions and, when blocked, can protect cells from excitotoxic insult (Mattson et al., 2000). High levels of cytoplasmic Ca^{2+} activate cysteine proteases called calpains that degrade a variety of substrates including cytoskeletal proteins, membrane receptors, and metabolic enzymes (Bi et al., 1996; Caba et al., 2002; Guttmann et al., 2002). Calpains have also been shown to activate caspases and promote apoptotic cascades (Leist et al., 1997). High levels of cytoplasmic Ca^{2+} also increase oxidative stress through the activation of oxygenases (Smaili et al., 2009), deviation of normal mitochondrial calcium and energy metabolism (Sengpiel et al., 1998), and induction of membrane lipid peroxidation (Goodman et al., 1996). ROS are generated in response to glutamate-induced Ca^{2+} influx and include the superoxide anion radical, hydrogen peroxide, hydroxyl radical and peroxynitrite (Culcasi et al., 1994; Sengpiel et al., 1998). Although oxidative stress is induced by excitotoxicity, studies have shown that neurons are more readily killed by glutamate when they are under conditions of increased oxidative stress prior to excitotoxic insult (Kruman et al., 1999). Glutamate-mediated cell death was originally described in the retina in 1957 before the 'discovery' of excitotoxicity (Lucas & Newhouse, 1957) and has been a focus of study ever since.

1.12 Memantine Hydrochloride

Currently, memantine hydrochloride (memantine) is prescribed to control dementia related to Alzheimer's Disease because of its effects in moderating excitotoxicity (Schneider & Sano, 2009). Memantine is a food and drug administration (FDA)-approved low-affinity voltage-dependent uncompetitive antagonist of NMDA receptors (Appendix B: Figure 1.9; Lipton, 2004). It is currently marketed under the brand names: Axura®, Akatinol®, Namenda®, Ebixa®, Abixa® and Memox®. Memantine rapidly passes the blood-brain barrier (Riemer et al., 2008) and has been shown to pass the blood-retinal barrier (Kusari et al., 2007). Memantine is completely absorbed by the gastrointestinal tract and reaches peak concentrations in the blood between five and eight hours after consumption (Ebixa® Data sheet, 2009). Memantine is metabolized into three inactive byproducts in the liver. Finally, 60-80% of memantine and its metabolites are eliminated via the urine with 10-25% of the drug eliminated in the bile and feces. The elimination half-life is 60-100 hours.

At highly negative cell membrane potentials, the NMDA receptor is typically blocked by the binding of a magnesium ion within the conductance pore. This can only occur when the pore has been opened by the binding of glutamate. As the cell depolarizes and membrane potential increases, Mg^{2+} is removed from the pore increasing cation influx and excitotoxic insult. Memantine acts in a similar fashion to Mg^{2+} but memantine has a higher affinity to NMDA receptors (Rogawski & Wenk, 2003). When NMDA receptors are opened memantine binds within the conductance pore essentially blocking cation influx. Though memantine has a higher affinity to NMDA receptors compared to Mg^{2+}, memantine is still considered to have a low-affinity. The low-affinity and high 'off' rate kinetics of memantine preserve the physiological function of the NMDA receptor and protects it from over stimulation (Rogawski & Wenk, 2003). It is important to preserve physiological function of these receptors because when completely blocked potential for a coma is elevated (Lipton, 2004). Memantine has a high potential to ease diseases of the central nervous system, including retinal degeneration, by moderating excitotoxicity (Hare et al., 2004).

1.13 Central Hypothesis and Research Aims

I hypothesized that oxidative stress-induced excitotoxicity is the causative factor of retinal degeneration in the *hq* mouse. With the naturally elevated levels of endogenous ROS in the *hq* mouse, cells surpass a threshold and trigger apoptosis. In extreme cases the cell may die through necrosis, releasing intracellular contents into the synaptic space. The release of high levels of glutamate increases ROS in downstream neurons through excitotoxic insult beginning a deadly chain reaction. Consequently, treatment with memantine, a potential neuroprotective drug, should slow or stop disease progression in the *hq* mouse. There are three primary aims to my research: 1) To characterize *hq* retinal degeneration and assess proposed similarities to human glaucoma. 2) To test whether memantine hydrochloride's anti-excitotoxic effects can substantially conserve retinal function in the aging wild type mouse and the *hq* disease mouse. 3) To evaluate oxidative stress-induced excitotoxicity as a possible disease mechanism through detailed ocular phenotyping of the *hq* disease mouse. The aims of this research will be achieved by the testing of specific predictions. First, I predicted that the *hq* mutant mouse model would demonstrate initial degeneration of peripheral ganglion cells leading to a disease phenotype mimicking that of glaucoma. I predicted that memantine would slow retinal degeneration in the normal wild type (WT) aging process and would preserve retinal function in the *hq* disease model. I predicted that retinal degeneration would be preceded by an increased level of ROS in the *hq* disease retina. I predicted that levels of programmed cell death and programmed cell necrosis (Festjens et al., 2006) are elevated in the *hq* retina due to ROS production. Finally, I predicted that cellular death would lead to an increased level of ROS in downstream neurons causing a deadly chain reaction through excitotoxic insult.

Chapter 2 - Materials and Methods

2.1 Experimental Design

In order to reduce sources of variation at all levels in the experimental design, a block design was employed (Piegorsch et al., 1995). A block design refers to the treatment of animals, processing of samples and performance of assays for representative members of all study groups in parallel in order to have the nonexperimental or confounding variation spread equally across the experimental design. All experimental protocols were approved by the Canadian Council on Animal Care (CCAC) prior to the study's start date (Appendix A). The experimental design consisted of 100 mice, 50 male wild type (WT) and 50 male *hq* mice (Appendix B: Figure 2.1). These were further divided into four groups of animals consisting of 25 animals each: male WT untreated mice, male WT mice exposed to memantine hydrochloride, male *hq* untreated mice and male *hq* mice exposed to memantine hydrochloride. The cohorts of untreated animals received regular drinking water *ad libitum* as a vehicle control. The memantine-treated cohorts received drinking water containing dissolved memantine hydrochloride (Sigma-Aldrich, St. Louis, MO) *ad libitum.* Drug-treated mice had a target memantine dosage of 30 mg/kg/day (Minkeviciene et al., 2004). Memantine delivery began when animals reached one month of age. Retinal function was assessed *in vivo* using electroretinography (ERG) testing in a longitudinal fashion beginning at two months of age and continuing monthly until date of euthanization. Similarly, eye structure was assessed *in vivo* using Ocular Coherence Tomography (OCT) imaging beginning at two months of age and continuing monthly until date of euthanization. Five mice per experimental cohort were euthanized at two, four, six, eight and ten months of age. Postmortem histopathology was performed on all eyes to determine significant changes in eye structure that could be associated with a loss in retinal function.

2.2 Breeding of *harlequin* Transgenic Mice

Female harlequin (*hq)* mice (B6CBACa $A^{w-J}/A\text{-}Pdcd8^{Hq}/J$) at four months of age and heterozygous for the *hq* mutation ($X^{hq}X$) were obtained from The Jackson Laboratory (Bar Harbor, ME). These mice were bred to 3-month-old male C57Bl/6J mice, obtained from Taconic Farms (Germantown, NY). Progeny in the F1 generation were either hemizygous for the *hq* mutation ($X^{hq}Y$), heterozygous for the *hq* mutation ($X^{hq}X$), or wild type (XX or XY). F1 female mice heterozygous for the *hq* mutation ($X^{hq}X$) were bred with F1 male mice hemizygous for the *hq* mutation and were subsequently bred to the CBA/CaJ inbred mouse strain for four to six generations. Mice selected for this study were male hemizygous *harlequin* disease ($X^{hq}Y$; *hq)* or male wild type (XY) mice. Obvious phenotypes such as low body mass and sparse fur were noted and initially used to identify *hq* mice for this study prior to genotyping. Animals were ear notched for identification and tail clipped for genotyping purposes 10-12 days after birth. Three weeks after birth, WT animals were weaned from their mother and included in the experimental design. Due to developmental delays, *hq* mice were allowed to stay with their mother for additional time to increase body mass.

2.3 Genotyping of Wild Type and *harlequin* Mice

DNA was extracted from frozen tail clippings of 10 - 12 day old mice using a small-scale genomic DNA extraction protocol. Tail clippings were initially minced and placed into a 200 µl PCR tube containing TENS buffer and Proteinase K (Invitrogen, Burlington, ON). The tissues were incubated at 55°C for 16 hours followed by a 5 min incubation at 95°C. The suspension was then transferred to a 1.5 ml phase lock gel tube (Qiagen, Mississauga, ON) with an equal volume of a 50:50 phenol:chloroform mix. The suspension was centrifuged for 5 minutes at 14,000 rpm and supernatant was transfered to a clean 1.5 ml eppendorf tube. DNA was precipitated using 100% ethanol stored at -20°C and centrifugation at 14,000 rpm for 10 minutes. Ethanol was removed and the pellet was allowed to air dry prior to dissolving overnight in 30 µl of TE buffer.

The *Aif* genotype of each mouse was determined by Polymerase Chain Reaction (PCR) amplification of WT and mutant *Aif* genes using a triprimer mixture (Klein et al., 2002; Stringer et al., 2004). These primers were designed to have a 'wild type forward': 5' - CTA TGC CCT TCT CCA TGT AGT T - 3', 'wild type reverse': 5' - AGT GTC CAG TCA AAG TAC CGG G - 3', and a 'proviral insertion forward': 5' - GAA CAA GGA AGT ACA GAG AGG C - 3'. PCR reaction tubes (VWR, Mississauga, ON) were filled with 30 µl of reaction mixture composed of the following: 1.2 µg DNA, 0.1 mM of each *Aif* primer, 0.2 mM of each dNTP, 3µL 10x PCR buffer, 0.6 U *Taq* polymerase, and 2 mM $MgCl_2$. PCR amplification was performed in a GeneAmp PCR System 9700 (Applied Biosystems, Foster City, CA) with an initial template denaturation step at 94°C for 3 minutes. The initial template denaturation was followed by 35 cycles of amplification using a 30 second denaturation step at 94°C, a 1 minute annealing step at

62°C and a 1 minute elongation step at 72°C. The amplification was completed with a final 10 minute elongation step at 72°C and was held at 4°C. PCR amplicons were electrophoresed through a 1.5% agarose gel in order to assess amplicon sizes. The wild type *Aif* allele generated a 537 bp PCR amplicon with the 'wild type forward' and 'reverse' primers, while the *hq Aif* allele generated a 725 bp PCR amplicon with the 'proviral insertion forward' and 'wild type reverse' primers.

2.4 Animal Housing

All experimental mice were housed on the same rack in the animal facility (*The* University *of* Western Ontario, London, Ontario). Mice were housed individually according to a protocol approved by the Canadian Council on Animal Care (Appendix A). Housing room conditions included a 10/14 hour light/dark cycle at 21°C (±1°C) with a relative humidity of 44 to 60%. The mice received food (PMI foods, St. Louis, MO) and water or memantine dissolved in water *ad libitum* depending on the experimental animal group.

2.5 Delivery of Memantine Hydrochloride

Memantine hydrochloride was delivered to experimental animals via ingestion. Custom drinking tubes were designed to monitor water consumption on a daily basis. The drinking tubes were comprised of a stainless steel drinking tip (Ancare, Bellmore, NY) placed in a 25 ml Corning disposable serological pipette (Fisher Scientific, Ottawa, ON) with both ends removed. The stainless steel drinking tip was held in place by Tygon® Silicone tubing (Cole Parmer, Montreal, QC) with an inner diameter of 0.313" and an outer diameter of 0.500" creating a water tight seal. The other end of the pipette was plugged with a size "00" rubber stopper (VWR) creating an air tight feeding tube that allowed for determination of water consumption. Initially, a modified drinking tube filled with water was set up in an empty cage to determine levels of water loss from an unused drinking tube. An average water loss of 0.4 ± 0.09 ml per week was determined on weeks where the housing rack was immobile. On weeks of routine cleaning involving hydrofoaming of the room and the movement of the housing racks, an average water loss of 0.6 ± 0.15 ml per week was determined. Average water consumption therefore, could be a slight over estimate but not an underestimate.

Memantine hydrochloride was purchased from Sigma-Aldrich (St. Louis, MO) and dissolved into the drinking water for animals. Weanlings ingesting memantine hydrochloride were initially given water via custom drinking tubes to determine average water consumption per day. At the end of the week a mass was determined for the weanling. The average daily water consumption from the previous week was used to determine the estimated water consumption for the following week, including a 15% overestimation. This 15% overestimation was used because of water leakage while the animal was drinking, eating or while the cart was being moved. This also allows for the variation of water consumption between weeks and allows for some left over water so that the animal was never without drinking water. The mass and average daily water consumption were used to determine a weekly volume of water and concentration of memantine needed to approach 0.030 mg/g/day of memantine ingestion (Minkeviciene et al., 2004). Body weight was measured at the end of every week and water consumption was measured daily until date of euthanization.

2.6 Euthanization of Mice and Tissue Harvest

Mice were euthanized by CO_2 inhalation at two, four, six, eight and ten months of age in photopic conditions. Upon euthanization, the mass of each mouse was recorded along with any visually noticeable abnormalities. Immediately following blood collection, the left eye (OS) was enucleated and pierced with a 30 G needle. The OS was then placed into the top left corner of a cryomold containing optimal cutting temperature media (Somagen Diagnostics, Edmonton, Alberta). The orientation of the OS was monitored closely so that reproducible cross sections of the eye could be taken when mounted on a cryostat stage. The cryomolds were then flash-frozen in liquid nitrogen prior to storage in a -80°C freezer. The right eye (OD) was enucleated and placed into an eppendorf tube containing 1 ml of Telly's fixative (5 ml of Glacial Acetic Acid, 10 ml of 40% Formalin, 85 ml of 70% Ethanol) for a minimum of 48 hours at room temperature prior to storage in 70% ethanol at room temperature. Genotyping of animals (see section 2.3) was confirmed after the date of euthanization. Multiple tissues were also harvested, flash frozen in liquid nitrogen and stored in cryovials in a -80°C freezer for future analysis.

2.7 Mouse Anesthesia and Anticholinergic Drug Delivery

Mice needed to be deeply anesthetized for all *in vivo* assays in order to reduce movement and obtain accurate results. Deep anesthetization was achieved using a ketamine Xylazine cocktail (Permit #: 2007-097-09). Ketamine (Bioniche Animal Health Canada, Belleville, Ontario) is classified as an NMDA receptor antagonist and leads to analgesia, anesthesia, elevated blood pressure and bronchodilation. Ketamine is typically used with a sedative to achieve deep anesthesia. Xylazine (Bayer AG, Leverkusen, Germany) is a lipid soluble sedative typically used in large animals but also commonly paired with ketamine in rodent research. Xylazine is an agonist at the α_2 class of adrenergic receptors, a class of G protein-coupled receptors. Unfortunately, Xylazine can have adverse effects including bradycardia making a ketamine Xylazine cocktail dangerous. The cocktail typically has an estimated 10% mortality rate in rodents which can reach 50% in some experiments (Woodward et al., 2007).

Mouse body mass was measured in the early morning on date of anesthetization. A mixture of ketamine and Xylazine was made freshly and specifically for each animal containing 0.1 mg/g body mass of ketamine and 0.005 mg/g body mass of Xylazine. The cocktail was made by combining 1 ml of a stock solution of ketamine at a concentration of 100 mg/ml to 0.25 ml of a stock solution of Xylazine at a concentration of 20 mg/ml. This mixture was then diluted using 1.75 ml of 1X Phosphate Buffered Saline (PBS) (Santa Cruz Biotechnology, Santa Cruz, CA) and delivered at a concentration of 0.003 ml/g body mass in order to achieve approximately 45 minutes of anesthesia. Anesthetic was delivered by an intraperitoneal injection using a 1 cc (100 unit) insulin syringe with a permanently attached ½" 27 G needle (Terumo medical, Vaughan, Ontario). Depth of anesthesia was assessed by a toe pinch. If there was any sign of reflex, anesthesia was terminated and tried two days later. Animals did not receive anesthetic if body mass was under 13 g, the animal was noticeably dehydrated (tested by pinching the scruff of the animal and watching elasticity of the skin), or the animal did not have a typical response to handling likely due to illness. Finally, mice were maintained on a circulating water heating pad (Gaymar, Orchard Park, New York) to keep core body temperature as close to 37°C as possible.

An anticholinergic drug was delivered for protection due to the low body weight and compromised heart of the *harlequin* disease mouse. The drug was delivered to both *harlequin* disease and wild type mice to eliminate variability between cohorts. The anticholinergic drug, atropine (Ayerst Veterinary Laboratories, Guelph, ON), was used at a dose of 0.01 mg/kg. Atropine increases heart rate by increasing the firing rate of both the sinoatrial and atrioventricular nodes of the heart while reducing bronchiole secretions simultaneously. This is important because Xylazine lowers heart rate and causes large secretions in the mouse leading to possible heart failure and/or drowning during anesthesia. Mice with a mass equal to or above 35 g received a dose of atropine from a stock concentration of 0.04 mg/ml in order to have an injection volume below 0.05 ml. Animals with a mass below 35 g received the same dose from a diluted solution of atropine at a concentration of 0.008 mg/ml in order to have an injection volume above 0.001 ml. Atropine was delivered by a subcutaneous injection with a 3/10 cc (30 unit) insulin syringe with a permanently attached ½" 29 G needle (Terumo) immediately upon deep anesthesia.

2.8 Reversion of Mouse Anesthesia

Animals were removed from anesthetic using a reversal agent, atipamezole, to avoid heart failure. The brand name drug known as antisedan® (Orion Pharma, Espoo, Finland) is a synthetic α_2-adrenergic antagonist used for the reversal of the sedatives dexmedetomidine and medetomedine in dogs, however it has also been used to reverse a ketamine Xylazine cocktail in rodent research (Pertovaara et al., 2005). This allows for control over the length of sedation reducing the chances of bradycardia and heart failure often occurring at the end of anesthesia.

Antisedan® was delivered at a dose of 1 mg/kg in order for animals to recover from the dosage of anesthetic. Again, animals with a body mass equal to or above 35 g received a dose of antisedan® from a stock solution at a concentration of 5 mg/ml in order to have a low injection volume. However, animals with a mass below 35 g received a similar dose from a diluted solution of antisedan® with the concentration of 1 mg/ml in order to have a large enough injection volume to be easily controlled. Antisedan® was delivered via an intramuscular injection in the hamstring muscle of the animals using a 3/10 cc (30 unit) insulin syringe with a permanently attached ½" 29 G needle (Terumo). Time of delivery depended on length of assays but was typically 30-40 minutes after anesthetic delivery. Animals were monitored on a circulating water heating pad until they were able to enter the sternally recumbent position on their own accord. Animals were then placed back in their cage and were monitored occasionally for a further 45 minutes.

2.9 Dark Adaptation of Mice In Preparation of Electroretinography Testing

Animals were weighed for anesthetic drug dosage purposes prior to the electroretinography (ERG) procedure (see section 2.2). A maximum of 4 animals were then dark adapted for a minimum of 4 hours prior to the ERG experiment. This occurred in two modified Rubbermaid totes (Canadian Tire, London, ON) with 0.265" holes drilled into the top of them which blocked light and allowed for adequate airflow. Individual totes were large enough to hold two separate cages with feed (PMI foods, St. Louis, MO) and water bottles or modified drinking tubes *ad libitum* to ensure hydration to the animal. Animals were kept in totes underneath a covered desk until their specific electroretinography experiment to ensure continuous dark adaptation. Electroretinography room conditions included a constant dark cycle at 21°C (±1°C) with a relative humidity of 44 to 60%. Cardboard was used to eliminate all exogenous light that could enter the room and all power lights on machinery were covered using folded paper towel and electrical tape.

2.10 Electroretinography Experimental Protocol

All animals were anesthetized with a freshly prepared cocktail of ketamine and Xylazine (see section 2.2). This achieved 45 minutes worth of deep sedation for each testing session. Animals were not subjected to testing if a low body mass or sickness was encountered (see section 2.7). Anesthetized animals were placed on a circulating water heating pad to keep the animals' body temperature regulated avoiding a decline in ERG amplitude. The circulating water heating pad interfered with electroretinography amplification causing artifacts in the traces, so animals were transfered to a heated microwavable corn bag (Petstages, Northbrook, IL) which was placed underneath a 100W infrared heat lamp (Exo Terra, Montreal, QC) throughout electroretinography experiments.

Pupil dilation was attained by two commonly used topical drops: a 2.5% solution of Mydfrin (Alcon, Hünenberg, Switzerland), and a 1% solution of Mydriacyl (Alcon, Hünenberg, Switzerland) with a minimum of 5 minutes between topical administrations. The cornea of the mouse was then further anesthetized with a 0.5% solution of Alcaine (Alcon, Hünenberg, Switzerland) and kept hydrated using a natural tear gel (Novartis, Dorval, QC).

Electroretinography mimicked scotopic conditions due to levels of dark adaptation. A reference lead (Grass Technologies, West Warwick, Rhode Island) was placed in the mouth of the anesthetized animal with a gold mini-plate resting on the tongue (Appendix B: Figure 2.2). A grounding lead (Grass Technologies, West Warwick, Rhode Island) was attached to the animal using a small needle inserted subcutaneously in the tail close to the body. Non-invasive electrodes (Grass Technologies, West Warwick, Rhode Island but modified at the University of Ottawa (Ottawa, Canada)), were formed by a small wire twisted into a small loop that would fit comfortably on the eye of the animal. These electrodes were placed on the cornea and were designed to record the electrical response of the retina from the corneal surface. Optimal responses were recorded when the electrode made contact with the center of the cornea. Electrical response from the retina was triggered by a series of white light flashes coming from a colordome stimulator (Diagnosys, Lowell, Massachusetts) placed over the animals head. These flashes steadily increased in intensity over eleven different steps. The first of these steps having the intensity of 0.01 cd.s/m^2 increasing to 25 cd.s/m^2 in the eleventh step. Five flashes exist in each of these eleven steps but were separated by an interstimulus interval to maintain a state of dark adaptation and photoreceptor recovery between flashes. In the initial steps, the interstimulus interval lasted for a period of five seconds but at higher intensities the interstimulus interval increased to a full 10 seconds between flashes. While turned on, the infrared heat lamp caused a dampening in wave amplitude. Dampening was initially observed by turning the infrared lamp on in the third flash of a specific step to assess its effects. The infrared lamp was turned off during ERG experiments but the ERG program was paused for five minutes between the 6th and 7th step. The heat lamp was turned on to warm the animal during this 5 minute pause. The outputs from the leads were differentially amplified and digitized at a sensible rate ($\geq$ 1000

Hz) and was recorded using Espion software from Diagnosys (Lowell, Massachusetts). After all eleven steps had been completed, the electrodes were removed and the animal was returned to the circulating water heating pad to await subsequent testing.

2.11 Electroretinography Data Analysis

Electroretinography data analysis began immediately after electroretinography experimentation. Traces were observed to determine if any abnormalities may have occurred. In cases where electrodes lost contact with the eye, traces were removed from data analysis but kept in an archive. The Espion software automatically determines a-wave and b-wave amplitudes based on expected latency periods. All wave amplitudes were verified and adjusted according to true wave amplitudes. Averages were taken from all 5 traces at each step and all eleven steps were exported as an excel file for data analysis. Data were organized according to mouse age and experimental cohort. The tenth step was chosen for further data analysis because it contained a mix of rod and cone responses and provided the most information of all steps. Photoreceptor response time was assessed over the lifespan of all cohorts by analyzing a-wave latencies. Further analysis of photoreceptor health included analysis of a-wave amplitudes. Whole retinal response time was determined by analysis of b-wave latencies for each mouse on a monthly basis and as a total over experimental lifespan. Further analysis of whole retinal function included analysis of b-wave amplitudes to determine how well the visual signal was being transported through the retina. Data points were excluded from analysis if technical error such as a malfunctioning electrodes occurred or unrealistic data were obtained. For example, a dramatic increase in b-wave amplitude at a specific month but typical amplitudes for previous and later months. Additional cohorts of WT and *hq* mice were added to determine effects of multiple dates of anesthetization and ERG testing. The WT cohort consisted of six animals: one animal at nine months of age, one animal at ten months of age, two animals at eleven months of age and two animals at twelve months of age. The *hq* cohort consisted of three animals: one animal at nine months of age, one animal at ten months of age and one animal at eleven months of age. Mice were tested a single time using ERG and data were averaged and presented as eleven month data sets. The data from these mice have been presented as the WT single ERG cohort and *hq* single ERG cohort, respectively.

2.12 Correlation Studies Using Electroretinography Data

Correlation studies were performed using Microsoft Excel Software (Redmond, WA) to determine if specific *in vivo* variables correlated with retinal function. For each mouse, data from electroretinography studies (a-wave latency, a-wave amplitude, b-wave latency and b-wave amplitude) were compared to additional data obtained *in vivo* (body mass, water consumption and drug concentration). Body mass correlation tests were performed using the untreated and memantine-treated *hq* cohorts at two, four and six months of age when sample size was large. Body mass correlation tests were used to determine whether retinal degeneration was correlated with lower body mass in diseased animals. Water consumption correlation tests were performed using untreated and memantine-treated *hq* cohorts at two, four and six months of age. Water consumption correlation tests were used to determine whether hydration was inversely correlated with retinal degeneration. Drug concentration correlation tests were performed with the memantine-treated WT and *hq* cohorts at two, four and six months of age when sample size was adequate. Drug correlation tests were used to determine whether the concentration of memantine slowed retinal degeneration. A coefficient of determination (R^2) was obtained after plotting data points. The correlation coefficient (*p*) was determined and assigned a positive or negative value based on the slope of linear correlation. No correlation was measured between variables if **p** was lower than 0.1 or -0.1. Small linear correlations were determined if the **p** fell within 0.1 to 0.3 or -0.1 to -0.3. Medium linear correlations were determined if **p** fell within 0.3 to 0.5 or -0.3 to -0.5. Finally, a strong linear correlation was assigned to **p** falling within 0.5 to 1.0 or -0.5 to -1.0.

2.13 Animal Preparation for Ocular Coherence Tomography Imaging

A custom platform was designed for OCT imaging by the Engineering department at *The* University *of* Western Ontario (Appendix B: Figure 2.3). This design allowed for minute manipulation allowing for precise alignment of the animals eye in front of the OCT machine for highly reproducible images. In short, the platform can be rotated 360° in both the horizontal and vertical plane which allowed for a properly oriented animal. The platform can also be vertically raised and lowered and moved in any of the four horizontal planes. The platform allowed quick and easy imaging of both the anterior (cornea) and posterior (retina) segments of the eye.

2.14 Ocular Coherence Tomography Image Capture

Anesthetized animals (see section 2.2) were subjected to OCT testing using the Visante™ Ocular Coherence Tomography Machine (Zeiss Canada, Missassauga, Ontario). Animals were not subjected to testing if a low body mass or sickness was encountered (see section 2.7). Animals were taken directly from electroretinography testing (see section 2.3) while under the same anesthetic to reduce insult to the animal. Anesthetized animals were placed on the custom platform with a heat lamp (Exo Terra) directly overhead for the full duration of imaging. The platform was manipulated to line up the right eye (OD) of the animal so that the apex of the cornea was pointed directly into the machine. A high definition cross sectional image of the cornea was captured that spanned from the temporal cornea to the nasal cornea. A second quad high definition image was captured to image the dorsal and ventral cornea. The platform was inched closer to the machine in the horizontal plane in order to capture images of the retina. The animals' pupils were still dilated from electroretinography testing allowing for imaging of the retina in the anesthetized mouse. Similarly, a high definition image was captured containing the temporal and nasal retina and a quad high definition image was captured of the dorsal and ventral retina. The platform was then rotated 180° in the horizontal direction to image the left eye (OS) of the animal in a similar fashion. After imaging, the mouse was returned to the circulating water heating pad (Gaymar) and injected with the anesthetic reversal agent (see section 2.8)

2.15 Ocular Coherence Tomography Data Analysis

Eight measurements were made in all OCT images using the digital caliper built into the Visante™ OCT software (Zeiss) (Appendix B: Figure 2.4). Five of the measurements were obtained from images of the anterior chamber of each eye. The central corneal (CC), nasal peripheral cornea (NPC) and temporal peripheral cornea (TPC) were obtained to determine if significant corneal thinning or thickening occurred. Measurements obtained for CC, NPC and TPC thickness were used separately for all statistical comparisons. Corneal thickness will refer to the grouping of all three measurements unless stated otherwise. Statistical comparisons of OS and OD eyes were made in each specific cohort for each corneal measurement. Anterior chamber width (ACW) and anterior chamber depth (ACD) were measured to determine microophthalmia or abnormal lens placement. Three measurements were taken in the posterior segment of the eyes of mice including the anterior retinal (AR), posterior retinal (PR) and central whole retinal (CWR) thickness. The AR is a measurement of the neural retina from the ganglion cell layer to the segments of the photoreceptors (G. Bootsma, Zeiss Canada, personal communication). The PR is a measurement of the pigmented tissues at the back of the eye including the retinal pigmented epithelium and choroid. The CWR was a measurement combining the AR and PR at the center of the retinal image. OCT determined retinal thickness will refer to the grouping of all three measurements. Data were excluded if gross abnormalities were found such as microophthalmia. Additional cohorts of WT and *hq* mice were added to determine effects of multiple dates of anesthetization and OCT imaging. The WT cohort consisted of six animals: one animal at nine months of age, one animal at ten months of age, two animals at eleven months of age and two animals at twelve months of age. The *hq* cohort consisted of three animals: one animal at nine months of age, one animal at ten months of age and one animal at eleven months of age. These mice were tested a single time using OCT and were averaged and presented as eleven month data sets. These mice have been presented as the WT single OCT and *hq* single OCT cohorts. Some findings such as a structurally abnormal iris led to the exclusion of some electroretinography data points because light was impeded from the retina.

2.16 Embedding of Left and Right Eyes Postmortem

After fixation and storage of the OD (see section 2.4) the tissue was processed using a Leica ASP300 (Leica Microsystems, Richmond Hill, ON) fully enclosed paraffin wax tissue processor at the Pickering Tissue Pathology Core Lab Facility in the Robarts Research Institute (London, Ontario). Briefly, tissue samples were dehydrated using 1 hour ethanol washes, with increasing concentrations beginning at 70%, followed by 95%, and ending with three washes using 100% ethanol. The right eye (OD) was then subjected to three 1-hour Xylene treatments (Sigma-Aldrich), followed by three 1-hour treatments with molten paraffin wax to impregnate the tissue. The automated processes took 12 to 16 hours and were performed overnight.

The following day, tissue was embedded in paraffin wax. A mold was selected based on tissue size and filled with molten wax. The mold was briefly moved onto a cold plate to form a thin solid layer of wax on the bottom of the mold. The eye was placed into the wax and oriented in the horizontal plane with the cornea facing the right and the optic nerve facing the left of the mold. All eyes were processed with the eye in identical orientation. Tissue cassettes (VWR) were labelled using pencil and placed on top of the molten wax. A small amount of wax was added to the cassette to promote adhesion and the mould was moved to a cold plate to solidify. After the wax had solidified the right eye was ready for sectioning. No tissue processing was needed for the OS as it was frozen in optical cutting temperature media (see section 2.4).

2.17 Sectioning of the Left and Right Eyes

Eyes embedded in paraffin wax were sectioned using a Leica RM2255 Microtome (Leica Microsystems). Eyes were cut in 5 μm cross sections and placed on positively charged poly-L-lysine microscope slides (VWR). Each slide contained a minimum of two sections from various cuts of the eye. Ten slides were B-cut sections containing peripheral cornea and retina and an iris that spanned the entire tissue (Appendix B: Figure 2.5). Ten additional slides held C-cut sections containing the central cornea, central retina, optic nerve, and pupil. The slides were then stored at room temperature.

OS embedded in optimal cutting temperature media (Somagen Diagnostics) were removed from a -80°C freezer and kept frozen on dry ice until sectioning. Tissues were cryosectioned at 10 μm progressively through the eye using a Leica CM350 Cryostat (Leica Microsystems). A minimum of two sections were placed on a positively charged poly-L-lysine microscope slide (VWR) and were placed into a 100 groove slide box (VWR) on dry ice. Ten slides held B-cut sections containing peripheral cornea and retina and an iris that spanned the entire tissue. Ten additional slides held C-cut sections containing the central cornea, central retina, optic nerve, and pupil. Cryosectioned eye samples were kept in a -20°C freezer until further experimentation.

2.18 Hematoxylin and Eosin Staining Protocol

Hematoxylin and Eosin staining was performed on fixed OD tissue that had been embedded in paraffin wax and sectioned with a 5 μm thickness (see section 2.5). Two slides were used for each animal based on high integrity of the sections, for example an attached retina and intact lens. In cases where intact sections could not be found the adjacent sections were used. One slide contained B-cut sections and one slide contained C-cut sections in order to assess structural integrity for multiple areas of the eye. It was necessary to deparaffinize the tissues prior to H&E staining in order to achieve the best absorption of stain. In short, slides were immersed in a Xylene bath for two 5-minute treatments. Tissue sections were rehydrated by briefly dipping in 100% ethanol followed by a 3 minute incubation in a reservoir containing fresh 100% ethanol. Sections were then immersed in 95% ethanol, 80% and then 70% ethanol for 5 minutes each. Tissues were then rinsed with tap water and subjected to H&E staining.

Slides containing eye sections were initially stained with Hematoxylin for 5 minutes and rinsed with water until runoff was colourless. This effectively removed any excess Hematoxylin from the slides. Following Hematoxylin staining, samples were repeatedly dipped in 70% ethanol containing 5 drops of 1N hydrochloric acid and quickly immersed in tap water. Eye sections were then briefly immersed in 1% lithium carbonate (BDH Laboratory Supplies, Poole, England). Sections were counterstained with Eosin Y (Sigma-Aldrich) for 30 seconds prior to dehydration. Dehydration was achieved by rinsing the sections in sequential 1 minute treatments of 50%, 70%, 95% and 100% ethanol, followed by a 4 minute wash in fresh 100% ethanol. Slides were then submerged in two xylene treatments for 2 minutes each and were stored for a maximum of 20 minutes in Xylene. A single drop of Clarion™ Aqueous Mounting Media (Sigma-Aldrich) was placed on each section and sections were covered with a coverslip (VWR) prior to tissue analysis.

2.19 Data Analysis for Hematoxylin and Eosin Images

Based on the survivorship of mice, sample sizes varied between cohorts and age groups in postmortem analysis but remained constant for each assay unless stated otherwise (Appendix B: Table 2.1). Images were captured at 2X magnification to assess whole eye orientation, eye structure and gross tissue abnormalities using an Arcturus Veritas microdissection system (Molecular Devices, Sunnyvale, CA). Further imaging was performed at 20X magnification to quantitate cell nuclei and tissue layer thickness while identifying any histopathologies. Two of the images captured at 20X magnification were peripheral retinal images located 300 μm from the retinal and ciliary body commissure (ora serrata). At least seven images were obtained for analysis at different regions across the retina. Among these pictures were images of the retina approximately 300 μm from the apex of the retina. This was done to keep retinal location as consistent as possible for data analysis. Dorsal peripheral, ventral peripheral and central retinal images were analyzed by quantifying cellular nuclei and retinal layer thickness. Six separate vertical nuclei counts were taken and averaged for each of the outer nuclear layer and inner nuclear layer and were used to calculate layer thickness based on cell nuclei (Appendix B: Figure: Figure 2.6). A digital caliper (Canadian Tire, London, Ontario) was used to measure retinal layer thickness for each of the inner plexiform layer, outer plexiform layer and inner and outer segments of the photoreceptors. Six measurements were made for each retinal layer to obtain an average layer thickness. To ensure a correct measurement was taken, a scale was determined from the digital caliper in the Veritas software. This scale was measured prior to the start of every measurement session and every image was opened with the same program ensuring the image canvas had consistent height, width and pixel ratios. A 100 μm measurement was taken along the ganglion cell layer and full cell nuclei within the measurement were quantified. Finally, six measurements of total retinal thickness were averaged. Images of the cornea were captured at 20X magnification. Corneal epithelium was measured at six locations and averaged to determine corneal epithelial degeneration. Multiple images of the cornea were captured to assess peripheral and central corneal structure.

2.20 Trichrome and Modified Gram Staining

A subset of ten mid-adult (eight and ten months of age) mice were selected for further histopathology analysis. Select animals experiencing corneal thickening were included in this subset to determine a possible cause of inflammation. Ten slides containing B-cut samples and ten slides containing C-cut samples were sent to the University Hospital (*The* University *of* Western Ontario, London, ON) for additional staining (Trichrome with Lillie's modification). Slides were deparaffinized and rehydrated using dilutions of ethanol as previously described (see section 2.18). Slides were then incubated at 58°C for 60 minutes in zinc chloride (0.05g/ml). Samples were then washed in running tap water for two minutes. Slides were then placed in a Celestin Blue mixture for four minutes, rinsed in water and placed in Mayers Haemalum solution for an additional four minutes. Samples were then differentiated in acid alcohol (6 dips), placed in ammonium water for 30 seconds and then washed with water. Slides were then incubated in a Biebrich Scarlet/Acid Fuchsin mixture for three minutes and rinsed with distilled water. Slides were then incubated for a minute in phosphotungstic acid/Phosphomolybdic acid solution. Slides were then drained but not washed. Samples were placed in a 1% fast Green FCF and 1%

acetic acid solution for 45 seconds. Samples were then differentiated using a 1% acetic acid solution until collagen retains green only (6 dips), rinsed quickly in 95% ethanol and dehydrated using 100% Ethanol.

Ten slides containing B-cut samples and ten slides containing C-cut samples from the same subset of animals were sent to the University Hospital (*The* University *of* Western Ontario, London, ON) for additional staining (Gram Testing). Slides were immersed in Crystal Violet solution for one minute and rinsed with water. Slides were then immersed in Iodine for a minute and rinsed with water. Samples were then exposed to Acetone Alcohol for 15 seconds and rinsed with water. Finally, samples were exposed to a counterstain (Safranin) for one minute before rinsing with water. Trichrome stained tissues were imaged at 20X magnification and gram stained images were captured at 40X magnification using an Arcturus Veritas microdissection system (Molecular Devices). Images were assessed qualitatively with no quantification or statistical analyses.

2.21 Dihydroethidium Staining Protocol

Dihydroethidium (DHE) staining was performed on cryogenically preserved OS tissue that had been frozen in optimal cutting temperature media and sectioned at a 10 μm thickness (see section 2.5). DHE staining was performed specifically on C-cut sections in order to determine levels of reactive oxygen species in the peripheral and central retina and cornea. DHE solution was prepared and stored under nitrogen. A stock solution of DHE was made by dissolving 5 mg of DHE powder (Sigma-Aldrich) into 317 μl of dimethyl sulfoxide (DMSO) creating a 0.05 M solution (Takimoto et al., 2005). Two separate 5 μM DHE working solutions were created by aliquoting 5 µl of stock solution into 50 ml of DMSO or Acetone. Frozen slides were heated on a 45°C heat block to evaporate moisture and bring tissues to room temperature. A negative Reactive Oxygen Species (ROS) control was created by pipetting 20 µl of 1000 U/ml superoxide dismutase (SOD) on to the sample and incubating for 10 minutes at room temperature to remove superoxide anions ($O_2^{\bullet}$). Negative controls were created and analyzed using mice from different genotypes and treatment specific cohorts at multiple ages. A positive control was created in the dark by pipetting 20 µl of a 0.5 M hydrogen peroxide (H_2O_2) solution onto the sample and incubating for 5 minutes at room temperature. Positive and negative controls were created and analyzed using mice from genotype and treatment specific cohorts at two, four, six, eight and ten months of age. Both the SOD and H_2O_2 solutions were removed prior to continuing with DHE staining. All samples were transferred to a dark room and a 50 µl aliquot of 0.05 M DHE working DMSO solution was pipetted onto experimental tissue samples and the negative control. The positive control was only efficient when 50 µl of the DHE working acetone solution was pipetted onto the sample. All tissues were incubated in the dark for 30 minutes in a humidified incubator. Tissue sections were then analyzed.

2.22 Dihydroethidium Data Analysis

Light microscopy images were captured at 2X magnification and low intensity for orientation of the whole eye section using an Arcturus Veritas microdissection system (Molecular Devices). Further imaging was performed at 20X magnification under a green filter (Excitation: 503-548 nm; Emission: > 565 nm) because ethidium bromide has an excitation wavelength of 530 nm and an emission wavelength of 590 nm. The fluorescent bulb was set to a brightness of

'2' for all analyses ensuring that the intensity of fluorescence was consistent across all sections. DHE staining has a very short duration of fluorescence before quenching begins to occur. Immediately upon fluorescence exposure, an image of the peripheral retina was captured. Ten consecutive images from the dorsal peripheral retina to the ventral peripheral retina were captured using identical exposure times. Five consecutive images across the cornea were captured to assess levels of superoxide in the corneal epithelium. DHE stained fluorescent images were quantified using the software ImageJ (National Institute of Health, Bethesda, Maryland). ImageJ quantifies the fluorescence intensity by assigning the detected fluorescence using a grey scale brightness value. A total of six fluorescence measurements per cell layer (eg. outer nuclear layer, inner nuclear layer, ganglion cell layer) were made from each of the peripheral and central retinal images. Standardization was achieved by measuring 20 cell nuclei per measurement in the outer nuclear layer, 6 cell nuclei in the inner nuclear layer, and a 10 x 30 μm box in the ganglion cell layer. In the corneal epithelium, 10 x 30 μm box was used for superoxide quantification. Standardization of ROS was important for statistical analysis among intercohort levels of ROS in specific cell layers. Levels of ROS among cell layers of cohorts were assessed qualitatively due to different standardization measures in the corneal epithelium, ganglion cell, inner nuclear and outer nuclear layers.

2.23 Terminal Deoxynucleotidyl Transferase dUTP Nick End Labeling Protocol

Terminal Deoxynucleotidyl Transferase dUTP Nick End Labeling (TUNEL) staining (Roche Canada, Mississauga, ON) was performed on cryogenically preserved tissue that had been frozen in optimal cutting temperature media and sectioned with a 10 μm thickness (see section 2.5). TUNEL was performed specifically on C-cut sections in order to determine levels of apoptosis in the peripheral and central retina and cornea. Tissues were prepared using a 20 minute fixation step at room temperature using 4% paraformaldehyde solution mixed in 1X phosphate buffered saline solution with a pH of 7.4 freshly prepared. This was followed by a 30 minute wash in clean 1X PBS. Tissues were made permeable using a 3 min immersion in a 0.1% Triton X-100 and 0.1% sodium citrate mix with a temperature between 2-8°C. Slides were then rinsed twice with a clean solution of 1X PBS solution and area around tissue was dried. Slides were moved into a dark room and 50 µl of the TUNEL reaction mixture was pipetted onto each tissue. The slides were then incubated in a 37°C humidified incubator for 60 minutes. After incubation slides were rinsed in the dark in clean 1X PBS. Positive control samples were created by freshly preparing a stock solution of 0.5 ml 50mM Tris-HCl with a pH 7.5 and 1mg/ml bovine serum albumin. Addition of 5 µl of DNase I recombinant at a concentration of 173 U/µl created a 2 U/µl DNase recombinant solution. In order to have significant double stranded breaks a 50 µl aliquot of positive control solution was pipetted onto the samples and incubated for 10 minutes at room temperature. Negative control samples were incubated with TUNEL solution lacking terminal transferase.

2.24 Data Analysis of Cellular Apoptosis

Light microscopy images were captured at 2X magnification for orientation using an Arcturus Veritas microdissection system (Molecular Devices). Further imaging was performed at 20X magnification under a blue filter with an excitation wavelength in the range of 455 - 495 nm and an emission > 510 nm. The fluorescent bulb was set to a brightness of '6' for all analyses ensuring that the intensity of fluorescence was consistent across all sections. The whole retina was analyzed and apoptotic cells were organized based on retinal layer of occurrence (eg. outer nuclear layer, inner nuclear layer or ganglion cell layer) and location (eg. peripheral or central retina). Levels of fluorescence were quantified after TUNEL staining using the software ImageJ (National Institute of Health, Bethesda, Maryland) (see section 2.22). Cells with a minimum diameter of 1.5 μm and a grey scale value above 160 were considered apoptotic. Images of the cornea were also obtained to determine levels of apoptosis occurring in the corneal epithelium.

2.25 Statistical Analyses of Experimental Data

Data were plotted to determine whether the values fell on a normal curve. A single-factor ANOVA statistical test was used to compare OD and OS in experimental cohorts for both ERG and OCT data. An OD and OS comparison was performed in each cohort at each month of age to determine if visual function and eye structure was significantly different between OD and OS. Cohorts at each month of age were compared using a single-factor ANOVA statistical test to determine any significant differences between genotypes or drug treatments of mice. In ERG experiments, no statistical analysis could be performed using the untreated WT cohort at seven months of age due to a lack of experimental data. Data were not obtained on this month due to mechanical errors in the ERG machine. Similarly, no data comparisons could be made using the untreated and memantine-treated *hq* cohorts at nine months of age due to a lack of ERG data. In OCT imaging experiments, no data comparisons could be made using the untreated and memantine-treated *hq* cohorts at nine months of age due to a lack of images. The *hq* mice were not anesthetized at nine months of age due to risk of anesthetic complications and the potential loss of the ten-month-old cohort data. Similarly, layer thickness and cell counts, mean DHE fluorescence intensities, whole retinal apoptosis and outer nuclear layer apoptosis levels were compared using a single-factor ANOVA statistical test to determine any significant differences between mouse genotypes or drug treatment. All ANOVAs were performed in a Microsoft Excel spreadsheet (Microsoft, Redmond, VA).

Linear regression analyses were performed on the a-wave and b-wave amplitudes using SPSS analytical software (SPSS, Chicago, Illinois). The minimum and maximum confidence intervals of the Y-intercept and of the slope were used to determine if differences occurred. A Fisher's exact test was used to compare overall DHE profiles between cohorts using StatXact statistical analysis software (Cytel Software, Cambridge, MA). A Fisher's exact test was used to compare apoptosis patterns over the life span of the cohorts (Cytel). A Fisher's exact test was used to compare apoptosis patterns of the outer nuclear layer in the central retina over the life span of the cohorts (Cytel). Statistical significance was accepted at a P-Value of < 0.05.

Chapter 3 - Results

3.1 Confirmation of Experimental Genotypes

The genotypes of all mice were confirmed postmortem (Figure 3.1). A total of 49 mice were positive for a 537 bp PCR amplicon demonstrating a normal *Aif* gene. A total of 32 mice were positive for a 725 bp PCR amplicon demonstrating the *hq Aif* insertion. Phenotypic determination of *hq* mice included low body mass and a lack of fur eight to ten days post birth and led to a 100% success rate in genotype prediction.

3.2 Survivorship of Mice

All untreated WT mice survived the full experimental design (Figure 3.2 A). A single memantine-treated WT mouse died prematurely at seven months of age during anesthetization for *in vivo* eye testing. Eleven untreated *hq* mice died prematurely (Figure 3.2 B). Five of which had poor health determined by the observation of low body mass, abnormal behavior in response to handling and dehydration. One mouse died after the first anesthetization and was immediately dissected but included in the two month cohort. The other four mice died between five and seven months of age due to complications associated with the anesthetic. Eight mice in the memantine-treated *hq* cohort died prematurely. Two mice were observed to have poor health and six mice died due to complications with the anesthetic. Mice that died prematurely were excluded from all data sets since the data could be artifactual, based on poor health leading to

Figure 3.1 - Wild type and *harlequin* disease status was evaluated postmortem using PCR amplification. *Aif* genotyping PCR amplicons were electrophoresed through a 1.5% agarose gel. A 725 bp PCR amplicon revealed a $X^{hq}Y$ genotype. A 537 bp PCR amplicon revealed an XY genotype. **A.** Track-It™ 100 bp DNA ladder (Invitrogen, Burlington, ON) was used to determine fragment size. Negative controls were created with PCR master mix with ddH_2O added instead of DNA. DNA from a carrier $X^{hq}X$ mouse used as a positive control. **B.** Track-It™ 100 bp DNA ladder (Invitrogen, Burlington, ON) was used to determine fragment size. Negative controls were created with PCR master mix with ddH_2O added instead of DNA. DNA from a carrier $X^{hq}X$ mouse used as a positive control. **C.** Track-It™ 100 bp DNA ladder (Invitrogen, Burlington, ON) was used to determine fragment size. Negative controls were created with PCR master mix with ddH_2O added instead of DNA. DNA from a carrier $X^{hq}X$ mouse used as a positive control. **D.** Track-It™ 100 bp DNA ladder (Invitrogen, Burlington, ON) was used to determine fragment size. Negative controls were created with PCR master mix with ddH_2O added instead of DNA. DNA from a carrier $X^{hq}X$ mouse used as a positive control.

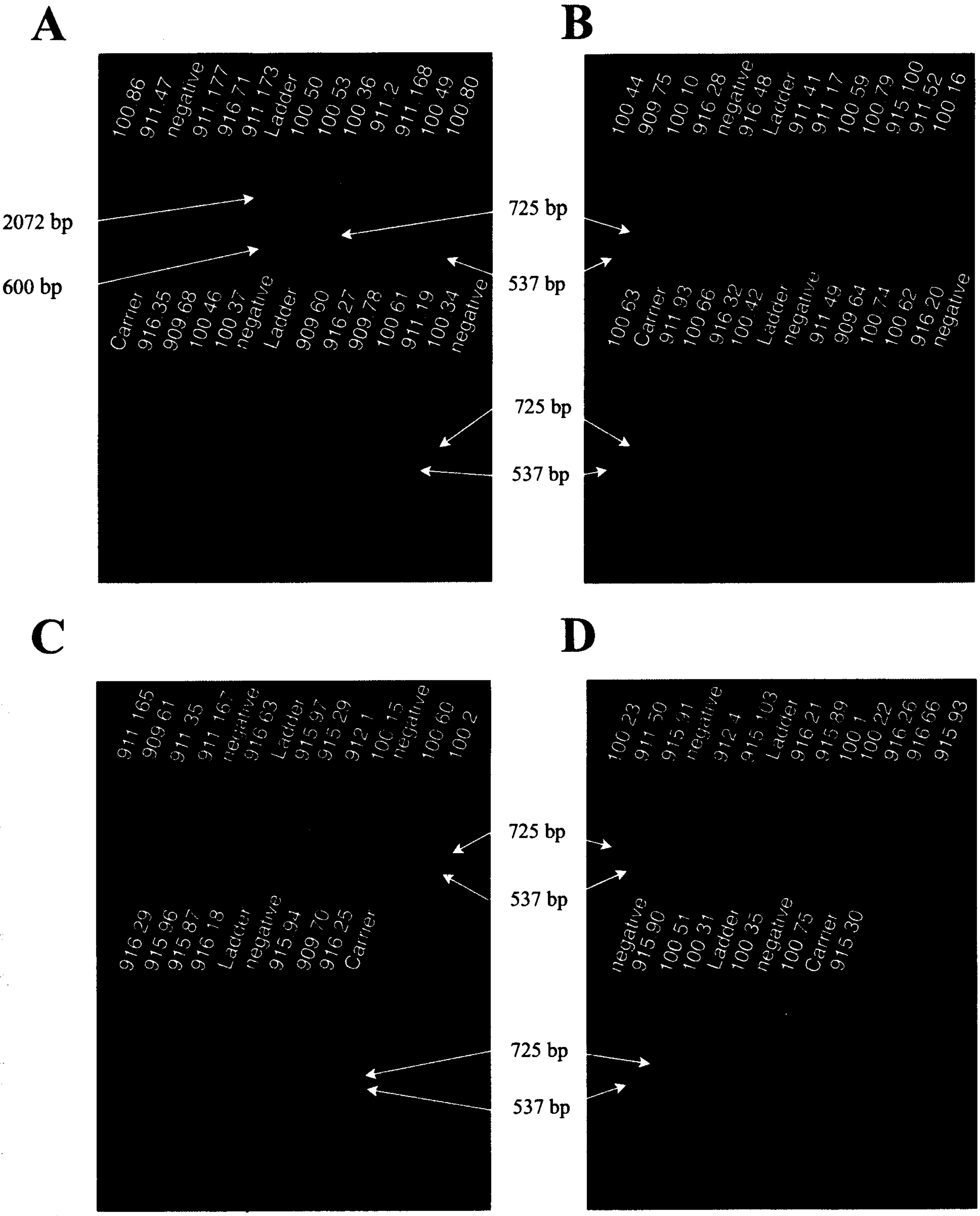
A
100.86 911.47 negative 911.177 916.71 911.173 Ladder 100.50 100.53 100.36 911.2 911.168 100.49 100.80
2072 bp
600 bp
Carrier 916.35 909.68 100.46 100.37 negative Ladder 909.60 916.27 909.78 100.61 911.19 100.34 negative
725 bp
537 bp
725 bp
537 bp
B
100.44 909.75 100.10 916.28 negative 916.48 Ladder 911.41 911.17 100.59 100.79 915.100 911.52 100.16
725 bp
537 bp
100.63 Carrier 911.93 100.66 916.32 100.42 Ladder negative 911.49 909.64 100.74 100.62 916.20 negative
725 bp
537 bp
C
911.165 909.61 911.35 911.167 negative 916.63 Ladder 915.97 915.29 912.1 100.15 negative 100.60 100.2
725 bp
537 bp
916.29 915.96 915.87 916.18 Ladder negative 915.94 909.70 916.25 Carrier
725 bp
537 bp
D
100.23 911.50 915.91 negative 912.4 915.103 Ladder 916.21 915.89 100.1 100.22 916.26 916.66 915.93
725 bp
537 bp
negative 915.90 100.51 100.31 Ladder 100.35 negative 100.75 Carrier 915.30
725 bp
537 bp

Figure 3.2 - Kaplan-Meier curve of survivorship through the experimental timeline of ten months. A. Untreated and memantine-treated wild type (WT) cohorts began with 25 animals each. A single memantine-treated WT mouse died prematurely at seven months of age. The experimental design had five animals from each cohort euthanized at two, four, six, eight and ten months of age. **B.** Untreated and memantine-treated *harlequin* (*hq*) cohorts began with 25 animals each. The experimental design had five animals from each cohort euthanized at two, four, six, eight and ten months of age. Two animals died in each of the untreated and memantine-treated *hq* cohorts at one month of age. A single untreated *hq* mouse died at three months of age. Four animals in both the untreated and memantine-treated *hq* cohorts died at five months of age. A single untreated *hq* mouse and two memantine-treated *hq* mice died at seven months of age. Two untreated *hq* mice died prematurely at nine months of age. Animals that died at one, three, five, seven and nine months of age were not used in data analysis.

A

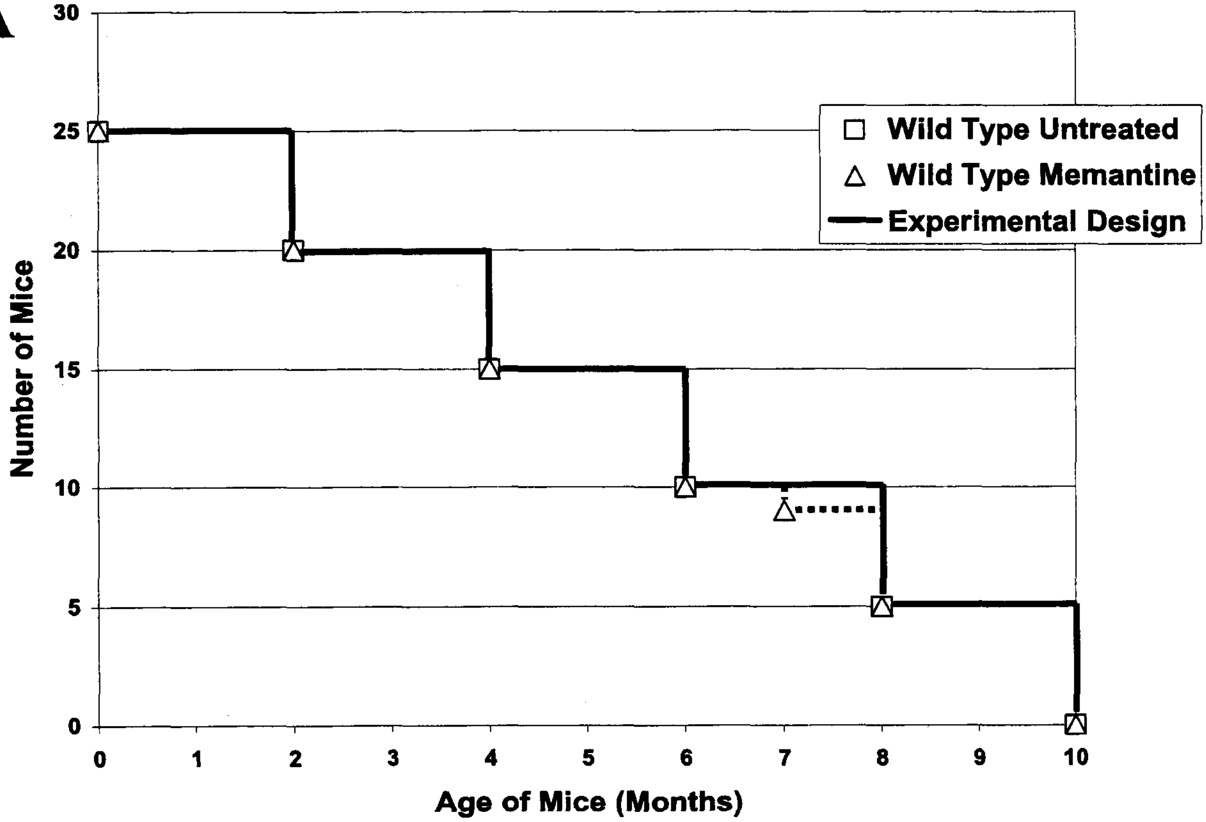
30
25
20
15
10
5
0
Number of Mice
0
1
2
3
4
5
6
7
8
9
10
Age of Mice (Months)
Wild Type Untreated
Wild Type Memantine
Experimental Design

B

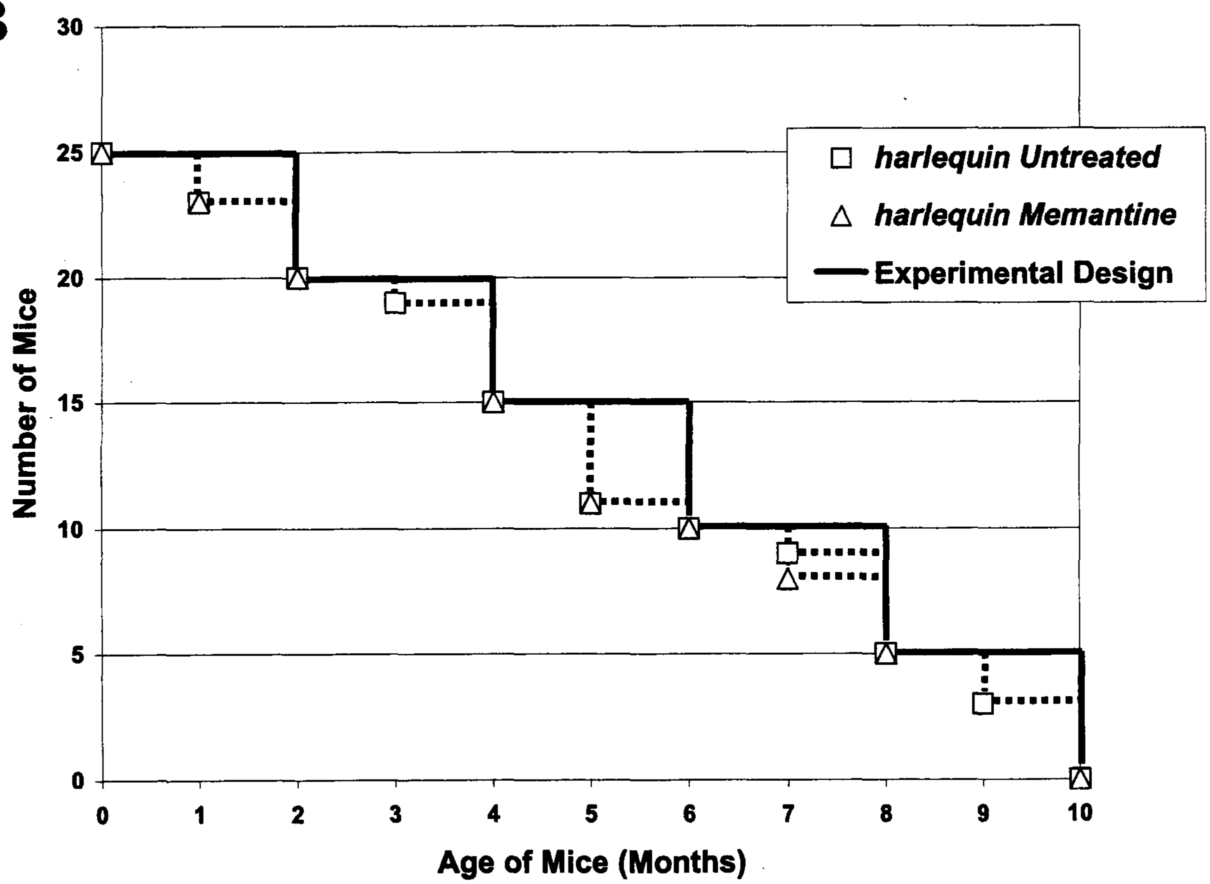
30
25
20
15
10
5
0
Number of Mice
0
1
2
3
4
5
6
7
8
9
10
Age of Mice (Months)
harlequin Untreated
harlequin Memantine
Experimental Design

premature death. A total of 81 mice survived the block design. Three-hundred and twenty-two anesthetizations were performed over the experimental period with twelve resulting in death leading to a 3.7% mortality rate during anesthetization.

3.3 Comparison of Body Mass Between Mouse Cohorts

All WT mice were weaned within the first month post birth. Untreated *hq* mice were not weaned until a minimum body mass of 9 g was achieved with the exception of a single mouse (Identification number: 911.173) who was 8 g at 6 weeks of age. Untreated WT mice had an average body mass of 20.7 ± 0.46 g (n = 25) at date of weaning (Figure 3.3). This was significantly higher than untreated *hq* mice which had an average body mass of 13.2 ± 0.8 g (n = 15) at date of weaning ($P < 0.001$). Untreated WT mice continued to have a significantly higher average body mass up to ten months of age compared to untreated *hq* cohorts. Body mass of the untreated WT mice increased by 1-2 g intervals until a maximum average body mass of 38.1 ± 2.30 g (n = 5) was reached at nine months of age. Untreated WT mice were an average of 15 g larger than untreated *hq* mice at nine months of age ($P < 0.01$; *hq*: 23.4 ± 0.37 g [n = 3]). Differences in body mass were observed and confirmed postmortem at two, four, six, eight and ten months of age by a dramatic reduction in the amount of intraperitoneal adipose tissue.

Memantine-treated WT mice had an average body mass of 19.9 ± 0.44 g (n = 24) at date of weaning. No differences in body mass were observed between untreated and memantine-treated WT mice at dates of weaning. A higher average body mass was seen in the untreated WT cohort at two months of age ($P < 0.0001$; untreated: 25.8 ± 0.31 g [n = 25], treated: 21.1 ± 0.45 g [n = 24]). As mice aged and cohort size reduced, differences in body mass declined but

Figure 3.3 - Mean body mass of experimental cohorts of mice from weaning to ten months of age. Mean body mass (g) of experimental cohorts with the mass at date of weaning plotted at one month of age. Data are presented as Mean ± SEM.

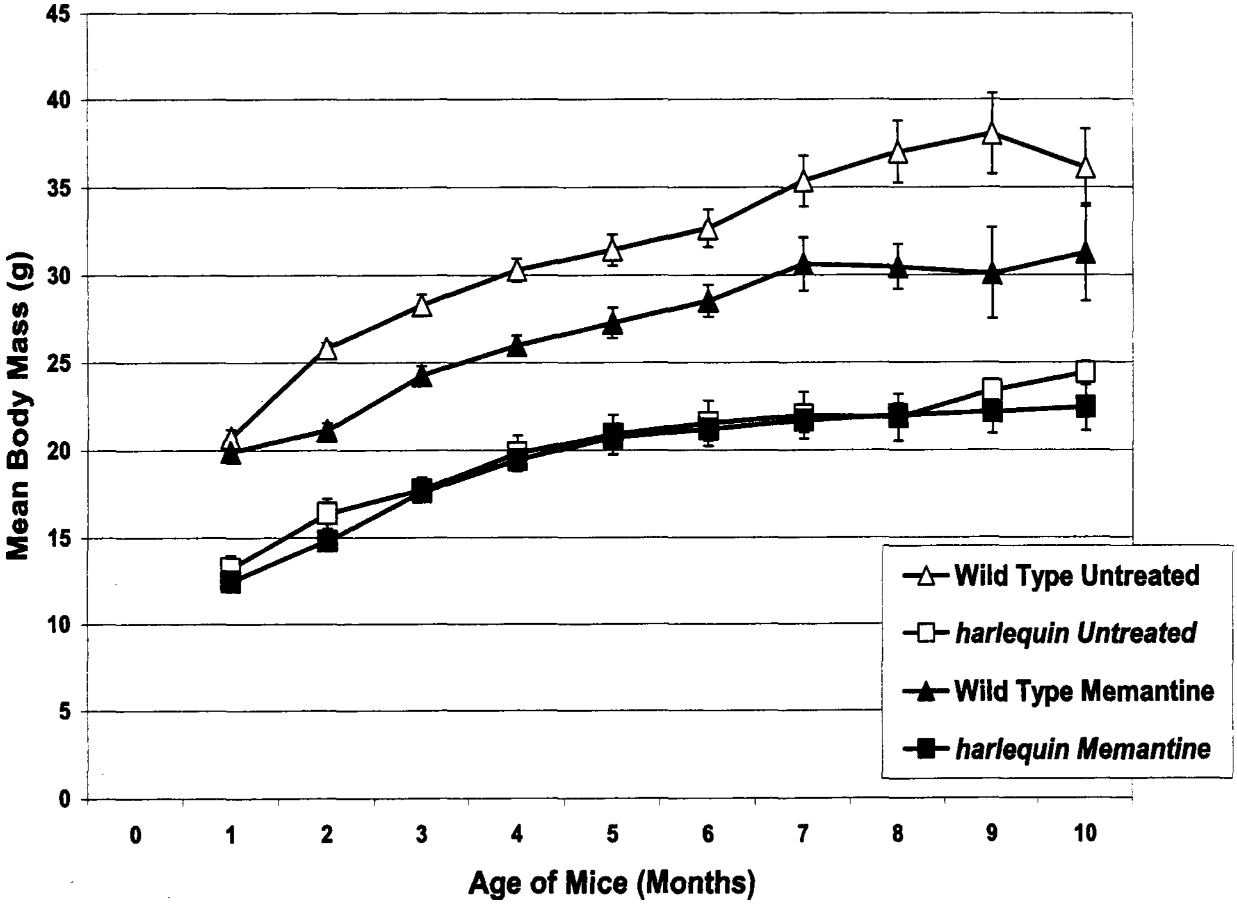
45
40
35
30
25
20
15
10
5
0
Mean Body Mass (g)
0
1
2
3
4
5
6
7
8
9
10
Age of Mice (Months)
Wild Type Untreated
harlequin Untreated
Wild Type Memantine
harlequin Memantine

remained significant until late in the experimental design. By seven months of age, the body mass of memantine-treated WT mice reached 30.6 ± 1.53 g (n = 9) while untreated mice remained significantly higher ($P < 0.05$; treated: 35.4 ± 1.46 g [n = 10]). By ten months of age, body mass was no longer considered different between untreated and memantine-treated WT mice (untreated: 36.1 ± 2.22 g [n = 5], treated: 31.3 ± 2.76 g [n = 5]).

The average time of weaning for memantine-treated *hq* mice was four to five weeks post birth. Memantine-treated *hq* mice had an average body mass of 12.5 ± 0.57 g (n = 18) at dates of weaning. No significant differences were found when comparing untreated and memantine-treated cohorts of *hq* mice at each month of age. Lower *hq* body mass appeared to be associated with lower coverage of body hair measured by qualitative inspection of *hq* dorsal pelts. Mice with lower body mass and body hair coverage also had a higher mortality rate compared to mice in the same cohort.

Memantine-treated mice of both mouse genotypes had significant differences in body mass through the duration of the experiment. At date of weaning, memantine-treated *hq* mice had a significantly lower body mass ($P < 0.001$; WT: 19.9 ± 0.44 g [n = 24], *hq*: 12.5 ± 0.57 g [n = 18]. Memantine-treated WT mice had an increased body mass until eight months of age ($P < 0.001$; WT: 31 ± 1.29 g [n = 9], *hq*: 22 ± 0.68 g [n = 9]). At ten months of age, memantine-treated cohorts continued to be significantly different in body mass ($P < 0.05$; WT: 31 ± 2.76 g [n = 5], *hq*: 22 ± 1.35 g [n = 5]). Mice did not display any obvious abnormalities during their life span such as tumor growth, abnormal hair loss, skin lesions or abnormal behavior due to drug treatment. Calculated P-Values for all statistical analyses have been provided (Appendix C).

3.4 Comparison of Water Consumption Between Mouse Cohorts

Average daily water consumption was corrected for body mass in all experimental cohorts. Average daily water consumption in the untreated WT cohort was highest at two months of age and slowly decreased with age (Figure 3.4). At two months of age, untreated WT mice consumed significantly less water per day compared to the untreated *hq* cohort ($P < 0.05$; WT: 0.21 ± 0.007 ml/g/day [n = 25], *hq*: 0.28 ± 0.039 ml/g/day [n = 15]). Differences continued into three months of age when untreated WT mice consumed on average 0.18 ± 0.006 ml/g/day (n = 20), significantly less than that of untreated *hq* mice ($P < 0.001$; *hq*: 0.25 ± 0.019 ml/g/day [n = 12]). Untreated *hq* mice continued to consume more water through four ($P < 0.001$), five ($P < 0.001$), six ($P < 0.01$) seven ($P < 0.05$) and nine months of age ($P < 0.001$; WT: 0.13 ± 0.004 ml/g/day [n = 5], *hq*: 0.19 ± 0.007 ml/g/day [n = 3]).

At two months of age, memantine-treated WT mice had a higher average water consumption than untreated mice ($P < 0.001$; untreated: 0.21 ± 0.006 ml/g/day [n = 25], treated: 0.25 ± 0.008 ml/g/day [n = 24]). The increased water consumption found in the memantine-treated WT cohort continued into three ($P<0.01$; untreated: 0.18 ± 0.006 ml/g/day [n = 20], treated: 0.20 ± 0.006 ml/g/day [n = 19]) and four months of age ($P < 0.05$; untreated: 0.16 ± 0.006 ml/g/day [n = 20], treated: 0.19 ± 0.009 ml/g/day [n = 19]).

By two months of age, memantine-treated *hq* mice were consuming 0.28 ± 0.10 ml/g/day on average (n = 18), similar to that of untreated *hq* mice (0.28 ± 0.039 ml/g/day; n = 15). Water consumption between untreated and memantine-treated *hq* mice remained similar through all months of age. Variation between mice within the *hq* cohorts was larger than that found in the

Figure 3.4 - Mean daily water consumption by experimental mice corrected for body mass. Mean daily water consumption (ml/g/day) was averaged for each month of age and presented at the end of the month. For example: mean daily water consumption from one to two months of age is presented at the two month time point. Data are presented as Mean ± SEM.

WT cohorts. By ten months of age, water consumption between untreated and memantine treated *hq* mice was quite similar (untreated: 0.15 ± 0.020 ml/g/day [n = 3], treated: 0.16 ± 0.020 ml/g/day [n = 5]).

At two months of age, memantine-treated *hq* mice had a higher average water consumption than memantine-treated WT mice ($P < 0.01$; WT: 0.25 ± 0.008 ml/g/day [n = 24], *hq*: 0.28 ± 0.010 ml/g/day [n = 18]). This difference in water consumption continued from three to eight months of age with a similar level of significance ($P < 0.05$).

3.5 Comparison of Average Daily Drug Consumption Between Mouse Cohorts

Memantine-treated WT mice began receiving memantine hydrochloride one week post weaning (Figure 3.5). The week following weaning the mice drank untreated water in order to determine memantine concentrations necessary for adequate consumption. Memantine-treated *hq* mice began receiving memantine hydrochloride between one and two months of age. Memantine delivery began one week post weaning in all mice. Memantine-treated WT mice approached 0.03 mg/g/day drug consumption at nine (0.0270 ± 0.0007 mg/g/day; n = 5) and ten months of age (0.0298 ± 0.0013 mg/g/day; n = 5) but were not significantly different from memantine-treated *hq* mice over the course of the study.

3.6 Retinal Function Assessed By Electroretinography Between OS and OD *In Vivo*

The left (OS) and right (OD) eyes of mice were statistically compared in each specific cohort. No significant differences in photoreceptor response times were found between OS and OD of the untreated WT, *hq* and memantine-treated WT, *hq* cohorts. No cross cohort statistical

Figure 3.5 - Mean daily memantine consumption by drug-treated mice from two to ten months of age. Mean daily memantine consumption (mg/g/day) was averaged for each month of age and presented at the end of the month. For example: mean daily memantine consumption from one to two months of age is presented at the two month time point. Data are presented as Mean ± SEM.

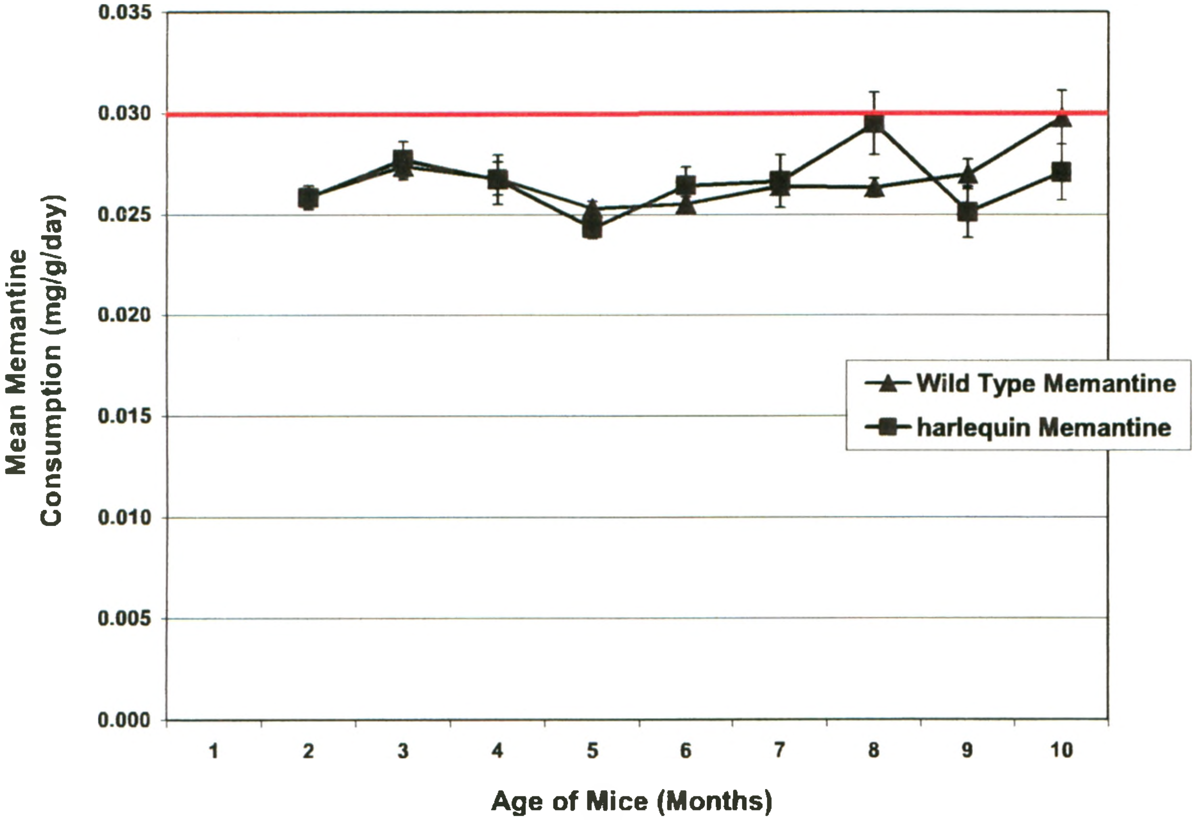

0.035
0.030
0.025
0.020
0.015
0.010
0.005
0.000
Mean Memantine Consumption (mg/g/day)
1
2
3
4
5
6
7
8
9
10
Age of Mice (Months)
Wild Type Memantine
harlequin Memantine

comparisons were made with OS and OD. For example, the OS of untreated WT mice were never compared to the OD of memantine-treated WT mice. The OS and OD were considered to be independent variables because the OS was not consistently lower or higher than the OD.

3.7 Photoreceptor Response Time Assessed by Electroretinography a-wave Latency

Untreated WT mice had a photoreceptor response time that varied between 18 and 21 ms but was relatively unchanged between weeks (Figure 3.6 A). Untreated *hq* mice had slower photoreceptor response times which were exacerbated with age and unaffected by memantine treatment. The untreated *hq* cohort had a slower photoreceptor response time by two months of age compared to untreated WT mice ($P < 0.001$; WT: 19.0 ± 0.45 ms [n = 30], *hq*: 22.3 ± 0.79 ms [n = 28]). At four and five months of age, photoreceptor response time began to improve in the untreated *hq* cohort but remained significantly different ($P < 0.001$). At six months of age, untreated *hq* mice had a photoreceptor response time of 26.5 ± 2.44 ms (n = 4) which was slower than age-matched, untreated WT mice ($P < 0.001$; WT: 18.8 ± 0.42 ms [n = 28]). Data obtained from untreated cohorts at ten months of age revealed slower a-wave latencies in the *hq* cohort ($P < 0.001$; WT: 19.2 ± 0.70 ms [n = 9], *hq*: 34.5 ± 1.62 ms [n = 6]). When assessing a-wave latencies holistically from two to ten months of age, an average improvement in photoreceptor response time of the untreated WT cohort was found (- 0.05 ms/month). Untreated *hq* mice had a slowing rate of photoreceptor response time from two to ten months of age (1.33 ms/month).

Memantine-treated WT mice had slower photoreceptor response times compared to their untreated WT counterparts at two months of age ($P < 0.05$; untreated: 19.0 ± 0.45 ms [n = 30], treated: 20.8 ± 0.56 ms [n = 28]) and three months of age ($P < 0.01$; untreated: 19.8 ± 0.37 ms

Figure 3.6 - Photoreceptor response time measured by a-wave latency from two to ten months of age. A. Electroretinography testing began at two months of age. The retina was stimulated by a 10 cd.s/m^2 flash of light. Photoreceptor response time was assessed by a-wave latencies (ms) from two to ten months of age. No data point is presented if no mice were tested at a certain age in a specific cohort. A cohort of untreated WT mice tested with ERG a single time is presented at eleven months of age. A cohort of untreated *hq* mice tested with ERG a single time is presented at eleven months of age. Data are presented as Mean ± SEM. **B.** Mean body mass (g) data from the untreated *hq* cohort were plotted against a-wave latencies. **C.** Mean body mass data from memantine-treated *hq* mice (g) were plotted against a-wave latencies.

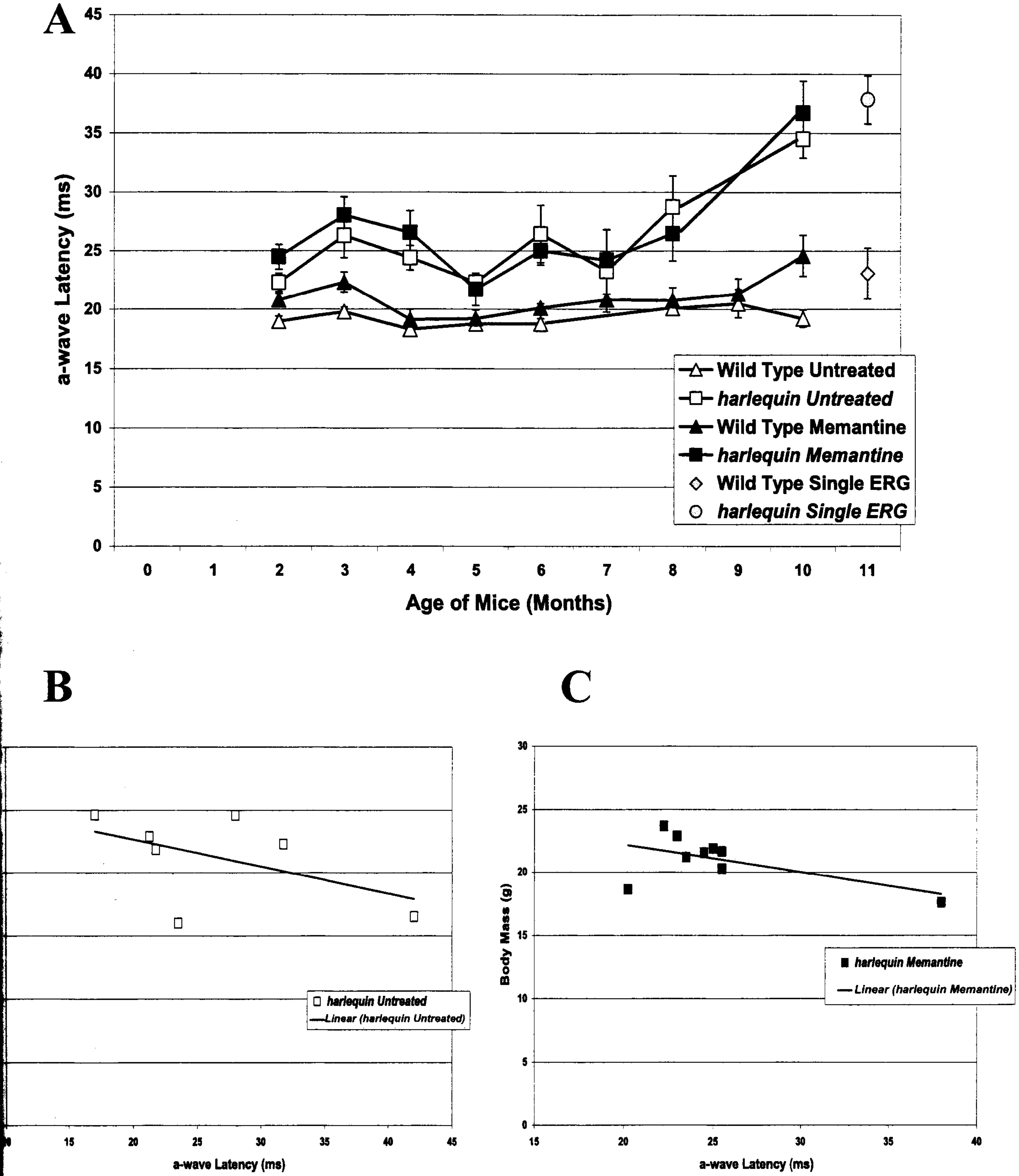
A
a-wave Latency (ms)
Age of Mice (Months)
Wild Type Untreated
harlequin Untreated
Wild Type Memantine
harlequin Memantine
Wild Type Single ERG
harlequin Single ERG
B
harlequin Untreated
Linear (harlequin Untreated)
a-wave Latency (ms)
C
Body Mass (g)
harlequin Memantine
Linear (harlequin Memantine)
a-wave Latency (ms)

[n=36], treated: 22.3 ± 0.87 ms [n = 30]). A significantly slower photoreceptor response was found in the memantine-treated WT cohort at ten months of age ($P < 0.05$; untreated: 19.2 ±0.70 ms [n = 9], treated: 24.6 ± 1.77 ms [n = 10]). Memantine-treated WT mice had an average reduced rate of photoreceptor response time (0.48 ms/month) from two to ten months of age.

The untreated *hq* and memantine-treated *hq* cohorts had no difference in a-wave latencies from two to ten months of age. The memantine-treated *hq* cohort had an average increase in photoreceptor response time less than that found in the untreated *hq* cohort from two and ten months of age (1.01 ms/month).

Memantine-treated *hq* mice had a significant reduction in a-wave latency at two months of age compared to memantine-treated WT mice ($P < 0.01$; WT: 20.8 ± 0.56 ms [n = 28], *hq*: 24.5 ± 1.05 ms [n = 36]). This significant difference continued into the third and fourth month of age ($P < 0.01$). At six and seven months of age, memantine-treated *hq* mice had significantly slower photoreceptor response times ($P < 0.001$) which continued to ten months of age ($P < 0.001$; WT: 24.6 ± 1.77 ms [n = 10], *hq*: 36.7 ± 2.70 ms [n = 10]).

No differences in a-wave latencies were found between the ten-month-old untreated WT cohort and the untreated WT cohort experiencing a single ERG experiment (WT single ERG: 23.1 ± 2.20 ms [n = 12]). No differences in a-wave latencies were found between the ten-month-old untreated *hq* cohort and the untreated *hq* cohort experiencing a single ERG experiment (*hq* single ERG: 37.8 ± 2.03 ms; n = 6). A significant reduction in a-wave latency was found in the *hq* single ERG cohort when compared to the WT single ERG cohort ($P < 0.001$).

3.8 Correlation Studies of Photoreceptor Response Time

Correlation was assessed in both untreated and memantine-treated *hq* cohorts to determine if reduced body mass was an accurate predictor of retinal disease severity. Untreated WT mice had low standard errors of mean in both mean body mass and mean values measured for electroretinography data. Correlation tests comparing body mass would likely be negligible in the untreated WT cohort and were not performed. At two months of age, a low correlation between body mass and a-wave latencies was observed in both the untreated *hq* (***p*** = - 0.12; n = 14) and memantine-treated *hq* cohorts (***p*** = - 0.12; n = 15). By four months of age, a medium correlation was found for untreated *hq* (***p*** = - 0.43; n = 9) and memantine-treated *hq* cohorts (***p*** = - 0.39; n = 10). Correlations continued to increase by six months of age reaching a high level of correlation in both cohorts (untreated: ***p*** = - 0.51 [n = 7]; treated: ***p*** = - 0.57 [n = 9]; Figure 3.6 B, 3.6 C).

At two months of age, untreated *hq* mice had a low correlation between water consumption and a-wave latencies (***p*** = - 0.23). Memantine-treated *hq* mice had no correlation between water consumption and a-wave latencies at two months of age (***p*** < 0.1). At four months of age, untreated *hq* mice had a high correlation between water consumption and photoreceptor response times (***p*** = - 0.54). However, memantine-treated *hq* mice were found to have a low correlation at four months of age (***p*** = - 0.28). Correlation was lost in both untreated and memantine-treated *hq* cohorts by six months of age (***p*** < 0.1).

At two months of age, memantine-treated WT mice had no correlation between memantine consumption and a-wave latencies (n = 13). Memantine-treated *hq* mice had a medium correlation between drug consumption and a-wave latencies at two months of age (***p*** = 0.49). By four months of age, memantine-treated WT mice had a medium correlation (***p*** = -

0.35; n = 8) while memantine-treated *hq* mice had no correlation between variables. Memantine-treated *hq* cohort had a high correlation (***p*** = 0.57) by six months of age, but the memantine-treated WT cohort did not (***p*** = - 0.16; n = 13).

3.9 Photoreceptor Health Assessed by Electroretinography a-wave Amplitude

Untreated WT mice had relatively unchanged photoreceptor function at young months of age (Figure 3.7 A). Photoreceptor function began to decline at six months of age in the untreated WT cohort and continued to decline in following months. By three months of age untreated *hq* mice had reduced photoreceptor health compared to untreated WT mice (P < 0.05; WT: 185.5 ± 5.98 μV [n = 35], *hq*: 162.9 ± 9.09 μV [n = 18]). A single data point (Mouse ID#: 915.91 OD; 687.4 μV) was removed from the three month untreated WT data set as an outlier due to electrode malfunction. Differences continued through four (P < 0.01) and five months of age (P < 0.05; WT: 193.2 ± 7.70 μV [n = 24], *hq*: 155.8 ± 14.38 μV [n = 12]). A single mouse was removed from the six month untreated *hq* data set because data were significantly lower than previous and following months (OD and OS; 34.25 μV and -9.87 μV). Reduced photoreceptor function in the untreated *hq* cohort continued at six (P < 0.001) and eight months of age (P < 0.01; WT: 156.3 ± 9.51 μV [n = 12], *hq*: 104.9 ± 11.49 μV [n = 8]). Photoreceptor function slowly decreased in the untreated WT cohort by 2.88 μV/month on average. The untreated *hq* mice had an elevated rate of photoreceptor decline averaging 12.80 μV/month.

Memantine treatment appeared to subtly reduce photoreceptor function over the course of the experiment in both WT and *hq* cohorts. At four months of age, memantine-treated WT mice had a significantly reduced a-wave amplitude compared to untreated WT mice (P < 0.01;

Figure 3.7 - Photoreceptor function assessed by a-wave amplitude from two to ten months of age. A. Electroretinography testing began at two months of age. The retina was stimulated by a 10 cd.s/m^2 flash of light. Photoreceptor function was assessed by a-wave amplitude (μV) from two to ten months of age. No data point is presented if no mice were tested at a certain age in a certain cohort. A cohort of untreated WT mice tested with ERG a single time is presented at eleven months of age. A cohort of untreated *hq* mice tested with ERG a single time is presented at eleven months of age. Data are presented as Mean ± SEM. **B.** Mean body mass (g) data from the untreated *hq* cohort were plotted against a-wave amplitudes. **C.** Mean body mass (g) data from memantine-treated *hq* mice were plotted against a-wave amplitudes.

A

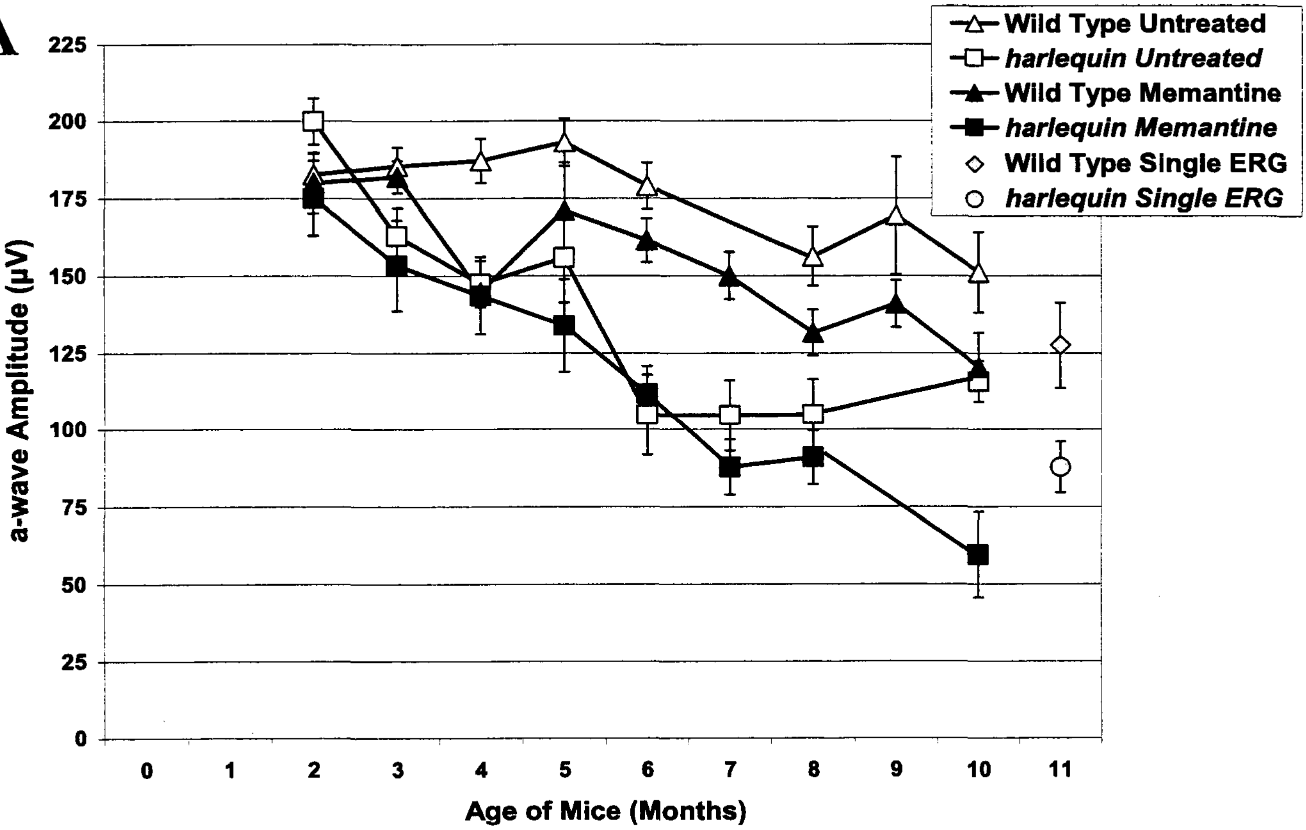
Wild Type Untreated
harlequin Untreated
Wild Type Memantine
harlequin Memantine
Wild Type Single ERG
harlequin Single ERG
a-wave Amplitude (µV)
225
200
175
150
125
100
75
50
25
0
0
1
2
3
4
5
6
7
8
9
10
11
Age of Mice (Months)

B

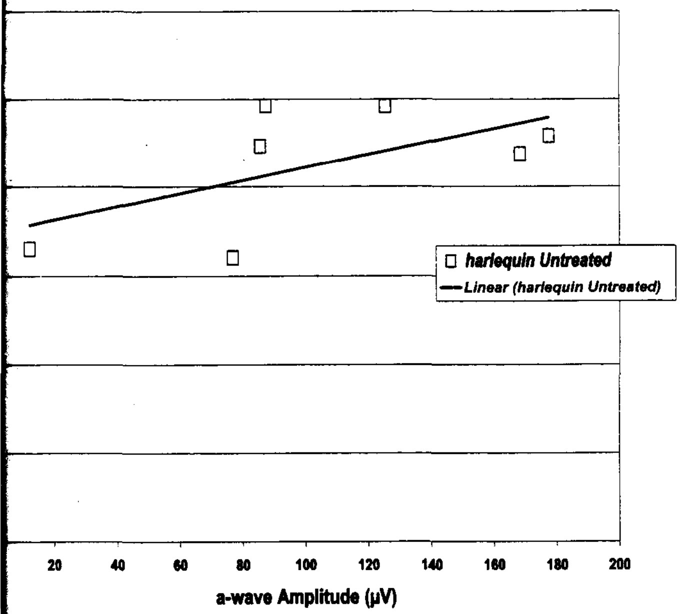
harlequin Untreated
Linear (harlequin Untreated)
20
40
60
80
100
120
140
160
180
200
a-wave Amplitude (µV)

C

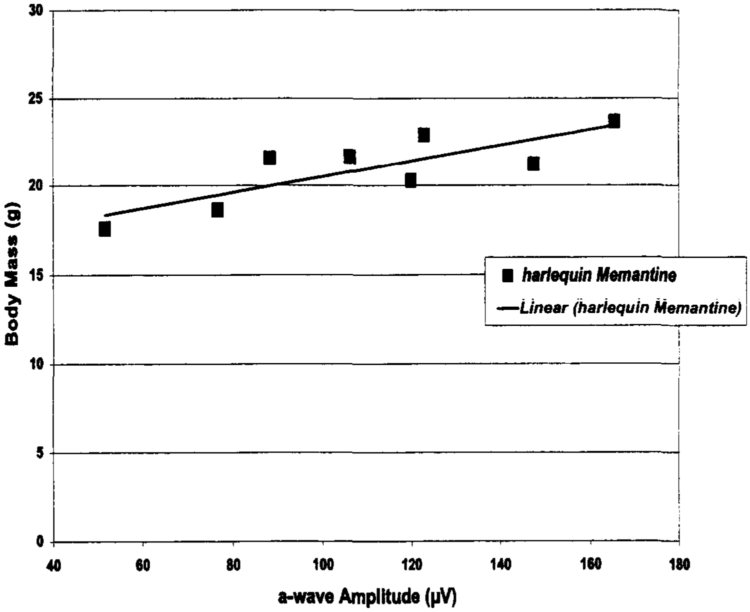
30
25
20
15
10
5
0
Body Mass (g)
harlequin Memantine
Linear (harlequin Memantine)
40
60
80
100
120
140
160
180
a-wave Amplitude (µV)

untreated:187.1 ± 7.19 μV [n = 40], treated: 144.8 ± 4.85 μV [n = 14]). Two data points from a single mouse were removed as outliers from the five month data set. The data obtained for this mouse was not reproducible in subsequent months (OD and OS; 67.2 μV and 50.1 μV). Memantine-treated WT mice had a slow rate of decline in photoreceptor health from two to ten months of age (7.44 μV/month).

A single data point was excluded from the four-month-old memantine-treated *hq* cohort (OD: 256 μV) because the data point was not reproduced in the following months. Similarly, a single data point (OD: 47.4 μV) was removed from the five month untreated *hq* cohort because datum was not reproduced in the following months of testing. Memantine-treated *hq* mice had reduced a-wave amplitudes at ten months of age compared to untreated *hq* mice ($P < 0.01$; untreated: 115.8 ± 6.58 μV [n = 6], treated: 59.5 ± 13.83 μV [n = 10]). Memantine-treated *hq* mice had the highest rate of photoreceptor degeneration (14.26 μV/month) from two to ten months of age.

Memantine-treated *hq* mice had a significantly reduced photoreceptor function by three months of age compared to memantine-treated WT mice ($P < 0.05$; WT: 182.0 ± 5.26 μV [n = 30], *hq*: 153.3 ± 14.54 μV [n = 22]). Memantine-treated *hq* mice had significantly reduced photoreceptor function from six to ten months of age (6 and 7 months: $P < 0.001$; 8 and 10 months: $P < 0.01$).

No difference in a-wave amplitude was found between the ten-month-old untreated WT cohort and the age-matched, untreated WT cohort experiencing a single ERG experiment (WT single ERG: 127.5 ± 11.1 μV; n = 12). A significantly lower a-wave amplitude was found in the *hq* single ERG cohort compared to the untreated *hq* cohort (P < 0.001; *hq* single ERG: 87.7 ± 8.2 μV; n = 6). A significant reduction in a-wave amplitude was found in the *hq* single ERG cohort when compared to the WT single ERG cohort (P < 0.05).

3.10 Linear Regression Analysis of a-wave Amplitudes

All a-wave amplitudes followed a linear rate of decline from two to ten months of age. The confidence interval minimum and maximum Y intercepts of all experimental cohorts were overlapping implying no significant differences in initial a-wave amplitudes. The Y-intercept confidence interval minimum and maximum values have been provided (Appendix C). The confidence interval of the slope of the untreated WT cohort was shallow ranging from a minimum of -1.2 μV to a maximum -6.2 μV. A similar slope was found in the memantine-treated WT cohort with a minimum of -5.0 μV and a maximum of -9.4 μV. Both of the untreated and memantine-treated *hq* cohorts had more dramatic rates of decline. The untreated *hq* cohort had a minimum slope of -10.1 μV and a maximum slope of - 16.5 μV. The memantine-treated *hq* cohorts had a more severe minimum slope of -10.1 μV and a maximum slope of -18.3 μV. No difference in slope was observed between the untreated and memantine-treated *hq* cohorts. The Y-intercept minimum and maximum values have been provided (Appendix C).

3.11 Correlation Studies of Photoreceptor Health

At two months of age, untreated *hq* mice had a high correlation between body mass and photoreceptor health ($p = 0.54$). In the memantine-treated *hq* cohort a medium correlation was found between variables at two months of age ($p = 0.42$). Correlation in the untreated *hq* cohort reduced and inverted by four months of age (p = - 0.43) but increased in the memantine-treated *hq* cohort (p = - 0.68). By six months of age, both untreated and memantine-treated *hq* (n = 8) mice had a high correlation between body mass and photoreceptor health (p = 0.60 and p = 0.82, respectively; Figure 3.7 B, 3.7 C).

No correlation between water consumption and photoreceptor health was found in the untreated *hq* cohort at two months of age. Memantine-treated mice had a low correlation between variables at the same age (p = 0.11). By four months of age, correlation had improved in the untreated *hq* cohort (p = 0.25) but reduced in the memantine-treated *hq* cohort where no correlation was found. By six months of age, untreated *hq* mice still had a low level of correlation between water consumption and photoreceptor health (p = 0.23). However, memantine-treated *hq* mice had a high correlation (p = 0.50).

Memantine-treated WT mice had a medium level of correlation between memantine consumption and photoreceptor health at two months of age (p = - 0.46). By four months of age, correlation had reduced and inverted (p = 0.24). No correlation was found between memantine consumption and photoreceptor health at two or four months of age. By six months of age, a medium level of correlation was found in both memantine-treated WT and *hq* cohorts (p = 0.322 and p = 0.40, respectively)

3.12 Retinal Response Time Assessed by Electroretinography b-wave Latency

In general, there did not appear to be any meaningful change in b-wave latency between WT and *hq* mice over the course of the experiment. At four months of age, a significantly longer response time was found in the untreated *hq* cohort compared to the untreated WT cohort (P <

0.001; WT: 73.9 ± 1.89 ms [n = 40], 88.9 ± 4.19 ms [n = 18]; Figure 3.8 A). Whole retinal response time had improved by an average of 0.81 ms/month in the untreated WT cohort. Similarly, the retinal response time had improved in the untreated *hq* cohort by 0.19 ms/month on average.

In general, there did not appear to be any meaningful change in b-wave latency between memantine-treated and untreated mice over the course of the experiment. A final difference was encountered at ten months of age, revealing a slowing retinal response time in the memantine-treated WT cohort ($P < 0.01$; untreated: 77.3 ± 3.51 ms [n = 10], treated: 93.5 ± 4.74 ms [n = 10]). Fluctuations in the retinal response times of memantine-treated WT mice led to an average slowing in retinal response time of 1.85 ms/month, opposite to that of untreated cohorts.

Untreated *hq* mice had an initial retinal response time of 80.8 ± 4.19 ms (n = 28), found at two months of age. Age-matched, memantine-treated *hq* mice had a retinal response time similar to that found in the untreated cohort (79.6 ± 3.71 ms; n = 36). No differences were found between *hq* cohorts from two to seven months of age. No difference was noted between *hq* cohorts at ten months of age. Memantine-treated *hq* mice had a 1.29 ms/month average rate of improvement in retinal response time.

No differences in retinal response times were observed between memantine-treated WT and *hq* mice from two to seven months of age. Memantine-treated *hq* mice had much faster retinal response times compared to memantine-treated WT counterparts at eight months of age ($P < 0.01$; WT: 87.4 ± 3.73 ms [n = 16], *hq*: 63.8 ± 6.79 ms [n = 12]). Memantine-treated *hq* mice had response times of 78.3 ± 8.36 ms (n = 10) at similar ages.

Figure 3.8 - Retinal response assessed by b-wave latency from two to ten months of age. A. Electroretinography testing began at two months of age. The retina was stimulated by a 10 cd.s/ m^2 flash of light. Retinal response was assessed by b-wave latencies (ms) from two to ten months of age. No data point is presented if mice were not tested at a certain age in a specific cohort. A cohort of untreated WT mice tested with ERG a single time is presented at eleven months of age. A cohort of untreated *hq* mice tested with ERG a single time is presented at eleven months of age. Data are presented as Mean ± SEM. **B.** Memantine consumption (mg/g/ day) data from the memantine-treated WT cohort were plotted against b-wave latencies. **C.** Memantine consumption (mg/g/day) data from the memantine-treated *hq* cohort were plotted against b-wave latencies.

A

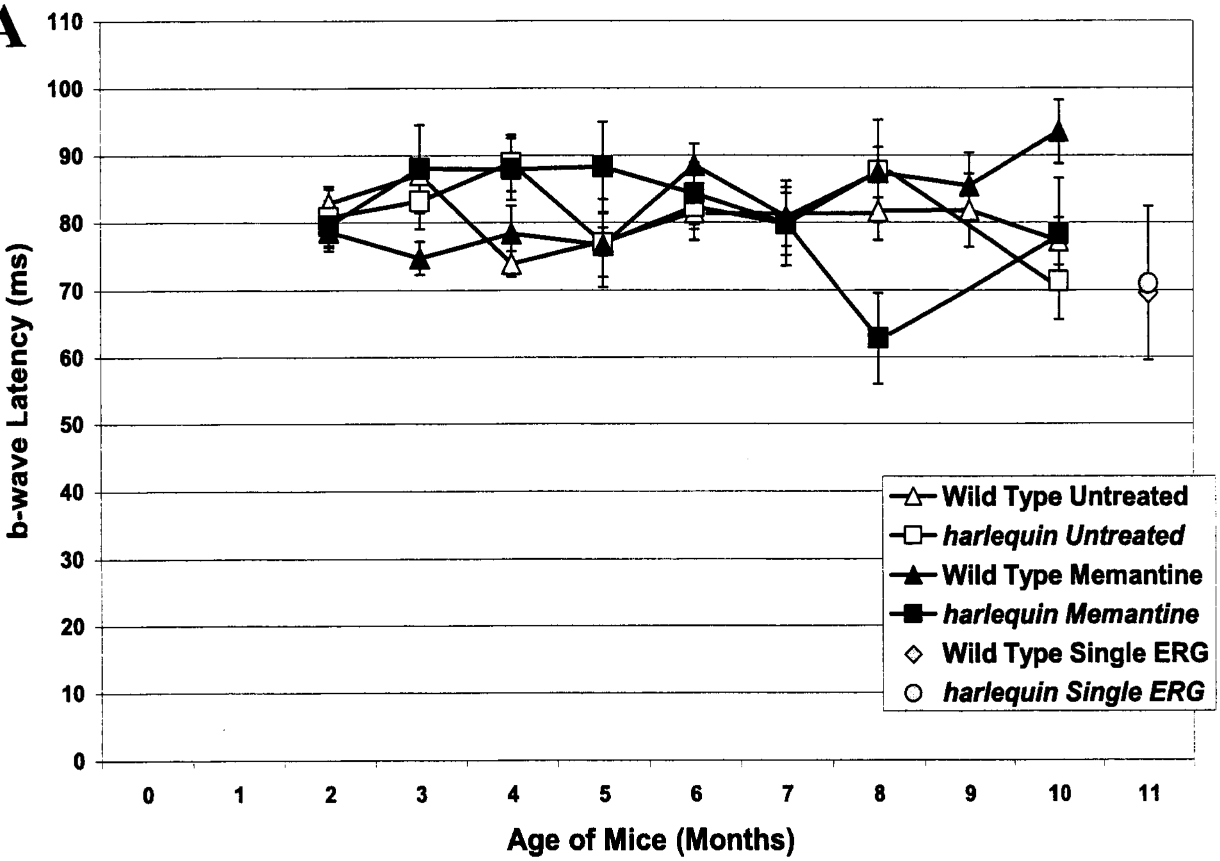
110
100
90
80
70
60
50
40
30
20
10
0
b-wave Latency (ms)
0
1
2
3
4
5
6
7
8
9
10
11
Age of Mice (Months)
Wild Type Untreated
harlequin Untreated
Wild Type Memantine
harlequin Memantine
Wild Type Single ERG
harlequin Single ERG

B

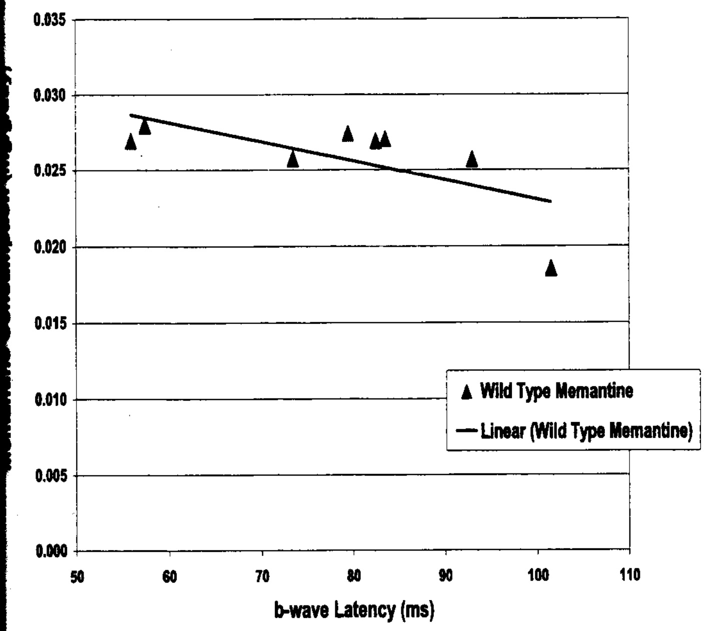
0.035
0.030
0.025
0.020
0.015
0.010
0.005
0.000
50
60
70
80
90
100
110
b-wave Latency (ms)
Wild Type Memantine
Linear (Wild Type Memantine)

C

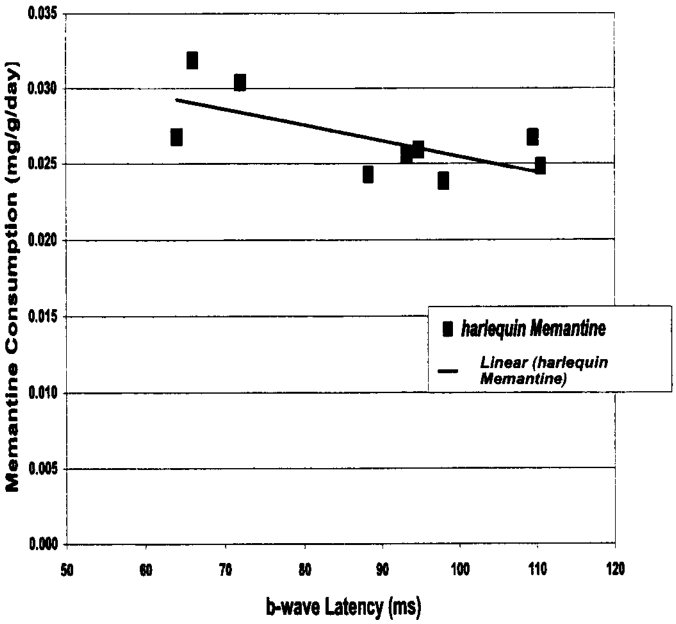
Memantine Consumption (mg/g/day)
0.035
0.030
0.025
0.020
0.015
0.010
0.005
0.000
50
60
70
80
90
100
110
120
b-wave Latency (ms)
harlequin Memantine
Linear (harlequin Memantine)

No differences in retinal response times were found between the ten-month-old untreated WT cohort and the age-matched, untreated WT cohort experiencing a single ERG experiment (WT single ERG: 69.6 ± 4.51 ms; n = 12). No difference in b-wave latencies were found between untreated *hq* mice at ten months of age and the *hq* cohort experiencing a single ERG test (*hq* single ERG: 71.0 ± 11.41 ms; n = 6). No differences in b-wave latencies were found between the WT and *hq* single ERG cohorts.

3.13 Correlation Studies of Retinal Response Time

No correlation between body mass and whole retinal response time was observed in either the untreated or memantine-treated *hq* cohorts at two months of age. By four months of age, both cohorts were found to have low correlation between variables (untreated: $\boldsymbol{p}$ = - 0.20; treated: $\boldsymbol{p}$ = 0.12). By six months of age, there was no correlation between body mass and whole retinal response time in both *hq* cohorts ($\boldsymbol{p}$ < 0.1/- 0.1).

Untreated *hq* mice had no correlation between water consumption and whole retinal response time at two months of age. Memantine-treated *hq* mice had a low correlation at the same age ($\boldsymbol{p}$ = 0.15). By four months of age, untreated *hq* mice had a low correlation between water consumption and whole retinal response ($\boldsymbol{p}$ = 0.14). However, memantine-treated *hq* mice no longer had a correlation between variables. By six months of age, untreated *hq* mice had a high level of correlation between variables ($\boldsymbol{p}$ = 0.59). Memantine-treated *hq* mice also had an increase in correlation between variables however the value was inverted ($\boldsymbol{p}$ = - 0.32).

Memantine-treatment at two months of age had a high correlation with whole retinal response time in the memantine-treated WT cohort (***p*** = - 0.63). In memantine-treated *hq* mice an inverted effect was found with a slightly lower correlation at two months of age (***p*** = 0.46). By four months of age, both the memantine-treated WT and *hq* cohorts had a high level of correlation between drug consumption and whole retinal response time (***p*** = - 0.59 and ***p*** = - 0.68, respectively; Figure 3.8 B, 3.8 C). By six months of age, correlation was lost in the memantine-treated WT cohort but remained very high in the memantine-treated *hq* cohort (***p*** = - 0.67).

3.14 Retinal Function Measured by Electroretinography b-wave Amplitude

Retinal function in WT mice reduces with age but age-related degeneration was severe in the *hq* cohort (Figure 3.9 A). Comparisons of untreated WT and *hq* cohorts revealed nine months of differences in retinal function. A single mouse (OD and OS; 37.1 μV and 45.2 μV) was excluded from the untreated *hq* cohort data set because retinal function values could not be reproduced in the following months. The most likely cause of data artifacts was poor electrode contact with the cornea of the mouse. At two months of age, untreated *hq* mice had a significant reduction in retinal function compared to untreated WT mice ($P < 0.05$; WT: 636.0 ± 19.59 μV [n = 30], *hq*: 557.5 ± 29.63 μV [n = 28]). Differences continued at three months ($P < 0.001$) and four months of age ($P < 0.001$). Significant differences were observed between cohorts at five ($P < 0.05$), six ($P < 0.001$), eight ($P < 0.001$) and ten months of age ($P < 0.001$). A single mouse (OD and OS; 12.2 μV and 5.6 μV) was excluded from the nine month untreated WT data

Figure 3.9 - Retinal function assessed by b-wave amplitude from two to ten months of age. **A.** Electroretinography testing began at two months of age. The retina was stimulated by a 10 cd.s/m^2 flash of light. Retinal function was assessed by b-wave amplitude (μV) from two to ten months of age. No data point is presented if mice were not tested at a certain age in a specific cohort. A cohort of untreated WT mice tested with ERG a single time is presented at eleven months of age. A cohort of untreated *hq* mice tested with ERG a single time is presented at eleven months of age. Data are presented as Mean ± SEM. **B.** Body mass (g) data from the memantine-treated *hq* cohort were plotted against the b-wave amplitudes. **C.** Memantine consumption (mg/g/day) in memantine-treated WT mice were plotted against b-wave amplitudes.

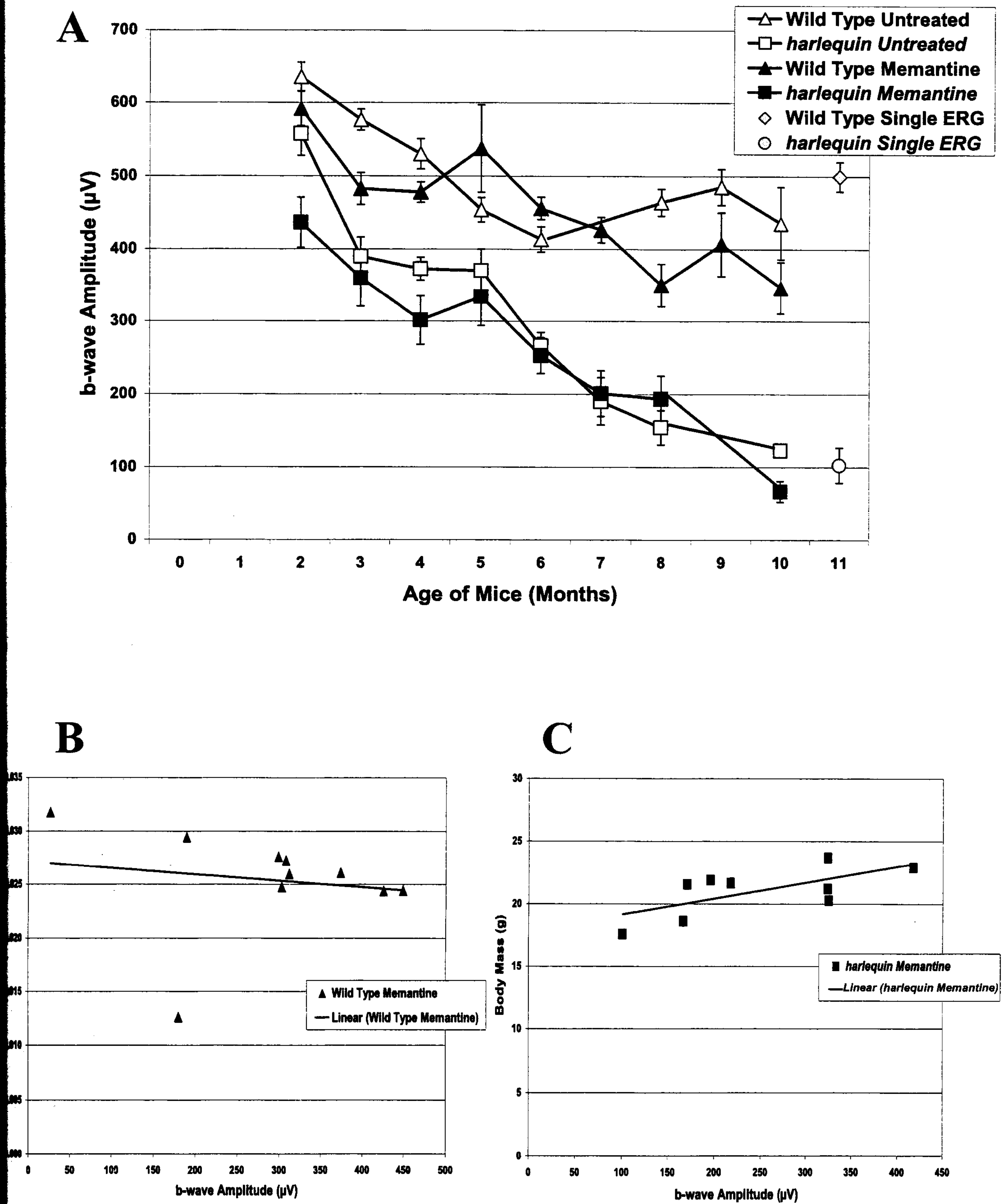
A
Wild Type Untreated
harlequin Untreated
Wild Type Memantine
harlequin Memantine
Wild Type Single ERG
harlequin Single ERG
b-wave Amplitude (µV)
Age of Mice (Months)
B
Wild Type Memantine
Linear (Wild Type Memantine)
b-wave Amplitude (µV)
C
harlequin Memantine
Linear (harlequin Memantine)
Body Mass (g)
b-wave Amplitude (µV)

set due to abnormal b-wave traces. Untreated WT mice had a rate of retinal degeneration averaging 32.36 μV/month. Age-matched, untreated *hq* mice had an average rate of retinal degeneration reaching 59.81 μV/month.

Memantine appeared to be associated with a subtle reduction in retinal function in both WT and *hq* mice. The memantine-treated WT cohort had multiple data points excluded from the final experimental data set. These artifacts were most likely due to poor electrode contact with the cornea of the mice. A single mouse was excluded from the two month data set (OD and OS; 108.8 μV and 142.4 μV). Two additional mice were excluded from the three month data set (OD and OS; 367.1 μV and 318.0 μV; OD and OS; 288.1 μV and 243.2 μV). A final mouse was excluded from the five month data set (OD and OS; 265.7 μV and 157.6 μV). By three months of age, memantine-treated WT mice had reduced retinal function compared to untreated WT mice ($P < 0.001$; untreated: 576.7 ± 14.31 μV [n = 36], treated: 592.1 ± 23.62 μV [n = 21]). At eight months of age, memantine-treated WT mice had a significantly lower retinal function ($P < 0.01$; untreated: 464.4 ± 18.31 μV [n = 12], treated: 350.2 ± 29.53 μV [n = 16]). A 30.71 μV/ month average rate of retinal degeneration was calculated for memantine-treated WT mice, similar to that of untreated WT mice.

Significantly reduced retinal function was found in the memantine-treated *hq* cohort compared to the untreated *hq* cohort at two months of age ($P < 0.05$; untreated: 557.5 ± 29.63 μV [n = 28], treated: 436.4 ± 34.53 μV [n = 36]). A second difference was found at ten months of age when memantine-treated *hq* mice had a minimal b-wave amplitude ($P < 0.01$; untreated:

123.1 ± 6.22 μV [n = 6], treated: 66.5 ± 14.40 μV [n = 10]). The average rate of retinal degeneration was 43.74 μV/month in the memantine-treated *hq* cohort, reduced from that of the untreated *hq* cohort.

Memantine-treated *hq* mice had a reduction in retinal function from two to five months of age compared to memantine-treated WT mice ($P < 0.01$). By six months of age, memantine-treated WT mice had a b-wave amplitude of 456.1 ± 15.12 μV (n = 28). Age-matched, memantine-treated *hq* mice had a much lower b-wave amplitude of ($P < 0.001$; *hq*: 252.7 ± 24.63 μV [n = 20]). Differences in retinal function continued between memantine-treated cohorts from seven to ten months of age ($P < 0.001$).

No differences in b-wave amplitudes were found between the untreated WT cohort and the WT single ERG cohort (WT single ERG: 499.6 ± 20.06 μV; n = 12). No differences in retinal function were found between untreated *hq* mice at ten months of age and the *hq* cohort experiencing a single ERG test (*hq* single ERG: 102.8 ± 24.25 μV; n = 6). A significantly lower b-wave amplitude was found in the *hq* single ERG cohort when compared to the WT single ERG cohort ($P < 0.01$).

3.15 Linear Regression Analysis of b-wave Amplitudes

All b-wave amplitudes followed a linear rate of decline from two to ten months of age. The confidence interval minimum and maximum of the Y-intercepts in the untreated *hq*, untreated WT and memantine-treated WT cohorts were overlapping showing no significant differences in initial b-wave amplitudes at birth. The minimum and maximum value for the memantine-treated *hq* Y-intercept fell below that of all other cohorts implying significantly reduced b-wave amplitudes. The Y-intercept confidence interval minimum and maximum values have been provided (Appendix C). The confidence interval of the slope of the untreated WT cohort was relatively shallow ranging from a minimum of -19.6 μV to a maximum -33.7 μV. A similar slope was found in the memantine-treated WT cohort with a minimum of -20.0 μV and a maximum of -33.6 μV. Both of the untreated and memantine-treated *hq* cohorts had more dramatic rates of decline. The untreated *hq* mice had a minimum slope of -48.97 μV and a maximum slope of -66.9 μV. The memantine-treated *hq* mice had a slope with a minimum of -32.2 μV and a maximum slope of -52.8 μV. The minimum and maximum values of the slope of retinal function have been provided (Appendix C).

3.16 Correlation Studies of Retinal Function

No correlation was found between body mass and whole retinal function at two months of age in the untreated and memantine-treated *hq* cohorts. Untreated *hq* mice had a low correlation, while memantine-treated *hq* mice had a high level of correlation between variables at four months of age ($p = 0.29$ and $p = 0.62$, respectively). Relationships between body mass and whole retinal function increased to a moderate correlation in the untreated *hq* cohort ($p = 0.41$) and memantine-treated *hq* cohort by six months of age ($p = 0.67$; Figure 3.9 B).

A low relationship between water consumption and whole retinal response was found in the untreated *hq* cohort at two months of age ($p = 0.15$). No correlation was found in the memantine-treated *hq* cohort. By four months of age, no correlation was found in the untreated *hq* cohort but was found to be low in the memantine-treated cohort ($p = 0.15$). Both untreated and memantine-treated *hq* mice had a low correlation between water consumption and whole retinal response at six months of age ($p = -0.12$ and $p = -0.26$, respectively).

Finally, a low correlation between memantine consumption and whole retinal response was found for the memantine-treated WT cohort at two months of age ($p = -0.16$). Memantine-treated *hq* mice were found to have a moderate level of correlation between variables at two months of age ($p = 0.36$). By four months of age, the relationship between drug consumption and whole retinal response had increased in the memantine-treated WT cohort ($p = -0.66$; Figure 3.9 C) but was lower in the memantine-treated *hq* cohort ($p = -0.15$). Both of the memantine-treated WT and *hq* cohorts had low correlation between drug consumption and whole retinal response by six months of age ($p = -0.14$ and $p = -0.10$, respectively).

3.17 Comparison of Tissue Thickness Between OS and OD *In Vivo*

Untreated WT mice had similar corneal thickness in the OS and OD through the first nine months of age. No significant corneal thickness differences were found between OS and OD of memantine-treated WT mice at any age of imaging. No NPC or temporal peripheral corneal (TPC) thickness differences were found between OS and OD of memantine-treated *hq* mice.

No differences in anterior chamber width (ACW) or anterior chamber depth (ACD) occurred between OS and OD of untreated WT mice at any age of imaging. Also, untreated *hq* mice had no significant differences in ACW or ACD between OS and OD. No further differences were found in the ACW or ACD of memantine-treated WT mice. No differences between OS and OD were found for either ACW or ACD of memantine-treated *hq* mice.

A significantly thicker CWR thickness was measured in the OD (OD: 0.336 ± 0.008 mm; OS: 0.302 ± 0.013 mm [n = 10]) of the untreated WT cohort at ten months of age ($P < 0.05$; n = 10). No further differences in retinal thickness were observed at any age for untreated WT mice. No differences in retinal thickness were found in untreated *hq* mice at any age of imaging. An increased PR thickness was found in the OD of the memantine-treated WT cohort at six months of age ($P < 0.05$; n = 29). No differences in retinal thickness were found between OS and OD of memantine-treated *hq* mice at any month of age.

3.18 Assessment of Corneal Thickness Between Mouse Cohorts

Subtle increases in corneal thickness were associated with aging in the untreated WT cohort. Memantine-treated *hq* mice had a dramatic increase in corneal thickness specifically in the central and nasal peripheral cornea at eight and ten months of age. Untreated *hq* mice had an increase in TPC thickness from 0.118 ± 0.005 mm (n = 10) at three months of age to 0.135 ± 0.01 mm (n = 10) by four months of age (Figure 3.10). This resulted in a significant TPC thickening when compared to the untreated WT cohort ($P < 0.01$; WT: n = 20, *hq*: n = 10). A single data point was removed from the untreated *hq* data sets (OS; Figure 3.11) beginning at six months of age due to an iris that was continuous with the cornea making accurate measurements of corneal thickness impossible. At ten months of age, a thickening of the TPC was measured in the untreated *hq* cohort reaching a thickness of 0.142 ± 0.002 mm. This led to a significant difference in TPC thickness between the untreated cohorts ($P < 0.05$; WT: n = 10, *hq*: n = 6).

Figure 3.10 - Corneal thickness assessed by ocular coherence tomography imaging. A. Nasal peripheral corneal thickness (mm) was not significantly different over the the ten months of experimentation. A cohort of untreated WT mice tested with OCT a single time is presented at eleven months of age. A cohort of untreated *hq* mice tested with OCT a single time is presented at eleven months of age. Data are presented as Mean ± SEM. **B.** Central corneal thickness (mm) was not significantly different over the ten months of experimentation. A cohort of untreated WT mice tested with OCT a single time is presented at eleven months of age. A cohort of untreated *hq* mice tested with OCT a single time is presented at eleven months of age. Data are presented as Mean ± SEM. **C.** Temporal peripheral corneal thickness (mm) was not significantly different between cohorts over the ten months of experimentation. A cohort of untreated WT mice tested with OCT a single time is presented at eleven months of age. A cohort of untreated *hq* mice tested with OCT a single time is presented at eleven months of age. Data are presented as Mean ± SEM.

A

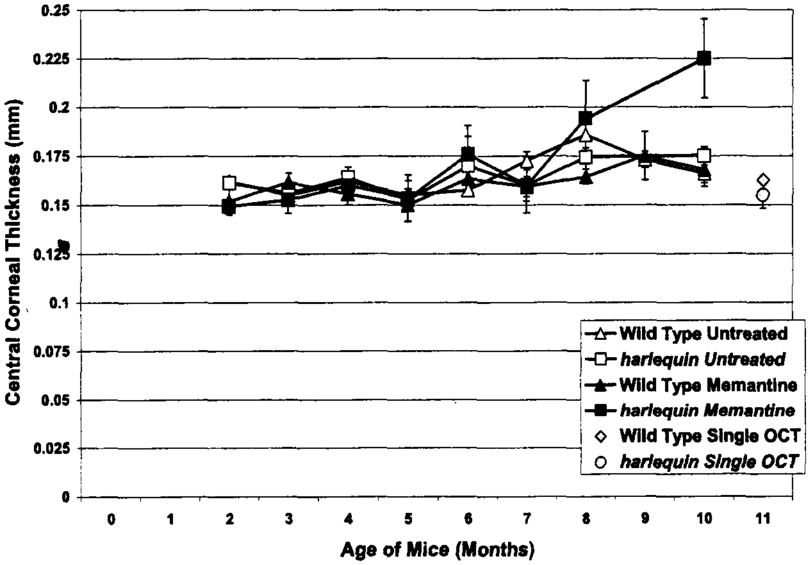
Central Corneal Thickness (mm)
Age of Mice (Months)
Wild Type Untreated
harlequin Untreated
Wild Type Memantine
harlequin Memantine
Wild Type Single OCT
harlequin Single OCT

B

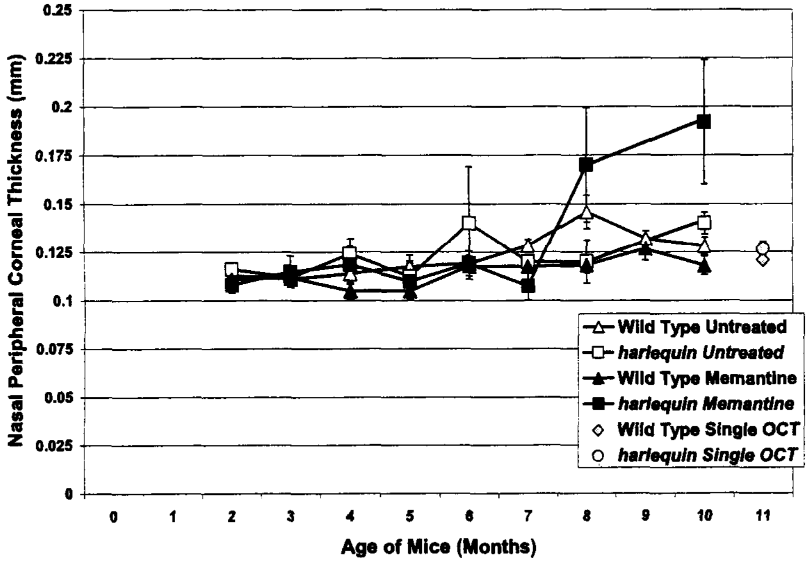
Nasal Peripheral Corneal Thickness (mm)
Age of Mice (Months)
Wild Type Untreated
harlequin Untreated
Wild Type Memantine
harlequin Memantine
Wild Type Single OCT
harlequin Single OCT

C

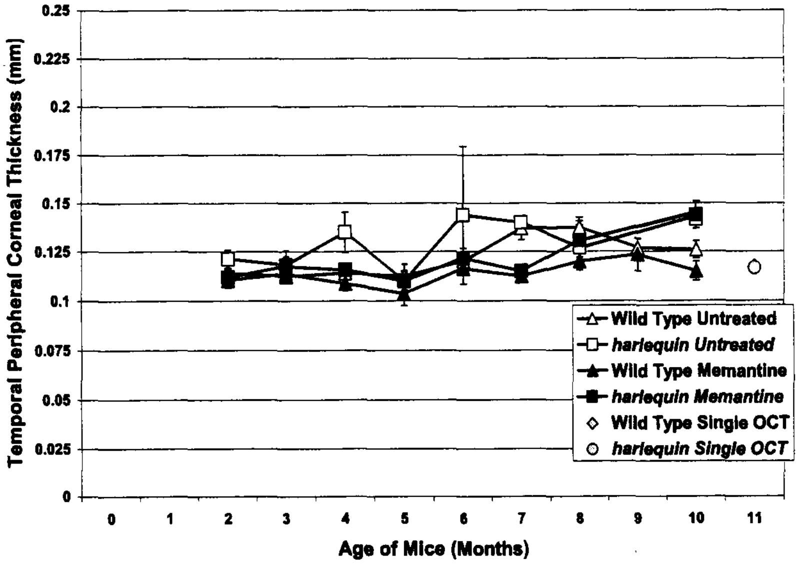
Temporal Peripheral Corneal Thickness (mm)
Age of Mice (Months)
Wild Type Untreated
harlequin Untreated
Wild Type Memantine
harlequin Memantine
Wild Type Single OCT
harlequin Single OCT

Figure 3.11 - A fusion between the iris and cornea of a mouse led to the exclusion of a single data point from the untreated *hq* data set. The left eye (OS) of mouse 100.2 had an abnormal iris that appeared to be fused with the cornea. The iris could not be moved with the administration of dilator eye drops. Measurements of corneal thickness, anterior chamber width, anterior chamber depth, and retinal thickness could not be accurately obtained from these images. Accurate measurements were still obtained and included from the right eye (OD) of mouse 100.2.

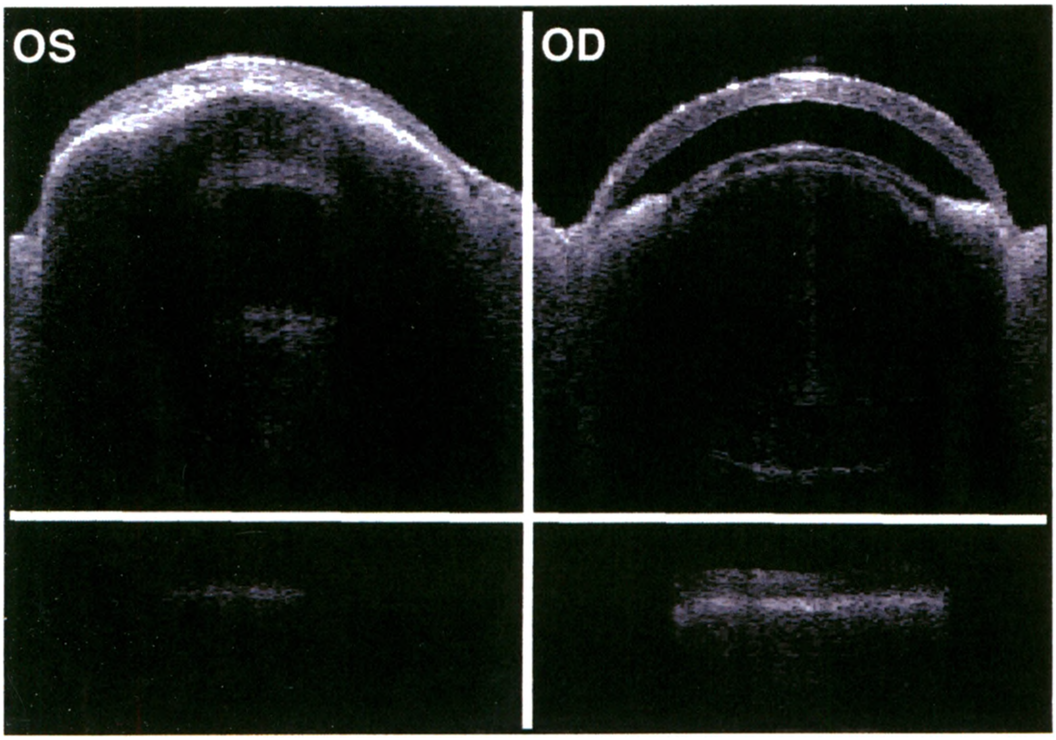
OS
OD

By four months of age, a significant reduction in the NPC thickness of memantine-treated WT mice was measured compared to untreated WT mice (P < 0.05; untreated: n = 20, treated: n = 16). This was due to a thickening NPC in the untreated WT cohort (0.114 ± 0.002 mm) and a thinning NPC in the memantine-treated WT cohort (0.105 ± 0.004 mm). Untreated WT mice had significantly increased NPC (P < 0.01) and TPC thickness (P < 0.001) by seven months of age (untreated: n = 12; treated: n = 16). This significant increase in tissue thickness continued into eight months of age (untreated: n = 12; treated: n = 16) and affected all corneal measurements (CC: P < 0.01; NPC: P < 0.01; TPC: P < 0.05).

Images captured at two months of age showed a significant decrease in central corneal thickness of the memantine-treated *hq* cohort compared to the untreated *hq* cohort (P < 0.05; untreated: 0.116 ± 0.002 mm [n = 16], treated: 0.108 ± 0.004 mm [n = 26). Imaging of the memantine-treated *hq* cohort at eight months of age revealed a mouse with an OD CC thickness of 0.38 mm (OD: Figure 3.12C). The CC thickness continued to increase in the treated *hq* cohort reaching the highest average CC thickness of 0.225 ± 0.020 mm (n = 10) by ten months of age. At least one eye in all mice of the memantine-treated *hq* cohort at ten months of age demonstrated CC thickening. The maximum CC thickness of 0.36 mm was obtained in the OD of a single mouse (OD: Figure 3.12 D). Average NPC thickness also increased to 0.170 ± 0.029 (n = 12) at eight months of age and continued to increase until ten months of age (0.192 ± 0.032 mm; n = 10). A much smaller increase in TPC was observed (0.144 ± 0.007 mm; n = 10) in the memantine-treated *hq* cohort at ten months of age. Corneal thickening was accompanied with a corneal opacity in the OCT images and appeared to impede light from reaching the retina.

Figure 3.12 - Corneal thickening and opacity were observed using ocular coherence tomography imaging. A. An example of OCT imaging from a healthy untreated WT mouse at ten months of age. Both the left (OS) and right (OD) eyes had representative corneal thickness, anterior chamber width, anterior chamber depth, and retinal thickness of the untreated WT cohort at ten months of age. **B.** An example of OCT imaging from a healthy untreated *hq* mouse at ten months of age. Both OS and OD had representative corneal thickness, anterior chamber width, anterior chamber depth, and retinal thickness of the untreated *hq* cohort at ten months of age. **C.** Nasal peripheral corneal thickening and central corneal thickening can be observed at eight months of age in both OS and OD of a memantine-treated mouse (Mouse ID#: 909.77). Corneal thickness and opacity is shown to impede light from reaching the retina. **D.** Nasal peripheral corneal thickening and central corneal thickening can be observed at ten months of age in both OS and OD of a memantine-treated mouse (Mouse ID#: 909.60). Corneal thickness and opacity is shown to impede light from reaching the retina.

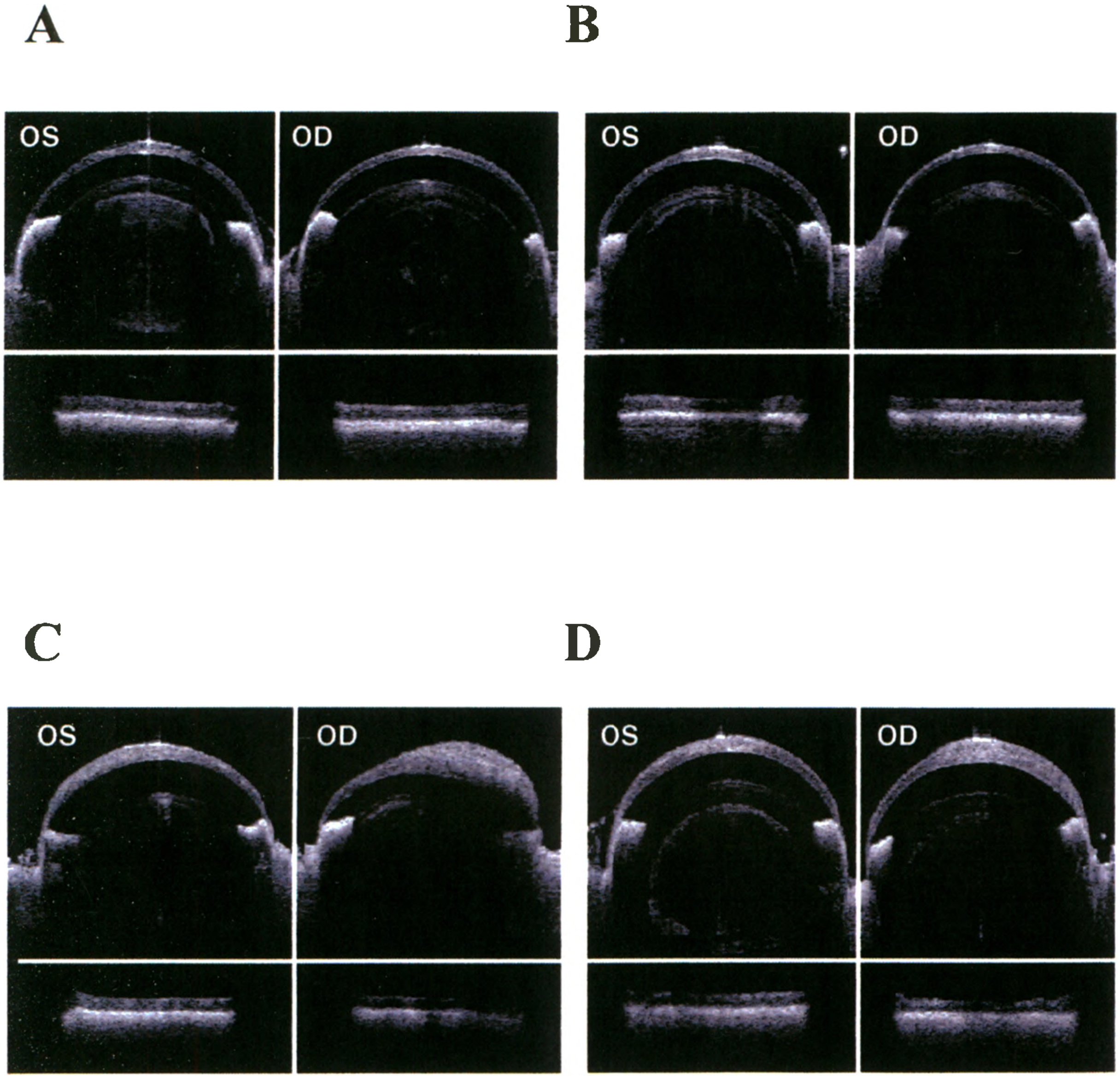
A
OS
OD
B
OS
OD
C
OS
OD
D
OS
OD

The CC thickness in the memantine-treated *hq* cohort increased by 0.03 mm between seven and eight months of age. This was a statistically significant CC thickening compared to the memantine-treated WT cohort ($P < 0.05$; WT: n = 16, *hq*: n = 12). All three corneal thickness measurements were significantly higher in memantine-treated *hq* mice (WT: n = 10, *hq*: n = 10) at ten months of age (CC: $P < 0.05$; NPC: $P < 0.05$; TPC: $P < 0.001$).

Ten-month-old WT mice were compared to an untreated WT control cohort that were imaged a single time using OCT. No difference in corneal thickness was observed (WT single OCT; CC: 0.16 ± 0.001 mm, NPC: 0.12 ± 0.001 mm, TPC: 0.12 ± 0.002 mm [n = 12]). A significantly thinner CC and TPC was measured in the *hq* single OCT cohort (*hq* single OCT; CC: 0.16 ± 0.007 mm, NPC: 0.13 ± 0.004 mm, TPC: 0.12 ± 0.002 mm [n = 6]) compared to the untreated *hq* cohort ($P < 0.05$ and $P < 0.001$; respectively). A significantly larger NPC thickness was measured in the *hq* single OCT cohort compared to the WT single OCT cohort ($P < 0.05$).

3.19 Assessment of Anterior Chamber Width and Depth Between Mouse Cohorts

Anterior chamber width increased as untreated WT mice aged. However, anterior chamber depth remained relatively consistent from two to ten months of age in the untreated WT cohort. Untreated *hq* mice had a reduced anterior chamber width from two to ten months of age but the anterior chamber depth was comparable to that found in the untreated WT cohort. Memantine treatment did not appear to have any significant effect on anterior chamber width or depth over the course of the experiment. Comparison of untreated WT and *hq* mice revealed a significantly smaller ACW in both the OD and OS of *hq* mice (Figure 3.13 A). This genotype-specific reduction in ACW was first noted at two months of age ($P < 0.01$; WT: n = 10, *hq*: n =

Figure 3.13 - Anterior chamber width and depth assessed using ocular coherence tomography. A. Anterior chamber width has been plotted for experimental cohorts from two to ten months of age. No data point is presented if mice were not tested at a certain age in a specific cohort. A cohort of untreated WT mice tested with OCT a single time is presented at eleven months of age. A cohort of untreated *hq* mice tested with OCT a single time is presented at eleven months of age. Data are presented as Mean ± SEM. **B.** Anterior chamber depth has been plotted for experimental cohorts from two to ten months of age. No data point is presented if mice were not tested at a certain age in a specific cohort. A cohort of untreated WT mice tested with OCT a single time is presented at eleven months of age. A cohort of untreated *hq* mice tested with OCT a single time is presented at eleven months of age. Data are presented as Mean ± SEM. **C.** An example of OCT imaging from a healthy untreated WT mouse at ten months of age. Both the left (OS) and right (OD) eyes had representative anterior chamber width and anterior chamber depth of the untreated WT cohort at ten months of age. **D.** An example of OCT imaging from a memantine-treated *hq* mouse at ten months of age demonstrating microophthalmia in the OS. The OD of the same animal was considered to be of proper size.

A

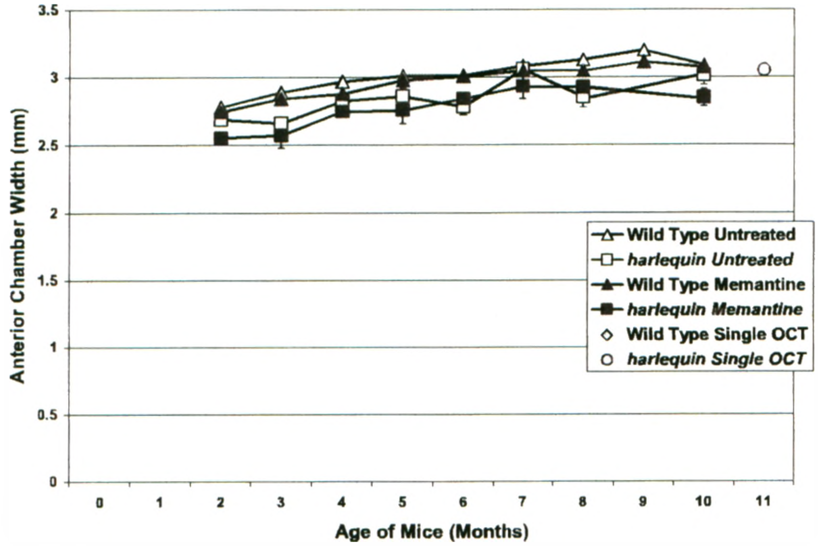
Anterior Chamber Width (mm)
Age of Mice (Months)
Wild Type Untreated
harlequin Untreated
Wild Type Memantine
harlequin Memantine
Wild Type Single OCT
harlequin Single OCT

B

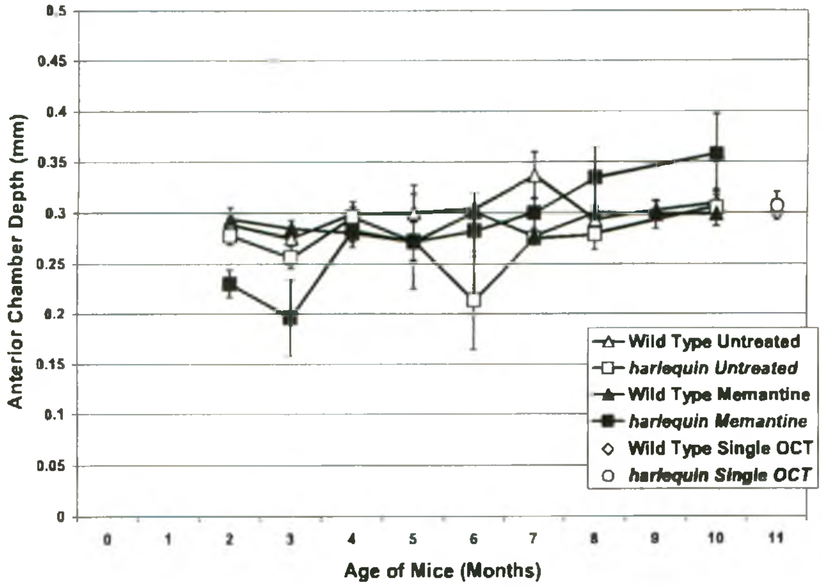
Anterior Chamber Depth (mm)
Age of Mice (Months)
Wild Type Untreated
harlequin Untreated
Wild Type Memantine
harlequin Memantine
Wild Type Single OCT
harlequin Single OCT

C

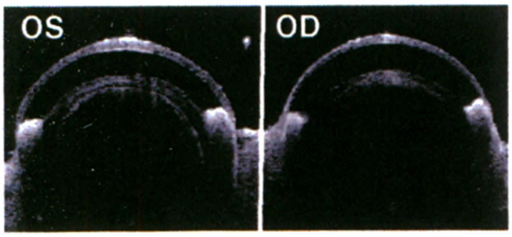
OS
OD

D

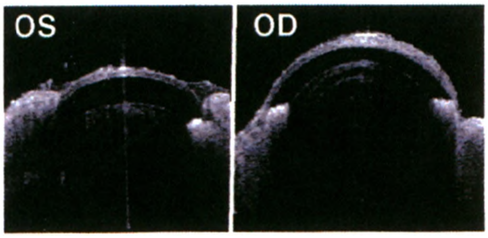
OS
OD

16). A single data point was removed from the untreated *hq* data set (OS) after five months of age due to an iris fused to its cornea making accurate measurements of the ACW and ACD impossible. At six (WT: n = 12; *hq*: n = 5) and eight months of age (WT: n = 12; *hq*: n = 7) significantly larger ACW in the WT cohort continued (6 months: $P < 0.01$; 8 months: $P < 0.001$). Untreated *hq* mice had a more shallow ACD compared to their untreated WT counterparts (WT: 0.304 ± 0.015 mm; *hq*: 0.213 ± 0.049 mm) at six months of age ($P < 0.05$; WT: n = 12, *hq*: n = 5; Figure 3.13 B).

A lower ACW was observed in the memantine-treated WT cohort at three ($P < 0.05$; untreated: 2.88 ± 0.017 mm [n = 16], treated: 2.84 ± 0.017 mm [n = 20]), four ($P < 0.01$; untreated: n = 20, treated: n = 16) and eight months of age ($P < 0.05$; untreated: 3.13 ± 0.030 mm [n = 12], treated: 3.04 ± 0.027 mm [n = 16]). Memantine-treated *hq* mice had an increased ACD at seven months of age ($P < 0.01$; untreated: n = 12, treated: n = 16).

Memantine-treated *hq* mice had a significantly lower average ACW ($P < 0.05$) and ACD ($P < 0.05$) at two months of age (untreated: n = 18; treated: n = 26) compared to the untreated *hq* cohort. A single memantine-treated *hq* mouse had a dramatically lower ACW at ten months of age and was considered to have microophthalmia (OS: Figure 3.13 D).

At two months of age, memantine-treated WT mice had a significantly larger ACW compared to memantine-treated *hq* mice ($P < 0.001$; WT: 2.74 ± 0.024 mm [n = 18], *hq*: 2.55 ± 0.042 mm n = 26). Differences in ACW were accompanied with a significantly deeper ACD in memantine-treated WT mice at two months of age ($P < 0.01$; WT: n = 18, *hq*: n = 26). At three months of age, significant differences in the ACW ($P < 0.001$) and ACD ($P < 0.01$) between cohorts (WT: n = 20; *hq*: n = 12) were observed. Differences were measured in the ACW between memantine-treated WT and *hq* cohorts at four ($P < 0.01$; WT: n = 16, *hq*: n = 12), five ($P < 0.05$; WT: n =16, *hq*: n = 14) and six months of age ($P < 0.001$; WT: n = 8, *hq*: n = 6). Memantine-treated *hq* mice continued to have a smaller ACW through eight ($P < 0.05$; WT: n = 16, *hq*: n = 12) and ten months of age ($P < 0.01$; WT: n = 10, *hq*: n = 10).

No differences were found in ACW or ACD between untreated WT mice with multiple tests and the WT single OCT cohort (WT single OCT; ACW: 3.04 ± 0.024 mm, ACD: 0.30 ± 0.007 mm [n = 12]). No differences were found in ACW and ACD between untreated *hq* mice with multiple tests and the *hq* single OCT cohort (*hq* single OCT; ACW: 3.05 ± 0.014 mm, ACD: 0.31 ± 0.014 mm [n = 6]). No differences were observed between the WT and *hq* single OCT cohorts.

3.20 Assessment of Retinal Thickness Between Mouse Cohorts

Anterior retinal thickness in untreated WT mice was relatively constant over the course of experimentation (Figure 3.14). Untreated *hq* mice had comparable anterior chamber thickness until eight months of age but a significant reduction was noted at ten months of age. Overall trends of anterior retinal thickness were supported by measures of central whole retinal thickness. The posterior retinal thickness remained consistent despite differences in genotype and treatment. A single data point was excluded from the untreated *hq* cohort (OD) at two months of age due to the observation of a significantly low measurement that was not reproduced in following months of imaging. Data were excluded from the untreated *hq* cohort after six months of age (OS) due to an iris fused to the cornea of the eye impeding light from reaching the retina. A single measurement from the five month data set (OS) and a single measurement from

Figure 3.14 - Retinal thickness assessed by ocular coherence tomography imaging. A. Anterior retinal thickness (mm) is a measure of the neural retinal thickness. A cohort of untreated WT mice tested with OCT a single time is presented at eleven months of age. A cohort of untreated ***hq*** mice tested with OCT a single time is presented at eleven months of age. Data are presented as Mean ± SEM. **B.** Posterior retinal thickness (mm) is a measure of the retinal pigment epithelium and choroid thickness. A cohort of untreated WT mice tested with OCT a single time is presented at eleven months of age. A cohort of untreated ***hq*** mice tested with OCT a single time is presented at eleven months of age. Data are presented as Mean ± SEM. **C.** Central whole retinal thickness (mm) was a cumulative measure of the anterior and posterior retinal thickness. A cohort of untreated WT mice tested with OCT a single time is presented at eleven months of age. A cohort of untreated ***hq*** mice tested with OCT a single time is presented at eleven months of age. Data are presented as Mean ± SEM.

A

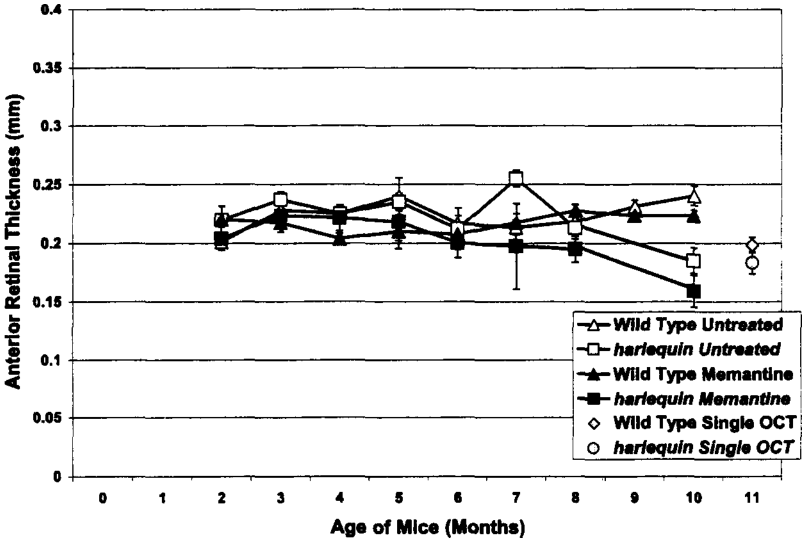
Anterior Retinal Thickness (mm)
0.4
0.35
0.3
0.25
0.2
0.15
0.1
0.05
0
0 1 2 3 4 5 6 7 8 9 10 11
Age of Mice (Months)
Wild Type Untreated
harlequin Untreated
Wild Type Memantine
harlequin Memantine
Wild Type Single OCT
harlequin Single OCT

B

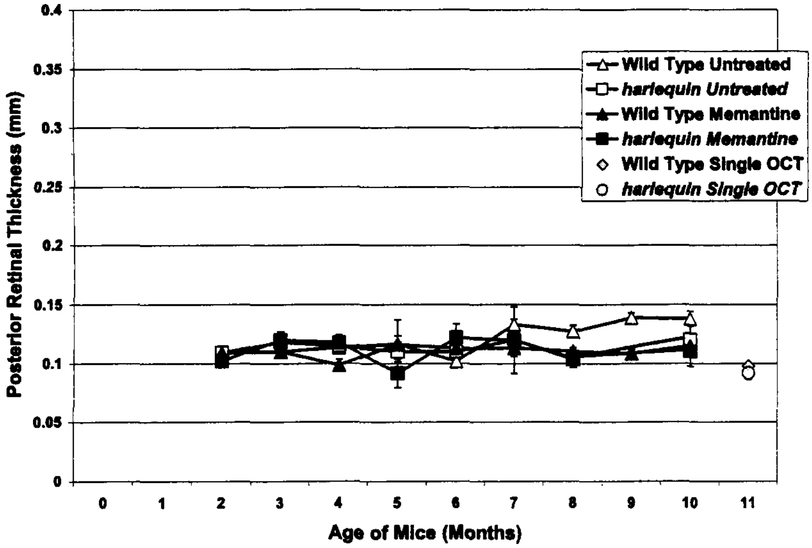
Posterior Retinal Thickness (mm)
0.4
0.35
0.3
0.25
0.2
0.15
0.1
0.05
0
0 1 2 3 4 5 6 7 8 9 10 11
Age of Mice (Months)
Wild Type Untreated
harlequin Untreated
Wild Type Memantine
harlequin Memantine
Wild Type Single OCT
harlequin Single OCT

C

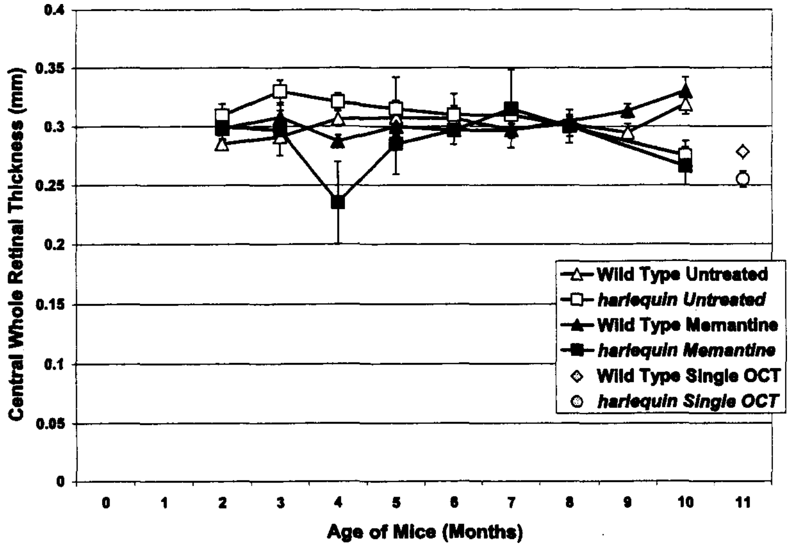
Central Whole Retinal Thickness (mm)
0.4
0.35
0.3
0.25
0.2
0.15
0.1
0.05
0
0 1 2 3 4 5 6 7 8 9 10 11
Age of Mice (Months)
Wild Type Untreated
harlequin Untreated
Wild Type Memantine
harlequin Memantine
Wild Type Single OCT
harlequin Single OCT

the eight month data set (OS) were also excluded from the untreated WT cohort due to a significantly low measurement that was not reproduced in the following months and poor image quality, respectively. A significantly thinner AR ($P < 0.001$; WT: 0.240 ± 0.008 mm, *hq*: 0.185 ± 0.011 mm) and CWR ($P < 0.01$; WT: 0.319 ± 0.010 mm, *hq*: 0.275 ± 0.013 mm) were measured for the untreated *hq* cohort at ten months of age (WT: n = 10; *hq*: n = 6).

A significantly greater CWR thickness was observed in the memantine-treated WT cohort compared to the untreated WT cohort at three months of age ($P < 0.05$; untreated: n = 16, treated: n = 20). The following month had a significantly reduced thickness (treated: n = 20, untreated: n = 16) in all layers of the memantine-treated WT retina (AR: $P < 0.01$; PR: $P < 0.05$; CWR: $P < 0.05$). Untreated WT mice had a significantly thicker PR at seven ($P < 0.001$; treated: 0.133 ± 0.005 mm [n = 12], untreated: 0.113 ± 0.003 mm [n = 30]), eight ($P < 0.01$; treated: n = 12, untreated: n = 16), nine ($P < 0.001$; treated: n = 10, untreated: n = 6) and ten months of age ($P < 0.01$; treated: n = 10, untreated: n = 10).

A single mouse (OD and OS) was removed from the three month data set of the memantine-treated *hq* cohort because light was not penetrating to the retina. An additional measurement was removed from the three month data set of the memantine-treated *hq* cohort (OS) due to poor image quality. No retinal thickness differences were measured between the untreated and memantine-treated *hq* cohorts at any month of age.

By eight months of age, memantine-treated *hq* mice had a significant reduction in AR thickness compared to memantine-treated WT mice ($P < 0.01$; WT: n = 16, *hq*: n = 12). Significance in AR thickness continued into ten months of age ($P < 0.001$; WT: 0.223 ± 0.005

mm [n = 10], *hq*: 0.159 ± 0.014 mm [n = 10]). The average CWR was also significant in the final month of imaging ($P < 0.01$; WT: 0.330 ± 0.012 mm [n = 10], *hq*: 0.266 ± 0.016 [n = 10]).

Significant reductions were observed in all retinal layers of the WT single OCT cohort (WT single OCT; AR: 0.20 ± 0.006 mm, PR: 0.10 ± 0.002 mm, CWR: 0.28 ± 0.006 mm [n = 12]) compared to the untreated WT cohort (AR: $P < 0.001$, PR: $P < 0.001$ and CWR: $P < 0.001$). No differences in retinal thickness were observed between the untreated *hq* cohort with multiple testing and the *hq* single OCT test cohort. A significant reduction in CWR thickness was found in the *hq* single OCT cohort compared to the WT single OCT cohort ($P < 0.05$).

3.21 Quantitation of the Structural Integrity of the Cornea

Structural analysis of the cornea revealed no significant abnormalities in the untreated WT cohort at any month analyzed. A few untreated *hq* mice demonstrated minor corneal histopathology, whereas memantine-treated *hq* mice demonstrated more severe corneal histopathology. Analysis of eyes from untreated WT mice established normal corneal histology at two months of age, with an average corneal epithelium (CE) thickness of 37.1 ± 3.0 μm (Figure 3.15 A). A single mouse appeared to have the recruitment of neutrophils into the cornea at ten months of age and an additional mouse had a thin corneal epithelium compared to the cohort average (CE =13.8 μm). CE thickness was 27.1 ± 4.9 μm at ten months of age in the untreated WT cohort.

Untreated *hq* mice had an initial CE thickness of 21.0 ± 9.0 μm with a single mouse having a cornea containing many neutrophils and a severely reduced corneal epithelium (CE = 6.8 μm). The eight-month-old untreated *hq* cohort had a single mouse with minor

Figure 3.15 - Corneal histopathology assessed using the fixed right eye (OD) of mice postmortem. **A.** Hematoxylin and Eosin stained cornea of an untreated WT mouse at two months of age. Image was captured at 20X magnification using an Arcturus Veritas microdissection system (Molecular Devices, Sunnyvale, CA). Normal corneal epithelium (CE) and corneal stroma (CS) histology can be observed. **B.** Hematoxylin and Eosin stained cornea of a memantine-treated *hq* mouse at two months of age. Image was captured at 20X magnification using an Arcturus Veritas microdissection system (Molecular Devices, Sunnyvale, CA). A severe recruitment of neutrophils (N) can be observed in the corneal stroma. **C.** Trichrome staining of a sever corneal histopathology observed in a ten-month-old memantine-treated *hq* mouse. Corneal histopathology included: a thinning corneal epithelium (TCE), unorganized collagen, mineralization (M), neutrophil recruitment (N), and neovascularization (NV). Image was captured at 20X magnification using an Arcturus Veritas microdissection system (Molecular Devices, Sunnyvale, CA). Collagen is stained green, cytoplasm and muscle are stained red. **D.** Modified Gram staining of the mouse with severe corneal histopathology. No bacterial infection was detected in the corneal stroma or epithelium of the mouse. Image was captured at 40X magnification using an Arcturus Veritas microdissection system (Molecular Devices, Sunnyvale, CA). **E.** Measures of corneal epithelium thickness (μm) in experimental cohorts euthanized at two, four, six, eight and ten months of age. Untreated and memantine-treated *hq* cohorts at six months of age are composed of a single mouse and do not have a ± SEM. The six month untreated and memantine-treated *hq* cohorts were not included in statistical analysis.

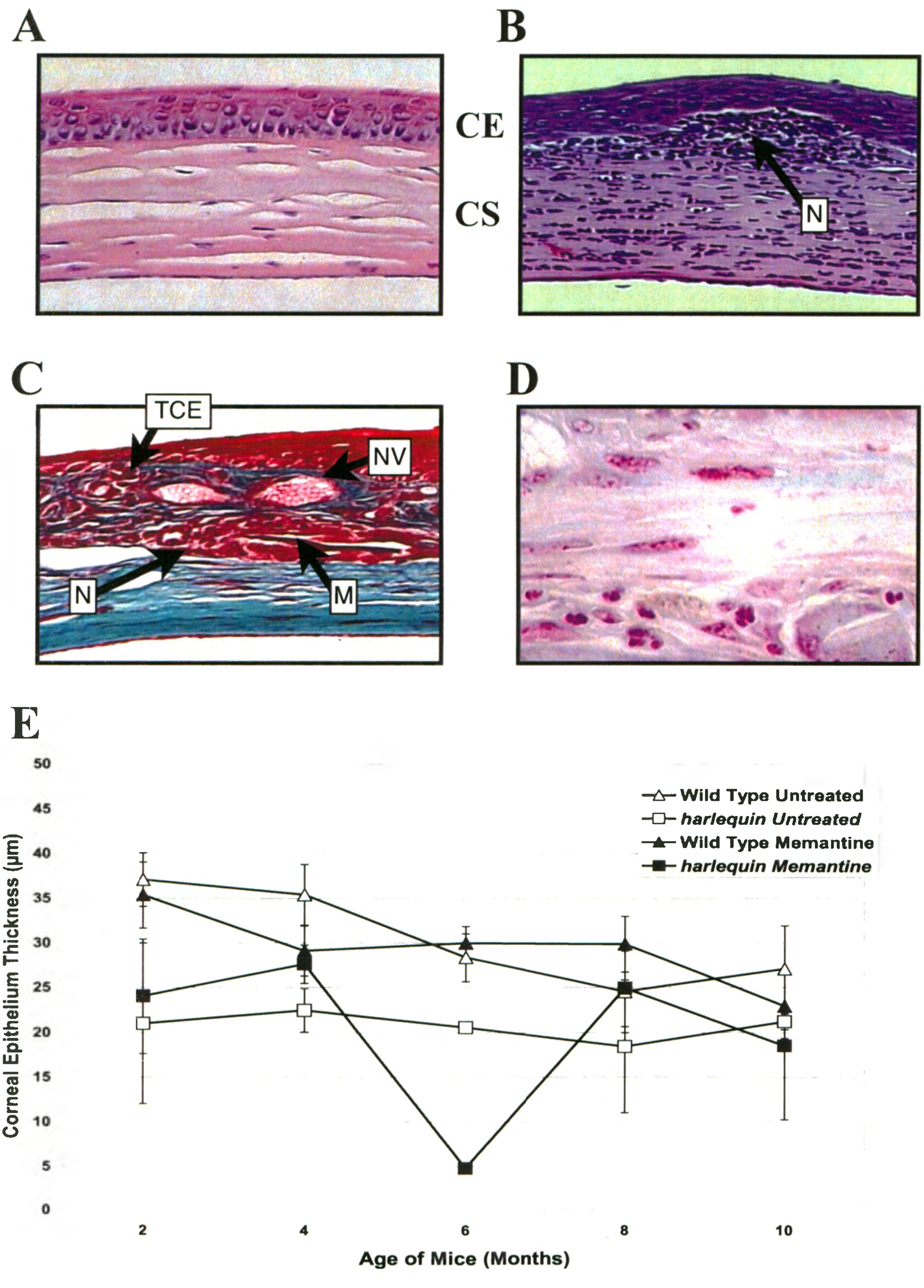
A
B
CE
CS
N
C
D
TCE
NV
N
M
E
Wild Type Untreated
harlequin Untreated
Wild Type Memantine
harlequin Memantine
Corneal Epithelium Thickness (µm)
Age of Mice (Months)
0
5
10
15
20
25
30
35
40
45
50
2
4
6
8
10

neovascularization in the corneal stroma. No corneal abnormalities were observed at ten months of age in the untreated *hq* cohort and a CE thickness of 21.2 ± 0.9 μm was measured.

Memantine-treated WT mice had healthy corneal histology at two months of age with an initial CE thickness of 35.4 ± 3.7 μm. Corneal histology remained healthy in the four, six and eight month memantine-treated WT cohorts. A single mouse had the recruitment of neutrophils in the ten month memantine-treated WT cohort. A final CE thickness of 23.0 ± 3.6 μm was measured.

The two-month-old memantine-treated *hq* cohort had two mice with severe neutrophil infiltration (Figure 3.15B). CE thickness was 24.1 ± 6.4 μm in the two-month-old memantine-treated *hq* cohort. The four-month-old memantine-treated *hq* cohort had a single mouse with neutrophils present in the cornea. The six-month-old cohort consisted of a single mouse with a very thin CE (4.8 μm). A single mouse in the eight month cohort demonstrated neovascularization in the stroma of the cornea. The OD of a mouse in the ten month memantine-treated *hq* cohort ruptured upon enucleation and was excluded from the results. A second mouse was observed to have a very thin CE (CE = 8.4 μm). A severe corneal histopathology was observed using H&E and trichrome staining in a ten-month-old memantine-treated *hq* mouse (Figure 3.15 C). This histopathology included severe thinning of the corneal epithelium (CE = 4.8 μm), unorganized collagen, mineralization, neutrophil infiltration, and severe neovascularization of the cornea. Modified gram staining was performed on a subset of mice to confirm neovascularization and identify whether a bacterial infection was the cause of neutrophil recruitment (Figure 3.15 D). Modified gram tests were negative for bacterial infection. CE thickness was 18.6 ± 8.3 μm in the ten-month-old memantine-treated *hq* cohort.

Untreated *hq* mice had a significantly reduced thickness of the corneal epithelium when compared to untreated WT mice at two ($P < 0.05$) and four months of age ($P < 0.05$; Figure 3.15 E). No significant differences were found in corneal epithelium thickness at eight or ten months of age. No significant differences in the thickness of the corneal epithelium were found between untreated and memantine-treated WT mice at any age analyzed. No significant differences were found in the thickness of the corneal epithelium between untreated and memantine-treated *hq* mice at any age. Finally, no statistically significant differences were found in the thickness of the corneal epithelium between memantine-treated WT and *hq* mice.

3.22 Quantitation of the Structural Integrity of the Ganglion Cell Layer

Untreated WT mice had relatively consistent ganglion cell counts from two to ten months of age with a slight reduction in central ganglion cell counts at late months of age. Untreated *hq* mice had similar cell counts with a minor reduction noted in the central retina at four months of age but similar counts in the central retina at eight and ten months of age. Memantine-treatment resulted in subtle improvements in ganglion cell counts in all retinal regions from two to ten months of age. Untreated *hq* mice No significant differences in ganglion cell counts of the dorsal peripheral retina (DR) were observed between untreated WT and *hq* mice at any age of analysis (Figure 3.16 A). Ganglion cell counts of the DR were also similar between the untreated and memantine-treated WT cohorts with no differences observed. The two-month-old *hq* cohort treated with memantine had a significantly higher ganglion cell count in the DR compared to the

Figure 3.16 - Ganglion cell counts of the retina assessed using the fixed right eye (OD) of mice postmortem. Ganglion cell counts (nuclei) were obtained from the retina of experimental cohorts euthanized at two, four, six, eight and ten months of age. Images of hematoxylin and eosin stained retinas were captured at 20X magnification using an Arcturus Veritas microdissection system (Molecular Devices, Sunnyvale, CA). **A.** Ganglion cell nuclei were counted in the dorsal peripheral retina of experimental cohorts. **B.** Ganglion cell nuclei were counted in the central retina of experimental cohorts. **C.** Ganglion cell nuclei were counted in the ventral peripheral retina of experimental cohorts

A

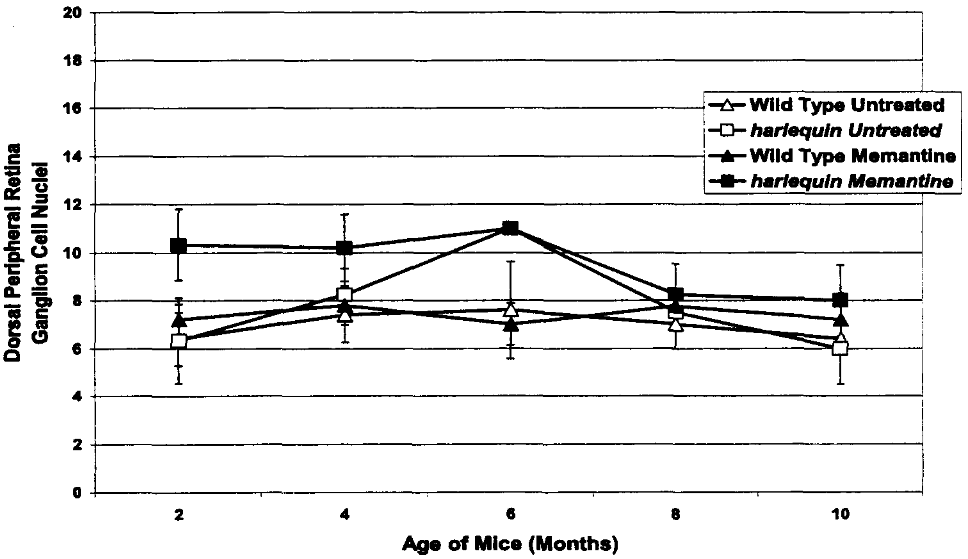
Dorsal Peripheral Retina Ganglion Cell Nuclei
Age of Mice (Months)
Wild Type Untreated
harlequin Untreated
Wild Type Memantine
harlequin Memantine

B

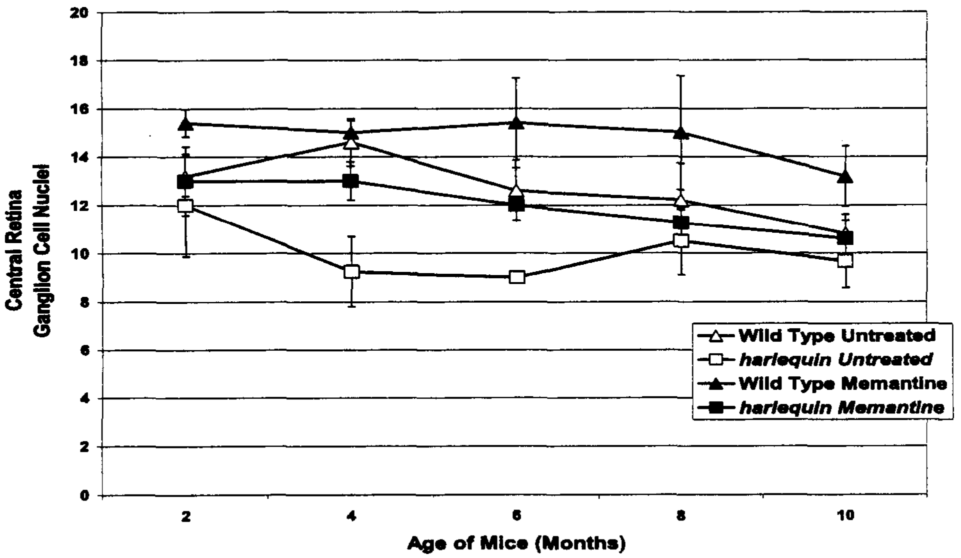
Central Retina Ganglion Cell Nuclei
Age of Mice (Months)
Wild Type Untreated
harlequin Untreated
Wild Type Memantine
harlequin Memantine

C

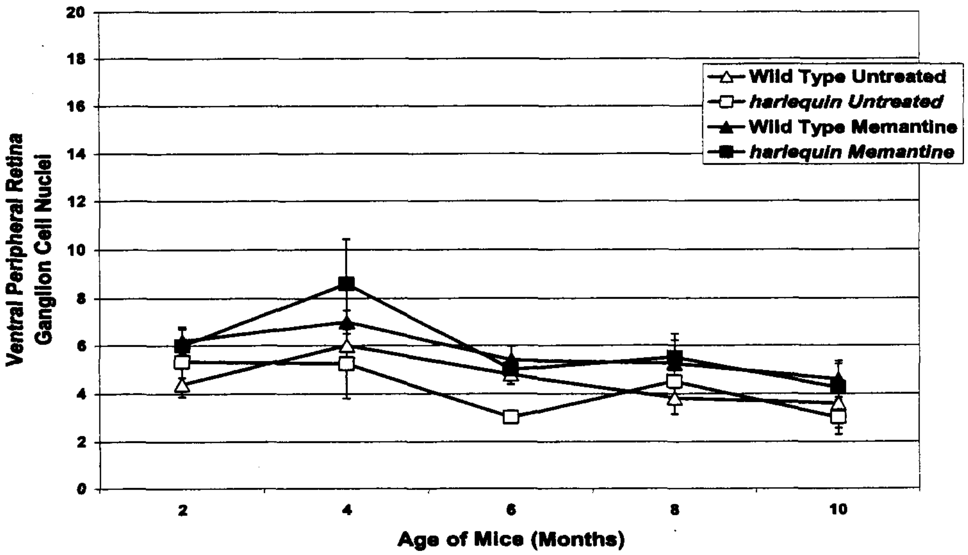
Ventral Peripheral Retina Ganglion Cell Nuclei
Age of Mice (Months)
Wild Type Untreated
harlequin Untreated
Wild Type Memantine
harlequin Memantine

memantine-treated WT cohort ($P < 0.05$: WT: 7.2 ± 0.7 nuclei, *hq*: 10.3 ± 1.5 nuclei). No differences in the ganglion cell counts of the DR were observed between memantine-treated cohorts at any other month of analysis.

WT mice treated with memantine had a higher number of ganglion cells in the central retina (CR) compared to untreated WT mice at two months of age ($P < 0.05$; untreated: 13.2 ± 0.8 nuclei, treated:15.4 ± 0.6 nuclei; Figure 3.16 B). Untreated *hq* mice had a reduction in CR ganglion cell numbers ($P < 0.01$; WT: 14.6 ± 1.0 nuclei, *hq*: 9.3 ± 1.4 nuclei) compared to the untreated WT cohort at four months of age. However, memantine-treated *hq* mice had higher levels of CR ganglion cells than their untreated littermates at four months of age ($P < 0.05$). No differences in ganglion cell counts of the CR were observed among cohorts at six, eight and ten months of age.

Memantine-treated WT mice had an elevated number of ganglion cells in the ventral retina (VR) compared to the untreated WT mice at two months of age ($P < 0.05$; untreated: 4.4 ± 0.3 nuclei, treated: 6.2 ± 0.6 nuclei; Figure 3.16 C). No other differences in VR ganglion cell counts were observed between untreated and memantine-treated WT cohorts. No differences were observed in ganglion cell counts between untreated and memantine-treated *hq* mice. Memantine-treated WT and *hq* mice also had similar VR retinal ganglion cell counts at all observed months of age.

3.23 Quantitation of the Structural Integrity of the Inner Plexiform Layer

The inner plexiform layer of untreated WT mice was thinner in the peripheral retina but was relatively unchanged from two to ten months of age. Untreated *hq* mice had a similar inner plexiform thickness in all retinal regions until ten months of age where degeneration was first noted. Memantine-treatment appeared to subtly conserve inner plexiform layer thickness of all retinal regions from two to ten months of age. No differences in inner plexiform layer thickness of the DR were measured among cohorts at two, four, six and eight months of age (Figure 3.17 A). At ten months of age, memantine-treated *hq* mice had a thicker inner plexiform layer in the DR compared to untreated *hq* mice ($P < 0.05$; untreated: 17.1 ± 0.6 μm, treated: 23.3 ± 1.5 μm). No other differences in inner plexiform layer thickness were found among cohorts at ten months of age.

The central retinal (CR) inner plexiform layer was 49.9 ± 2.5 μm thick in untreated WT mice at two months of age (Figure 3.17 B). At six months of age, the average inner plexiform layer thickness in the CR was 42.5 ± 3.1 μm. A final inner plexiform layer thickness of the CR in untreated WT mice was 43.9 ± 2.9 μm. Inner plexiform layer thickness in the CR was not different among cohorts at any age analyzed.

Inner plexiform layer thickness measurements were 24.4 ± 2.8 μm in the ventral retina (VR) of the two-month-old untreated WT cohort (Figure 3.17 C). An inner plexiform layer thickness of 25.1 ± 1.2 μm was observed at four months of age in the untreated WT cohort. A final inner plexiform layer thickness of 15.8 ± 2.7 μm was measured in the ten-month-old untreated WT cohort. Inner plexiform layer thickness in the VR was consistent among all cohorts and no significant differences were observed at any age analyzed.

Figure 3.17 - Inner plexiform layer thickness of the retina assessed using the fixed right eye (OD) of mice postmortem. Inner plexiform layer thicknesses (μm) were obtained from the retina of experimental cohorts euthanized at two, four, six, eight and ten months of age. Images of hematoxylin and eosin stained retinas were captured at 20X magnification using an Arcturus Veritas microdissection system (Molecular Devices, Sunnyvale, CA). **A.** Inner plexiform layer thickness was measured in the dorsal peripheral retina of experimental cohorts. **B.** Inner plexiform layer thickness of the central retina was measured in experimental cohorts. **C.** Inner plexiform layer thickness of the ventral peripheral retina was measured in all experimental cohorts.

A

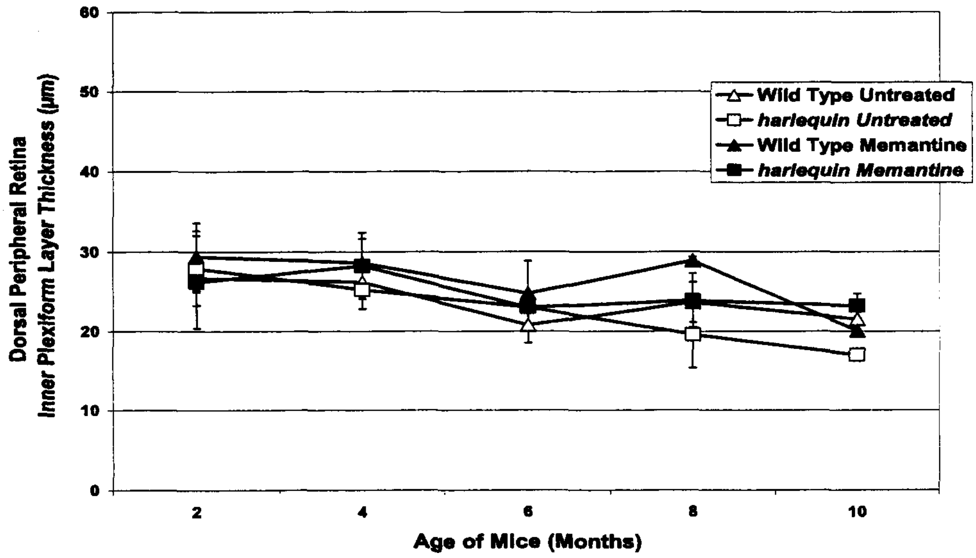
60
50
40
30
20
10
0
Dorsal Peripheral Retina
Inner Plexiform Layer Thickness (µm)
Wild Type Untreated
harlequin Untreated
Wild Type Memantine
harlequin Memantine
2
4
6
8
10
Age of Mice (Months)

B

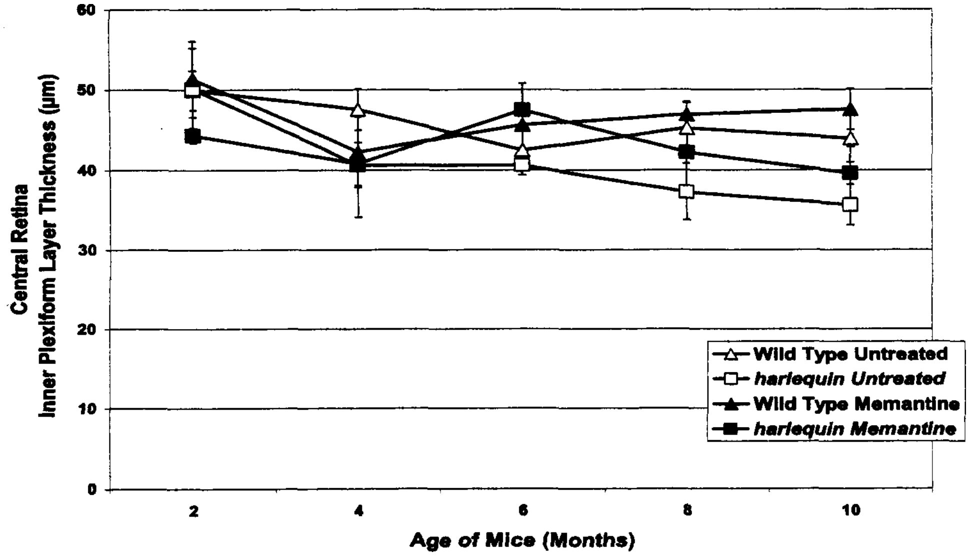
60
50
40
30
20
10
0
Central Retina
Inner Plexiform Layer Thickness (µm)
Wild Type Untreated
harlequin Untreated
Wild Type Memantine
harlequin Memantine
2
4
6
8
10
Age of Mice (Months)

C

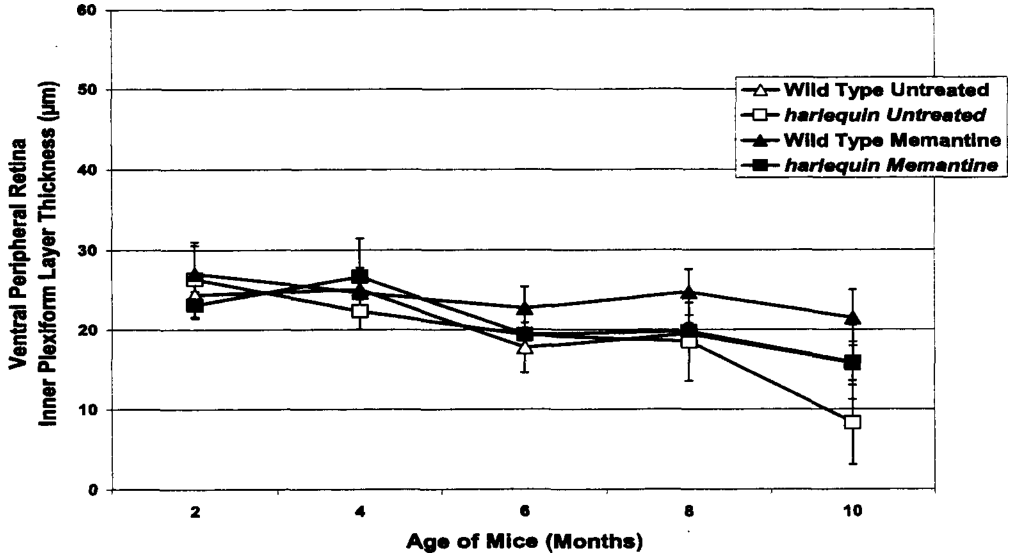
60
50
40
30
20
10
0
Ventral Peripheral Retina
Inner Plexiform Layer Thickness (µm)
Wild Type Untreated
harlequin Untreated
Wild Type Memantine
harlequin Memantine
2
4
6
8
10
Age of Mice (Months)

3.24 Quantitation of the Structural Integrity of the Inner Nuclear Layer

Untreated WT mice had peripheral inner nuclear layer cell counts that slightly declined as the mice aged. Untreated *hq* mice had similar cell counts in the peripheral retina but reduced cell counts in the central retina by ten months of age. Memantine-treatment appeared to subtly conserve inner nuclear layer cell counts in all retinal regions from two to ten months of age. Untreated WT mice at two months of age had an average inner nuclear layer thickness of 3.6 ± 0.3 cell nuclei in the dorsal retina (DR; Figure 3.18 A). At four months of age, untreated WT mice had an inner nuclear layer thickness of 4.0 ± 0.6 cell nuclei. Inner nuclear layer thickness reached 3.0 ± 0.4 nuclei in the untreated WT cohort at ten months of age. No differences in inner nuclear layer cell counts of the DR were observed among cohorts at any age analyzed.

Inner nuclear cell counts were similar among cohorts of mice from two to eight months of age (Figure 3.18 B). Ten-month-old untreated *hq* mice had a significant reduction in inner nuclear cell counts of the CR when compared to age-matched, untreated WT mice ($P < 0.05$; WT: 5.6 ± 0.3 nuclei, *hq*: 4.3 ± 0.4 nuclei; Figure 3.18 B). Memantine-treated *hq* mice have a reduction in the cell nuclei counts of the inner nuclear layer when compared to memantine-treated WT mice at ten months of age ($P < 0.05$; WT: 6.0 ± 0.3 nuclei, *hq*: 4.8 ± 0.4 nuclei).

Comparison of the four month cohorts revealed a significantly thicker inner nuclear layer in the memantine-treated *hq* cohort when compared to the untreated *hq* cohort ($P < 0.01$; untreated: 2.5 ± 0.3 nuclei, treated: 4.2 ± 0.2 nuclei; Figure 3.18 C). A second difference between cohorts was noted when memantine-treated *hq* mice had an increased inner nuclear layer thickness compared to memantine-treated WT mice at four months of age ($P < 0.05$; WT: 3.4 ± 0.3 nuclei, *hq*: 4.2 ± 0.2 nuclei). Memantine-treated WT mice demonstrated a thicker inner

Figure 3.18 - Inner nuclear layer cell counts of the retina assessed using the fixed right eye (OD) of mice postmortem. Inner nuclear layer cell counts (nuclei) were obtained from the retina of experimental cohorts euthanized at two, four, six, eight and ten months of age. Images of hematoxylin and eosin stained retinas were captured at 20X magnification using an Arcturus Veritas microdissection system (Molecular Devices, Sunnyvale, CA). **A.** Inner nuclear layer cell counts of the dorsal peripheral retina were obtained from experimental cohorts. **B.** Inner nuclear layer cell counts were obtained in the central retina of the experimental cohorts. **C.** Inner nuclear layer cell counts were measured in the ventral peripheral retina of experimental cohorts.

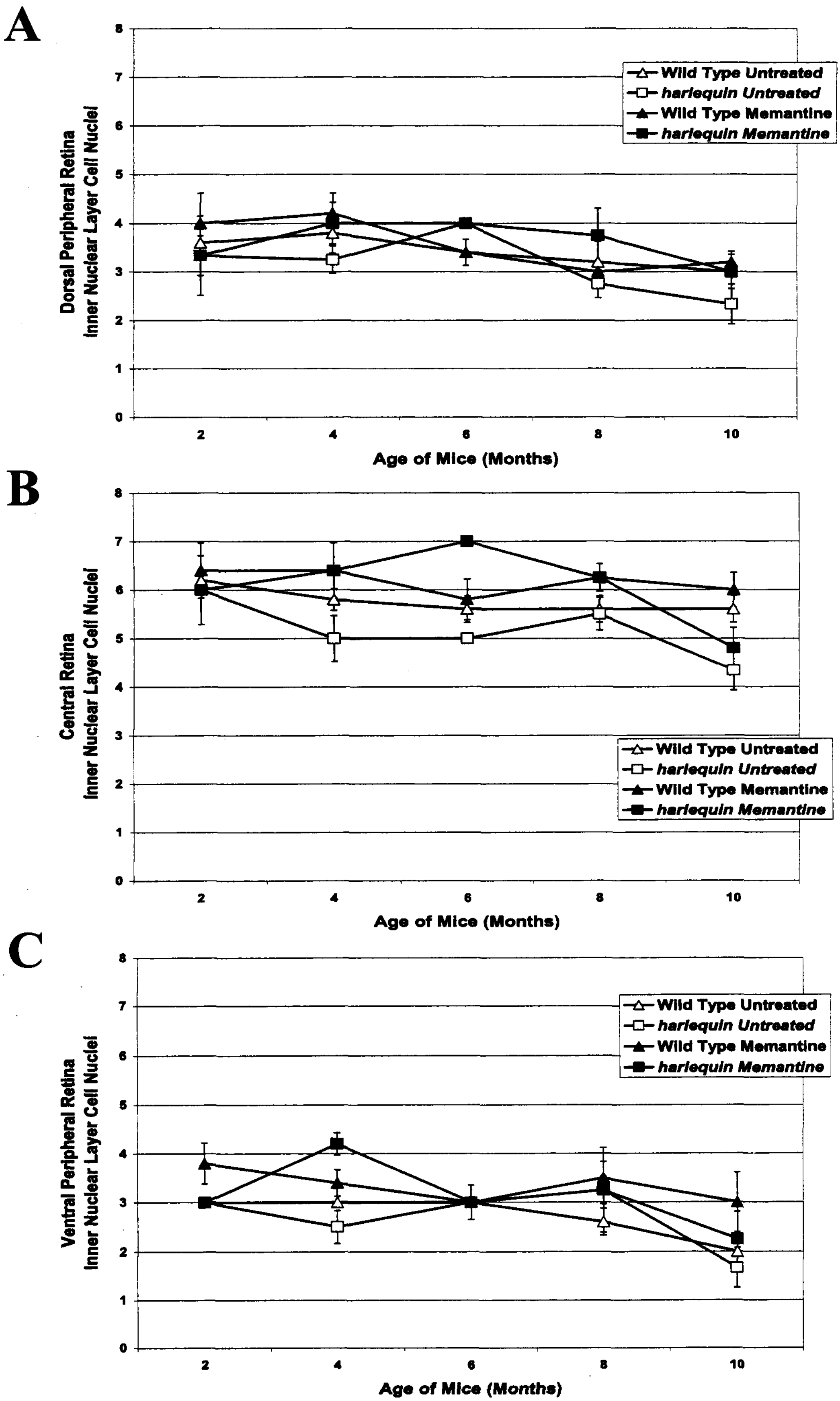
A
Wild Type Untreated
harlequin Untreated
Wild Type Memantine
harlequin Memantine
Dorsal Peripheral Retina
Inner Nuclear Layer Cell Nuclei
Age of Mice (Months)
B
Central Retina
Inner Nuclear Layer Cell Nuclei
Age of Mice (Months)
C
Ventral Peripheral Retina
Inner Nuclear Layer Cell Nuclei
Age of Mice (Months)

nuclear layer in the VR than untreated WT mice at eight months of age ($P < 0.05$; untreated: 2.6 ± 0.3 nuclei, treated: 3.5 ± 0.3 nuclei). No other differences in inner nuclear layer thickness of the VR were observed when comparing cohorts.

3.25 Quantitation of the Structural Integrity of the Outer Plexiform Layer

Outer plexiform layer thickness reduced in the dorsal peripheral retina of untreated WT mice as the mice age but central and ventral layer thickness remained relatively constant. Untreated *hq* mice had similar peripheral outer plexiform layer thickness until ten months of age but a significantly thinned outer plexiform layer in the central retina at eight and ten months of age. Memantine treatment did not appear to conserve outer plexiform layer thickness. Two-month-old untreated WT mice had an outer nuclear layer that was 11.1 ± 0.8 μm thick in the dorsal retina (DR) on average (Figure 3.19 A). The average outer nuclear layer thickness of untreated WT mice at four months of age was 10.62 ± 1.3 μm and reached 8.1 ± 1.2 μm in the six-month-old cohort. At ten months of age, a final DR outer plexiform layer thickness of 7.1 ± 0.6 μm was measured in the untreated WT cohort. No differences in the outer plexiform layer thickness of the dorsal retina were found among cohorts of mice at two, four, six and eight months of age. A single difference was measured between untreated WT and *hq* mice at ten months of age ($P < 0.01$; *hq*: 3.8 ± 0.8 μm).

At two months of age, memantine-treated *hq* mice were found to have a reduced outer plexiform layer in the CR when compared to age-matched, memantine-treated WT mice ($P < 0.05$; WT: 18.7 ± 1.1, μm *hq*: 15.1 ± 1.0 μm; Figure 3.19 B). A significantly reduced outer plexiform layer was first noted between untreated WT and *hq* cohorts at eight months of age (P <

Figure 3.19 - Outer plexiform layer thickness of the retina assessed using the fixed right eye (OD) of mice postmortem. Outer plexiform layer thicknesses (μm) were obtained from the retina of experimental cohorts euthanized at two, four, six, eight and ten months of age. Images of hematoxylin and eosin stained retinas were captured at 20X magnification using an Arcturus Veritas microdissection system (Molecular Devices, Sunnyvale, CA). **A.** Outer plexiform layer thickness was measured in the dorsal peripheral retina of experimental cohorts. **B.** Outer plexiform layer thickness was measured in the experimental cohorts. **C.** Outer plexiform layer thickness of the ventral peripheral retina was measured in the experimental cohorts.

A

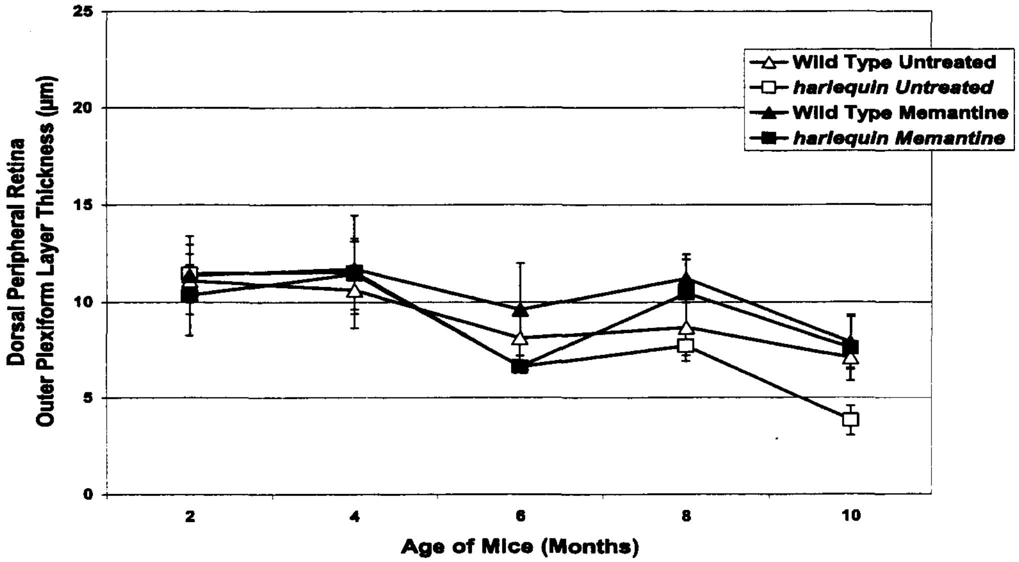
Dorsal Peripheral Retina
Outer Plexiform Layer Thickness (µm)
Age of Mice (Months)
Wild Type Untreated
harlequin Untreated
Wild Type Memantine
harlequin Memantine

B

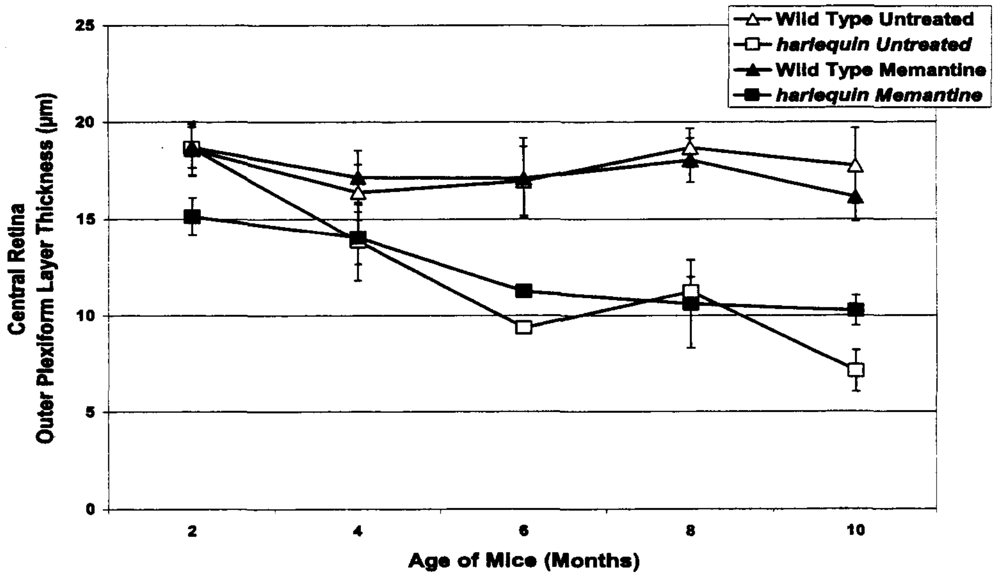
Central Retina
Outer Plexiform Layer Thickness (µm)
Age of Mice (Months)
Wild Type Untreated
harlequin Untreated
Wild Type Memantine
harlequin Memantine

C

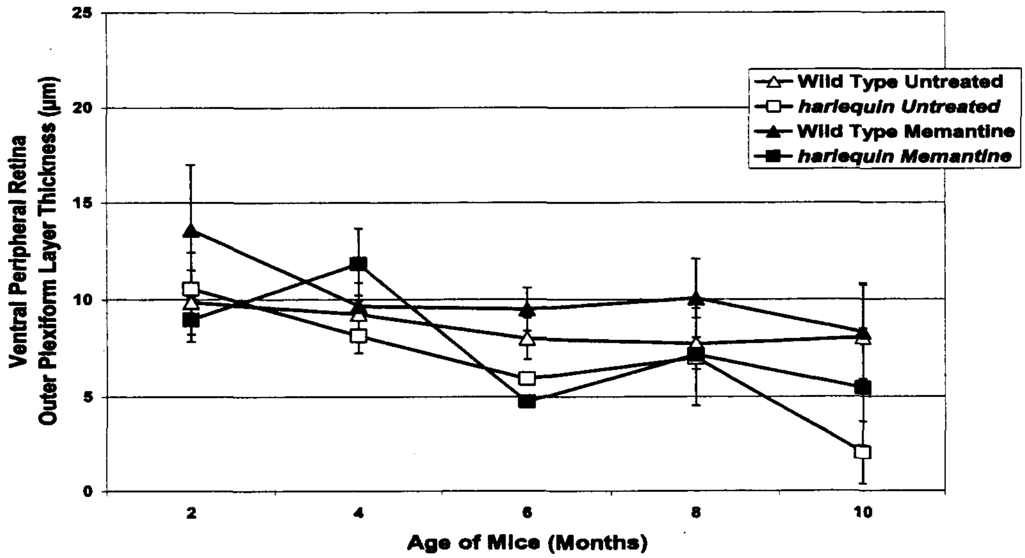
Ventral Peripheral Retina
Outer Plexiform Layer Thickness (µm)
Age of Mice (Months)
Wild Type Untreated
harlequin Untreated
Wild Type Memantine
harlequin Memantine

0.001; WT: 18.7 ± 1.0 μm, *hq*: 11.2 ± 0.8 μm) and continued between the ten-month cohorts (P < 0.01; WT: 17.7 ± 1.9 μm, *hq*: 7.1 ± 1.1 μm). Memantine-treated *hq* mice had a significantly thicker outer plexiform layer thickness at ten months of age when compared to age-matched, untreated hq mice (P < 0.03).

At two months of age, untreated WT mice had an average VR outer plexiform layer thickness of 9.9 ± 1.6 μm (Figure 3.19 C). This was followed by an outer plexiform layer thickness of 9.2 ± 1.0 μm at four and 8.0 ± 1.1 μm at six months of age in the VR. Average thickness of the outer plexiform layer fluctuated in the final two months of analysis, reaching 8.0 ± 2.7 μm at ten months of age in the untreated WT cohort. No significant differences were found in outer plexiform layer thickness in the VR among cohorts at any age of analysis.

3.26 Quantitation of the Structural Integrity of the Outer Nuclear Layer

Untreated WT mice had consistent outer nuclear layer cell counts until six months of age followed by a slight reduction in all retinal regions at eight and ten months of age. Untreated *hq* mice have similar peripheral outer nuclear layer cell counts compared to untreated WT mice but central outer nuclear layer cell counts begin to significantly decline by four months of age. Memantine treatment does not appear to have any significant effects on outer nuclear layer cell counts in any retinal region from two to ten months of age. The dorsal peripheral retina (DR) had an average outer nuclear layer (photoreceptor cell layer) thickness of 7.2 ± 0.4 nuclei in untreated WT mice at two months of age (Figure 3.20 A). By six months of age, the DR outer nuclear layer was 5.0 ± 0.8 nuclei thick and was supported by measurements taken in the ten month cohort (5.2 ± 0.4 nuclei). By four months of age, memantine-treated WT mice had a

Figure 3.20 - Photoreceptor cell counts of the retina assessed using the fixed right eye (OD) of mice postmortem. Photoreceptor cell counts (nuclei) were obtained from the retina of experimental cohorts euthanized at two, four, six, eight and ten months of age. Images of hematoxylin and eosin stained retinas were captured at 20X magnification using an Arcturus Veritas microdissection system (Molecular Devices, Sunnyvale, CA). **A.** Photoreceptor cell counts were measured in the dorsal peripheral retina of the experimental cohorts. **B.** Photoreceptor cell counts were measured in the central retina of the experimental cohorts. **C.** Photoreceptor cell counts were measured in the ventral peripheral retina of experimental cohorts.

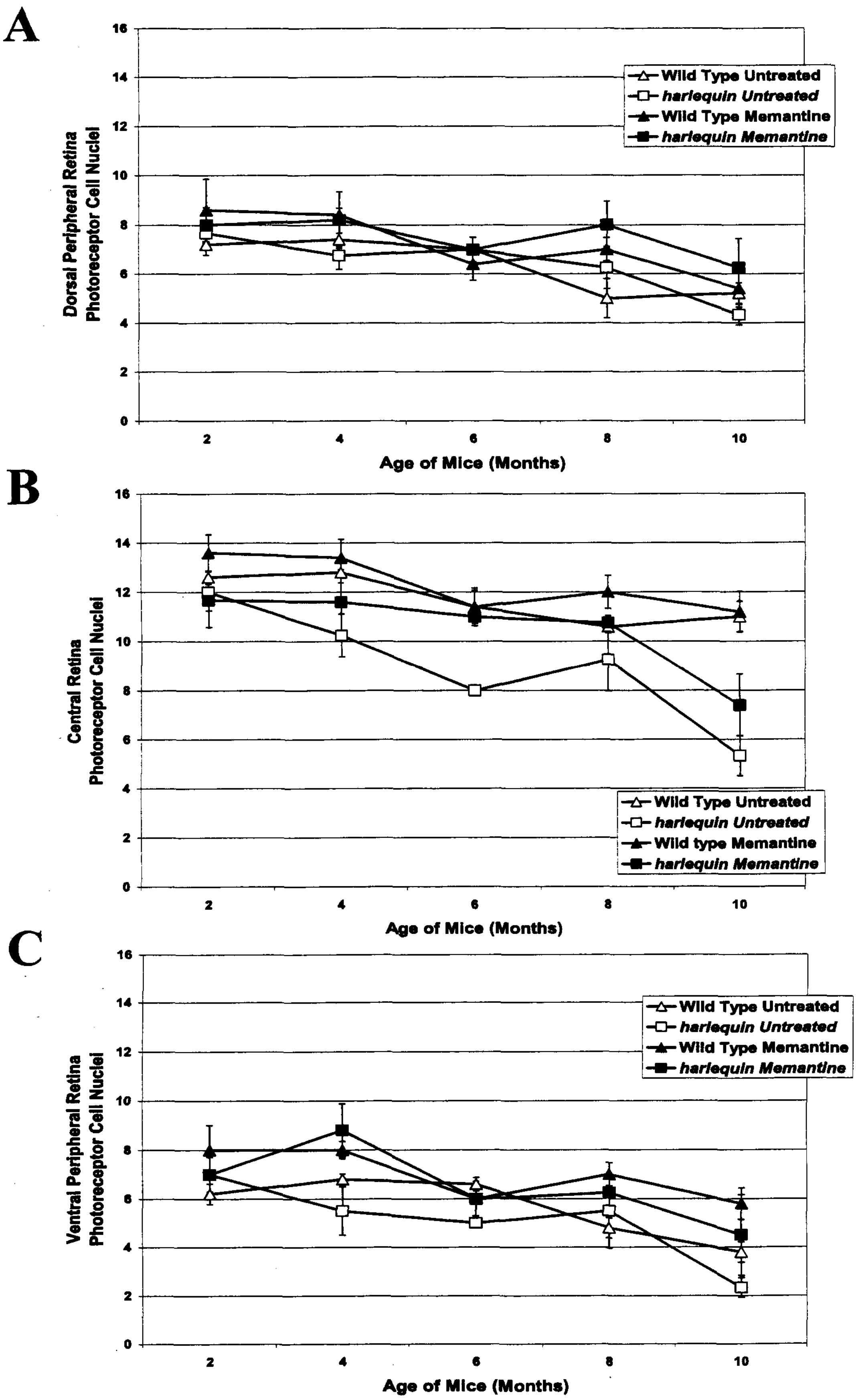
A
Dorsal Peripheral Retina Photoreceptor Cell Nuclei
Age of Mice (Months)
Wild Type Untreated
harlequin Untreated
Wild Type Memantine
harlequin Memantine
B
Central Retina Photoreceptor Cell Nuclei
Age of Mice (Months)
Wild Type Untreated
harlequin Untreated
Wild type Memantine
harlequin Memantine
C
Ventral Peripheral Retina Photoreceptor Cell Nuclei
Age of Mice (Months)
Wild Type Untreated
harlequin Untreated
Wild Type Memantine
harlequin Memantine

higher number of photoreceptor nuclei in the DR when compared to age-matched, untreated WT mice ($P < 0.05$; untreated: 7.4 ± 0.3 nuclei, treated: 8.4 ± 0.3 nuclei). No significant differences in outer nuclear layer thickness of the DR were observed among cohorts of mice for the final months of analysis.

At four months of age, untreated *hq* mice had a reduction in outer nuclear layer cell counts of the CR when compared to untreated WT mice ($P < 0.05$; WT: 12.8 ± 0.4 nuclei, *hq*: 10.3 ± 0.9 nuclei; Figure 3.20 B). A dramatic reduction in the cell counts of untreated and memantine-treated *hq* cohorts occurred in the ten month cohorts (untreated: 5.3 ± 0.8 nuclei; treated: 7.4 ± 1.3 nuclei). Untreated *hq* mice had significantly lower outer nuclear layer counts than untreated WT mice ($P < 0.001$; WT: 11.0 ± 0.6 nuclei).

By four months of age, memantine-treated WT mice had a significantly higher photoreceptor count in the VR when compared to untreated littermates ($P < 0.05$; untreated: 6.8 ± 0.2 nuclei, treated: 8.0 ± 0.4 nuclei; Figure 3.20 C). Significant increases in the outer nuclear layer thickness of memantine-treated *hq* mice compared to untreated *hq* mice were also noted at four months of age ($P < 0.05$; untreated: 5.5 ± 1.0 nuclei, treated: 8.8 ± 1.1 nuclei). The differences in outer nuclear layer thickness in untreated and memantine-treated WT mice continued at eight ($P < 0.01$; untreated: 4.8 ± 0.5, treated: 7 ± 0.5 nuclei) and ten months of age ($P < 0.05$; untreated: 3.8 ± 0.4 nuclei, treated: 5.8 ± 0.7 nuclei). A final difference was noted at ten months of age, untreated *hq* mice had a reduced cell count in the outer nuclear layer of the VR when compared to untreated WT mice ($P < 0.05$; *hq*: 2.3 ± 0.4 nuclei).

3.27 Quantitation of the Structural Integrity of the Photoreceptor Segments

Photoreceptor segment layer thickness appeared to decline as untreated WT mice aged with the most notable thinning in the peripheral retina. Untreated *hq* mice appeared to have similar segment thickness in all retinal regions from two to ten months of age. Memantine treatment did not appear to conserve photoreceptor segment thickness in any retinal region tested from two to ten months of age. No differences in photoreceptor thickness of the DR were observed among cohorts until eight months of age (Figure 3.21 A). Memantine-treated WT mice had a significant increase in thickness of the photoreceptor segments compared to age-matched, untreated WT mice ($P < 0.01$; untreated: 13.1 ± 2.2 μm treated: 22.2 ± 1.4 μm). No significant differences in photoreceptor thickness of the DR were measured among cohorts at ten months of age.

Untreated WT mice had photoreceptor segments with a length of 33.0 ± 2.7 μm in the central retina (CR) at two months of age (Figure 3.21 B). Photoreceptor segment thickness in the four-month-old untreated WT cohort was 34.1 ± 2.4 μm in the CR. By ten months of age, untreated WT mice had a photoreceptor segment thickness of 23.7 ± 2.4 μm in the CR. At ten months of age, untreated WT mice had an increased thickness of the photoreceptor segments compared to age-matched, untreated *hq* mice ($P < 0.01$; *hq*: 15.9 ± 2.4 μm). No other differences in photoreceptor thickness were measured among cohorts in the CR.

A significantly thicker photoreceptor segment thickness was seen in the memantine-treated WT cohort when compared to memantine-treated *hq* mice at two months of age ($P < 0.05$; WT: 22.9 ± 2.1 μm, *hq*: 14.8 ± 2.9 μm; Figure 3.21 C). At eight months of age, memantine-

Figure 3.21 - Photoreceptor segment thickness of the retina assessed using the fixed right eye (OD) of mice postmortem. Photoreceptor segment thicknesses (μm) were obtained from the retina of experimental cohorts euthanized at two, four, six, eight and ten months of age. Images of hematoxylin and eosin stained retinas were captured at 20X magnification using an Arcturus Veritas microdissection system (Molecular Devices, Sunnyvale, CA). **A.** Photoreceptor segment thickness was measured in the dorsal peripheral retina of experimental cohorts. **B.** Photoreceptor segment thickness was measured in the central retina of experimental cohorts. **C.** Photoreceptor segment thickness was measured in the ventral peripheral retina of the experimental cohorts.

treated WT mice preserved photoreceptor thickness compared to untreated WT mice ($P < 0.001$; untreated: 8.34 ± 2.6 μm, treated: 19.8 ± 1.9 μm). No differences among cohorts were measured in photoreceptor thickness of the VR at ten months of age.

3.28 Quantitation of the Structural Integrity of the Retina

Untreated WT mice had a consistent whole retinal thickness until six months of age followed by slight thinning at eight and ten months of age predominantly in the ventral peripheral retina. Untreated *hq* mice had a similar retinal thickness in all retinal regions until ten months of age, with the most significant thinning in the central retina. Memantine treatment appeared to subtly conserve retinal thickness noticeable by ten months of age in all retinal regions. Untreated WT mice had a maximum dorsal retinal (DR) thickness of 138.4 ± 5.7 μm at two months of age (Figure 3.22 A). Analysis of the four month cohort revealed an average retinal thickness of 133.2 ± 5.6 μm in the DR. By ten months of age, untreated WT mice had a minimum average DR retinal thickness of 92.8 ± 6.6 μm. All cohorts had similar DR thicknesses with only a single month of significant thinning in the untreated *hq* cohort compared to untreated WT mice at ten months ($P < 0.05$; *hq*: 72.9 ± 2.0 μm).

No significant differences were observed in CR thickness between two and eight months of age (Figure 3.22 B). By ten months of age, *hq* CR thinning became significant in both the untreated and memantine-treated *hq* cohorts (untreated: 128.6 ± 9.7 μm, treated: 163.3 ± 14.7 μm) compared to untreated and memantine-treated WT cohorts (treated: 201.7 ± 8.5 μm) respectively ($P < 0$ .05; $P < 0.05$; Figure 3.23).

Figure 3.22 - Whole retinal thickness of the retina assessed using the fixed right eye (OD) of mice postmortem. Whole retinal thicknesses (μm) were obtained from the retina of experimental cohorts euthanized at two, four, six, eight and ten months of age. Images of hematoxylin and eosin stained retinas were captured at 20X magnification using an Arcturus Veritas microdissection system (Molecular Devices, Sunnyvale, CA). **A.** Whole dorsal peripheral retinal thickness was measured in the experimental cohorts. **B.** Whole central retinal thickness was measured in the experimental cohorts. **C.** Whole ventral peripheral retinal retinal thickness was measured in the experimental cohots.

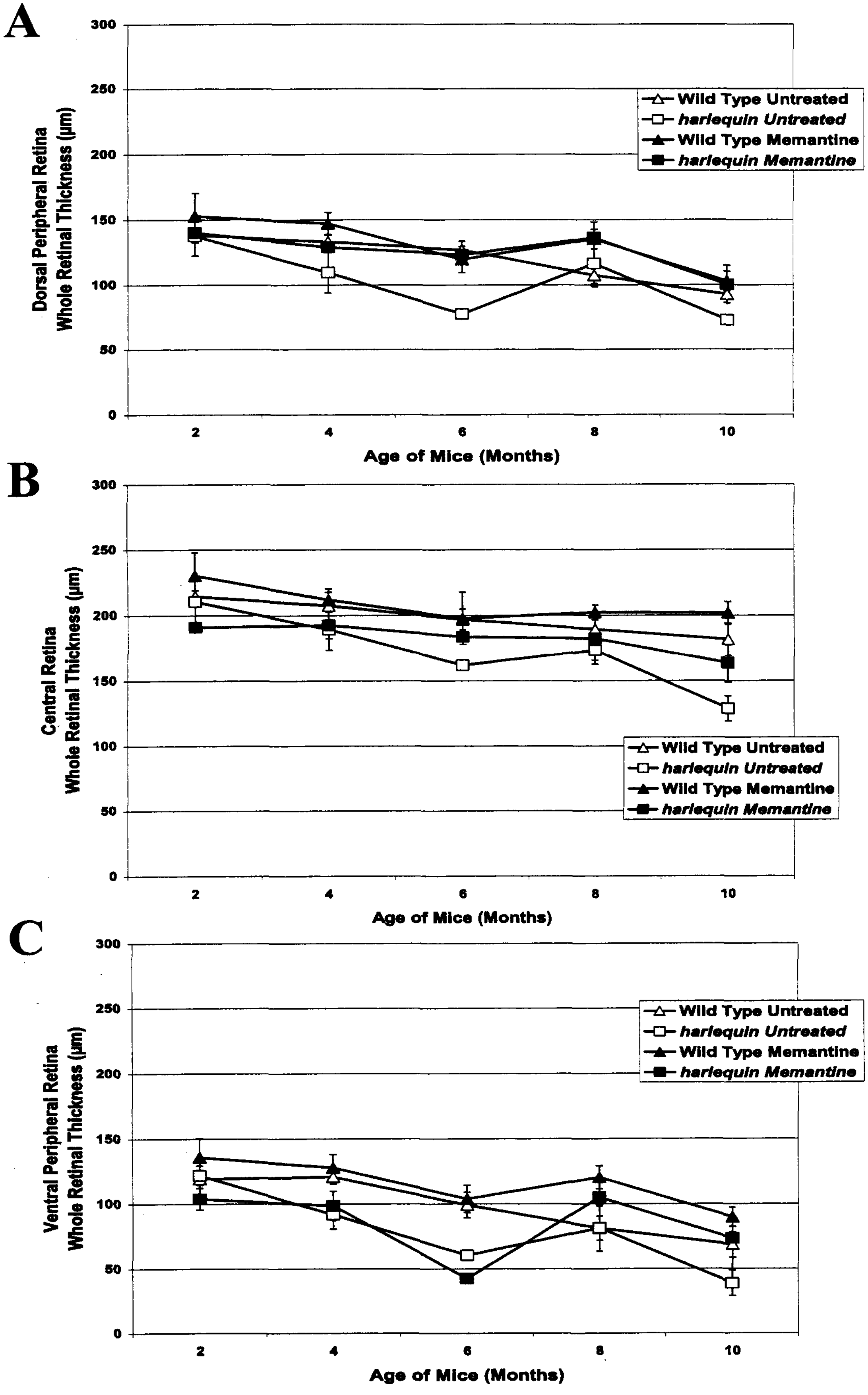
A
Dorsal Peripheral Retina
Whole Retinal Thickness (µm)
300
250
200
150
100
50
0
2
4
6
8
10
Age of Mice (Months)
Wild Type Untreated
harlequin Untreated
Wild Type Memantine
harlequin Memantine
B
Central Retina
Whole Retinal Thickness (µm)
Age of Mice (Months)
Wild Type Untreated
harlequin Untreated
Wild Type Memantine
harlequin Memantine
C
Ventral Peripheral Retina
Whole Retinal Thickness (µm)
Age of Mice (Months)
Wild Type Untreated
harlequin Untreated
Wild Type Memantine
harlequin Memantine

Figure 3.23 - Structural integrity of the central retina of experimental cohorts at ten months of age. Representative images of cohort retina's obtained at ten months of age. Images of hematoxylin and eosin stained retinas were captured at 20X magnification using an Arcturus Veritas microdissection system (Molecular Devices, Sunnyvale, CA). GCL: ganglion cell layer; IPL: inner plexiform layer; INL: inner nuclear layer; OPL: outer plexiform layer; ONL: outer nuclear layer; OS: outer segments of photoreceptors. **A.** Untreated WT cohort. **B.** Untreated *hq* cohort. **C.** Memantine-treated WT cohort. **D.** Memantine-treated *hq* cohort.

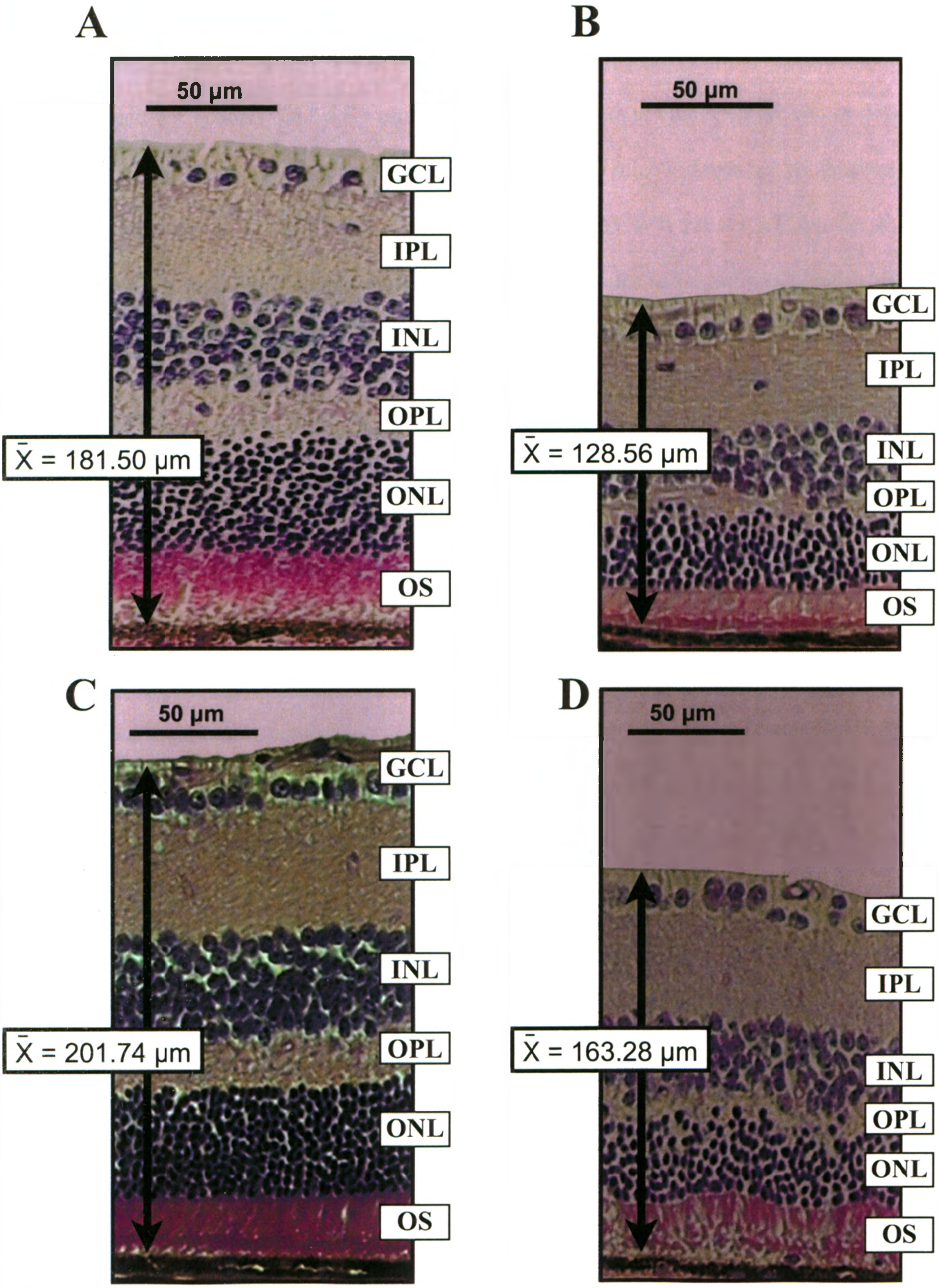
A
50 µm
GCL
IPL
INL
OPL
X̄ = 181.50 µm
ONL
OS
B
50 µm
GCL
IPL
X̄ = 128.56 µm
INL
OPL
ONL
OS
C
50 µm
GCL
IPL
INL
X̄ = 201.74 µm
OPL
ONL
OS
D
50 µm
GCL
IPL
X̄ = 163.28 µm
INL
OPL
ONL
OS

The ventral retina (VR) of untreated WT mice had a thickness of 119.3 ± 14.1 μm at two months of age (Figure 3.22 C). At four months of age, a similar VR thickness was measured in the untreated WT cohort (120.8 ± 5.3 μm). A final VR thickness of 68.6 ± 9.8 μm was measured in the untreated WT cohort at ten months of age. Untreated *hq* mice had reduced VR thickness compared to untreated WT mice at four months of age ($P < 0.05$; WT: 120.8 ± 5.3 μm, *hq*: 91.6 ± 10.9 μm). By eight months of age, memantine-treated WT mice had significantly higher VR thickness compared to untreated WT mice ($P < 0.05$; untreated: 81.2 ± 9.3 μm, treated: 120.4 ± 8.7 μm).

3.29 Comparison of Reactive Oxygen Species Profiles in the Mouse Eye

Whole eye reactive oxygen species (ROS) profiles at two, four, six, eight and ten months of age were compared to identify differences in ROS patterns among cohorts at specific ages (Figure 3.24 A, 3.24 B). Levels of ROS in the corneal epithelium varied but were similar to those found in the inner nuclear layer's of the retina at each age. The lowest levels of ROS were found in the ganglion cell layer of the retinal regions. Levels of reactive oxygen species increased in the inner nuclear layer and had a maximum intensity in the outer nuclear layers of the retinal regions. Typically, the layers of the ventral retina (VR) had the highest levels of ROS in the eye. ROS in the layers of the dorsal (DR) and central retina (CR) were similar with the exception of the four month cohorts. No differences in ROS profiles were observed among cohorts at two, four, six, eight and ten months of age. Positive ($n = 4$) and negative controls ($n =$

Figure 3.24 - Quantification of reactive oxygen species in the mouse eye of experimental cohorts. A. Whole eye reactive oxygen species (ROS) profiles were obtained for each experimental cohort at two, four, six, eight and ten months of age. Profiles were created by measuring levels of ROS in the corneal epithelium (red dot: 1), dorsal retinal ganglion cell layer (red dot: 2), dorsal retinal inner nuclear layer (red dot: 3), dorsal retinal outer nuclear layer (red dot: 4), central retinal ganglion cell layer (red dot: 5), central retinal inner nuclear layer (red dot: 6), central retinal outer nuclear layer (red dot: 7), ventral retinal ganglion cell layer (red dot: 8), ventral retinal inner nuclear layer (red dot: 9), ventral retinal outer nuclear layer (red dot: 10). **B.** Dihydroethidium (DHE) was diluted in dimethyl sulfoxide (DMSO) to a concentration of 5 μM. Cryosectioned eye samples 10 μM thick were covered with 50 μl of DMSO-diluted DHE and incubated for 30 minutes at 37°C in a humidified, light-protected chamber. The level of superoxide anions was detected at 20x magnification for each tissue section under fluorescence using an Arcturus Veritas microdissection system (Molecular Devices, Sunnyvale, CA). The fluorescent light was set at a brightness of '2' in order to ensure that the intensity of fluorescence light subject to the tissue samples was consistent across all eye sections. Positive controls were created by exposing C-cut eye sections to 0.5 M hydrogen peroxide solution for 5 minutes. Negative controls were created by exposing C-cut eye sections to 20 μl of a 1000 U/ml superoxide dismutase (SOD) solution for 10 minutes. GCL: ganglion cell layer; INL: inner nuclear layer; ONL: outer nuclear layer **C.** ROS profiles of the untreated WT eye over two, four, six, eight and ten months of age. Positive and negative controls have been plotted to demonstrate ROS fluorescence but have been removed from other graphs to reduce complexity of graphs **D.** ROS profiles of the untreated *hq* eye at two, four, six, eight, and ten months of age. **E.** ROS profiles of memantine-treated WT eye at two, four, six, eight, and ten months of age. **F.** ROS profiles of the memantine-treated *hq* eye at two, four, six, eight, and ten months of age.

A

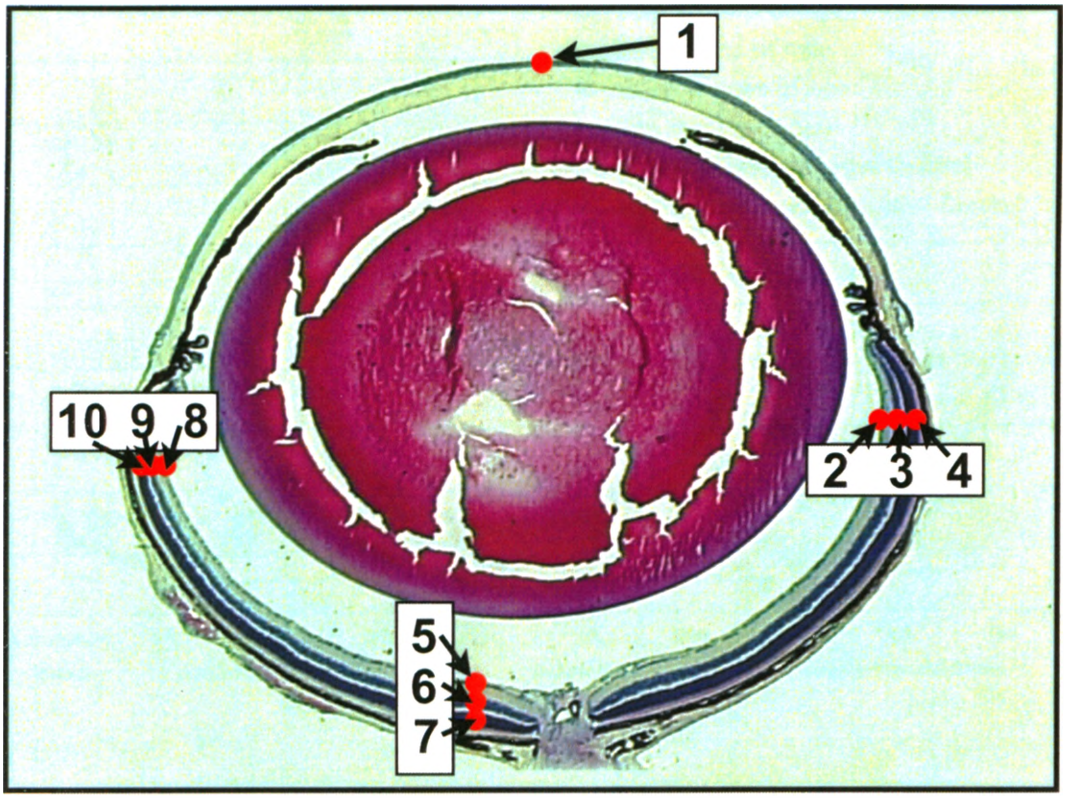

B

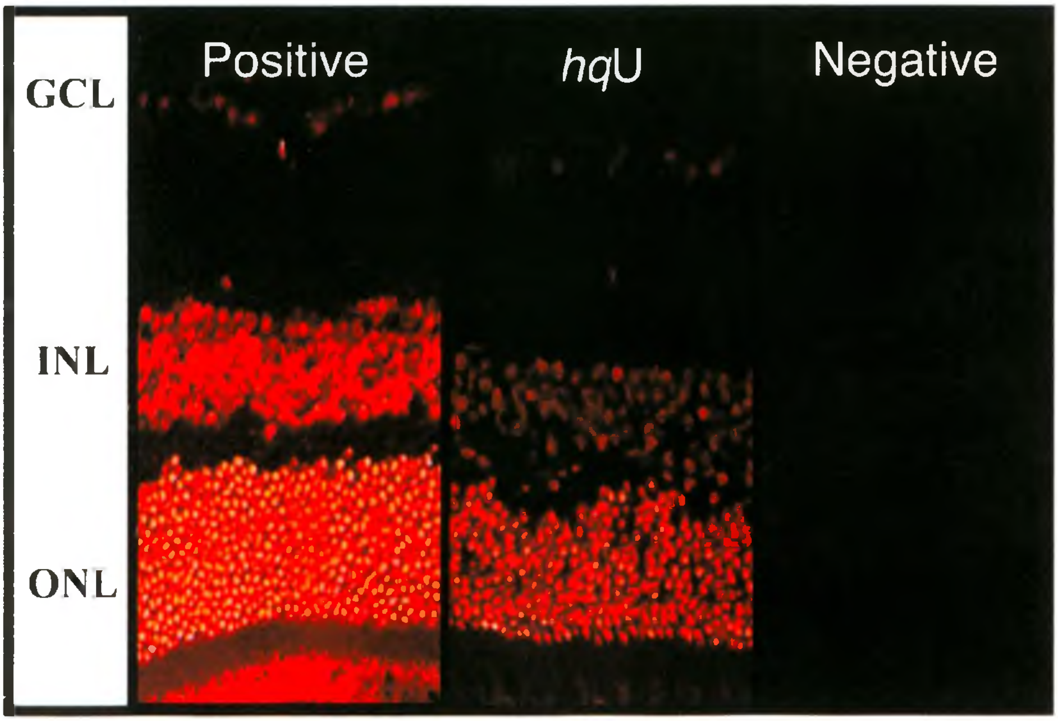

C

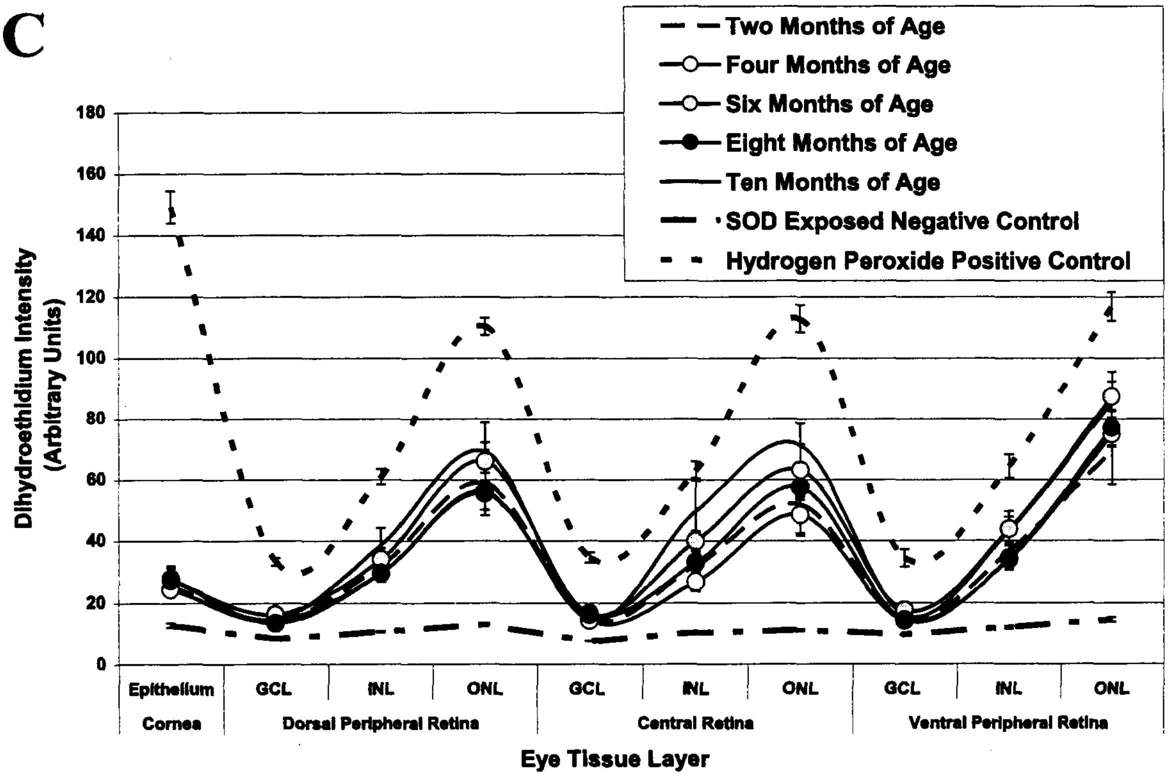
Two Months of Age
Four Months of Age
Six Months of Age
Eight Months of Age
Ten Months of Age
SOD Exposed Negative Control
Hydrogen Peroxide Positive Control
Dihydroethidium Intensity (Arbitrary Units)
0
20
40
60
80
100
120
140
160
180
Epithelium
GCL
INL
ONL
GCL
INL
ONL
GCL
INL
ONL
Cornea
Dorsal Peripheral Retina
Central Retina
Ventral Peripheral Retina
Eye Tissue Layer

D

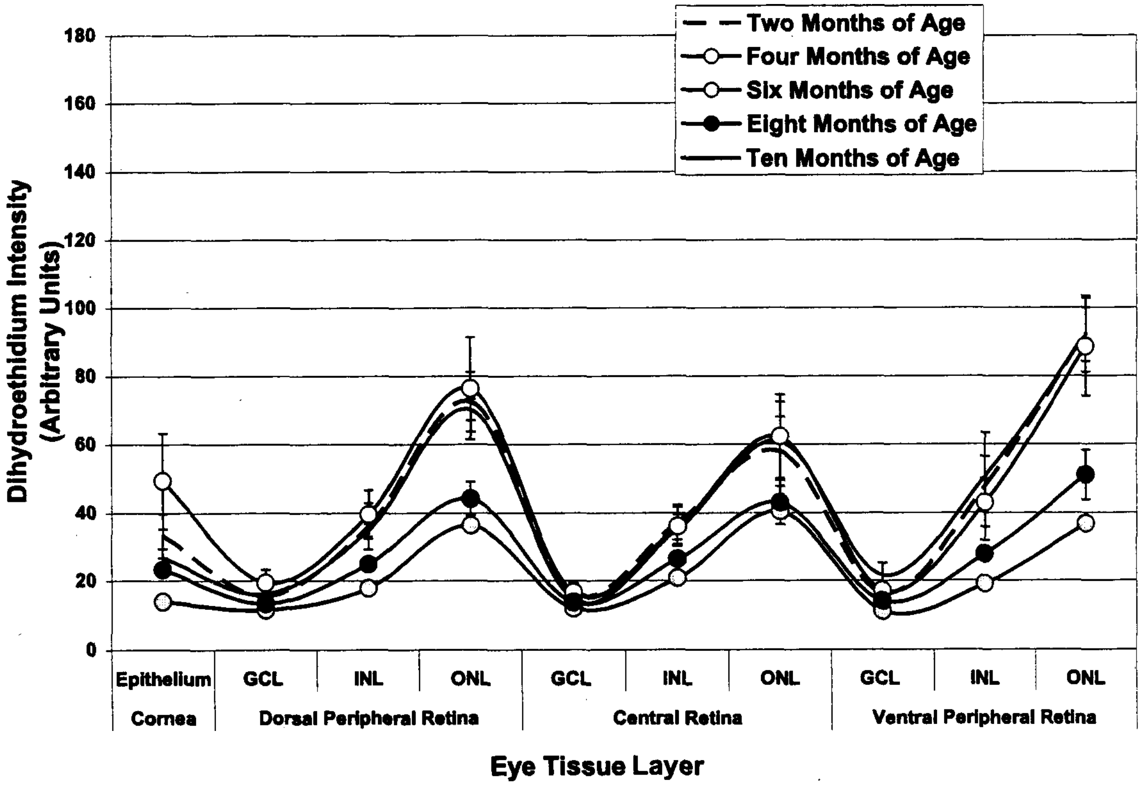
Two Months of Age
Four Months of Age
Six Months of Age
Eight Months of Age
Ten Months of Age
Dihydroethidium Intensity (Arbitrary Units)
0
20
40
60
80
100
120
140
160
180
Epithelium
GCL
INL
ONL
GCL
INL
ONL
GCL
INL
ONL
Cornea
Dorsal Peripheral Retina
Central Retina
Ventral Peripheral Retina
Eye Tissue Layer

E

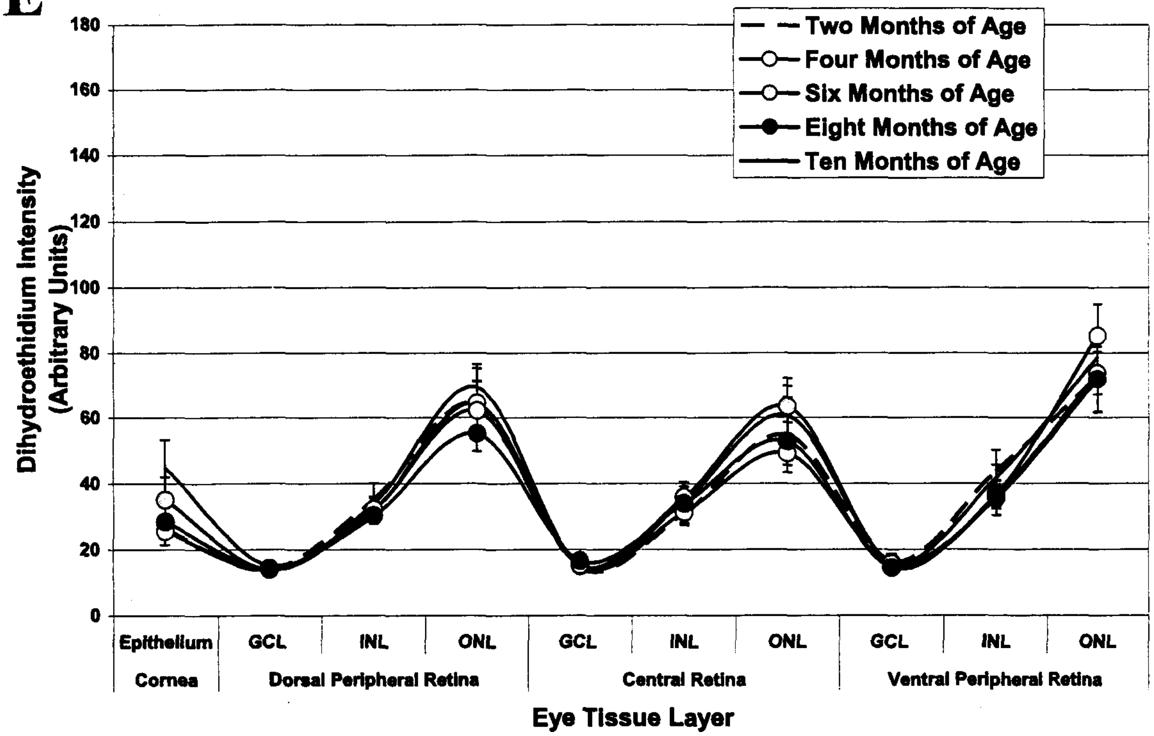
Two Months of Age
Four Months of Age
Six Months of Age
Eight Months of Age
Ten Months of Age
180
160
140
120
100
80
60
40
20
0
Dihydroethidium Intensity
(Arbitrary Units)
Epithelium
GCL
INL
ONL
GCL
INL
ONL
GCL
INL
ONL
Cornea
Dorsal Peripheral Retina
Central Retina
Ventral Peripheral Retina
Eye Tissue Layer

F

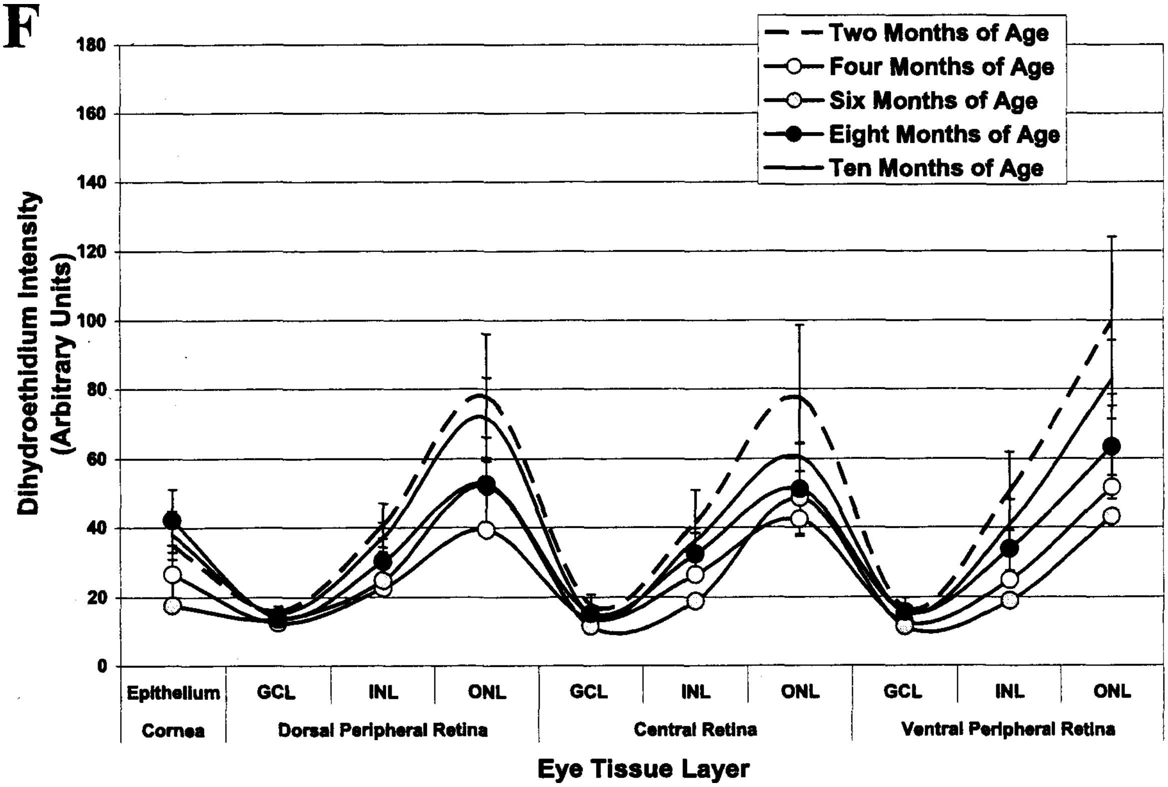
Two Months of Age
Four Months of Age
Six Months of Age
Eight Months of Age
Ten Months of Age
180
160
140
120
100
80
60
40
20
0
Dihydroethidium Intensity
(Arbitrary Units)
Epithelium
GCL
INL
ONL
GCL
INL
ONL
GCL
INL
ONL
Cornea
Dorsal Peripheral Retina
Central Retina
Ventral Peripheral Retina
Eye Tissue Layer

6) have been included with the profiles of the two month cohorts. Average dihydroethidium (DHE) fluorescence was extremely consistent in positive and negative controls between months and were removed from figures to reduce profile complexity.

Analysis of the ROS profiles of the untreated WT cohorts revealed the highest levels of ROS at ten months of age (Figure 3.24 C). Two and four months of age had the lowest levels of ROS in the untreated WT cohorts. The highest levels of ROS in the untreated *hq* cohorts were found at two, four and ten months of age (Figure 3.24 D). Six and eight months of age had lower levels of ROS in the cellular layers of all retinal regions in the untreated *hq* cohorts. The highest levels of ROS in the memantine-treated WT cohorts were found at ten months of age (Figure 3.24 E). Memantine-treated *hq* mice appeared to have the highest levels of ROS at two months of age (Figure 3.24 F).

3.30 Comparison of Reactive Oxygen Species in the Corneal Epithelium

Memantine-treated *hq* mice had the highest average DHE intensity in the corneal epithelium (34.73 ± 8.24 au) at two months of age (Figure 3.25). By four months of age, untreated *hq* mice had the highest corneal epithelium ROS levels (49.35 ± 13.97 au). At six months of age, memantine-treated WT mice had the highest level of ROS in the corneal epithelium (35.01 ± 6.97 au). Memantine-treated *hq* mice once again had the highest levels of ROS in the corneal epithelium at eight months of age (42.02 ± 9.11 au). Analysis of the ten month cohorts revealed a high level of ROS in both of the memantine-treated WT and *hq*

Figure 3.25 - Quantification of reactive oxygen species in the mouse eye of experimental cohorts at specific ages. A. Comparison of ROS profiles of experimental cohorts at two months of age. Positive controls were created by exposing C-cut eye sections to 0.5 M hydrogen peroxide solution for 5 minutes. Negative controls were created by exposing C-cut eye sections to 20 μl of a 1000 U/ml superoxide dismutase (SOD) solution for 10 minutes. **B.** Comparison of ROS profiles of experimental cohorts at four months of age. **C.** Comparison of ROS profiles of experimental cohorts at six months of age. No comparisons were made using the untreated and memantine-treated *hq* cohorts at six months of age because of inadequate sample sizes. **D.** Comparison of ROS profiles of experimental cohorts at eight months of age. **E.** Comparison of ROS profiles of experimental cohorts at ten months of age.

A

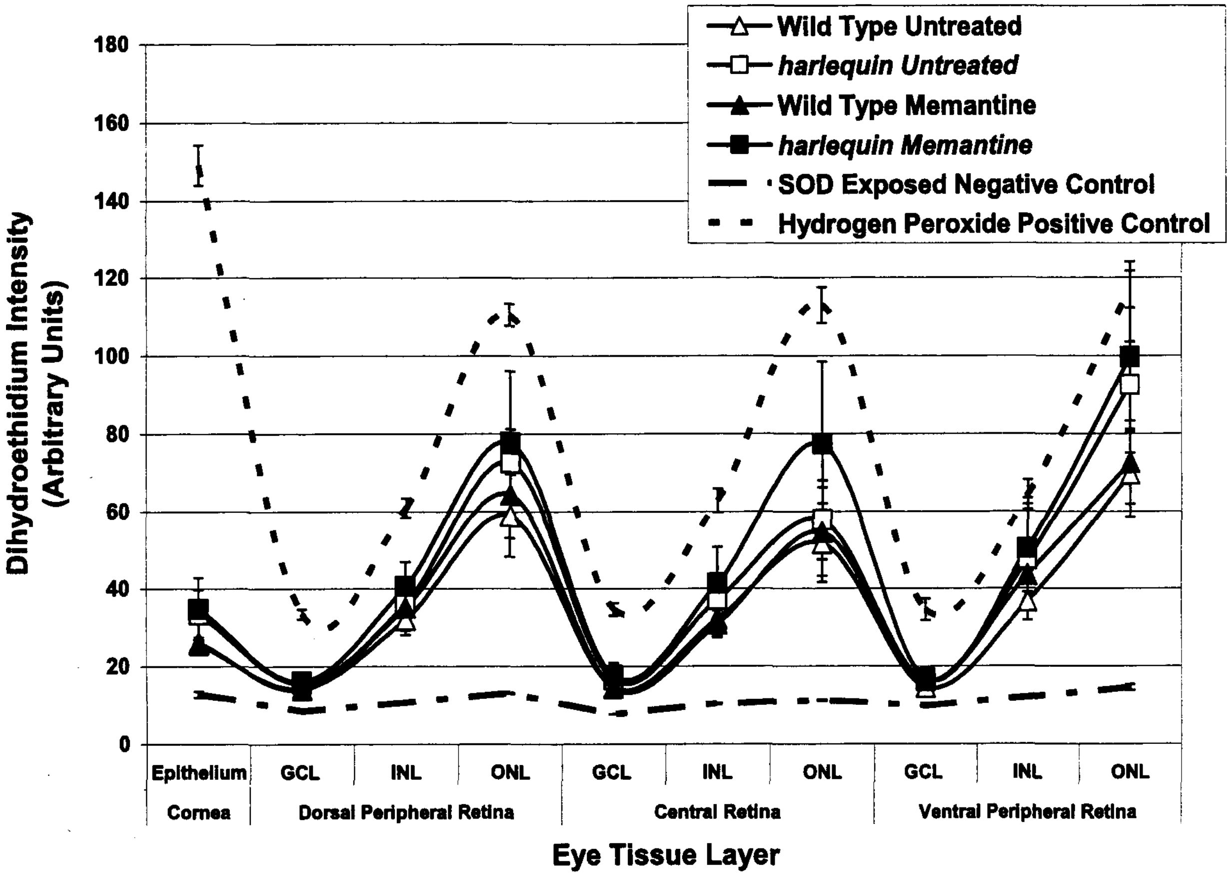

Wild Type Untreated
harlequin Untreated
Wild Type Memantine
harlequin Memantine
SOD Exposed Negative Control
Hydrogen Peroxide Positive Control
Dihydroethidium Intensity (Arbitrary Units)
180
160
140
120
100
80
60
40
20
0
Epithelium
GCL
INL
ONL
GCL
INL
ONL
GCL
INL
ONL
Cornea
Dorsal Peripheral Retina
Central Retina
Ventral Peripheral Retina
Eye Tissue Layer

B

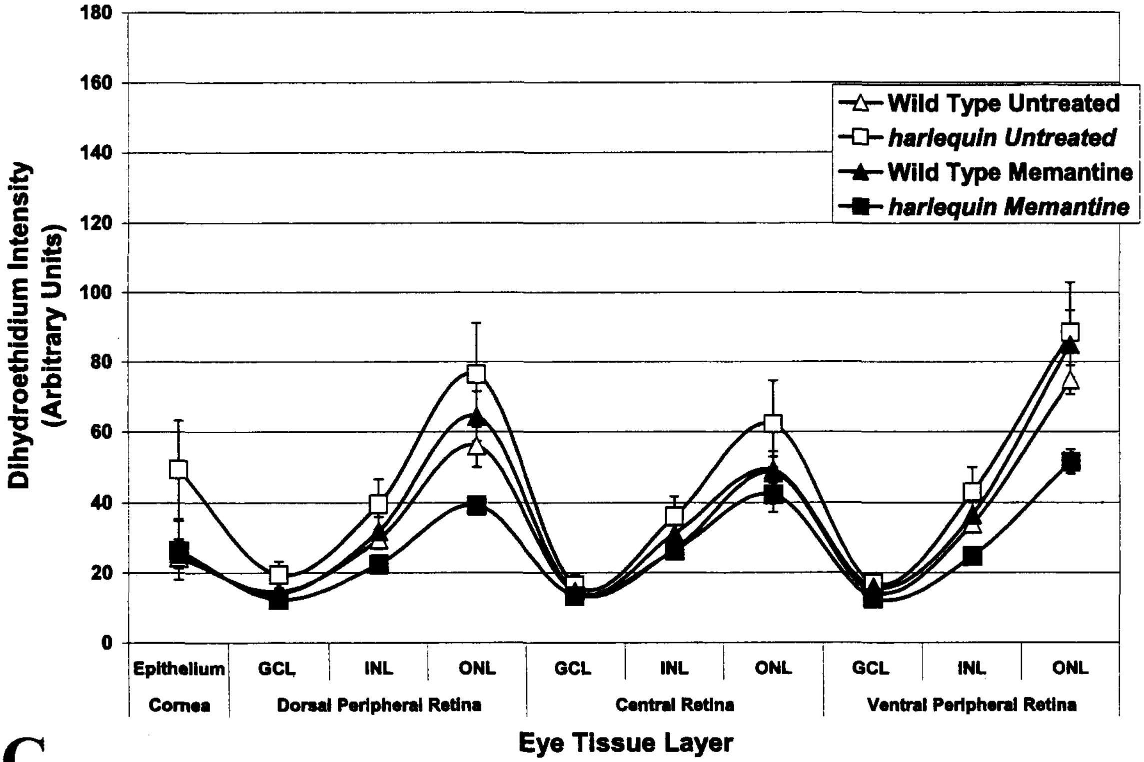
180
160
140
120
100
80
60
40
20
0
Dihydroethidium Intensity
(Arbitrary Units)
Wild Type Untreated
harlequin Untreated
Wild Type Memantine
harlequin Memantine
Epithelium
GCL
INL
ONL
GCL
INL
ONL
GCL
INL
ONL
Cornea
Dorsal Peripheral Retina
Central Retina
Ventral Peripheral Retina
Eye Tissue Layer

C

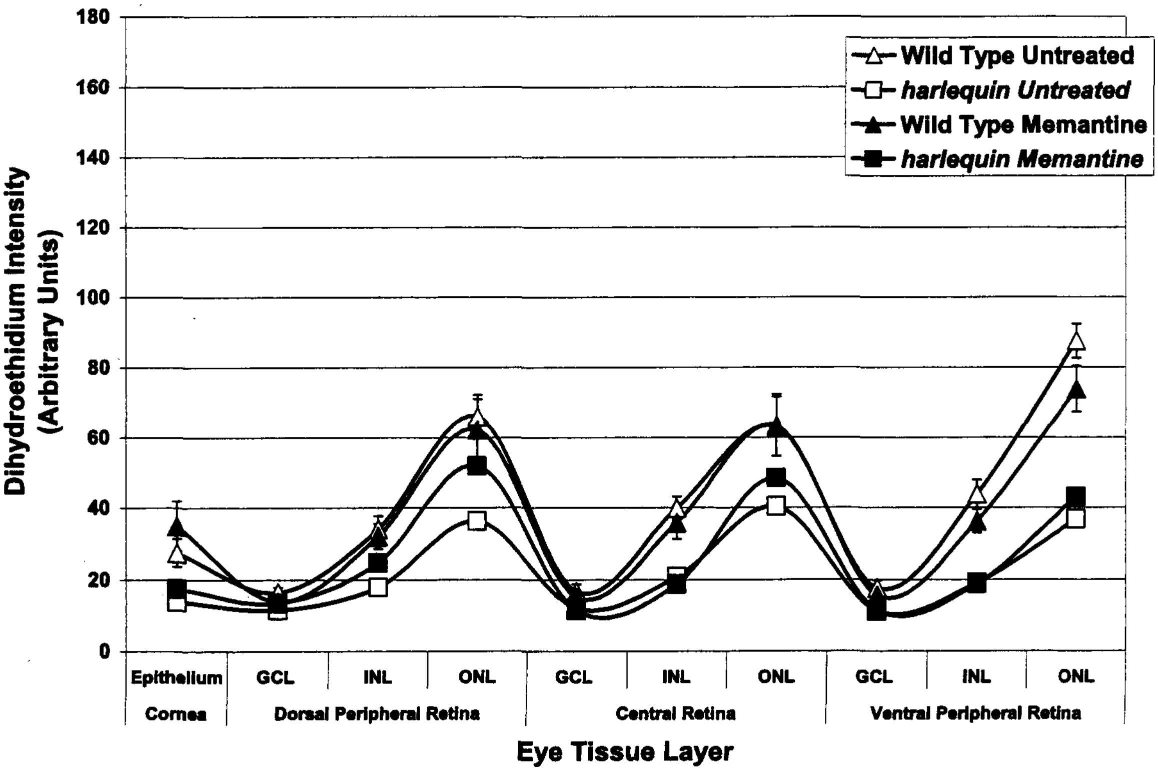
180
160
140
120
100
80
60
40
20
0
Dihydroethidium Intensity
(Arbitrary Units)
Wild Type Untreated
harlequin Untreated
Wild Type Memantine
harlequin Memantine
Epithelium
GCL
INL
ONL
GCL
INL
ONL
GCL
INL
ONL
Cornea
Dorsal Peripheral Retina
Central Retina
Ventral Peripheral Retina
Eye Tissue Layer

D

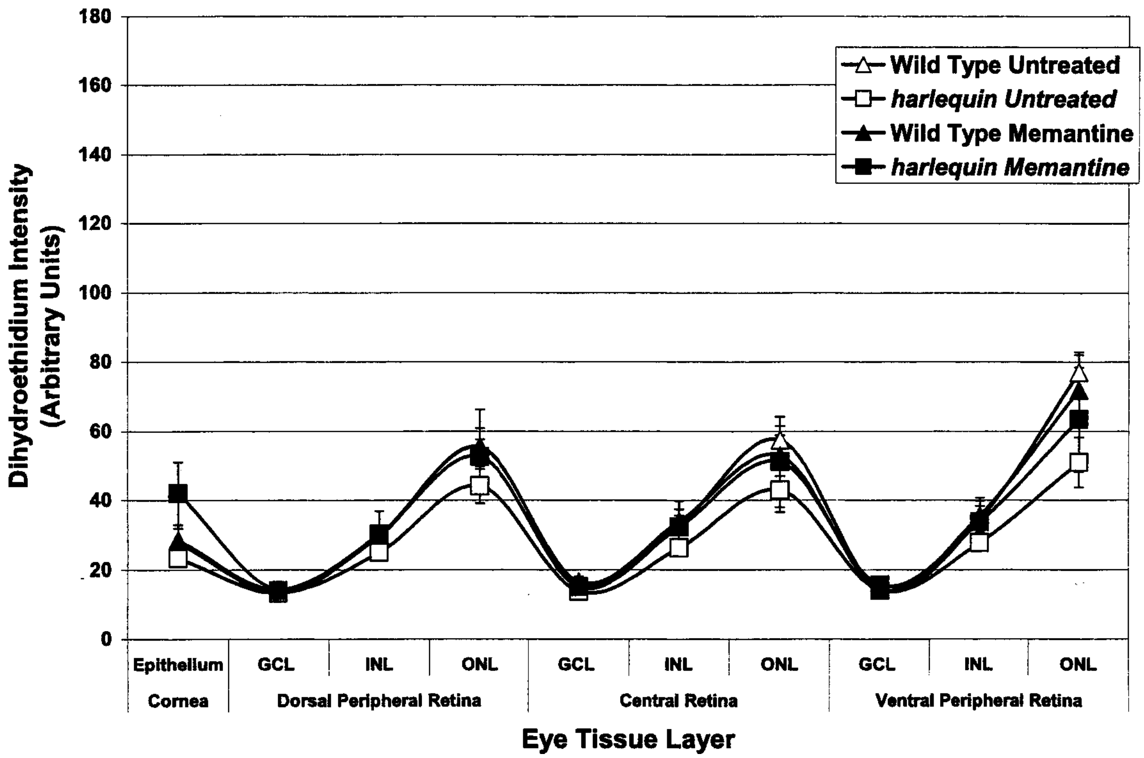
180
160
140
120
100
80
60
40
20
0
Dihydroethidium Intensity (Arbitrary Units)
Wild Type Untreated
harlequin Untreated
Wild Type Memantine
harlequin Memantine
Epithelium
GCL
INL
ONL
GCL
INL
ONL
GCL
INL
ONL
Cornea
Dorsal Peripheral Retina
Central Retina
Ventral Peripheral Retina
Eye Tissue Layer

E

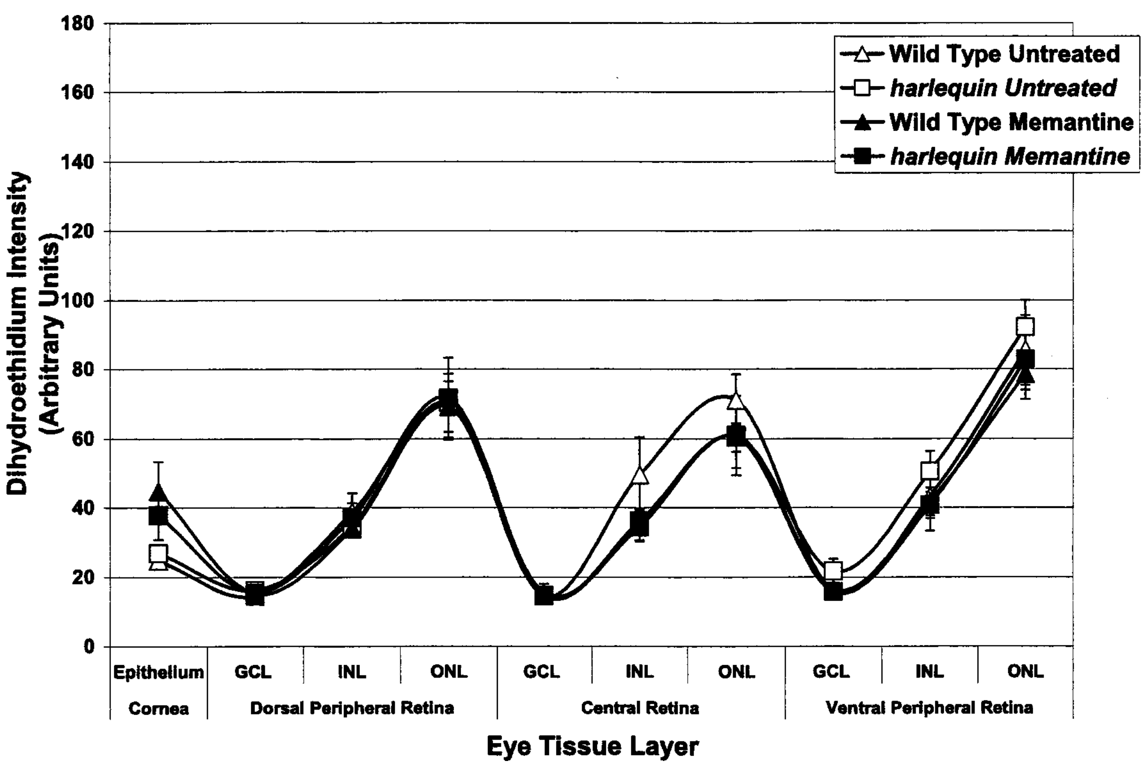
180
160
140
120
100
80
60
40
20
0
Dihydroethidium Intensity (Arbitrary Units)
Wild Type Untreated
harlequin Untreated
Wild Type Memantine
harlequin Memantine
Epithelium
GCL
INL
ONL
GCL
INL
ONL
GCL
INL
ONL
Cornea
Dorsal Peripheral Retina
Central Retina
Ventral Peripheral Retina
Eye Tissue Layer

cohorts. Memantine-treated WT mice had a significantly higher DHE intensity of 44.80 ± 8.59 au compared to age-matched, untreated WT mice ($P < 0.05$; untreated: 24.76 ± 1.40 au).

3.31 Comparison of Reactive Oxygen Species in the Ganglion Cell Layer

ROS levels in the ganglion cell layer were extremely consistent among cohorts and across retinal regions. At two months of age, ROS in the DR ganglion cell layer ranged from 14.09 ± 1.48 au in the memantine-treated WT cohort to 16.02 ± 1.33 au in the memantine-treated *hq* cohort. Levels of ROS in the ganglion cell layer of the central and ventral retina were similar to those found in the DR. A significant increase in ROS levels were found in the VR ganglion cell layer of memantine-treated WT mice compared to memantine-treated *hq* mice at four months of age ($P < 0.05$; WT: 15.94 ± 0.95, *hq*: 12.70 ± 0.65). No other differences in ROS levels were found among cohorts in the ganglion cell layer of all retinal regions.

3.32 Comparison of Reactive Oxygen Species in the Inner Nuclear Layer

Memantine-treated *hq* mice had a significant reduction in inner nuclear layer DHE intensity of the DR when compared to untreated *hq* mice at four months of age ($P < 0.05$; untreated: 39.51 ± 7.08 au, treated: 22.58 ± 1.77 au). No significant difference in levels of ROS were found in the CR inner nuclear layer among cohorts at any age. By four months of age, the memantine-treated *hq* cohort had significantly reduced levels of ROS in the VR compared to the untreated *hq* cohort ($P < 0.05$; *hq* untreated: 42.86 ± 7.08 au, *hq* treated: 24.91 ± 2.25 au). Memantine-treated *hq* mice were also found to have a reduced level of ROS in the inner nuclear layer of the VR compared to memantine-treated WT mice ($P < 0.05$; WT: 36.64 ± 4.34 au).

3.33 Comparison of Reactive Oxygen Species in the Outer Nuclear Layer

The outer nuclear layer had the highest level of ROS in the eye based on DHE intensity measurements. By four months of age, memantine-treated *hq* mice had a significantly reduced level of ROS in the DR when compared to untreated littermates ($P < 0.05$; untreated: 76.42 ± 15.02 au, treated: 39.30 ± 1.95 au). DHE intensity dropped in the untreated *hq* cohort at eight months of age becoming significantly lower than that of untreated WT mice ($P < 0.05$; WT: 55.47 ± 2.06 au, *hq*: 44.11 ± 4.92 au). No significant differences in levels of ROS in the outer nuclear layer of the CR were found among cohorts at any month of age. By four months of age ROS dropped in the VR of the memantine-treated *hq* cohort (51.57 ± 3.44 au) becoming significantly lower than values obtained for untreated *hq* mice ($P < 0.05$; 88.58 ± 14.31 au) and memantine-treated WT mice ($P < 0.05$; 85.19 ± 9.79 au). By eight months of age, untreated *hq* mice had significantly lower levels of ROS in the VR compared to that found in untreated WT mice ($P < 0.05$; WT: 77.07 ± 5.88 au, *hq*: 50.93 ± 7.84 au).

3.34 Quantitation of Programmed Cell Death in the Mouse Retina

Whole retinal apoptosis profiles of untreated WT and *hq* mice, and memantine-treated WT and *hq* mice were compared over the life span of mice (Figure 3.26). Untreated WT mice had low levels of apoptosis in early months of age but reached a maximum at eight months of age. Whole retinal apoptosis profiles were similar between untreated WT and *hq* mice. No differences in whole retinal apoptosis profiles were found between untreated WT and

Figure 3.26 - Quantification of apoptosis in the mouse eye of experimental cohorts. A. Terminal Deoxynucleotidyl Transferase dUTP Nick End Labeling (TUNEL) staining (Roche Canada, Mississauga, ON) was performed on cryogenically preserved tissue that had been frozen in optimal cutting temperature media and sectioned with a 10 μm thickness. C-cut sections were used to determine levels of apoptosis in the retina of experimental cohorts. Positive control samples were created by addition of DNase I recombinant. Negative control samples were incubated with TUNEL solution lacking terminal transferase. GCL: ganglion cell layer; INL: inner nuclear layer; ONL: outer nuclear layer **B.** Whole retinal apoptosis profiles of experimental cohorts at two, four, six, eight and ten months of age (cells/mouse = apoptotic cells observed in C-cut sections corrected for the number of mice per cohort). **C.** Central retinal outer nuclear layer apoptosis profiles of experimental cohorts at two, four, six, eight and ten months of age (cells/mouse = apoptotic cells observed in C-cut sections corrected for the number of mice per cohort).

A

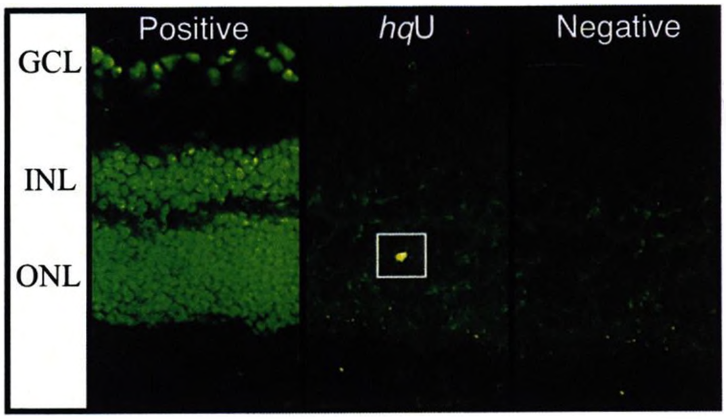
Positive
hqU
Negative
GCL
INL
ONL

B

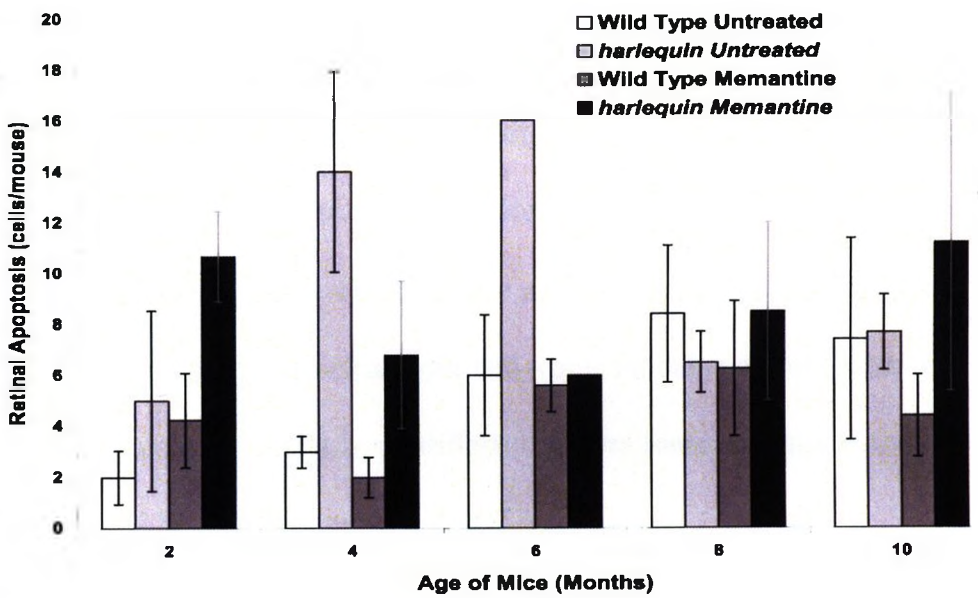
Wild Type Untreated
harlequin Untreated
Wild Type Memantine
harlequin Memantine
Retinal Apoptosis (cells/mouse)
0
2
4
6
8
10
12
14
16
18
20
2
4
6
8
10
Age of Mice (Months)

C

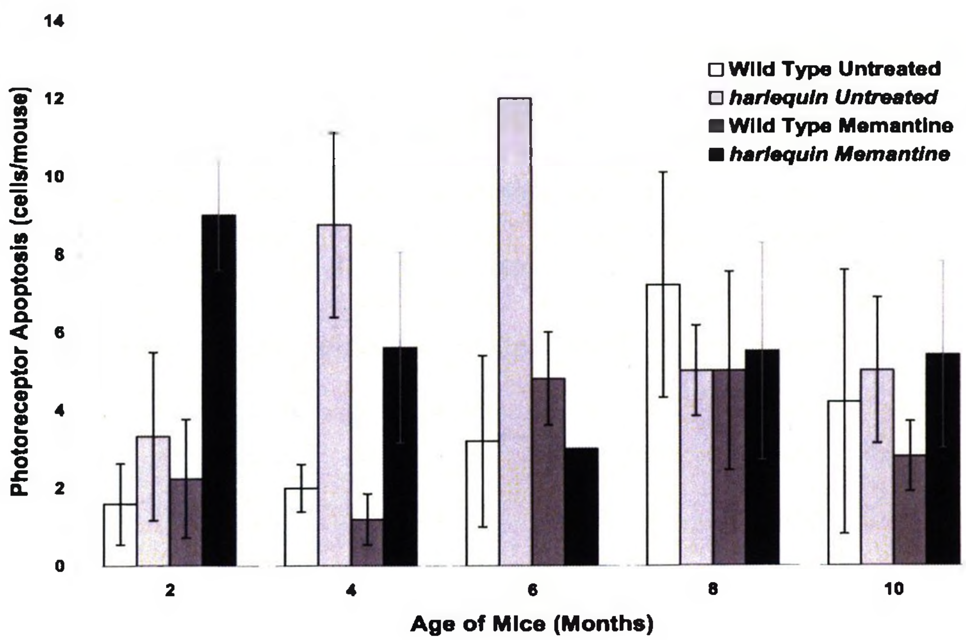
Wild Type Untreated
harlequin Untreated
Wild Type Memantine
harlequin Memantine
Photoreceptor Apoptosis (cells/mouse)
0
2
4
6
8
10
12
14
2
4
6
8
10
Age of Mice (Months)

memantine-treated WT mice. Memantine-treated *hq* mice had higher levels of apoptosis at two months of age which lowered at four and six months of age but increased again at eight and ten months of age. This was a significantly different profile of whole retinal apoptosis when compared to the untreated *hq* cohort ($P < 0.05$). No differences in whole retinal apoptosis profiles were found between memantine-treated WT and *hq* mice.

The central retinal outer nuclear layer had the highest levels of apoptosis. CR outer nuclear layer apoptosis profiles were compared over the life span of mice to determine any significant differences. No differences in CR outer nuclear layer apoptosis patterns were found among cohorts. CR outer nuclear layer apoptosis patterns were compared to whole retinal apoptosis patterns within each cohort. Comparisons were made to determine if apoptosis counts in the CR outer nuclear layer were sufficient to predict whole retinal apoptosis patterns. No differences between CR outer nuclear layer and whole retinal apoptosis patterns were found in the untreated WT cohort. Similarly, no differences were found among the untreated *hq*, memantine-treated WT and memantine-treated *hq* cohorts.

An elevated level of whole retinal apoptosis was found in the memantine-treated *hq* cohort when compared to memantine-treated WT mice at two months of age ($P < 0.05$; *hq*: 11 ± 1.8 cells). At four months of age, a dramatic increase in levels of whole retinal apoptosis was observed in the untreated *hq* cohort compared to age-matched, untreated WT mice ($P < 0.01$; WT: 3 ± 0.6 cells, *hq*: 14 ± 3.9 cells). No differences were found in levels of whole retinal apoptosis among cohorts at six, eight and ten months of age.

An elevated level of CR outer nuclear layer apoptosis was found in the memantine-treated *hq* cohort when compared to memantine-treated WT mice at two months of age ($P < 0.05$; *hq*: 9 ± 1.4 cells). At four months of age, a dramatic increase in levels of CR outer nuclear layer apoptosis was observed in the untreated *hq* cohort compared to age-matched, untreated WT mice ($P < 0.01$; WT: 2 ± 0.6 cells, *hq*: 9 ± 2.4 cells). A significant increase in levels of CR outer nuclear layer apoptosis was found in the memantine-treated *hq* cohort when compared to age-matched, memantine-treated WT mice at four months of age ($P < 0.05$; WT: 1 ± 0.7 cells, *hq*: 6 ± 2.4 cells). No differences were found in levels of whole retinal apoptosis among cohorts at six, eight and ten months of age.

Chapter 4 - Discussion

4.1 Summary

Detailed ocular phenotyping reveals key features of a narrowed time of disease onset, progression, underlying disease mechanisms and nature of *hq* retinal degeneration and memantine efficacy. The *hq* phenotype has a reduced survivorship, lower body mass and elevated water consumption. Deficits in retinal function precede structural degeneration in the *hq* mouse model of retinal degeneration. Structural degeneration does not occur in the peripheral retinal ganglion cell layer as initially reported by Klein et al. (2002). Instead, degeneration is first noted in the central outer nuclear layer of the *hq* retina and thus contrary to the initial prediction of disease progression mimicking human glaucoma. Levels of ROS are high in the retina, specifically in the outer nuclear layer, but ROS profiles in the eye are similar between *hq* and WT mice. Retinal degeneration is preceded by a trend of elevated ROS in the *hq* mouse retina. Mechanisms of cell death in the *hq* retina are biphasic with elevated apoptosis from two to four months of age likely followed by necrosis from eight to ten months of age. Excitoxicity is not evident in the *hq* mouse model of retinal degeneration. Thus, the *hq* phenotype of retinal degeneration most closely mimics human dry AMD. Memantine treatment reduces average body mass of WT mice and demonstrates early neurological impairment as an NMDA receptor antagonist. Memantine treatment does not preserve retinal function or structure significantly in normal aging or *hq* disease. ERG testing is most sensitive to retinal degeneration with detection of retinal function deficits as early as two months of age. The Visante™ OCT machine has a sensitivity conducive to detecting gross retinal thinning in mouse models of retinal degeneration while ensuring anterior segment integrity. Ocular phenotyping in *hq* mice is a valuable *in vivo* framework for therapeutic testing and understanding underlying disease mechanisms. The evidence and major findings presented here are valuable in the field of visual impairment and can be applied in future studies of retinal degenerative diseases.

4.2 New Features of the *harlequin* Phenotype

Herein, the *hq* phenotype is associated with decreased survivorship with observations of poor health (Figure 3.2). The *hq* mouse shows a decreased rate of H_2O_2 clearance and sensitivity to H_2O_2 dose-dependent insult (Klein et al., 2002; van Emple et al., 2005). Poor health may be related to activation-induced cell death of peripheral T cells in the *hq* mouse (Srivastava et al., 2007). The peripheral T cells of the *hq* mouse are susceptible to apoptosis triggered by H_2O_2 sensitivity, due to the downregulation of the superoxide-scavenging AIF protein (Srivastava et al., 2007). This reduces immune system response (Razvi & Welsh, 1993; Emoto et al., 2001) increasing the probability of infection and mortality. This hypothesis is supported by the observation of a low body mass, decreased behavioral response to handling and dehydration characteristic of poor health in the *hq* mice prior to death.

The *hq* phenotype results in decreased survivorship related to anesthetic delivery. Previous studies demonstrate that *hq* mice are susceptible to stress-induced heart failure (van Empel et al., 2005). The reduction in body mass of the *hq* mouse could lead to an increase in mortality, especially when coupled with anesthetic delivery. A ketamine and Xylazine cocktail is a harsh sedative that is lipid soluble and targets the brain immediately. Termination of the analgesic effect is due to redistribution of the drug in the body prior to metabolic inactivation (Shimoyama et al., 1997; Woodward et al., 2007). With the decrease in adipose tissue observed in the *hq* disease mouse, the anesthetic cocktail will be at higher concentrations in the brain increasing the likelihood of bradycardia and respiratory depression. It is apparent that precautions are necessary for anesthetization of *hq* mice. The precautions taken prior to anesthetic delivery including: assessment of mouse health, delivery of atropine during anesthesia and reversal of anesthetic at the earliest possible time point decrease mortality related to anesthetization and the *hq* phenotype.

The *hq* mouse phenotype has low mean body mass and reduced dorsal pelt coverage, both of which can be used as an indicator of disease severity (Figure 3.3; Benit et al., 2008). However, WT mice had no correlation between body mass and retinal function (data not shown). Large interanimal variation in *hq* body mass and dorsal fur coverage are consistent with diseases associated with mitochondrial dysfunction (Benit et al., 2008). Also, *hq* mice with the lowest body mass have the lowest coverage of fur on the dorsal pelt (Benit et al., 2008). Low body mass associated with low dorsal pelt coverage is supported by the research herein. Correlation studies also confirmed that body mass has a high correlation with retinal degeneration. The *hq* mice with the lowest body mass have the longest a-wave and b-wave latencies. Similarly, the *hq* mice with the lowest body mass have the lowest a-wave and b-wave amplitudes. Body mass and dorsal fur coverage assessed eight to ten days post birth can therefore be used as external and readily observable indicators of *hq* retinal disease severity, a novel correlation not noted in previous literature.

Low body mass related to the *hq* phenotype is not associated with low water consumption. Surprisingly, *hq* mice consume more water per gram of body mass than WT mice (Figure 3.4). Food intake accounts for 44% of body mass variation and water intake accounts for

31% of body mass variation assessed in multiple mouse strains including B6 and CBA mice (Bachmanov et al., 2002). Food and water intake are commonly dependent upon each other. This dependency results because of osmotic and volumetric stimulation of thirst (Zhang et al., 2007). However, in some strains of mice increases in water consumption are not associated with increases in food intake, demonstrating independent stimulation of thirst and hunger (Bachmanov et al., 2002). In addition, water intake is partially associated with the activity of the mouse (Skott, 2003). Increased locomotor activity is observed over the lifespan of the *hq* mouse (Laliberte, personal communication) which may lead to the increase in water consumption. The increased water consumption in the *hq* disease mouse is likely independent of decreased appetite. The assessment of food intake in both the WT and *hq* mouse is necessary in future research to determine the relationship between water intake and food consumption.

4.3 Detailed Characterization of the *harlequin* Eye Anterior Segment

Characterization of the *hq* mouse eye *in vivo* reveals a reduced transverse width of the anterior chamber (Figure 3.13a). Microphthalmia is defined as a globe (eye) with a total axial length or width that is at least two standard deviations below the mean for age (Anophthalmia/ microphthalmia overview, 2007). The reduced anterior chamber width is not severe and not considered to be microphthalmic in the *hq* mouse. However, a single *hq* mouse had microophthalmia, which is common in many inbred strains of mice (Figure 3.13d; Chase, 1942). The *hq* mice generated for use in this study have a low genetic background of C57BL/6J and a high genetic background of CBA/CaJ mice. The genetic heterogeneity is due to an initial breeding of purchased *hq* mice (B6CBACa A^{w-J}/A-$Pdcd8^{Hq}$/J) to the C57BL/6J inbred mouse strain for a single generation and subsequent breeding to the CBA/CaJ inbred mouse strain for a minimum of four generations. The C57BL/6J mouse has an incidence of microophthalmia ranging from 0.8 - 9.2% (Smith & Sundberg, 1995). No published data on microophthalmia incidence were found for the CBA/CaJ mouse and microophthalmia is not noted in CBA/CaJ phenotyping (JAX® Laboratories). The incidence of microophthalmia is low in the *hq* mouse and should not deter eye research with the *hq* mouse model of retinal degeneration.

The *hq* mouse model of retinal degeneration does not have severe corneal histopathology associated with aging. Thinning of the corneal epithelium is characteristic of normal aging in WT mice herein. The *hq* mouse has an aged corneal epithelium thickness present at two months of age i.e., similar to that of an eight to ten month old WT mouse (Figure 3.15E). The epithelium is the primary barrier of the cornea to the surrounding environment (Dohlman, 1971). A thin corneal epithelium decreases the protective barrier of the eye and increases risk of damage and infection by foreign bodies (Dohlman, 1971). The resulting risk increases the likelihood of bacterial infection leading to neovascularization and keratitis (Srinivasan et al., 2009; Yuan & Wilhelmus, 2009). The *hq* mouse appears to have an increased potential for corneal insult at young ages but no severe histopathology was observed herein.

4.4 Detailed Characterization of Reduced Retinal Function in the *harlequin* Mouse

The *hq* mouse demonstrates reduced retinal function at the earliest age tested (Figure 3.9A). Previously, it was demonstrated that retinal function in the *hq* mouse was normal at five weeks of age but was reduced at four months of age (Klein et al., 2002). Herein, retinal degeneration is initially observed in the *hq* mouse at two months of age, as measured by ERG b-wave amplitude. Mice were first tested at two months of age and degeneration could in fact begin prior to two months of age. A reduction in the leading edge of the a-wave amplitude at three months of age implies that the decrease in whole retinal function is at least partly due to a reduced function of the photoreceptors, an observation not previously reported (Figure 3.7 A). When photoreceptors are not functioning properly, they do not transmit the electrochemical signal to the depolarizing cells of the retina therefore reducing b-wave amplitude (Pinilla et al., 2005). Thus, retinal degeneration in the *hq* mouse is an early-onset disease associated with decreased photoreceptor function and has an age of onset prior to two months of age.

Retinal degeneration is exacerbated with age, with a progressive loss of retinal function. As the *hq* mouse ages, whole retinal function continues to decrease resulting in extremely low visual function by ten months of age. Aging-related retinal degeneration is supported by initial retinal phenotyping in the *hq* eye where retinal function was abolished by ten months of age in the *hq* mouse (Klein et al., 2002). Similarly, photoreceptors continue to degenerate with age. The combined hyperpolarizing response decreases, implying decreases in whole retinal function are partly due to a declining function of the aging photoreceptors. Retinal function in the *hq* mouse demonstrates age-related progression and is associated with a reduction in photoreceptor function.

4.5 Detailed Characterization of the *harlequin* Retina

Structural degeneration in the *hq* retina occurs primarily in the outer nuclear layer of the central retina. In previous studies, structural degeneration was first observed at three months of age in the peripheral retina (Klein et al., 2002). Structural degradation is primarily in the ganglion cells and amacrine cells located in the upper stratum of the inner nuclear layer (Klein et al, 2002). Herein, peripheral retinal degeneration in the ganglion cell layer does not occur at young ages (Figure 3.16 A and 3.16 C). The central retinal region is the area of most notable degeneration in the *hq* mouse. The ganglion cell layer is reduced in the *hq* mouse at four months of age but not in the following months (Figure 3.16 B). This implies that the retinal ganglion cells of the *hq* mouse degenerate earlier than in WT mice but ganglion cell degradation is normal in the aging process of the WT mouse, consistent with the hypothesis of premature aging in the *hq* mouse. The earliest and most notable degeneration occurs in the outer nuclear layer of *hq* mice at four months of age, two months following reductions in retinal function (Figure 3.20 B). Structural degeneration of the photoreceptors is supported by measures of the outer plexiform layer thickness in the central retina (Figure 3.19 B). Structural degradation of the outer nuclear layer continues to ten months of age in the *hq* mouse but not in WT mice. By ten months of age, degeneration in the inner nuclear layer occurs (Figure 3.18). Even though cell loss is apparent at four months of age in H&E stained sections, significant thinning of the complete neural retina cannot be observed with OCT or H&E until ten months of age in the *hq* mouse (Figure 3.14 A and 3.22). Degeneration in the peripheral retina occurs at ten months of age primarily in the outer nuclear and plexiform layers contrary to previous reports. Retinal degeneration in the *hq* mouse is characterized by a dramatic reduction of photoreceptors in the central retina prior to the the degeneration of additional retinal layers in following months.

4.6 New Insights into *harlequin* Disease Mechanisms

Increased levels of ROS do not appear to be associated with retinal degeneration in the *hq* disease model from two to ten months of age. Not surprisingly, qualitative assessment of ROS reveals the highest levels of ROS in the nuclei of the photoreceptors (Figure 3.24 and 3.25). The high concentration of mitochondria and metabolic activity of the photoreceptors (Hoang et al., 2002; Duong et al., 2002) lead to high levels of ROS production when stimulated by light (Yang et al., 2003). The outer nuclear layer of the *hq* mouse has a trend for increased ROS at two and four months of age but levels are not significantly increased. A high standard error of mean is observed with the *hq* phenotype likely relating to the disease heterogeneity which may be leading to the lack of significance (Benit et al., 2008). Levels of ROS are lower in the second-order cells of the retina and further reduced in the third-order ganglion cells of the retina. Levels of ROS observed in WT mice are extremely similar to those observed in the *hq* disease model. ROS scavengers such as catalase and glutathione are elevated in response to oxidative stress in the *hq* mouse (Klein et al., 2002). The elevation of catalase and glutathione is demonstrated in the post mitotic neurons of the cerebellum of *hq* disease mice. This increased expression of ROS scavengers could be sufficient to control levels of ROS in the eye keeping them around levels observed in the WT mouse. Interestingly, metabotropic glutamate receptors on oligodendrocytes, similar to those found in the inner nuclear layer of the retina, have been shown to reduce excitotoxicity and oxidative stress and could also account for similar levels of ROS between *hq* and WT mice (Deng et al., 2004). Levels of ROS increase with age (Shigenaga et al., 1994) and this association is observed in WT mice. Similarly, ROS was also increased in *hq* mice by ten months of age, likely associated with aging. Studies have demonstrated that an increased "burst" of elevated ROS during development is significant enough to induce premature aging (Wells et al., 2009). Levels of ROS prior to two months of age were not studied herein and is a limitation to the study. ROS levels in the *hq* mouse are similar to those found in the WT mouse from two to ten months of age, indicating a normal aging phenotype. Therefore, ROS do not appear to have a strong association with early *hq* retinal degeneration.

Levels of apoptosis are elevated in the outer nuclear layer of young *hq* mice but not aged *hq* mice (Figure 3.25). With a similar profile and level of ROS in the *hq* and WT retina, oxidative stress is likely not the only apoptotic trigger and cause of retinal degeneration. Increased levels of apoptosis at young ages can account for the decreased number of photoreceptor nuclei observed at four months of age. Levels of apoptosis were reduced in the *hq* retina at eight and ten months of age, but significant structural degradation was still observed. The apoptotic stressors are likely increasing as *hq* mice age, leading to necrosis (Festjens et al., 2006). Necrotic cells can be identified in H&E stained tissues based on the following criteria: shrunken eosinophilic cytoplasm, pyknotic nuclei and irregularly fragmented chromatin (Obernier et al, 2002). This identification is difficult in the outer nuclear layer based on the cellular morphology of the photoreceptors. Thus, necrosis is hypothesized to account for the cell loss not explicable by the observed levels of apoptosis. It is evident that a more sensitive assay for *in situ* detection of cellular necrosis is necessary to determine quantitative values of cellular necrosis. Increased levels of apoptosis at two and four months of age precedes structural degeneration in the *hq* retina but is likely surpassed by necrotic cell death between eight and ten months of age.

Excitoxicity does not appear to be associated with cell death in the *hq* mouse model of retinal degeneration. Excitotoxic insult is characterized by an increase of ROS in downstream neurons leading to cell death (Rego et al., 2003). If excitotoxic insult is occurring in the retina of the *hq* mouse we expect to see increased levels of ROS, apoptosis and necrosis in the second-order and third-order cells of the retina. Surprisingly, levels of ROS, apoptosis and necrosis are not elevated in the ganglion cell and inner nuclear layers of the *hq* mouse model of retinal degeneration. Again, metabotropic glutamate receptors, similar to those found on the bipolar cells of the inner nuclear layer, have been shown to reduce excitotoxicity and oxidative stress (Deng et al., 2004). This would essentially stop the deadly chain reaction and could serve as a excitotoxic protectant of the second- and third-order cells of the retina. With no elevation in ROS, apoptosis or necrosis in second-order and third-order cells of the retina, the likelihood of oxidative-stress induced excitotoxicity leading to retinal degeneration in the *hq* mouse is low.

4.7 Revised Hypothesis of Disease Mechanisms in the *harlequin* Mouse Model of Retinal Degeneration

With only a trend of increased levels of ROS in the *hq* retina, oxidative stress-induced retinal degeneration is likely not the sole mechanism of retinal degeneration. The second most likely mechanism of retinal degeneration is abnormal energy production (Trifunovic et al., 2005; Brink et al., 2009). The photoreceptor cells are metabolically demanding (Duong et al., 2002) and mitochondrial dysfunction could debilitate photoreceptor cells quite readily (Philp et al., 2003; Eckmiller, 2004). A decrease in AIF leads to compromised complex I function in the OXPHOS chain (Vahsen et al., 2004). The compromised complex I function results in reduced energy production in the mitochondria of cells leading to cell loss (Porter & Urbano, 2006). Compromised OXPHOS could also affect the metabolically active retinal pigment epithelium (Young & Bok, 1969) leading to photoreceptor cell death (Raymond & Jackson, 1995). Energy failure is supported by the loss of retinal function prior to the loss of retinal structures. Mitochondrial dysfunction is associated with common forms of retinal disease including both AMD (Miceli & Jazwinski, 2005; Hashizume et al., 2008) and glaucoma (Abu-Amero et al., 2006). Complex I productivity can be assessed in future work with the use of an electron donor, 2,6-dichloroindophenol, and spectrophotometric analysis (Janssen et al., 2007). Although the *hq* mouse does not follow the disease process originally hypothesized, it is an excellent candidate for photoreceptor related-retinal degeneration associated with mitochondrial dysfunction.

4.8 The *harlequin* Retinal Disease Mimics Human Dry-AMD not Glaucoma

Retinal degeneration in the *hq* mouse model of premature aging does not mimic glaucoma (Osborne et al., 1999) as initially predicted. The nerve fiber layer of the healthy mouse retina is extremely thin in the periphery and cannot be accurately quantified using hematoxylin and eosin staining. Levels of intraocular pressure and optic nerve damage were not assessed in the *hq* mouse. However, with no reduction in peripheral retinal ganglion cell nuclei we can also assume that the ganglion cell axons remain undamaged (Schlamp et al., 2006; Lukas et al., 2009). Current mouse models of glaucoma such as the DBA/2J mouse show elevated intraocular pressure and degeneration of peripheral ganglion cells making it the prime model for glaucoma research (Zhong et al., 2007; Libby et al., 2007; Calkins et al., 2008). Retinal degeneration occurs primarily in the central outer nuclear layer of the *hq* mouse and is therefore a poor candidate model for assessing treatments for human glaucoma.

The likely disease candidate in the *hq* mouse model of retinal degeneration is human atrophic (nonexudative) or dry AMD. Accurate mouse models of human dry AMD showing multiple components of the disease are rare. Many mouse models exhibit deposits in the basal lamina of the retina or disorganized retinal pigment epithelium (Edwards & Malek, 2007). The mouse model currently demonstrating an accurate model of dry AMD is the elongation of very long chain fatty acids protein 4 (ELOVL4) transgenic mouse. The ELOVL4 mouse model is characterized by central photoreceptor degeneration and atrophy of the retinal pigment epithelium with no retinal neovascularization (Karan et al., 2005). Photoreceptor degeneration is typically preceded by an accumulation of lipofuscin, pigment-granules composed of lipid-containing residues, in the retinal pigment epithelium (Karan et al., 2005). Lipofuscin production is associated with decreased mitochondrial function related with aging in the retinal pigment epithelium of humans demonstrating dry AMD (Vives-Bauza et al., 2008). The *hq* mouse has degeneration of photoreceptors in the central retina which is not associated with neovascularization, making the *hq* mouse a candidate of dry and not wet AMD. Further studies of the *hq* mouse need to include an in depth characterization of the retinal pigment epithelium. Lipofuscin is currently being examined in the *hq* mouse to determine whether accumulation of liposfuscin precedes photoreceptor degeneration (Data not presented). Further characterization should also include imaging of the interior surface of the eye opposite the lens (fundus; Tuo et al., 2007), immunohistochemistry (Imamura et al., 2006) and spectral profiling (Marmorstein et al., 2002) in order to determine if drusen-like deposits are present in the retinal pigment epithelium of the *hq* mouse. Complex I productivity can be assessed in future work with the use of an electron acceptor, 2,6-dichloroindophenol (DCIP), and spectrophotometric analysis (Janssen et al., 2007). NADH is oxidized by complex I, the liberated electron then reduces an artificial substrate which delivers the electron to DCIP. Mitochondrial DNA mutagenesis is also being assessed using the random mutation capture assay (Vermulst et al., 2008) in the *hq* mouse to determine whether mitochondrial dysfunction is associated with the *hq* phenotype (Data not presented). The *hq* mouse model of retinal degeneration most accurately represents dry AMD disease mechanisms. The *hq* mouse has the potential of being a valuable animal model for therapeutic testing in human dry AMD.

4.9 Memantine Treatment Reduces Body Mass in Wild Type but not *harlequin* Mice

Memantine treatment leads to a decreased body mass in wild type mice but not in *hq* mice (Figure 3.3). Memantine consumption was similar in both WT and *hq* mice over all months of delivery. Most importantly, WT mice did not consume more memantine than *hq* mice and vice versa (Figure 3.5). As a result, *in vivo* data were not skewed between memantine-treated WT and *hq* cohorts based on levels of memantine consumption. Memantine is not toxic in the body but has caused some adverse side effects characterized as 'nervous energy' such as pacing, fidgeting and insomnia (Monastero et al., 2007; Jarvis & Figgitt, 2003; Ishida & Kamei, 2009). Locomotor testing and video monitoring were not performed on memantine-treated mice herein, but can be used for the detection of 'nervous' energy in future research. Memantine can be used as an appetite suppressant in a baboon model of binge eating and is currently being considered a possible treatment for human obesity because of its effects on neurological impairment (Bisaga et al., 2008; Hermanussen & Tresguerres, 2005). Memantine treatment reduced body mass in WT mice, likely through appetite suppression and increased 'nervous energy'.

4.10 Memantine Treatment Demonstrated Neurological Impairment in the Retina

Memantine demonstrated effects as a neurological suppressant in the mouse retina. It is expected that memantine would inhibit some of the excitatory signal via NMDA receptor antagonism on the ganglion cell dendrites. The signal is being relayed from the photoreceptor cells to the ON bipolar cells (Rea et al., 2004). The ON bipolar cells then release glutamate at the synaptic terminal in the upper stratum of the inner nuclear layer. Memantine reduces glutamate stimulation of NMDA receptors on the ganglion cell dendrites by blocking the conductance pore (Rogawski & Wenk, 2003). However, the reduction of ganglion cell excitation cannot be assessed using electroretinography in the mouse (Nushinowitz et al., 2002). Herein, a general trend of reduced photoreceptor function (a-wave amplitude; Figure 3.7 A) and retinal function (b-wave amplitude; Figure 3.9 A) was observed in memantine-treated mice. This indicates that memantine may in fact be acting as a minor neurological suppressant unrelated to NMDA receptor antagonism, but has not been noted in literature to date. Correlation studies support memantine-mediated structural impediment of the electrochemical signal, as b-wave amplitude had low to moderate negative correlation to memantine consumption. As higher levels of memantine are consumed, retinal response decreases. Memantine demonstrates effects as a minor neurological suppressant via unknown mechanisms in the mouse retina.

4.11 Memantine Treatment did not Preserve Retinal Function

Memantine did not preserve retinal function in WT or *hq* mice as initially hypothesized. This is not surprising because NMDA receptors are located in the upper stratum of the inner nuclear layer on ganglion cell dendrites (Hartveit & Veruki, 1997; Fletcher et al., 2000). Linear regression analysis showed a slight reduction in rate of retinal degeneration in the memantine-treated *hq* mouse but memantine did not significantly preserve retinal function. Memantine does not slow the loss of retinal function in the normal aging process nor in the *hq* mouse model of early onset retinal degeneration.

4.12 Memantine Treatment Leads to Corneal Histopathology in *harlequin* Mice

Memantine treatment led to corneal thickening and opacity at late months of age in memantine-treated *hq* mice leading to artificially low ERG amplitudes (Figure 3.10 A and 3.10 B). Corneal abnormalities are most likely a result of multiple ERG and OCT testing in combination with memantine. Continual testing exposes the mouse to multiple dates of anesthetic, multiple exposures to topical eye drops and repeated corneal insult by electrode contact (Liang et al., 2008; Aylward et al., 1989). The combined effect of memantine exposure, the *hq* phenotype and multiple testing dates lead to corneal inflammation and corneal opacity. The opacity in the cornea impedes light from the retina and potentially lowers amplitudes in ERG data artificially (Rubin & Dawson, 1978). Corneal abnormalities and large reductions in ERG wave amplitudes were seen simultaneously at eight and ten months of age supporting the hypothesis of light impediment. Memantine treatment could in fact be preserving retinal function but a subsequent side effect is over shadowing any measurable benefits.

Corneal histopathology associated with memantine treatment was evident in both young and old *hq* mice (27% of mice). Interestingly, two memantine-treated *hq* mice had severe neutrophil infiltration by two months of age, prior to multiple dates of testing and corneal insult (Figure 3.15 B). No severe corneal epithelium thinning or ulceration is observed in these mice. Foreign bodies such as bedding possibly penetrated the compromised corneal epithelium of the *hq* mice, resulting in immune system response to the corneal stroma. However, foreign bodies were not observed in the memantine-treated *hq* mice experiencing corneal histopathology at two months of age. It is possible that memantine consumption is leading to an immune system response in the corneal stroma.

Corneal histopathology related to aging is common in many strains of mice (Smith et al., 2002a). Corneal subepithelial and anterior stromal mineralization are common in some laboratory strains of mice and were observed in a single memantine-treated *hq* mouse at ten months of age herein (Figure 3.15 C). These corneal deposits are extracellular and globular in appearance and are located in the superficial corneal stroma. Mineralization is likely associated with thinning and ulceration of the overlying corneal epithelium leading to evaporational drying of the corneal stroma enhancing mineral deposition (Smith et al., 2002b). Neovascularization and keratitis are also common in aging mice (Smith et al., 2002a). This can be related to trauma, typically foreign material such as bedding becoming embedded in the cornea. Again, foreign bodies were not observed in the memantine-treated *hq* mice experiencing minor to severe corneal histopathology. No bacterial infection was detected in the aging mice experiencing neutrophil recruitment supporting a memantine-associated immune system response to the cornea. The additive effects of the *hq* phenotype, memantine exposure and multiple testing dates likely lead to corneal histopathology in a small number of memantine-treated *hq* mice. Memantine treatment appeared to exacerbate corneal aging in the *hq* but not WT mouse.

4.13 Memantine Induced Predicted but Insufficient Protection of Ocular Structure

Memantine demonstrates a minor but insufficient protection of third-order cells in both the WT and *hq* mouse retinas (Figure 3.16). Memantine treatment leads to a significant increase in ganglion cell nuclei in the central retina of WT mice at two months of age. Though not significant, a general trend of increased ganglion cell counts was observed in both the memantine-treated WT and *hq* cohorts. These findings support a memantine-associated reduction in excitotoxic insult in the third-order cells of the retina (Dong et al., 2008; Tchedre & Yorio, 2008). Potentially, sample size and concentration of memantine in the *hq* mouse retina were insufficient in this study to observe the anticipated prophylactic effect. The concentration of memantine used herein mimicked that used in animal testing for Alzheimer's disease patients (Minkeviciene et al., 2004). Memantine demonstrates minor protection of third-order cells in both the WT and *hq* mouse retinas and subsequent drug testing should consider larger cohort sizes and multiple drug dosages.

4.14 Evaluation of Memantine Delivery to Wild Type and *harlequin* Mice

The proposed form of memantine delivery is ideal for the testing of neuroprotection in the *hq* mouse. In ocular disease, drugs are typically delivered via eye drops (Ishii et al., 2001), ingestion (Steigerwalt et al., 2008), ocular injection (Sagong et al., 2009) or the use of an ocular implant (Zhou et al., 1998). Both ocular injections and ocular implants increase risks of developing complications such as endophthalmitis, an inflammation of the internal layers of the eye, and retinal detachment (Bhavsar et al., 2007; Al-Torbak et al., 2005; Kim et al., 2009). Ingestion is a non-invasive form of drug delivery and should be used if the drug is not toxic with minimal side effects in the body and can readily pass the blood-retinal barrier. Furthermore, ingestion of memantine allows for a relatively constant delivery over the course of the day, week and month with minimal cost and effort. Injections cause high initial levels of drug followed by a subsequent absence of drug until the next injection characterized as under and over dosing. This under and over dosing creates large changes in ocular drug concentrations (Heiduschka et al., 2007). Also, the *hq* mouse has severe cerebellar degeneration (Klein et al., 2002) that likely impacts vision, so treating the eye alone could be insufficient. Ingestion is the preferred method of memantine delivery in the *hq* mouse model of retinal degeneration because it is cost effective, requires minimal effort, targets multiple components of vision and leads to relatively constant levels of drug throughout the experimental duration.

4.15 Therapeutic Intervention in the *harlequin* Mouse Model of Retinal Degeneration

In humans, memantine has been associated with visual problems including hallucinations, decreased visual acuity, and clouding of the cornea and lens (Villoslada et al., 2009; Monastero et al., 2007; Ebixa® Data Sheet, 2009). Herein, retinal function was shown to decrease after memantine treatment. It is predicted that the transmission of the electrochemical signal to the second- and third-order ganglion cells of the retina is impeded by memantine treatment leading to a decrease in visual acuity. Memantine is also shown to conserve cell counts and potentially reduce excitotoxic insult in the mouse retina, but further characterization of memantine-hydrochloride is necessary in an animal model of glaucoma.

Unfortunately, memantine was a poor candidate for therapeutic intervention in the *hq* mouse model of human dry AMD. Memantine was chosen for its potential as an effective therapeutic intervention in a model of excitoxicity and oxidative-stress induced retinal degeneration mimicking human glaucoma (Klein et al., 2002; Hare et al., 2004). In glaucoma, the degeneration of peripheral retinal ganglion cells precedes blindness and is thought to be caused by excitotoxic insult (Mali et al., 2005; Dong et al., 2008). After in depth characterization of the *hq* mouse model of retinal degeneration, glaucoma is no longer considered to be the disease being mimicked and consequently, memantine is not the prime candidate for *hq* disease intervention.

With the characterization of the *hq* mouse model of retinal degeneration, new potential therapeutic intervention strategies are possible. Evidence supporting human dry AMD disease mechanisms include the degeneration of retinal function prior to the loss of central photoreceptors, likely due to compromised complex I function of the OXPHOS chain and mitochondrial dysfunction (Trifunovic et al., 2005; Brink et al., 2009). Therapeutic intervention strategies should target the reduction of ROS specifically in the mitochondria. Mitochondrial DNA damage resulting from increased ROS produced by OXPHOS could lead to increased mitochondrial dysfunction. A class of steroid glycosides and triterpene saponins known as ginsenosides found exclusively in the plant genus *Panax* (ginseng), can protect against mitochondrial dysfunction through antioxidant defense (Shin et al., 2009). These ginsenosides are predicted to work synergistically with elevated levels of catalase and glutathione expression in the *hq* mouse retina. The additive antioxidant defense is predicted to further reduce initial levels of ROS, mitochondrial damage and apoptosis at young ages (Shin et al., 2009). Further characterization of the interaction of AIF with complex I of the OXPHOS chain is necessary in determining energy production in the mitochondria of *hq* mice. However, a supplement stabilizing mitochondrial energy production coupled with increased antioxidant defense could lead to preservation of retinal function in the *hq* mouse. Creatine is a nitrogenous organic acid that promotes mitochondrial energy production in vertebrates (Saks et al., 1980; Jacobus & Diffley, 1986; Wilken et al., 2000). A lack of creatine has been associated with neurological injuries and disorders (Wilken et al., 2000; Hausmann et al., 2002; Zhu et al., 2004). Supplementation of creatine coupled with increased antioxidant defense may be a novel and sufficient therapeutic intervention for slowing or ceasing the progression of retinal degeneration associated with the *hq* mouse phenotype.

4.16 ERG is a Sensitive Measure of Ocular Function Capable of Early Disease Detection

Full-field ERG, measuring the cumulative retinal response, is a powerful, well validated and sensitive assay used commonly for the assessment of retinal degeneration (Davis et al., 2008; Li et al., 2009; Cai et al., 2009). Full-field ERG testing is further validated in this study with the highest sensitivity in detecting retinal degeneration in the *hq* mouse. Deterioration of *hq* retinal function is evident at two months of age, prior to any structural degeneration of the retina assessed by postmortem histopathology. Full-field ERG allows for longitudinal studies providing evidence for rate of retinal degeneration over the lifespan of the *hq* mouse. ERG studies can also be used to determine quality of therapeutic intervention (Lund, 2008; Davis et al., 2008; Komeima et al., 2008) in the *hq* mouse. Full-field ERG is vital to the assessment of therapeutic intervention in the *hq* mouse model of retinal degeneration in future research.

The assessment of retinal function using ERG has limitations which can be avoided with the employment of a strict experimental protocol. Improper techniques strongly affect the ERG trace and greatly reduce the reliability and reproducibility of data. Variables that can affect the ERG include the improper use of anesthetics, variations in body temperature, insufficient dilation of the pupil, inadequate dark adaptation, and prolonged testing, all of which can artificially lead to a decrease in wave amplitude (Nushinowitz et al., 2002). A severe side effect caused by anesthetic delivery is the opacification (cataract) of the lens due to dehydration of the anterior chamber (Ridder et al., 2002). This can be prevented by lubrication of the cornea during the extent of anesthesia. A decrease in mouse body temperature by just a few degrees is associated with a virtually undetectable ERG trace (Mizota & Adachi-Usami, 2002). Furthermore, the location of the electrode on the eye can alter the amplitude of a signal by as much as 30-40% (Nusinowitz et al., 2002). Finally, repeated flashing in a single ERG test can reduce rod-mediated responses up to 20% unless an interstimulus interval is used to allow sufficient rod recovery. Currently, there are no internationally accepted standards for recording ERG traces in mice. For example, electrodes, methods of stimulating the eye, and experimental protocols vary between laboratories studying visual function in the mouse eye (Green et al., 1997; Ruether et al., 1997; Marti et al., 1998; Davis et al., 2008). Herein, an ERG program was specifically designed, with the aid of ERG experts from the University of Ottawa Eye Institute, to test retinal response from both rod and cone photoreceptor stimulation, simultaneously. Also, the experimental design reduces confounding variables as much as possible. Herein, the assessment of exacerbated retinal degeneration resulting from longitudinal ERG testing revealed no significant increases in retinal degeneration. With the use of an optimized and consistent ERG framework, longitudinal studies can be used to assesses mouse models of retinal degeneration and therapeutical intervention with high sensitivity and reproducibility.

Multi-focal ERG may provide an added sensitivity to detection of retinal degeneration and therapeutic intervention in the *hq* mouse. At the outset of this study, full-field electroretinography had been used to assess retinal function in many mouse models of retinal degeneration and was the standard in the field (Roman et al., 2007; White et al., 2007). Multi-focal ERG uses small localized areas of light and dark flashes to stimulate specific parts of the retina (Si et al., 1999). The ERG traces from the stimulated retina can be used to create a full retinal response profile based on small retinal regions. Multi-focal ERG shows which region of the retina is degenerating and adds a significant degree of sensitivity to the assay (Seeliger et al., 2000). Multi-focal ERG provides the necessary evidence needed to demonstrate the degeneration of central vision prior to peripheral vision in the *hq* mouse as hypothesized by this study.

4.17 OCT is Valuable in Detecting Retinal Degeneration and Anterior Structural Abnormalities

OCT imaging is a commonly used technique for the assessment of ocular structures in human clinical diagnosis (Martin et al., 2007; Wang et al., 2008; Schweitzer et al., 2009). The Visante™ machine is sensitive enough to detect gross retinal degeneration in the *hq* mouse and is supported by postmortem histopathology assessment. However, values obtained from *in vivo*

OCT imaging were slightly elevated, ~ 20 - 30 μm, compared to histological analysis. Also, OCT imaging revealed a slightly thinner neural retina in memantine-treated *hq* mice compared to untreated *hq* mice which was not supported by postmortem analysis. The differences in retinal thickness observed between *in vivo* and postmortem testing are likely due to the tissues contained within the eye. The Visante™ is designed to image the anterior chamber of the eye and accounts for the refraction indices of the cornea (1.388; Lehman et al., 2009) resulting in a sensitive measure with high reproducibility (Mohamed et al., 2007). However, refraction indices increase in an additive fashion through the anterior chamber, lens, and vitreous (the semi-fluid filled posterior segment of the eye; Sardar et al., 2007). This would lead to a significant and unavoidable amount of light scatter during imaging which creates image distortion. The Visante™ OCT machine can be used to determine gross levels of retinal thinning in models of retinal degeneration comparatively, but should not be used for determination of finite values of retinal thickness.

The Visante™ OCT machine can be used to detect retinal degeneration *in vivo* but is likely not as sensitive as the Cirrus™ HD-OCT machine. This is the first study that validates the use the Visante™ OCT machine as a monitor of gross retinal degeneration *in vivo*. Typically, separate machines are necessary for the imaging of both anterior and posterior segments of the human eye (Radhakrishnan et al., 2007; Memarzadeh et al., 2007; Gerth et al., 2009). With the relatively small axial depth of the mouse eye (Zhou et al., 2008), whole eye imaging with the Visante™ machine is possible. Herein, novel evidence supporting the use of the Visante™ OCT machine to assess whole eye structure and gross retinal degeneration simultaneously has been presented (Figures 3.14a and 3.23). Retinal thinning can in fact be determined in the neural retina but the Visante™ OCT is not sensitive enough to determine which retinal layers are degrading. Typically the retina of a human eye is visualized *in vivo* using a Stratus™ or Cirrus™ OCT instrument (Monteiro et al., 2008; Marmor et al., 2008; Schweitzer et al., 2009). The older Stratus™ OCT machine acquires images at a rate of 400 axial scans per second along a transverse plane and has an axial resolution of 10 μm (Forooghian et al., 2008). The more recent Cirrus™ HD-OCT machine uses the same principles as the Visante™ and Stratus™ OCT machines. However, the Cirrus™ HD-OCT machine acquires images at a dramatically increased rate of 20,000 axial scans per second, with an improved axial resolution of 5 μm (Forooghian et al., 2008). This allows for a detailed construction of a 3D image of the retina and can delineate boundaries of the retinal layers. Both the Stratus™ and Cirrus™ OCT machines account for the refractive indices of the whole eye allowing for accurate measurements of retinal thickness but cannot be used for assessment of the anterior segment. An advantage of the Visante™ OCT machine over the higher resolution machines, is the assessment of anterior structures of the eye including corneal opacity and pupil dilation, simultaneous with the detection of retinal degeneration. ERG should be paired with the Visante™ OCT in order to determine possible reasons for artificially reduced retinal function, such as corneal inflammation, corneal opacity, pupil dilation and lens opacity. The Cirrus™ HD-OCT machine is likely more sensitive in determining finite levels of retinal degeneration *in vivo*. However, The Visante™ OCT machine can be used to detect abnormalities in the anterior chamber leading to anomalies in ERG data while determining gross retinal degeneration.

4.18 Framework of Therapeutic Intervention in the *harlequin* Mouse Model of Retinal Degeneration

With the extensive characterization of the *hq* retinal phenotype, a more concise and sensitive experimental framework can be employed for future therapeutic testing. This experimental framework is targeted to the *hq* biomarkers for diseases onset, progression and drug targets. The experimental framework described here is extensive and time consuming. In order to make the experimental design efficient, ERG should be used beginning at very young ages to determine the earliest age of *hq* retinal disease onset, and possible therapeutic preservation of retinal function. ERG testing should be continued until six or eight months of age to determine rate of retinal disease progression. In future research, full-field ERG testing can be replaced by the more sensitive multi-focal ERG testing. In future research, the Cirrus™ HD-OCT machine can be used for more sensitive measurements of the mouse retina *in vivo* but should be paired with anterior imaging using the Visante™ OCT machine. *In vivo* imaging dramatically reduces animal numbers required in the experimental design because animals do not need to be euthanized for assessment of whole retinal thinning. Young *hq* mice, at two months of age, did not show structural changes in the retina. Postmortem structural analysis of retinal degeneration should commence at four months of age in the *hq* mouse. Cell counts and tissue layer thickness from B-cut tissues have been analyzed but omitted from this project. Data supported findings but were omitted because B-cut sections contain different levels of oblique retinal cuts and are not representative measures of true retinal thickness and cell counts (Data not included). Furthermore, structural analysis of the *hq* retina postmortem should be assessed beginning at four months of age. This will allow researchers to concentrate on fewer cohorts of mice containing larger sample sizes, important for statistical analyses. Particular attention should be paid to cell death in the outer nuclear and inner nuclear layers of the central retina. The research provided herein has led to an optimized framework for future therapeutic testing highlighting relevant biomarkers of retinal degeneration in the *hq* mouse.

4.19 Limitations

The experimental framework herein was incomplete and can be strengthened. No direct measure of memantine concentration has been obtained from the blood or retina of *hq* mice in this study. However, levels of memantine can be assessed in blood samples or specific tissues using mass spectrometry postmortem (Bynum et al., 2007; Almeida et al., 2007). A second limitation in the preceding research is the sample size of the experimental cohorts. A dramatic increase in mortality is related to the *hq* phenotype. This reduced sample sizes for *hq* mice in the six month cohorts to a single mouse and these cohorts consequently could not be used in any postmortem analysis. Similarly, *hq* cohorts are low in additional months analyzed, reducing the statistical power of the data obtained. Finally, the sheer number of statistical tests performed increased the number of type I and type II statistical errors. This means that the probability of detecting or not detecting significance by random chance increases greatly. Herein, approximately 1,500 statistical analyses have been performed meaning that approximately 75 tests were type error. The new optimal experimental framework will reduce unnecessary tests and increase sample sizes improving the statistical power of the research.

4.20 Conclusions

Retinal degeneration in the *hq* mouse model of premature aging does not mimic glaucoma. Retinal degeneration in *hq* mice is characterized by the degeneration of photoreceptors in the central retina and most closely mimics human dry AMD. *In vivo* and postmortem ocular phenotyping provides a detailed time line of functional and structural degeneration in the *hq* mouse (Figure 4.1). the most Retinal degeneration is not associated with a significant increase in ROS or excitotoxicity from two to ten months of age. Retinal degeneration mechanisms are now hypothesized to be associated with decreased energy production via mitochondrial dysfunction primarily in the active central photoreceptors. Retinal degeneration has an early-onset prior to two months of age. Levels of apoptosis are highest at early months of age in the *hq* retina. Mechanisms of cell death change from apoptosis in early months of age to necrosis at later months of age in the *hq* mouse retina. Therefore, intervention strategies must begin at very early stages of development and target mitochondrial energy production. The in depth characterization of the *hq* ocular phenotype supports the hypothesis of premature aging in the *hq* mouse model and makes it a valuable model for aging studies.

Memantine is a poor candidate for therapeutic intervention in the *hq* mouse model of retinal degeneration. However, this research demonstrates the effects of memantine hydrochloride as an effective NMDA receptor antagonist and provided possible reasoning for decreased vision in patients receiving memantine hydrochloride. This research also provides supporting evidence of weight reduction making it a possible candidate treatment for obesity. This research has resulted in a more optimal framework for therapeutic testing in the *hq* mouse

Figure 4.1 - Detailed ocular phenotyping in the *harlequin* mouse provides a novel timeline of functional and structural aspects of disease progression. At birth, qualitative assessment of *hq* mouse body mass and dorsal fur coverage can be used as visual biomarkers for retinal disease severity in following months. Functional deficits assessed using electroretinography precede histopathology and structural losses with disease onset occurring prior to two months of age assessed using electroretinography. By two months of age, *hq* mice demonstrate a thin corneal epithelium similar to that of an aged wild type mouse, increasing the likelihood of corneal histopathology. Retinal structural degeneration is evident at four months of age, primarily in the outer nuclear layer of the central retina. By ten months of age, *hq* mice demonstrate structural degeneration in additional layers of the central retina and the start of degeneration in the peripheral retina. By ten months of age, *hq* mice show dramatically reduced retinal function but vision loss is not complete. Consistent with premature aging, *hq* mice have slightly elevated levels of reactive oxygen species (ROS) at two and four months of age. At ten months of age, *hq* mice show elevated levels of ROS similar to levels observed with the WT aging process. Cell death appears to be biphasic in *hq* mice with apoptosis at young months of age and necrosis by late months of age.

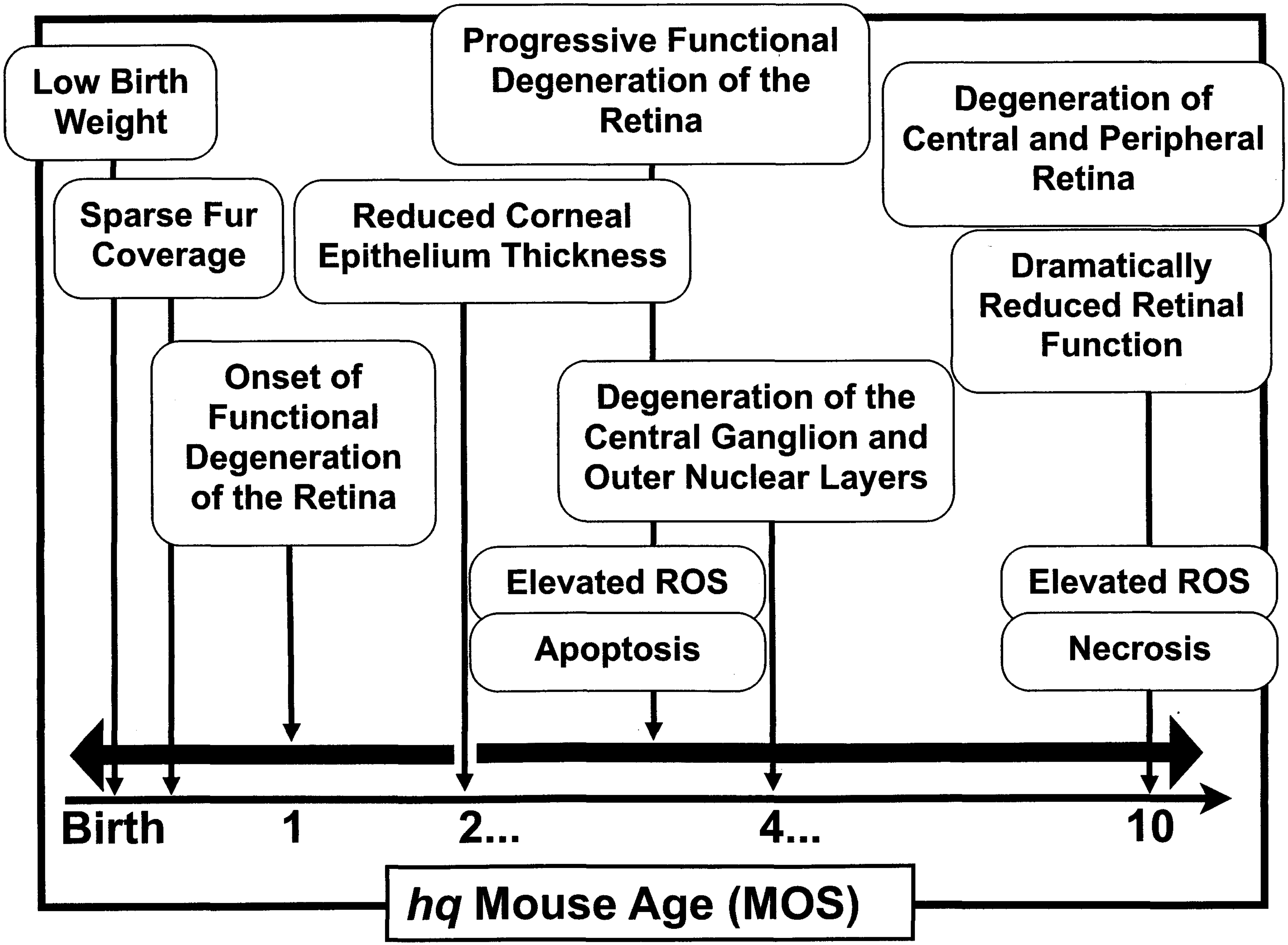
Low Birth Weight
Sparse Fur Coverage
Onset of Functional Degeneration of the Retina
Reduced Corneal Epithelium Thickness
Progressive Functional Degeneration of the Retina
Degeneration of the Central Ganglion and Outer Nuclear Layers
Elevated ROS
Apoptosis
Degeneration of Central and Peripheral Retina
Dramatically Reduced Retinal Function
Elevated ROS
Necrosis
Birth
1
2...
4...
10
hq Mouse Age (MOS)

model of retinal degeneration and can be extended to incorporate multiple mouse models of retinal degeneration and multiple therapeutic strategies. A large pharmaceutical company is currently in the process of supplying the second candidate drug with the potential of conserving retinal function in the *hq* mouse model of human dry AMD. The company will be collaborating with the Hill laboratory and will be using the optimized experimental framework proposed by this study.

Chapter 5 - References

Abu-Amero, K.K., Morales, J., Bosley, T.M. 2006. Mitochondrial abnormalities in patients with primary open-angle glaucoma. Invest. Ophthalmol. Vis. Sci. 47(6):2533-2541

Almeida, A.A., Campos, D.R., Bernasconi, G., Calafatti, S., Barros, F.A., Eberlin, M.N., Meurer, E.C., Paris, E.G., Pedrazzoli, J. 2007. Determination of memantine in human plasma by liquid chromatography-electrospray tandem mass spectrometry: application to a bioequivalence study. J. Chromatogr. B. Analyt. Technol. Biomed. Life Sci. 848(2):311-316

Al-Torbak, A.A., Al-Shahwan, S., Al-Jadaan, I., Alhommadi, A., Edward, D.P. 2005. Endophthalmitis associated with the Ahmed glaucoma valve implant. Br. J. Ophthalmol. 89(4):454-458

Anophthalmia/Microphthalmia Overview. *The National Institutes of Health: Gene Reviews* 2007; Available at: URL: http://www.ncbi.nlm.nih.gov/bookshelf/br.fcgi?book=gene&part=anophthalmia-ov. Accessed: October 14, 2009

Arnoult, D., Parone, P., Martinou, J.C., Antonsson, B., Estaquier, J., Ameisen, J.C. 2002. Mitochondrial release of apoptosis-inducing factor occurs downstream of cytochrome c release in response to several proapoptotic stimuli. J. Cell Biol. 159(6):923-929

Arshavsky, V.Yu., Bownds, M.D. 1992. Regulation of deactivation of photoreceptor G protein by its target enzyme and cGMP. Nature. 357(6377):416-417

Aylward, G.W., McClellan, K.A., Thomas, R., Billson, F.A. 1989. Transient corneal changes associated with the use of gold foil electrodes. Br. J. Ophthalmol. 73(12):980-984

Bachmanov, A.A., Reed, D.R., Beauchamp, G.K. Tordoff, M.G. 2002. Food intake, water intake, and drinking spout side preference of 28 mouse strains. Behav. Genet. 32(6):435-443

Barraco, R., Adorno, D.P., Bellomonte, L., Brai, M. 2009. A study of the human rod and cone electroretinogram a-wave component. J. Stat. Mech. P03007

Beatty, S., Koh, H., Phil, M., Henson, D., Boulton, M. 2000. The role of oxidative stress in the pathogenesis of age-related macular degeneration. Surv. Ophthalmol. 45(2):115-134

Bellan, L., Buske., L. 2007. Ophthalmology human resource projections: are we heading for a crisis in the next 15 years? Can. J. Ophthalmol. 42(1):34-38

Benit, P., Goncalves, S., Dassa, E.P., Briere, J.J., Rustin, P. 2008. The variability of the harlequin mouse phenotype resembles that of human mitochondrial-complex I-deficiency syndromes. PLoS. One. 3(9):e3208

Beuerman, R.W., Pedroza, L. 1996. Ultrastructure of the human cornea. Microsc. Res. Tech. 33(4):320-335

Bhavsar, A.R., Ip, M.S., Glassman, A.R.; DRCTnet and the SCORE study groups. 2007. The risk of endophthalmitis following intravitreal triamcinolone injection in the DRCRnet and SCORE clinical trials. Am. J. Ophthalmol. 144(3):454-456

Bi, X., Chang, V., Siman, R., Tocco, G., Baudry, M. 1996. Regional distribution and time-course of calpain activation following kainate-induced seizure activity in adult rat brain. Brain Res. 726(1-2):98-108

Bisaga, A., Danysz, W., Foltin, R.W. 2008. Antagonism of glutamatergic NMDA and mGluR5 receptors decreases consumption of food in baboon model of binge-eating disorder. Eur. Neuropsychopharmacol. 18(11):794-802

Blanco, R., de la Villa, P. 1999. Ionotropic glutamate receptors in isolated horizontal cells of the rabbit retina. Eur. J. Neurosci. 11(3):867-873

Bogue, M. 2003. Mouse Phenome Project: understanding human biology through mouse genetics and genomics. J. Appl. Physiol. 95(4):1335-1337

Bonanno, J.A. 2003. Identity and regulation of ion transport mechanisms in the corneal endothelium. Prog. Retin. Eye Res. 22(1):69-94

Bourla, D.H., Young, T.A. 2006. Age-related macular degeneration: a practical approach to a challenging disease. J. Am. Geriatr. Soc. 54(7)1130-1135

Bramley, T., Peeples, P., Walt, J.G., Juhasz, M., Hansen, J.E. 2008. Impact of vision loss on costs and outcomes in medicare beneficiaries with glaucoma. Arch. Ophthalmol. 126(6):849-856

Brink, T.C., Demetrius, L., Lehrach, H., Adjaye, J. 2009. Age-related transcriptional changes in gene expression in different organs of mice support the metabolic stability theory of aging. Biogerontology. 10(5):549-564

Burr, J., Azuara-Blanco, A., Avenell, A. 2005. Medical versus surgical interventions for open angle glaucoma. Cochrane. database. syst. rev. 18(2):CD004399

Bynum, N., Poklis, J., Garside, D., Winecker, R. 2007. Postmortem memantine concentrations. J. Anal. Toxicol. 31(4):233-236

Caba, E., Brown, Q.B., Kawasaki, B., Bahr, B.A. 2002. Peptidyl alpha-keto amide inhibitor of calpain blocks excitotoxic damage without affecting signal transduction events. J. Neurosci. Res. 67(6):787-794

Cai, X., Nash, Z., Conley, S.M., Fliesler, S.J., Cooper, M.J., Naash, M.I. 2009. A partial structural and functional rescue of a retinitis pigmentosa model with compacted DNA nanoparticles. PLoS. One. 4(4):e5290

Calkins, D.J., Horner, P.J., Roberts, R., Gradianu, M., Berkowitz, B.A. 2008. Maganese-enhanced MRI of the DBA/2J mouse model of hereditary glaucoma. Invest. Ophthalmol. Vis. Sci. 49(11):5083-5088

Calvert, P.D., Govardovskii, B.I., Krasnoperova, N., Anderson, R.E., Lem, J., Makino, C.L. 2001. Membrane protein diffusion sets the speed of rod phototransduction. Nature. 411(6833):90-94

Chase, H.B. 1942. Studies on an anophthalmic strain of mice. III. results of crosses with other strains. Genetics. 27(3):339-348

Chen, C.K., Zhang, K., Church-Kopish, J., Huang, W., Zhang, H., Chen, Y.J., Frederick, J.M., Baehr, W. 2001. Characterization of human GRK7 as a potential cone opsin kinase. Mol. Vis. 7:305-313

Chen, T.Y., Illing, M., Molday, L.L., Hsu, Y.T., Yau, K.W., Molday, R.S. 1994. Subunit 2 (or beta) of retinal rod cGMP-gated cation channel is a component of the 240-kDa channel-associated protein and mediates Ca^{2+}-calmodulin modulation. Proc. Natl. Acad. Sci. U. S. A. 91(24):11757-11761

Choi, S.Y., Borghuis, B.G., Rea, R., Levitan, E.S., Sterling, P., Kramer, R.H. 2005. Encoding light intensity by the cone photoreceptor synapse. Neuron. 48(4):555-562

Craft, C.M., Whitmore, D.H., Wiechmann, A.F. 1994. Cone arrestin identified by targeting expression of a functional family. J. Biol. Chem. 269(6):4613-4619

Cruess, A., Zlateva, G., Xu, X., Rochon, S. 2007. Burden of illness of neovascular age-related macular degeneration in Canada. Can. J. Ophthalmol. 42(6):836-843

Culcasi, M., Lafon-Cazal, M., Pietri, S., Bockaert, J. 1994. Glutamate receptors induce a burst of superoxide via activation of nitric oxide synthase in arginine-depleted neurons. J. Biol. Chem. 269(17):12589-12593

Curcio, C.A., Sloan, K.R., Kalina, R.E., Hendrickson, A.E. 1990. Human photoreceptor topography. J. Comp. Neurol. 292(4):497-523

Davis, R.J., Tosi, J., Janisch, K.M., Kasanuki, J.M., Wang, N.K., Kong, J., Tsui, I., Cilluffo, M., Woodruff, M.L., Fain, G.L., Lin, C.S., Tsang, S.H. 2008. Functional rescue of degenerating photoreceptors in mice homozygous for a hypomorphic cGMP phosphodiesterase 6 b allele (Pde6bH620Q). Invest. Ophthalmol. Vis. Sci. 49(11):5067-5076

Deng, W., Wang, H., Rosenberg, P.A., Volpe, J.J., Jensen, F.E. 2004. Role of metabotropic glutamate receptors in oligodendrocyte excitotoxicity and oxidative stress. Proc. Natl. Acad. Sci. U. S. A. 101(20):7751-7756

Derouiche, A. 1996. Possible role of the Muller cell in uptake and metabolism of glutamate in the mammalian outer retina. Vision Res. 36(24):3875-3878

DeVries, S.H. 2000. Bipolar cells use kainate and AMPA receptors to filter visual information into separate channels. Neuron. 28(3):847-856

Dizhoor, A.M., Hurley, J.B. 1999. Regulation of photoreceptor membrane guanylyl cyclases by guanylyl cyclasase activator proteins. Methods. 19(4):521-531

Doan, T., Mendez, A., Detwiler, P.B., Chen, J., Rieke, F. 2006. Multiple phosphorylation sites confer reproducibility of the rod's single-photon responses. Science. 313(5786):530-533

Dohlman, C.H. 1971. The function of the corneal epithelium in health and disease. Invest. Ophthalmol. 10(6): 383-407

Dong, C.J., Guo, Y, Agey, P., Wheeler, L., Hare, W.A. 2008. Alpha2 adrenergic modulation of NMDA receptor function as a major mechanism of RGC protection in experimental glaucoma and retinal excitotoxicity. Invest. Ophthalmol. Vis. Sci. 49(10):4515-4522

Drechsel, D.A., Patel, M. 2008. Role of reactive oxygen species in the neurotoxicity of environmental agents implicated in Parkinson's disease. Free Radic. Biol. Med. 44(11):1873-1886

Duong, T.Q., Ngan, S.C., Ugurbil, K., Kim, S.G. 2002. Functional magnetic resonance imaging of the retina. Invest. Ophthalmol. Vis. Sci. 43(4):1176-81

Ebixa® Data sheet. *New Zealand Medicines and Medical Devices Safety Authority* 2009; Available at URL: http://www.medsafe.govt.nz/Profs/Datasheet/e/Ebixatabsoln.htm. Accessed: September 28, 2009

Eckmiller, M.S. 2004. Defective cone photoreceptor cytoskeleton, alignment, feedback, and energetics can lead to energy depletion in macular degeneration. Prog. Retin. Eye Res. 23(5):495-522

Economic Burden of Illness in Canada, 1998. *Public Health Agency of Canada* 2002; Available at: URL: http://www.phac-aspc.gc.ca/publicat/ebic-femc98/index.html. Accessed: August 24, 2009

Edwards, A.O., Malek, G. 2007. Molecular genetics of AMD and current animal models. Angiogenesis. 10(2):119-132

Emoto, M., Miyamoto, M., Emoto, Y., Zerrahn, J., Kaufmann, S.H. 2001. A critical role of T-cell receptor gamma/delta cells in antibacterial protection in mice early in life. Hepatology. 33(4):887-893

Fang, Y.Z., Yang, S. Wu, G. 2002. Free radicals, antioxidants, and nutrition. Nutrition. 18(10):872-879

Feilchenfeld, Z., Yucel, Y.H., Gupta, N. 2008. Oxidative injury to blood vessels and glia of the pre-laminar optic nerve head in human glaucoma. Exp. Eye Res. 87(5):409-14

Festjens, N., Vanden Berghe, T., Vandenabeele, P. 2006. Necrosis, a well-orchastrated form of cell demise: signalling cascades, important mediators and concomitant immune response. Biochim. Biophys. Acta. 1757(9-10):1371-1387

Fink, A.I., Jordan, A.J. 1984. Laser trabeculoplasty and decay effects in glaucoma patients. J. R. Soc. Med. 77(2):97-101

Fletcher, E.L., Hack, I., Brandstatter J.H., Wassle, H. 2000. Synaptic localization of NMDA receptor subunits in the rat retina. J. Comp. Neurol. 420(1):98-112

Forooghian, F., Cukras, C., Meyerle, C.B., Chew, E.Y., Wong, W.T. 2008. Evaluation of time domain and spectral domain optical coherence tomography in the measurement of diabetic macular edema. Invest. Ophthalmol. Vis. Sci. 49(10)4290-4296

Foundations for a Canadian Vision Health Strategy. *The National Coalition for Vision Health* 2007; Available at: URL: http://www.visionhealth.ca/projects/documents/Foundations-For-A-Canadian-Vision-Health-Strategy.pdf. Accessed: August 24, 2009

Gerth, C., Zawadzki, R.J., Werner, J.S., Heon, E. 2009. Detailed analysis of retinal function and morphology in a patient with autosomal recessive bestrophinopathy (ARB). Doc. Ophthalmol. 118(3):239-246

Goodman, Y., Bruce, A.J., Cheng, B., Mattson, M.P. 1996. Estrogens attenuate and corticosterone exacerbates excitotoxicity, oxidative injury, and amyloid beta-peptide toxicity in hippocampal neurons.. J. Neurochem. 66(5):1836-1844

Gordon, M.K., Foley, J.W., Birk, D.E., Fitch, J.M., Linsenmayer, T.F. 1994. Type V collagen and Bowman's membrane. Quantification of mRNA in corneal epithelium and stroma. J. Biol. Chem. 269(40):24959-24966

Green, D.G., Kapousta-Bruneau, N.V., Hitchcock, P.F., Keller, S.A. 1997. Electrophysiology and density of retinal neurons in mice with a mutation that includes the Pax2 locus. Invest. Ophthalmol. Vis. Sci. 38(5):919-929

Grieve, K., Paques, M., Dubois, A., Sahel, J., Boccara, C., Le Gargasson, J.F. 2004. Ocular tissue imaging using ultrahigh-resolution, full field optical coherence tomography. Invest. Ophthalmol. Vis. Sci. 45(11):4126-4131

Guttmann, R.P., Sokol, S., Baker, D.L., Simpkins, K.L., Dong, Y., Lynch, D.R. 2002. Proteolysis of the N-methyl-d-aspartate receptor by calpain in situ. J. Pharmacol. Exp. Ther. 302(3):1023-1030

Hare, W.A., WoldeMussie, E., Lai, R.K., Ton, H., Ruiz, G., Chun, T., Wheeler, L. 2004. Efficacy and safety of memantine treatment for reduction of changes associated with experimental glaucoma in monkey, I: Functional measures. Invest. Ophthalmol. Vis. Sci. 45(8):2625-2639

Harlow, M.L., Ress, D., Stoschek, A., Marshall, R.M., McMahan, U.J. 2001. The architecture of active zone material at the frog's neuromuscular junction. Nature. 409(6819):479-484

Harman, D. 1956. Aging: a theory based on free radical and radiation chemistry. J. Gerontol. 11(3):298-300

Hartveit, E., Veruki, M.L. 1997. AII amacrine cells express functional NMDA receptors. Neuroreport. 8(5):1219-1223

Hashizume, K., Hirasawa, M., Imamura, Y., Noda, S., Shimizu, T., Shinoda, K., Kurihara, T., Noda, K., Ozawa, Y., Ishida, S., Miyake, Y., Shirasawa, T., Tsubota, K. 2008. Retinal dysfunction and progressive retinal cell death in SOD1-deficient mice. Am. J. Pathol. 172(5):1325-1331

Hausmann, O.N., Fouad, K., Wallimann, T., Schwab, M.E. 2002. Protective effects of oral creatine supplementation on spinal cord injury in rats. Spinal Cord. 40(9):449-456

Haverkamp, S., Grunert, U., Wassle, H. 2001. The synaptic architecture of AMPA receptors at the cone pedicle of the primate retina. J. Neurosci. 21(7):2488-2500

Hayreh, S.S. 1975. Segmental nature of choroidal vasculature. Br. J. Ophthalmol. 59(11):631-648

Heiduschka, P., Fietz, H., Hofmeister, S., Schultheiss, S., Mack, A.F., Peters, S., Ziemssen, F., Niggemann, B., Julien, S., Bartz-Schmidt, K.U., Schraermeyer, U. 2007. Penetration of bevacizumab through the retina after intravitreal injection in the monkey. Invest. Ophthalmol. Vis. Sci. 48(6):2814-2823

Hermanussen, M., Tresguerres, J.A. 2005. A new anti-obesity drug treatment: first clinical evidence that, antagonising glutamate-gated Ca^{2+} ion channels with memantine normalises binge-eating disorders. Econ. Hum. Biol. 3(2):329-337

Heynen, H., van Norren, D. 1985. Origin of the electroretinogram in the intact macaque eye--I. Principal component analysis. Vision Res. 25(5):697-707

Hoang, Q.V., Linsenmeier, R.A., Chung, C.K., Curcio, C.A. 2002. Photoreceptor inner segments in monkey and human retina: mitochondrial density, optics, and regional variation. Vis. Neurosci. 19(4):395-407

Imamura, Y., Noda, S., Hashizume, K., Shinoda, K., Yamaguchi, M., Uchiyama, S., Shimizu, T., Mizushima, Y., Shirasawa, T., Tsubota, K. 2006. Drusen, choroidal neovascularization, and retinal pigment epithelium dysfunction in SOD1-deficient mice: a model of age-related macular degeneration. Proc. Natl. Acad. Sci. U. S. A. 103(30):11282-11287

Ishida, T., Kamei, C. 2009. Characteristic effects of anti-dementia drugs on rat sleep patterns. J. Pharmacol. Sci. 109(3):449-455

Ishii, K., Tomidokoro, A., Nagahara, M., Tamaki, Y., Kanno, M., Fukaya, Y., Araie, M. 2001. Effects of topical latanoprost on optic nerve head circulation in rabbits, monkeys, and humans. Invest. Ophthalmol. Vis. Sci. 42(12):2957-2963

Izzotti, A., Sacca, S.C., Cartiglia, C., De Flora, S. 2003. Oxidative deoxyribonucleic acid damage in the eyes of glaucoma patients. Am. J. Med. 114(8):638-646

Jacobus, W.E., Diffley, D.M. 1986. Creatine kinase of heart mitochondria. Control of oxidative phosphorylation by the extramitochondrial concentrations of creatine and phosphocreatine. J. Biol. Chem. 261(35):16579-16583

Jaffe, D.B., Brown, T.H. 1994. Metabotropic glutamate receptor activation induces calcium waves within hippocampal dendrites. J. Neurophysiol. 72(1):471-474

Janssen, A.J., Trijbels, F.J., Sengers, R.C., Smeitink, J.A., van den Heuvel, L.P., Wintjes, L.T., Stoltenborg-Hogenkamp, B.J., Rodenburg, R.J. 2007. Spectrophotometric assay for complex I of the respiratory chain in tissue samples and cultured fibroblasts. Clin. Chem. 53(4):729-734

Jarvis, B., Figgitt, D.P. 2003. Memantine. Drugs Aging. 20(6):465-476

Joos, K.M., Kay, M.D., Pillunat, L.E., Harris, A., Gendron, E.K., Feuer, W.J., Steinwand, B.E. 1999. Effect of acute intraocular pressure changes on short posterior ciliary artery haemodynamics. Br. J. Ophthalmol. 83(1):33-38

Kamermans, M., Spekreijse, H. 1999. The feedback pathway from horizontal cells to cones. A mini review with a look ahead. Vision Res. 39(15):2449-2468

Karan, G., Lillo, C., Yang, Z., Cameron, D.J., Locke, K.G., Zhao, Y., Thirumalaichary, S., Li, C., Birch, D.G., Vollmer-Snarr, H.R., Williams, D.S., Zhang, K. 2005. Lipofuscin accumulation, abnormal electrophysiology, and photoreceptor degeneration in mutant ELOVL4 transgenic mice: a model for macular degeneration. Proc. Natl. Acad. Sci. U. S. A. 102(11):4164-4169

Kim, E.Y., Kim, J.W., Kim, J.B., Lew, H.M. 2009. Serous retinal detachment following combined photodynamic therapy and intravitreal bevacizumab injection. Korean J. Ophthalmol. 23(2):124-126

Klein, J.A., Longo-Guess, C.M., Rossmann, M.P., Seburn, K.L., Hurd, R.E., Frankel, W.N., Bronson, R.T., Ackerman, S.L. 2002. The harlequin mouse mutation downregulates apoptosis-inducing factor. Nature. 419(6905):367-374

Komeima, K., Usui, S., Shen, J., Rogers, B.S., Campochiaro, P.A. 2008. Blockade of neuronal nitric oxide synthase reduces cone cell death in a model of retinitis pigmentosa. Free. Radic. Biol. Med. 45(6):905-912

Kourlas, H., Abrams P. 2007. Ranibizumab for the treatment of neovascular age-related macular degeneration. Clin. Ther. 29(9):1850-1861

Kreft. M., Krizaj, D., Grilc, S., Zorec, R. 2003. Properties of exocytotic response in vertebrate photoreceptors. J. Neurophysiol. 90(1):218-225

Kruman, I.I., Pederson, W.A., Springer, J.E., Mattson, M.P. 1999. ALS-linked Cu/Zn-SOD mutation increases vulnerability of motor neurons to excitotoxicity by a mechanism involving increased oxidative stress and perturbed calcium homeostasis. Exp. Neurol. 160(1):28-39

Kusari, J., Zhou, S., Padillo, E., Clarke, K.G., Gil, D.W. 2007. Effect of memantine on neuroretinal function and retinal vascular changes of streptozotocin-induced diabetic rats. Invest. Ophthalmol. Vis. Sci. 48(11):5152-5159

Kwok, M.C., Holopainen, J.M., Molday, L.L., Foster, L.J., Molday, R.S. 2008. Proteomics of photoreceptor outer segments identifies a subset of SNARE and Rab proteins implicated in membrane vesicle trafficking and fusion. Mol. Cell Proteomics. 7(6):1053-1066

LaVail, M.M. 1981. Analysis of neurological mutants with inherited retinal degeneration. Friedenwald lecture. Invest. Ophthalmol. Vis. Sci. 21(5):638-657

Lamb, T.D., Collin, S.P., Pugh, E.N. 2007. Evolution of the vertebrate eye: opsins, photoreceptors, retina and eye cup. Nat. Rev. Neurosci. 8(12):960-976

Leamey, C.A., Protti, D.A., Dreher, B. (2008). Comparative survey of the mammalian visual system with reference to the mouse. In Chalupa, L.M., Williams, R.W., Eye, Retina, and Visual System of the Mouse. Cambridge, MA: The MIT Press

Lehman, B.M., Berntsen, D.A., Bailey, M.D., Zadnik, K. 2009. Validation of optical coherence tomography-based crystalline lens thickness measurements in children. Optom. Vis. Sci. 86(3):181-187

Leist, M., Volbracht, C., Kuhnle, S., Fava, E., Ferrando-May, E., Nicotera, P. 1997. Caspase-mediated apoptosis in neuronal excitotoxicity triggered by nitric oxide. Mol. Med. 3(11):750-764

Leskov, I.B., Klenchin, V.A., Handy, J.W., Whitlock, G.G., Govardovskii, V.I., Bownds, M.D., Lamb, T.D., Pugh, E.N. Jr., Arshavsky, V.Y. 2000. The gain of rod phototransduction: reconciliation of biochemical and electrophysiological measurements. Neuron. 27(3):525-537

Liang, H., Baudouin, C., Pauly, A., Brignole-Baudouin, F. 2008. Conjunctival and corneal reactions in rabbits following short- and repeated exposure to preservative-free tafluprost, commercially available latanoprost and 0.02% benzalkonium chloride. Br. J. Ophthalmol. 92(9):1275-1282

Libby, R.T., Howell, G.R., Pang, I.H., Savinova, O.V., Mehalow, A.K., Barter, J.W., Smith, R.S., Clark, A.F., John, S.W. 2007. Inducible nitric oxide synthase, Nos2, does not mediate optic neuropathy and retinopahthy in the DBA/2J glaucoma model. BMC Neurosci. 8:108

Li, F., Marchette, L.D., Brush, R.S., Elliott, M.H., Le, Y.Z., Henry, K.A., Anderson, A.G., Zhao, C., Sun, X., Zhang, K., Anderson, R.E. 2009. DHA does not protect ELOVL4 transgenic mice from retinal degeneration. Mol. Vis. 15:1185-1193

Lipton, S.A. 2004. Failures and successes of NMDA receptor antagonists: molecular basis for the use of open-channel blockers like memantine in the treatment of acute and chronic neurologic insults. NeuroRx. 1(1):101-110

Lovicu, F.J., McAvoy, J.W. 2005. Growth factor regulation of lens development. Dev. Biol. 280(1):1-14

Lucas, D.R., Newhouse, J.P. 1957. The toxic effect of sodium L-glutamate on the inner layers of the retina. AMA Arch. Ophthalmol. 58(2):193-201

Lukas, T.J., Wang, A.L., Yuan, M., Neufeld, A.H. 2009. Early cellular signaling responses to axonal injury. Cell Commun. Signal. 7:5

Lund, R. 2008. Cell-based therapies to limit photoreceptor degeneration. Arch. Soc. Esp. Oftalmol. 83(8):457:464

Mali, R.S., Cheng, M., Chintala., S.K. 2005. Plasminogen activators promote excitotoxicity-induced retinal damage. FASEB J. 19(10):1280-1289

Marklund, S.L., Westman, N.G., Lundgren, E., Roos, G. 1982. Copper- and zinc-containing superoxide dismutase, manganese-containing superoxide dismutase, catalase, and glutathione peroxidase in normal and neoplastic human cell lines and normal human tissues. Cancer Res. 42(5):1955-1961

Marmor, M.F., Choi, S.S., Zawadzki, R.J., Werner, J.S. 2008. Visual insignificance of the foveal pit: reassessment of foveal hypoplasia as fovea plana. Arch. Ophthalmol. 126(7):907-913

Marmorstein, A.D., Marmorstein, L.Y., Sakaguchi, H., Hollyfield, J.G. 2002. Spectral profiling of autofluorescence associated with lipofuscin, Bruch's Membrane, and sub-RPE deposits in normal and AMD eyes. Invest. Ophthalmol. Vis. Sci. 43(7):2435-2441

Marti, A., Hafezi, F., Lansel, N., Hegi, M.E., Wenzel, A., Grimm, C., Niemeyer, G., Reme, C.E. 1998. Light-induced cell death of retinal photoreceptors in the absence of p53. Invest. Ophthalmol. Vis. Sci. 29(5):846-849

Martin, R., de Juan, V., Rodriguez, G., Cuadrado, R., Fernandez, I. 2007. Measurement of corneal swelling variations without removal of the contact lens during extended wear. Invest. Ophthalmol. Vis. Sci. 48(7):3043-3050

Mattson, M.P. 1997. Cellular actions of beta-amyloid precursor protein and its soluble and fibrillogenic derivatives. Physiol. Rev. 77(4):1081-132

Mattson, M.P., Zhu, H., Yu, J., Kindy, M.S. 2000. Presenilin-1 mutation increases neuronal vulnerability to focal ischemia in vivo and to hypoxia and glucose deprivation in cell culture: involvement of perturbed calcium homeostasis. J. Neurosci. 20(4):1358-1364

McAvoy, J.W. 1978. Cell division, cell elongation and distribution of alpha-, beta- and gamma-crystallins in the rat lens. J. Embryol. Exp. Morphol. 44:149-165

Meek, K.M., Leonard, D.W. 1993. Ultrastructure of the corneal stroma: a comparative study. Biophys. J. 64(1):273-280

Memarzadeh, F., Tang, M., Li, Y., Chopra, V., Francis, B.A., Huang, D. 2007. Optical coherence tomography assessment of angle anatomy changes after cataract surgery. Am. J. Ophthalmol. 144(3):464-465

Mennerick, S., Matthews, G. 1996. Ultrafast exocytosis elicited by calcium current in synaptic terminals of retinal bipolar neurons. Neuron. 17(6):1241-1249

Miceli, M.V., Jazwinski, S.M. 2005. Nuclear gene expression changes due to mitochondrial dysfunction in ARPE-19 cells: implications for age-related macular degeneration. Invest. Ophthalmol. Vis. Sci. 46(5):1765-1773

Michalova, K., Wickremasinghe, S.S., Tan, T.H., Chang, A., Harper, C.A., Downie, J.A., Hunyor, A.P., Guymer, R.H. 2009. Ranibizumab treatment for neovascular age-related macular degeneration: from randomized trials to clinical practice. Eye. 23(8):1633-1640

Mills, G.C. 1960. Glutathione peroxidase and the destruction of hydrogen peroxide in animal tissues. Arch. Biochem. Biophys. 86:1-5

Minkeviciene, R., Banerjee, P., Tanila, H. 2004. Memantine improves spatial learning in a transgenic mouse model of Alzheimer's disease. J. Pharmacol. Exp. Ther. 311(2):677-682

Mittman, S., Taylor, W.R., Copenhagen, D.R. 1990. Concomitant activation of two types of glutamate receptor mediates excitation of salamander retinal ganglion cells. J. Physiol. 428:175-197

Mizota, A., Adachi-Usami, E. 2002. Effect of body temperature on electroretinogram of mice. Invest. Ophthalmol. Vis. Sci. 43(12):3754-3757

Mohamed, S., Lee, G.K., Rao, S.K., Wong, A.L., Cheng, A.C., Li, E.Y., Chi, S.C., Lam, D.S. 2007. Repeatability and reproducibility of pachymetric mapping with Visante anterior segment-optical coherence tomography. Inevest. Ophthalmol. Vis. Sci. 48(12):5499-5504

Monastero, R., Camarda, C., Pipia, C., Camarda, R. 2007. Visual hallucinations and agitation in Alzheimer's disease due to memantine: report of three cases. J. Neurol. Nuerosurg. Psychiatry. 78(5): 546

Monteiro, M.L., Cunha, L.P., Vessani, R.M. 2008. Comparison of retinal nerve fiber layer measurements using Sratus OCT fast and regular scan protocols in eyes with band atrophy of the optic nerve and normal controls. Arg. Bras. Ofthalmo. 71(4):534-539

Morrison, J.C., Fraunfelder, F.W., Milne, S.T., Moore, C.G. 1995. Limbal microvasculature of the rat eye. Invest. Ophthalmol. Vis. Sci. 36(3):751-756

Ng, E.W., Adamis, A,P. 2005. Targeting angiogenesis, the underlying disorder in neovascular age-related macular degeneration. Can. J. Ophthalmol. 40(3):352-368

Nikonov, S.S., Kholodenko, R., Lem, J., Pugh, E.N. Jr. 2006. Physiological features of the S- and M-cone photoreceptors of wild-type mice from single-cell recordings. J. Gen. Physiol. 127(4):359-374

Nushinowitz, S., Ridder, W.3rd., Heckenlively, J.R. (2002). Electrophysiological testing of the mouse visual system. In Smith R.S., John, S.W.M., Nishina, P.M., Sundberg, J.P, Systematic Evaluation of the Mouse Eye: Anatomy, Pathology, and Biomethods. Boca Raton, Fl: CRC Press

Obernier, J.A., Bouldin, T.W., Crews, F.T. 2002. Binge ethanol exposure in adult rats causes necrotic cell death. Alcohol. Clin. Exp. Res. 26(4):547-557

Ohia, S.E., Opere, C.A., Leday, A.M. 2005. Pharmacological consequences of oxidative stress in ocular tissues. Mutat. Res. 579(1-2):22-36

Okada, T., Ernst, O.P., Palczewski, K., Hofmann, K.P. 2001. Activation of rhodopsin: new insights from structural and biochemical studies. Trends Biochem. Sci. 26(5):318-24

Olney, J.W. 1969. Brain lesions, obesity, and other disturbances in mice treated with monosodium glutamate. Science. 164(880):719-721

Osborne, N.N., Chidlow, G., Nash, M.S., Wood, J.P. 1999. The potential of neuroprotection in glaucoma treatment. Curr. Opin. Ophthalmol. 10(2):82-92

Paglia, M.J., Mou, H., Cote, R.H. 2002. Regulation of photoreceptor phosphodiesterase (PDE6) by phosphorylation of its inhibitory gamma subunit re-evaluated. J. Biol. Chem. 277(7):5017-5023

Palczewski, K., Saari, J.C. 1997. Activation and inactivation steps in the visual transduction pathway. Curr. Opin. Neurobiol. 7(4):500-504

Parmeggiani, F., Costagliola, C., Gemmati, D., D'Angelo, S., Perri, P., Campa, C., Catozzi, L., Federici, F., Sebastiani, A., Incorvaia, C. 2008. Coagulation gene predictors of photodynamic therapy for occult choroidal neovascularization in age-related macular degeneration. Invest. Ophthalmol. Vis. Sci. 49(7):3100-3106

Pauleikhoff, D. 2005. Neovascular age-related macular degeneration: natural history and treatment outcomes. Retina. 25(8):1065-1084

Pelucchi, B., Grimaldi, A., Moriondo, A. 2008. Vertebrate rod photoreceptors express both BK and IK calcium-activated potassium channels, but only BK channels are involved in receptor potential regulation. J. Neurosci. Res. 86(1):194-201

Pertovaara, A., Haapalinna, A., Sirvio, J., Virtanen, R. 2005. Pharmacological properties, central nervous system effects, and potential therapeutic applications of atipamezole, a selective alpha2-adrenoceptor antagonist. CNS Drug Rev. 11(3):273-288

Philp, N.J., Ochrietor, J.D., Rudoy, C., Muramatsu, T., Linser, P.J. 2003. Loss of MCT1, MCT3, and MCT4 expression in the retinal pigment epithelium and neural retina of the 5A11/basigin-null mouse. Invest. Ophthalmol. Vis. Sci. 44(3):1305-1311

Piegorsch, W.W., Margolin, B.H., Shelby, M.D., Johnson, A., French, J.E., Tennant, R.W., Tindall, K.R. 1995. Study design and sample sizes for a lacI transgenic mouse mutation assay. Environ. Mol. Mutagen. 25(3):231-245

Pinilla, I., Lund, R.D., Lu, B., Sauve, Y. 2005. Measuring the cone contribution to the ERG b-wave to assess function and predict anatomical rescue in RCS rats. Vision Res. 45(5):635-641

Population Projections for Canada, Provinces and Territories. *Statistics Canada* 2005; Available at: URL: http://www.statcan.ca/english/freepub/91-520-XIE/0010591-520-XIE.pdf. Accessed: August 24, 2009

Porter, A.G., Urbano, A.G. 2006. Does apoptosis-inducing factor (AIF) have both life and death functions in cells? Bioessays. 28(8):834-843

Radhakrishnan, S., See, J., Smith, S.D., Nolan, W.P., Ce, Z., Friedman, D.S., Huang, D., Li, Y., Aung, T., Chew, P.T. 2007. Reproducibility of anterior chamber angle measurements obtained with anterior segment optical coherence tomography. Invest. Ophthalmol. Vis. Sci. 48(8):3683-3688

Radu, R.A., Hu, J., Peng, J., Bok, D., Mata, N.L., Travis, G.H. 2008. Retinal pigment epithelium-retinal G protein receptor-opsin mediates light-dependent translocation of all-trans-retinyl esters for synthesis of visual chromophore in retinal pigment epithelial cells. J. Biol. Chem. 283(28):19730-19738

Rao, R., Buchsbaum, G., Sterling, P. 1994. Rate of quantal transmitter release at the mammalian rod synapse. Biophys. J. 67(1):57-63

Raviola, E., Gilula, N.B. 1975. Intramembrane organization of specialized contacts in the outer plexiform layer of the retina. A freeze-fracture study in monkeys and rabbits. J. Cell. Biol. 65(1):192-222.

Raymond, S.M., Jackson, I.J. 1995. The retinal pigmented epithelium is required for development and maintenance of the mouse neural retina. Curr. Biol. 5(11):1286-1295

Razvi, E.S., Welsh, R.M. 1993. Programmed cell death of T lymphocytes during acute viral infection: a mechanism for virus-induced immune deficiency. J. Virol. 67(10):5754-5765

Rea, R., Li, J., Dharia, A., Levitan, E.S., Sterling, P., Kramer, R.H. 2004. Streamlined synaptic vesicle cycle in cone photoreceptor terminals. Neuron. 41(5):755-766

Rego, A.C., Monteiro, N.M., Silva, A.P., Gil, J., Malva, J.O., Oliveira, C.R. 2003. Mitochondrial apoptotic cell death and moderate superoxide generation upon selective activation of non-desensitizing receptors in hippocampal cultures. J. Neurochem. 86(4):792-804

Rey, S.M., Povazay, B., Hofer, B., Unterhuber, A., Hermann, B., Harwood, A., Drexler, W. 2009. Three- and four-dimensional visualization of cell migration using optical coherence tomography. J. Biophotonics. 2(6-7):370-379

Ridder, W.3rd., Nusinowitz, S., Heckenlively, J.R. 2002. Causes of cataract development in anesthetized mice. Exp. Eye Res. 75(3):365-370

Riemer, C., Burwinkel, M., Schwarz, A., Gultner, S., Mok, S.W., Heise, I., Holtkamp, N., Baier, M. 2008. Evaluation of drugs for treatment of prion infections of the central nervous system. J. Gen. Virol. 89:594-597

Rizzolo, L.J., Chen, X., Weitzman, M., Sun, R., Zhang, H. 2007. Analysis of the RPE transcriptome reveals dynamic changes during the development of the outer blood-retinal barrier. Mol. Vis. 13:1259-1273

Rogawski, M.A., Wenk, G.L. 2003. The neuropharmacological basis for the use of memantine in the treatment of Alzheimer's disease. CNS Drug Rev. 9(3):275-308

Roman, A.J., Boye, S.L., Aleman, T.S., Pang, J.J., McDowell, J.H., Boye, S.E., Cideciyan, A.V., Jacobson, S.G., Hauswirth, W.W. 2007. Electroretinographic analyses of Rpe65-mutant rd12 mice: developing an *in vivo* bioassay for human gene therapy trials of Lever congenital amaurosis. Mol. Vis. 13:1701-1710

Roska, B., Werblin, F. 2001. Vertical interactions across ten parallel, stacked representation in the mammalian retina. Nature. 410(6828):583-587

Rubin, M.L., Dawson, W.W. 1978. The transscleral VER: prediction of postoperative acuity. Invest. Ophthalmol. Vis. Sci. 17(1):71-74

Ruether, K., van de Pol, D., Jaissle, G., Berger, W., Tornow, R.P., Zrenner, E. 1997. Retinoschisislike alterations in the mouse eye caused by gene targeting of the Norrie disease gene. Invest. Ophthalmol. Vis. Sci. 38(3):710-718

Sagong, M., Kim, J., Chang, W. 2009. Intravitreal bevacizumab for the treatment of neovascular glaucoma associated with central retinal artery occlusion. Korean J. Ophthalmol. 23(3):215-218

Sakata, L.M., Lavanya, R., Friedman, D.S., Aung, H.T., Gao, H., Kuman, R.S., Foster, P.J., Aung, T. 2008. Comparison of gonioscopy and anterior segment ocular coherence tomography in detecting angle closure in different quadrants of the anterior chamber angle. Ophthalmology. 115(5):769-774

Saks, V.A., Kupriyanov, V.V., Elizarova, G.V., Jacobus, W.E. 1980. Studies of energy transport in heart cells. The importance of creatine kinase localization for the coupling of mitochondrial phosphorylcreatine production to oxidative phosphorylation. J. Biol. Chem. 255(2):755-763

Sardar, D.K., Swanland, G.Y., Yow, R.M., Thomas, R.J., Tsin, A.T. 2007. Optical properties of ocular tissues in the near infrared region. Lasers Med. Sci. 22(1):46-52

Sayre, L.M., Smith, M.A., Perry, G. 2001. Chemistry and biochemistry of oxidative stress in neurodegenerative disease. Curr. Med. Chem. 8(7):721-738

Schermer, A., Galvin, S., Sun, T.T. 1986. Differentiation-related expression of a major 64K corneal keratin in vivo and in culture suggests limbal location of corneal epithelial stem cells. J. Cell Biol. 103(1):49-62

Schlamp, C.L., Li, Y., Dietz, J.A., Janssen, K.T., Nickells, R.W. 2006. Progressive ganglion cell loss and optic nerve degeneration in DBA/2J mice is variable and asymmetric. BMC Neurosci. 7:66

Schneider, L.S., Sano, M. 2009. Current Alzheimer's disease clinical trials: methods and placebo outcomes. Alzheimers Dement. 5(5):388-397

Schweitzer, K.D., Ehmann, D., Garcia, R. 2009. Nerve fibre layer changes in highly myopic eyes by optical coherence tomography. Can. J. Ophthalmol. 44(3):e13-e16.

Seeliger, M.W., Narfstrom, K., Reinhard, J., Zrenner, E., Sutter, E. 2000. Continuous monitoring of the stimulated area in multifocal ERG. Doc. Ophthalmol. 100(2-3):167-184

Sengpiel, B., Preis, E., Krieglstein, J., Prehn, J.H. 1998. NMDA-induced superoxide production and neurotoxicity in cultured rat hippocampal neurons: role of mitochondria. Eur. J. Neurosci. 10(5)1903-1910

Sharts-Hopko, N.C., Glynn-Milley, C. 2009. Primary open-angle glaucoma. Am. J. Nurs. 109(2):40-47

Shigenaga, M.K., Hagen, T.M., Ames, B.N. 1994. Oxidative damage and mitochondrial decay in aging. Proc. Natl. Acad. Sci. U. S. A. 91(23):10771-10778

Shimoyama, M., Shimoyama, N., Inturrisi, C.E., Elliott, K. 1997. Oral ketamine produces a dose-dependent CNS depression in the rat. Life Sci. 60(1):9-14

Shin, E.J., Jeong, J.H., Kim, A.Y., Koh, Y.H., Nah, S.Y., Kim, W.K., Ko, K.H., Kim, H.J., Wie, M.B., Kwon, Y.S., Yoneda, Y., Kim, H.C. 2009. Protection against kainate neurotoxicity by Ginsenosides: attenuation of convulsive behavior, mitochondrial dysfunction, and oxidative stress. J. Neurosci. Res. 87(3):710-722

Sieck, G.C. 2003. Genetic models in applied physiology. J. Appl. Physiol. 94(4):1295-1296

Si, Y.J., Kishi, S., Aoyagi, K. 1999. Assessment of macular function by multifocal electroretinogram before and after macular hole surgery. Br. J. Ophthalmol. 83(4):420-424

Skott, O. 2003. Angiotensin II and control of sodium and water intake in the mouse. Am. J. Physiol. Regul. Integr. Comp. Physiol. 284(6):R1380-1381

Smaili, S., Hirata, H., Ureshino, R., Monteforte, P.T., Morales, A.P., Muler, M.L., Terashima, J., Oseki, K., Rosenstock, T.R., Lopes, G.S., Bincoletto, C. 2009. Calcium and cell death signaling in neurodegeneration and aging. An. Acad. Bras. Cienc. 81(3):467-475

Smith, R.S., Sundberg, J.P. 1995. Inbred C57 black mice: Microophthalmia and ocular infections. JAX® Notes. 463. Available at: URL: http://jaxmice.jax.org/jaxnotes/ archive/ 463a.html. Accessed: September 28th, 2009

Smith, R.S., Sundberg, J.P., John, S.W.M. (2002a). The Anterior Segment and Ocular Adnexae. In Smith R.S., John, S.W.M., Nishina, P.M., Sundberg, J.P, Systematic Evaluation of the Mouse Eye: Anatomy, Pathology, and Biomethods. Boca Raton, Fl: CRC Press

Smith, R.S., Sundberg, J.P., John, S.W.M. (2002b). The Anterior Segment. In Smith R.S., John, S.W.M., Nishina, P.M., Sundberg, J.P, Systematic Evaluation of the Mouse Eye: Anatomy, Pathology, and Biomethods. Boca Raton, Fl: CRC Press

Smith, R.S., John, S.W.M., Nishina, P.M. (2002c). Posterior segment and orbit. In Smith R.S., John, S.W.M., Nishina, P.M., Sundberg, J.P, Systematic Evaluation of the Mouse Eye: Anatomy, Pathology, and Biomethods. Boca Raton, Fl: CRC Press

Snellman, J., Kaur, T., Shen, Y., Nawy, S. 2008. Regulation of ON bipolar cell activity. Prog. Retin. Eye. Res. 27(4):450-463

Sonsalla, P.K., Albers, D.S., Zeevalk, G.D. 1998. Role of glutamate in neurodegeneration of dopamine neurons in several animal models of parkinsonism. Amino Acids. 14(1-3):69-74

Srinivasan, M., Lalitha, P., Mahalakshmi, R., Pragna, N.V., Mascarenhas, J., Chidambaram, J.D., Lee, S., Hong, K.C., Zegans, M., Glidden, D.V., McLeod, S., Whitcher, J.P., Lietman, T.M., Acharaya, N.R. 2009. Corticosteroids for bacterial corneal ulcers. Br. J. Ophthalmol. 93(2):198-202

Srivastava, S., Banerjee, H., Chaudhry, A., Khare, A., Sarin, A., George, A., Bal, V., Durdik, J.M., Rath, S. 2007. Apoptosis-inducing factor regulates death in peripheral T cells. J. immunol. 179(2):797-803

Starke-Reed, P.E., Oliver, C.N. 1989. Protein oxidation and proteolysis during aging and oxidative stress. Arch. Biochem. Biophys. 275(2):559-567

Steigerwalt, R.D., Gianni, B., Paolo, M., Bombardelli, E., Burki, C., Schonlau, F. 2008. Effects of Mirtogenol on ocular blood flow and intraocular hypertension in asymptomatic subjects. Mol. Vis. 14:1288-1292

Sterling, P. (2004). How retinal circuits optimize the transfer of visual information. In Chalupa, L.M., Werner, J.S., The Visual Neurosciences: Volume 1. Cambridge, MA: The MIT Press

Stone, R.A., Quinn, G.E., Francis, E.L., Ying, G.S., Flitcroft, D.I., Parekh, P., Brown, J., Orlow, J., Schmid, G. 2004. Diurnal axial length fluctuations in human eyes. Invest. Ophthalmol. Vis. Sci. 45(1):63-70

St-Pierre, J., Buckingham, J.A., Roebuck, S.J., Brand, M.D. 2002. Topology of superoxide production from different sites in the mitochondrial electron transport chain. J. Biol. Chem. 277(47):44784-44790

Strauss, O. 2005. The retinal pigment epithelium in visual function. Physiol. Rev. 85(3):845-881

Stringer, J.R., Larson, J.S., Fischer, J.M., Stringer, S.L. 2004. Increased mutation in mice genetically predisposed to oxidative damage in the brain. Mutat. Res. 556(1-2):127-134

Susin, S.A., Lorenzo, H.K., Zamzami, N., Marzo, I., Snow, B.E., Brothers, G.M., Mangion, J., Jacotot, E., Costantini, P., Loeffler, M., Larochette, N., Goodlett, D.R., Aebersold, R., Siderovski, D.P., Penninger, J.M., Kroemer, G. 1999. Molecular characterization of mitochondrial apoptosis-inducing factor. Nature. 397(6718):441-446

Tachibana, M., Okada, T. 1991. Release of endogenous excitatory amino acids from ON-type bipolar cells isolated from the goldfish retina. J. Neurosci. 11(7):2199-2208

Takimoto, E., Champion, H.C., Li, M., Ren, S., Rodriguez, E.R., Tavazzi, B., Lazzarino, G., Paolocci, N., Gabrielson, K.L., Wang, Y., Kass, D.A. 2005. Oxidant stress from nitric oxide synthase-3 uncoupling stimulates cardiac pathologic remodeling from chronic pressure load. J. Clin. Invest. 115(5):1221-1231

Tchedre, K.T., Yorio, T. 2008. Sigma-1 receptors protect RGC-5 cells from apoptosis by regulating intracellular calcium, Bax levels, and caspase-3 activation. Invest. Ophthalmol Vis Sci. 49(6):2577-2588

Trifunovic, A., Hansson, A., Wredenberg, A., Rovio, A.T., Dufour, E., Khvorostov, I., Spelbrink, J.N., Wibom, R., Jacobs, H.T., Larsson, N.G. 2005. Somatic mtDNA mutations cause aging phenotypes without affecting reactive oxygen species production. Proc. Natl. Acad. Sci. U. S. A. 102(50):17993-17998

Tsukamoto, Y., Morigiwa, K., Ueda, M., Sterling, P. 2001. Microcircuits for night vision in mouse retina. J. Neurosci. 21(21):8616-8623

Tuo, J., Bojanowski, C.M., Zhou, M., Shen, D., Ross, R.J. Rosenberg, K.I., Cameron, D.J., Yin, C., Kowalak, J.A., Zhuang, Z., Zhang, K., Chan, C.C. 2007. Murine ccl2/cx3cr1 deficiency results in retinal lesions mimicking human age-related macular degeneration. Invest. Ophthalmol. Vis. Sci. 48(8):3827-3826

Vahsen, N., Cande, C., Briere, J.J., Benit, P., Joza, N., Larochette, N., Mastroberardino, P.G., Pequignot, M.O., Casares, N., Laxar, V., Ferauid, O., Debili, N., Wissing S., Engelhardt, S., Madeo, F., Piacentini, M., Penninger, J.M., Schagger, H., Rustin, P., Kroemer, G. 2004. AIF deficiency compromises oxidative phosphorylation. EMBO J. 23(23):4679-4689

Vaishnav, R.A., Getchell, M.L., Huang, L., Hersh, M.A., Stromberg, A.J., Getchell, T.V. 2008. Cellular and molecular characterization of oxidative stress in olfactory epithelium of the harlequin mutant mouse. J. Neurosci. Res. 86(1):165-182

van Empel, V.P., Bertrand, A.T., van der Nagel, R., Kostin, S., Doeyendans, P.A., Crijns, H.J., de Wit, E., Sluiter, W., Ackerman, S.L., De Windt, L.J. 2005. Downregulation of apoptosis-inducing factor in harlequin mutant mice sensitizes the myocardium to oxidative stress-related cell death and pressure overload-induced decompensation. Circ. Res. 96(12):e92-e101

van Empel, V.P., Vertrand, A.T., can Oort, R.J., can der Nagel, R., Engelen, M., can Rijen, H.C., Doevendans, P.A., Crijns, H.J., Ackerman, S.L, Sluiter, W., De Windt, L.J. 2006. EUK-8, a superoxide dismutase and catalase mimetic, reduces cardiac oxidative stress and ameliorates pressure overload-induced heart failure in the harlequin mouse mutant. J. Am. Coll. Cardiol. 48(4):824-832

Vermulst, M., Bielas, J.H., Loeb, L.A. 2008. Quantification of random mutations in the mitochondrial genome. Methods. 46(4):263-268

Villoslada, P., Arrondo, G., Sepulcre, J., Alegre, M., Artieda, J. 2009. Memantine induces reversible neurologic impairment in patients with MS. Neurology. 72(19):1630-1633

Vives-Bauza, C., Anand, M., Shirazi, A.K., Magrane, J., Gao, J., Vollmer-Snarr, H.R., Manfredi, G., Finnemann, S.C. 2008. The age lipid A2E and mitochondrial dysfunction synergistically impair phagocytosis by retinal pigment epithelial cells. J. Biol. Chem. 283(36):24770-24780

Wang, P., Liang, X., Yi, J., Zhang, Q. 2008. Novel SOX2 mutation associated with ocular coloboma in a Chinese family. Arch. Ophthalmol. 126(5):709-713

Wells, P.G., McCallum, G.P., Chen, C.S., Henderson, J.T., Lee, C.J., Perstin, J., Preston, T.J., Wiley, M.J., Wong, A.W. 2009. Oxidative stress in developmental origins of disease: teratogenesis, neurodevelopmental deficits, and cancer. Toxicol. Sci. 108(1):4-19

Wenzel, A., Benke, D., Mohler, H., Fritschy, J.M. 1997. N-methyl-D-aspartate receptors containing the NR2D subunit in the retina are selectively expressed in rod bipolar cells. Neuroscience. 78(4):1105-1112

West, S.K., Munoz, B., Rubin, G.S., Schein, O.D., Bandeen-Roche, K., Zeger, S., German S., Fried, L.P. 1997. Function and visual impairment in a population-based study of older adults. Invest. Ophthalmol. Vis. Sci. 38(1):72-82

White, D.A., Fritz, J.J., Hauswirth, W.W., Kaushal, S., Lewin, A.S. 2007. Increased sensitivity to light-induced damage in a mouse model of autosomal dominant retinal disease. Invest. Ophthalmol. Vis. Sci. 48(5):1942-1951

Wilken, B., Ramirez, J.M., Probst, I., Richter, D.W., Handefeld, F. 2000. Anoxic ATP depletion in neonatal mice brainstem is prevented by creatine supplementation. Arch. Dis. Child Fetal Neonatal Ed. 82(3):F224-F227

Williams, T.P., Webbers, J.P., Giordano, L., Henderson, R.P. 1998. Distribution of photon absorption rates across the rat retina. J. Physiol. 508:515-522

Woodward, W.R., Choi, D., Grose, J., Malmin, B., Hurst, S., Pang, J., Weleber, R.G., Pillers, D.A. 2007. Isoflurane is an effective alternative to ketamine/xylazine/acepromazine as an anesthetic agent for the mouse electroretinogram. Doc. Ophthalmol. 115(3):187-201

Yamafuji, K., Uchida, Y. 1966. Liberation of adenine from deoxyribonucleic acid by hydrogen peroxide. Nature. 209(5020):301-302

Yang, J.H., Basinger, S.F., Gross, R.L., Wu, S.M. 2003. Blue light-induced generation of reactive oxygen species in photoreceptor ellipsoids requires mitochondrial electron transport. Invest. Ophthalmol. Vis. Sci. 44(3):1312-1319

Young, R.W., Bok, D. 1969. Participation of the retinal pigment epithelium in the rod outer segment renewal process. J. Cell. Biol. 42(2):392-403

Young, R.D. 1985. The ultrastructural organization of proteoglycans and collagen in the human and rabbit scleral matrix. J. Cell. Sci. 74:95-104

Yuan, X., Wilhelmus, K.R. 2009. Corneal neovascularization during experimental fungal keratitis. Mol. Vis. 15:1988-1996

Zhang, J., Li, W., Hoshi, H., Mills, S.L., Massey, S.C. 2005. Stratification of alpha ganglion cells and ON/OFF directionally selective ganglion cells in the rabbit retina. Vis. Neurosci. 22(4):535-549

Zhang, Z., Kindrat, A.N., Sharif-Naeini, R., Bourque, C.W. 2007. Actin filaments mediate mechanical gating during osmosensory transduction in rat supraoptic nucleus neurons. J. Neurosci. 27(15):4008-4013

Zhong, L., Bradley, J., Schubert, W., Ahmed, E., Adamis, A.P., Shima, D.T., Robinson, G.S., Ng, Y.S. 2007. Erythropoietin promotes survival of retinal ganglion cells in DBA/2J glaucoma mice. Invest. Ophthalmol. Vis. Sci. 48(3):1212-1218

Zhou, T., Lewis, H., Foster, R.E., Schwendeman, S.P. 1998. Development of a multiple-drug delivery implant for intraocular management of proliferative vitreoretinopathy. J. Control Release. 55(2-3):281-295

Zhou, X., Xie, J., Shen, M., Wang, J., Jiang, L., Qu, J., Lu, F. 2008. Biometric measurement of the mouse eye using optical coherence tomography with focal plane advancement. Vision Res. 48(9):1137-1143

Zhu, C., Wang, X., Huang, Z., Qiu, L., Xu, F., Vahsen, N., Nilsson, M., Eriksson, P.S., Hagberg, H., Culmsee, C., Plesnila, N., Kroemer, G., Blomgren, K. 2007. Apoptosis-inducing factor is a major contributor to neural loss induced by neonatal cerebral hypoxia-ischemia. Cell Death Differ. 14(4):775-784

Zhu, S., Li, M., Figueroa, B.E., Liu, A., Stavrovskaya, I.G., Pasinelli, P., Beal, M.F., Brown, R.G.Jr., Kristal, B.S., Ferrante, R.J., Friedlander, R.M. 2004. Prophylactic creatine administration mediates neuroprotection in cerebral ischemia in mice. J. Neurosci. 24(26):5909-5912

Zimmerman, A.L., Yamanaka, G., Eckstein, F., Bylor, D.A., Stryer, L. 1985. Interaction of hydrolysis-resistant analogs of cyclic GMP with the phosphodiesterase and light-sensitive channel of retinal rod outer segments. Proc. Natl. Acad. Sci. U. S. A. 82(24):8813-8817

Zitting, A., Savolainen, H., Nickels, J. 1981. Acute effects of 2-nitropropane on rat liver and brain. Toxicol. Lett. 9(3):237-246

Appendix A

The University _of_ Western Ontario Ethics Approval for Animal Use in Research

This appendix contains a copy of the ethics approval form for animal use in the Hill laboratory from the University Council on Animal Care and the Animal Use subcommittee.

Western

10.01.08
***This is the 1st Renewal of this protocol**
*A Full Protocol submission will be required in 2011

Dear Dr. **Hill**

Your Animal Use Protocol form entitled:

Excitotoxicity in Oxidative Stress Induced Retinal Degeneration: Mechanisms and Validation of a Potential Neuroprotective Agent

has had its yearly renewal approved by the Animal Use Subcommittee.

This approval is valid from **10.01.08** to **09.30.09**

The protocol number for this project remains as **2007-097**

1. This number must be indicated when ordering animals for this project.
2. Animals for other projects may not be ordered under this number.
3. If no number appears please contact this office when grant approval is received.
   If the application for funding is not successful and you wish to proceed with the project, request that an internal scientific peer review be performed by the Animal Use Subcommittee office.
4. Purchases of animals other than through this system must be cleared through the ACVS office. Health certificates will be required.

REQUIREMENTS/COMMENTS
Please ensure that individual(s) performing procedures on live animals, as described in this protocol, are familiar with the contents of this document.

c.c. Approved Protocol - K Hill, D Cheshuk, J Wasylenko
Approval Letter - D Cheshuk, J Wasylenko

The University *of* Western Ontario
Animal Use Subcommittee / University Council on Animal Care
Health Sciences Centre, • London, Ontario • CANADA – N6A 5C1
PH: 519-661-2111 ext. 86770 • FL 519-661-2028 • www.uwo.ca / animal

Appendix B

Supplementary Figures and Tables

This appendix contains supplementary figures and tables from chapters 1 and 2, used to aid in understanding of research presented within this study.

Figure 1.1 - Schematic illustration of the human eye demonstrating anatomy and orientation. A. The most anterior portion of the eye is the cornea, important in the initial refraction of light. Light then enters the anterior chamber and is directed into the eye through the pupil. The pupil size is controlled by the iris containing sphincter and dilator muscles. Light is then further refracted by the lens and focused onto the retina found in the posterior segment of the eye. The light travels through the semi-fluid vitreous before reaching the retina. The focal point of light falls on the macula which contains a rich number of cone photoreceptors. Axons from the retina exit the eye via the optic nerve. The retina is supplied nutrients via highly vascularized choroid beneath the retina. The eye is contained and protected by the sclera which becomes uniform with the cornea at the limbus. (Image was modified from: www.fightforsight.org.uk/anatomy-of-the-eye) **B.** The cornea and retina can be divided into four quadrants. Dorsal: quadrant closest to the top of the head; Ventral: quadrant closest to the bottom of the head; Nasal: quadrant closest to the nose; Temporal: quadrant closest to the ear.

A

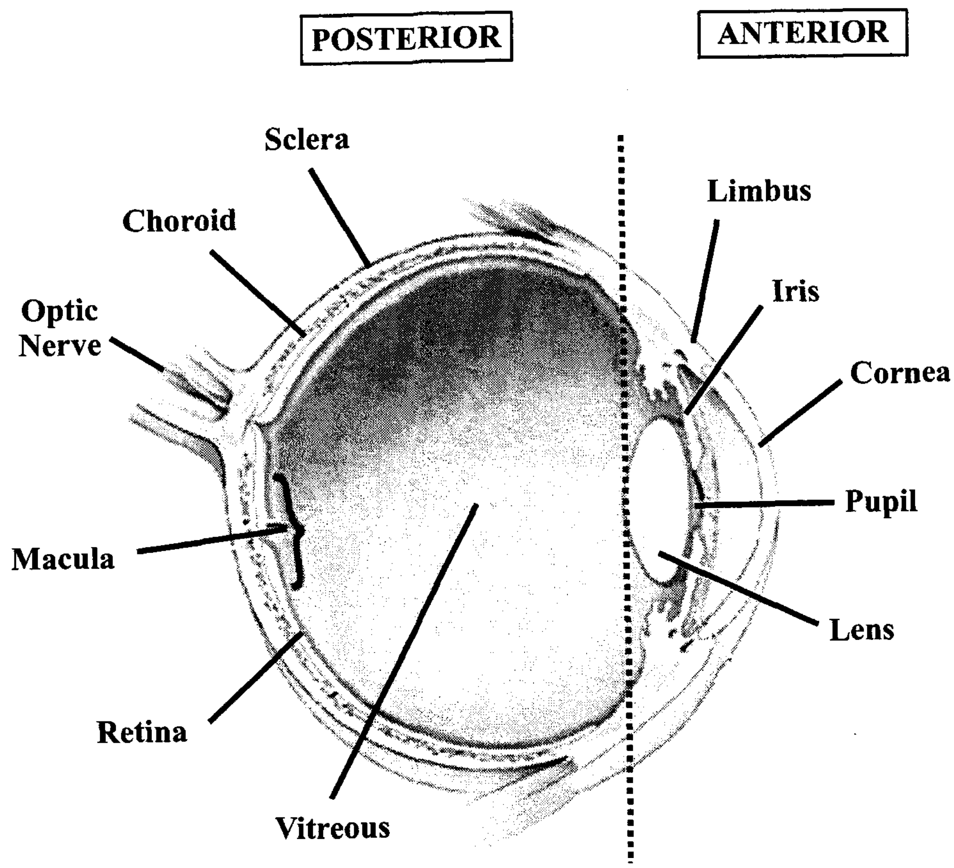
POSTERIOR
ANTERIOR
Sclera
Choroid
Optic Nerve
Macula
Retina
Vitreous
Limbus
Iris
Cornea
Pupil
Lens

B

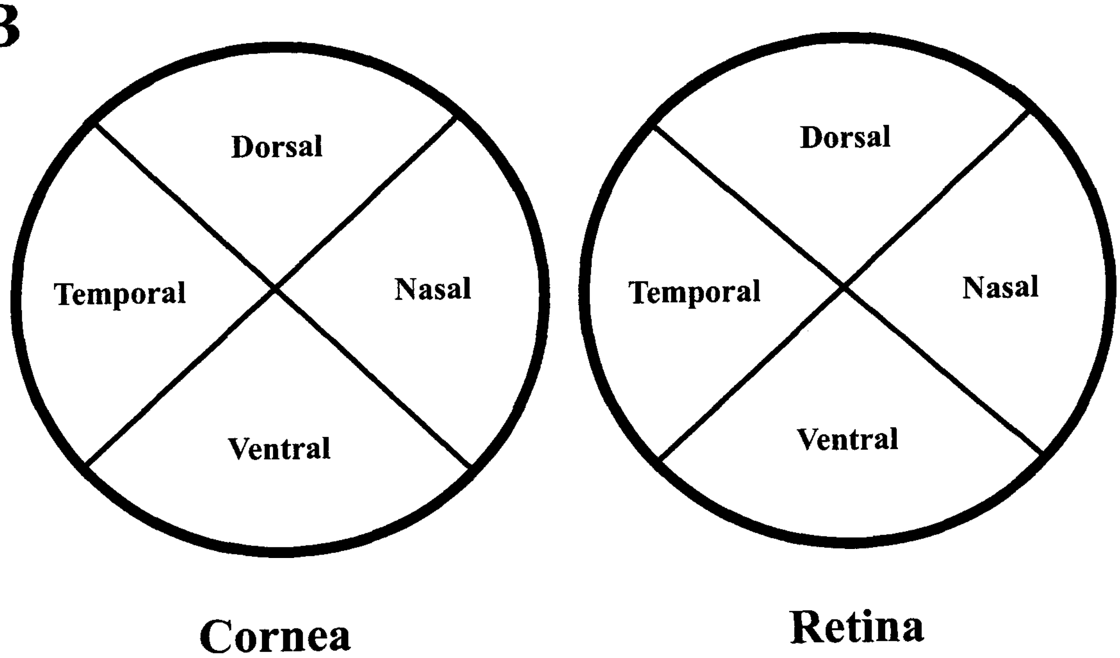
Dorsal
Temporal
Nasal
Ventral
Dorsal
Temporal
Nasal
Ventral
Cornea
Retina

Figure 1.2 - Visualization of human ocular structures using Ocular Coherence Tomography (OCT). OCT measures the reflection and impedance of light waves focused in a transverse plane to image ocular structures *in vivo*. Ocular structures from the anterior chamber to the posterior chamber can be assessed based on penetration of light and axial depth of imaging. Multiple machines have varying light penetration and axial depths of imaging for imaging of particular structures. **A.** OCT imaging of the anterior segment using of a human eye containing the cornea, iris and anterior portion of the lens. (image modified from: Rey et al., 2009). The Visante OCT (Zeiss) is typically used for anterior chamber imaging. **B.** OCT imaging of the posterior segment of the eye containing the retina, macula and choroid. The sclera can not be observed because the highly pigmented retinal pigment epithelium and choroid impede light waves. (image modified from: www.nyee.edu/aric_spectral.html). The Cirrus OCT (Zeiss) is typically used for retinal imaging in the human eye because of light penetration and axial depth of imaging.

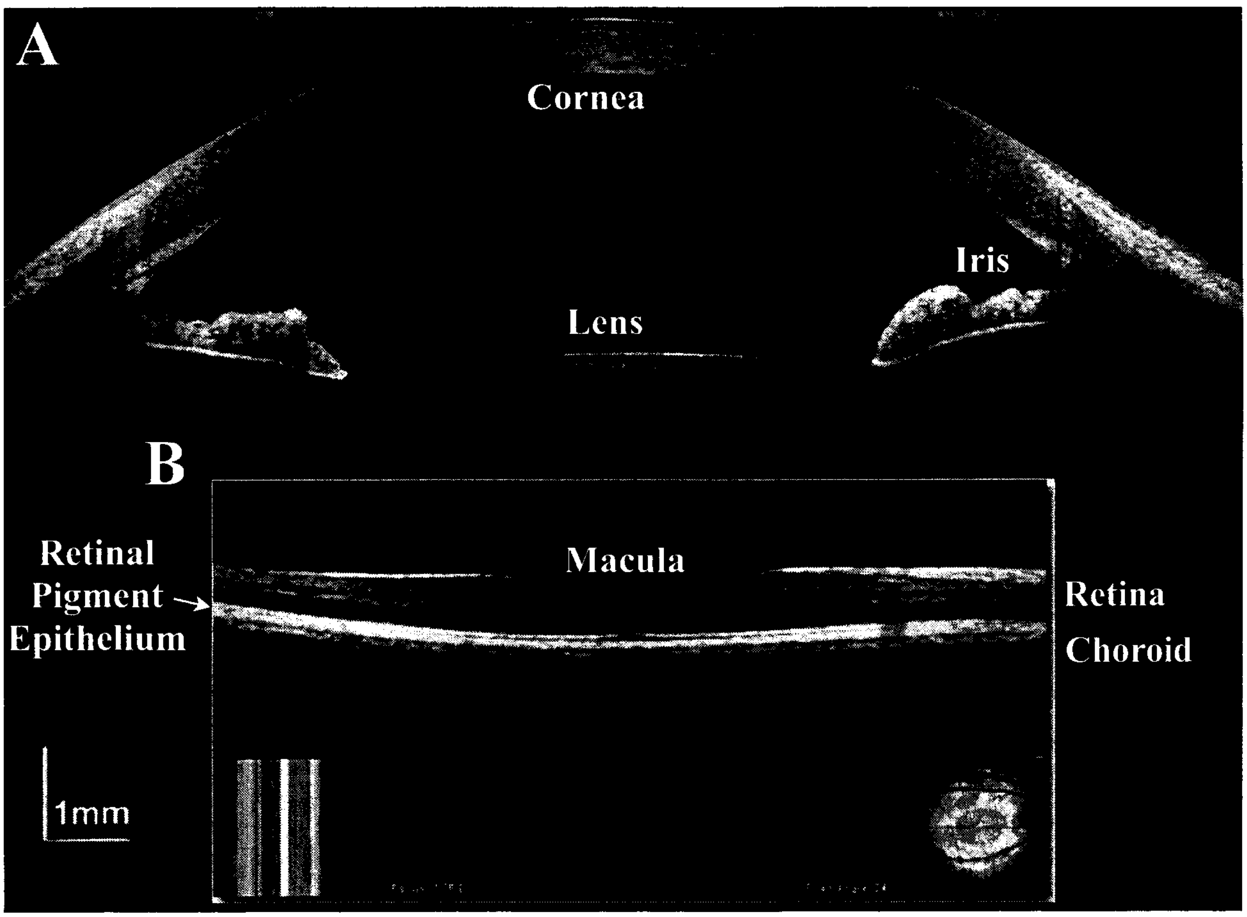

aphy
plane
terior
ltiple
cular
rnea,
OCT
nent
the
ified
tinal

Figure 1.3 - Schematic illustration of the mammalian retina indicating layer organization. Light enters the eye and travels through the layers of the retina before interacting with the outer segments of the photoreceptors. The outer segments of the photoreceptors rest on a bed of retinal pigment epithelial cells. The outer segments of the photoreceptors are attached to the cell bodies of the photoreceptors in the outer nuclear layer (first-order cells). The axons of the photoreceptor cells extend into the outer plexiform layer where they synapse with dendrites of second-order cells. The second order cell bodies are found in the inner nuclear layer. Axons of second-order cells extend into the inner plexiform layer where they synapse with dendrites of the third-order cells of the retina. Nuclei of ganglion cells reside in the inner nuclear layer of the retina. Axons of the ganglion cells extend to the optic nerve via the nerve fiber layer. (image adapted from: www.answersingenesis.org/tj/v13/i1/retina.asp)

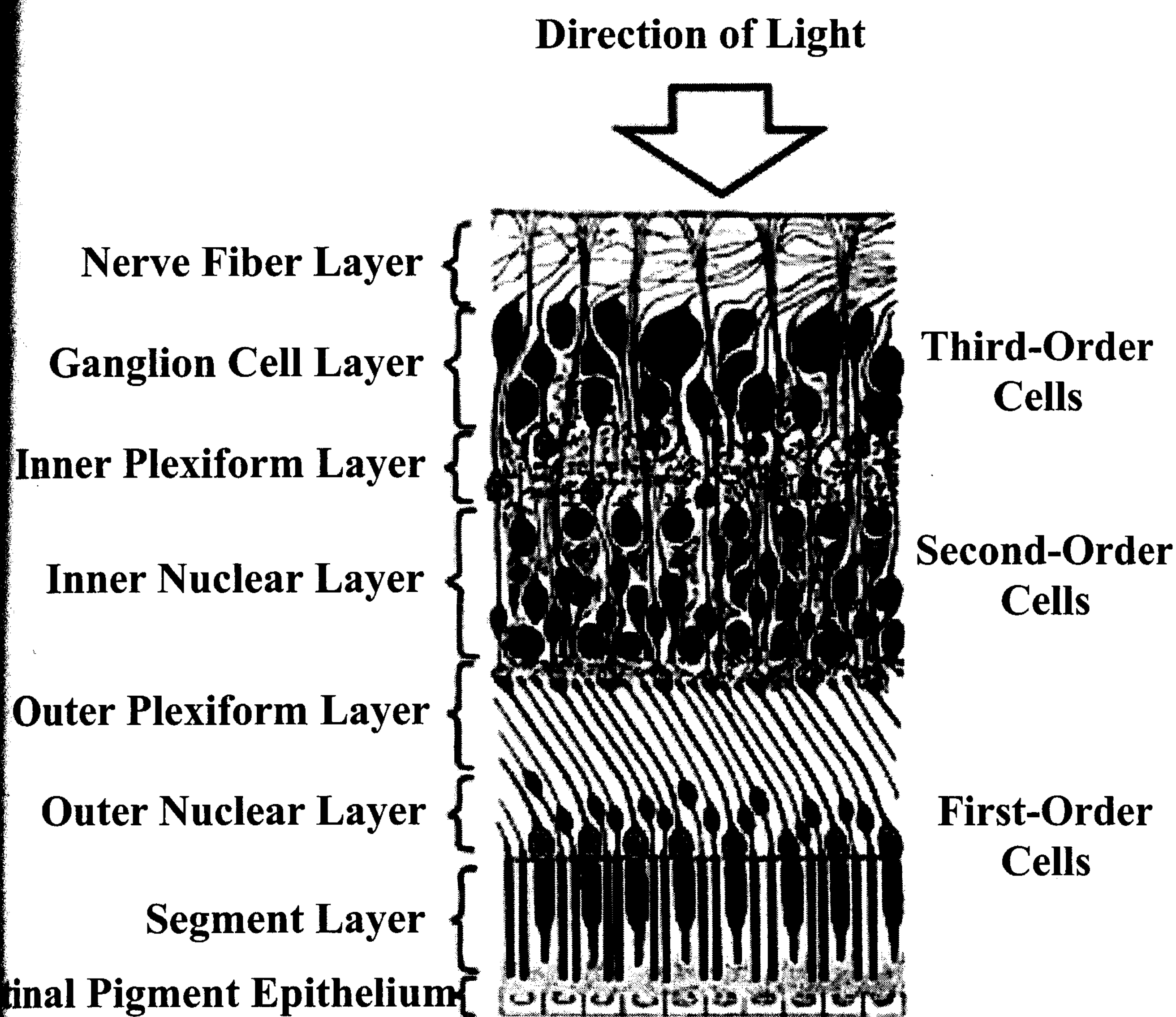

Direction of Light
Nerve Fiber Layer
Ganglion Cell Layer
Inner Plexiform Layer
Inner Nuclear Layer
Outer Plexiform Layer
Outer Nuclear Layer
Segment Layer
tinal Pigment Epithelium
Third-Order Cells
Second-Order Cells
First-Order Cells

Figure 1.4 - Schematic layout of a cone terminal synapse in the mammalian retina. The presynaptic ribbon (**SR**) with anchored vesicles is shown cut transversely in a cone cell. A superficial (**S**) synapse is shown between the axon of a cone photoreceptor and OFF-bipolar cell dendrite (**OFF - B**). An invaginating (**I**) synapse is shown with two horizontal (**H**) cell dendrites and a single ON-bipolar cell dendrite (**ON - B**). Directions of neurotransmitter release are indicated by arrows. Neurotransmitter receptors are indicated on the post-synaptic dendrite and include: iGluR - ionotropic glutamate receptors; mGluR6 - metabotropic glutamate receptor 6; GABA - γ-aminobutyric acid receptors.

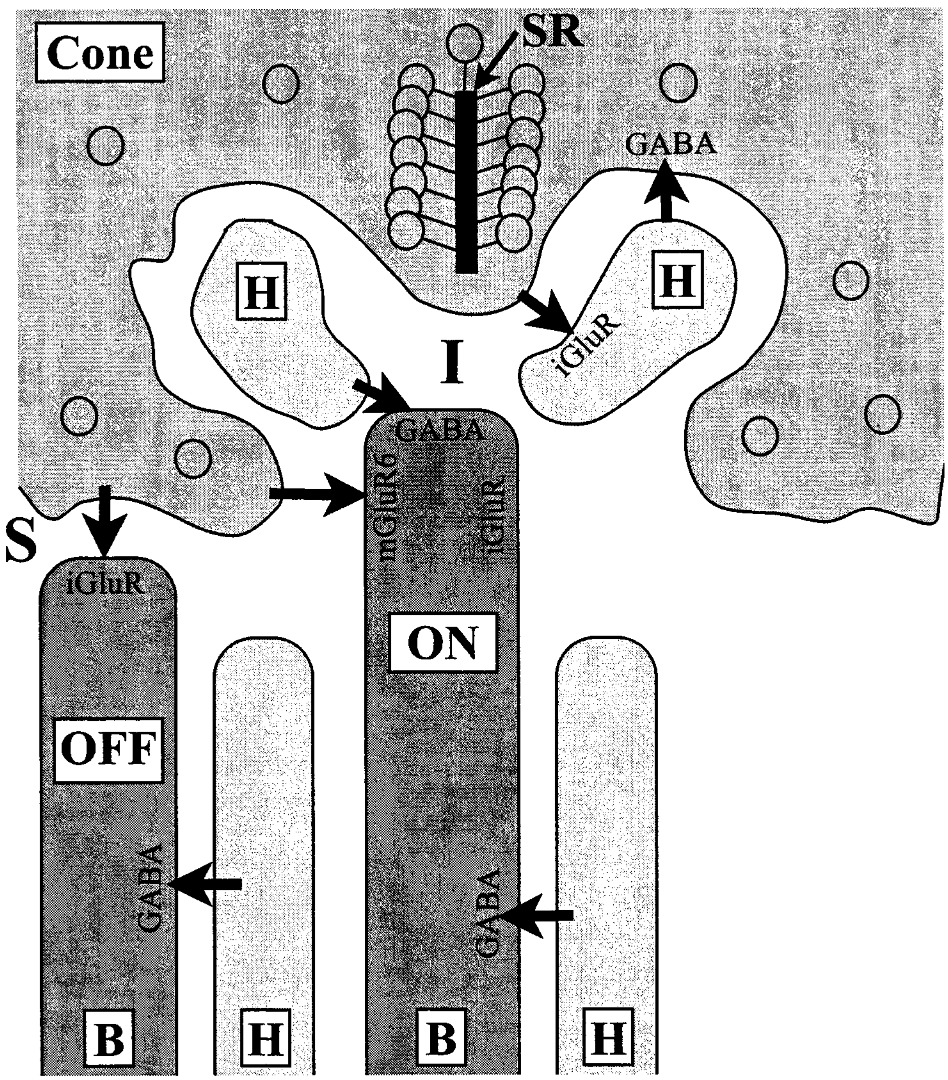
Cone
SR
GABA
H
H
iGluR
I
GABA
mGluR6
iGluR
S
iGluR
ON
OFF
GABA
GABA
B
H
B
H

Figure 1.5 - Schematic layout of the retina showing the basic plan of synaptic organization. Photoreceptors synapse (arrows) with the two classes of second-order neurons, bipolar and horizontal cells. Horizontal cells are lateral interneurons that provide feedback to photoreceptors and feedforward to the bipolar cells. The same general pattern is repeated in the inner retina, where bipolar cells synapse (arrows) directly with ganglion cells, but also provide input to amacrine cells. Amacrine cells are the lateral interneurons of the inner retina that provide feedback to bipolar cells and feedforward to ganglion cells. Both horizontal and amacrine cells have extensive synaptic connections between themselves.

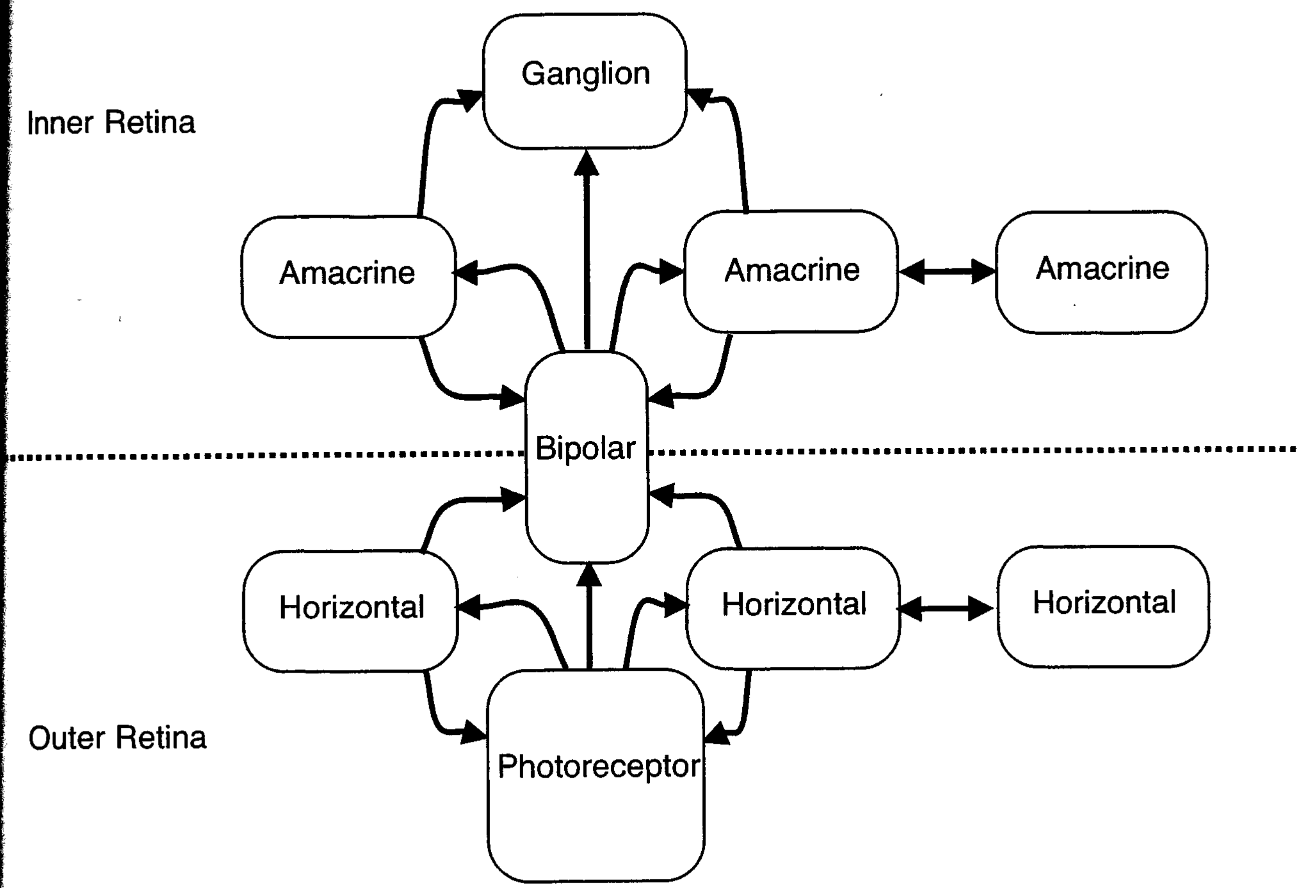
Inner Retina
Ganglion
Amacrine
Amacrine
Amacrine
Bipolar
Horizontal
Horizontal
Horizontal
Photoreceptor
Outer Retina

Figure 1.6 - Assessment of retinal function using an electroretinography (ERG) trace. In ERG testing, the retina is stimulated by a flash of light. An electrical response is recorded by electrodes placed on the cornea of a patient. The a-wave amplitude is a cumulative measure of the hyperpolarizing photoreceptor cells of the retina and is measured in μV (microvolts). The a-wave latency is the time taken for the signal to be detected from the cornea and is measured in ms (milliseconds). The b-wave amplitude is a cumulative measure of the depolarizing cells of the retina and demonstrates whole retinal function in response to light. The b-wave latency is the time taken for the signal to be detected from the cornea. Decreased wave amplitude and increased wave latency is an indication of retinal degeneration.

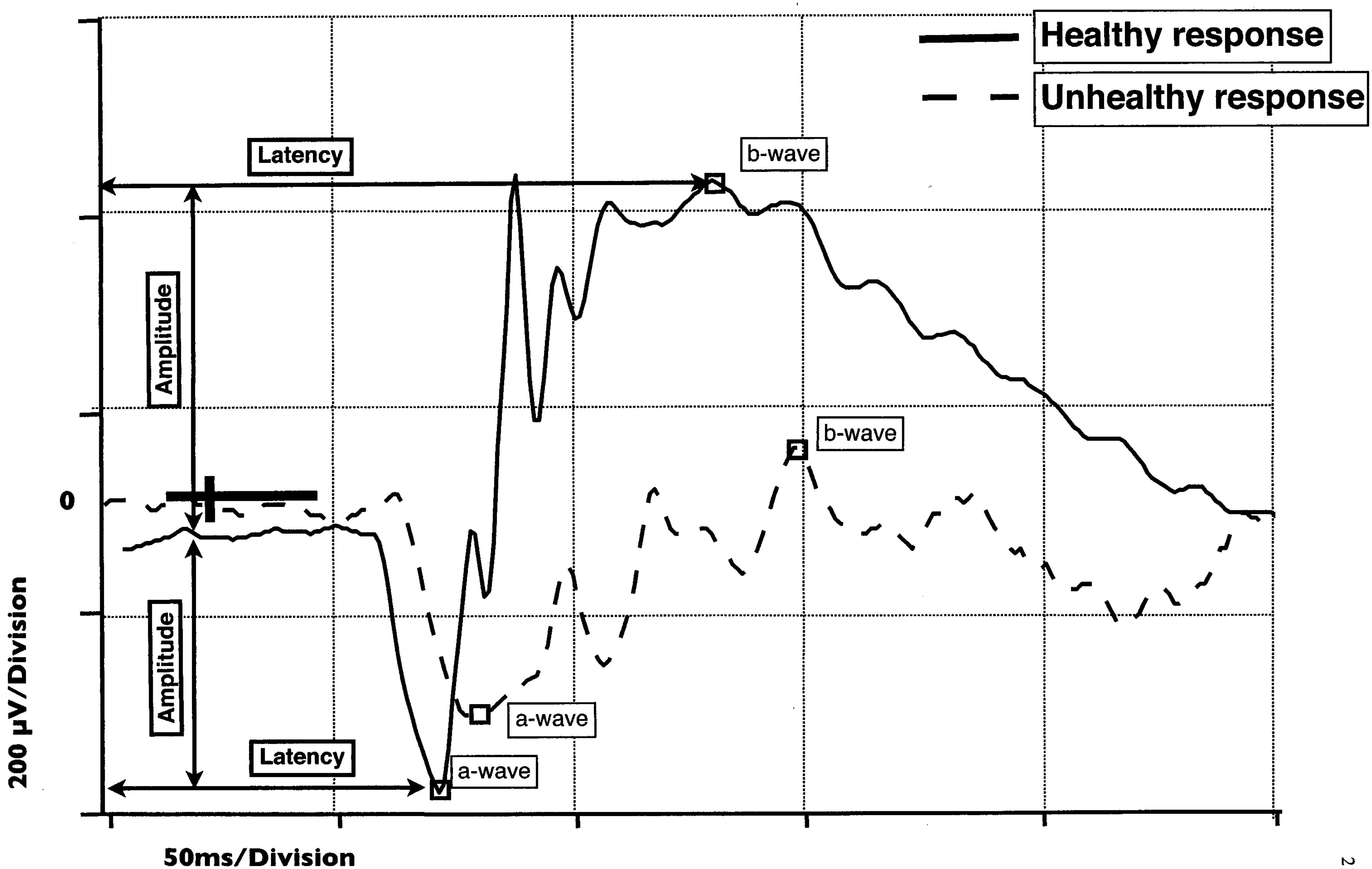

Healthy response
Unhealthy response
Latency
b-wave
Amplitude
0
b-wave
Amplitude
a-wave
Latency
a-wave
200 µV/Division
50ms/Division

Figure 1.7 - Examples of the two primary causes of age-related blindness in the developed world. A. An example of the vision of a healthy individual with no signs of age-related blindness. **B.** Central vision loss associated with age-related macular degeneration (AMD). AMD is the leading cause of blindness in the developed world, with 253,000 Canadians in advanced stages of the disease in 2006. **C.** Peripheral vision loss associated with the degeneration of peripheral ganglion cells in advanced glaucoma. Glaucoma is the second leading cause of blindness in the developed world, with 250,000 affected individuals in 2006.

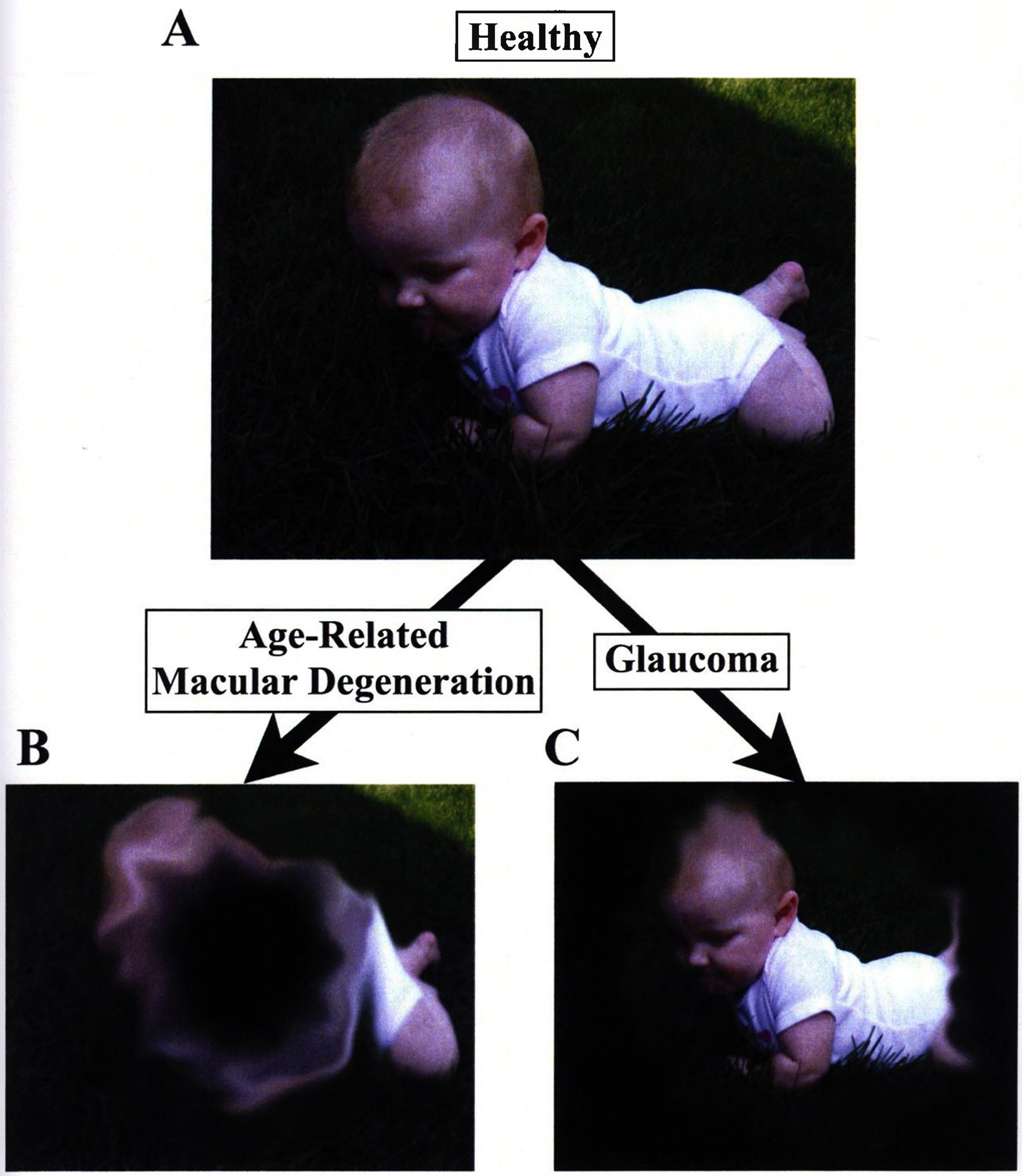
A
Healthy
Age-Related
Macular Degeneration
Glaucoma
B
C

Figure 1.8 - Cross-section of a mouse eye stained with hematoxylin and eosin indicating general anatomy. The mouse eye is dramatically smaller than the human eye; ~13% of the size. **A.** A hematoxylin and eosin stained cross section of the mouse eye. The cornea and lens are dramatically larger in the nocturnally-active mouse in relation to the human. **B.** A hematoxylin and eosin stained cross section of the mouse retina and posterior tissues. The mouse eye is contained and protected by the sclera. The choroid is a highly vascularized tissue at the back of the eye and provides the outer retina with nutrients and oxygen. The retinal pigment epithelium is an important component of the blood-retina barrier. The neural retina has the same cellular organization as the human retina but does not contain a macula.

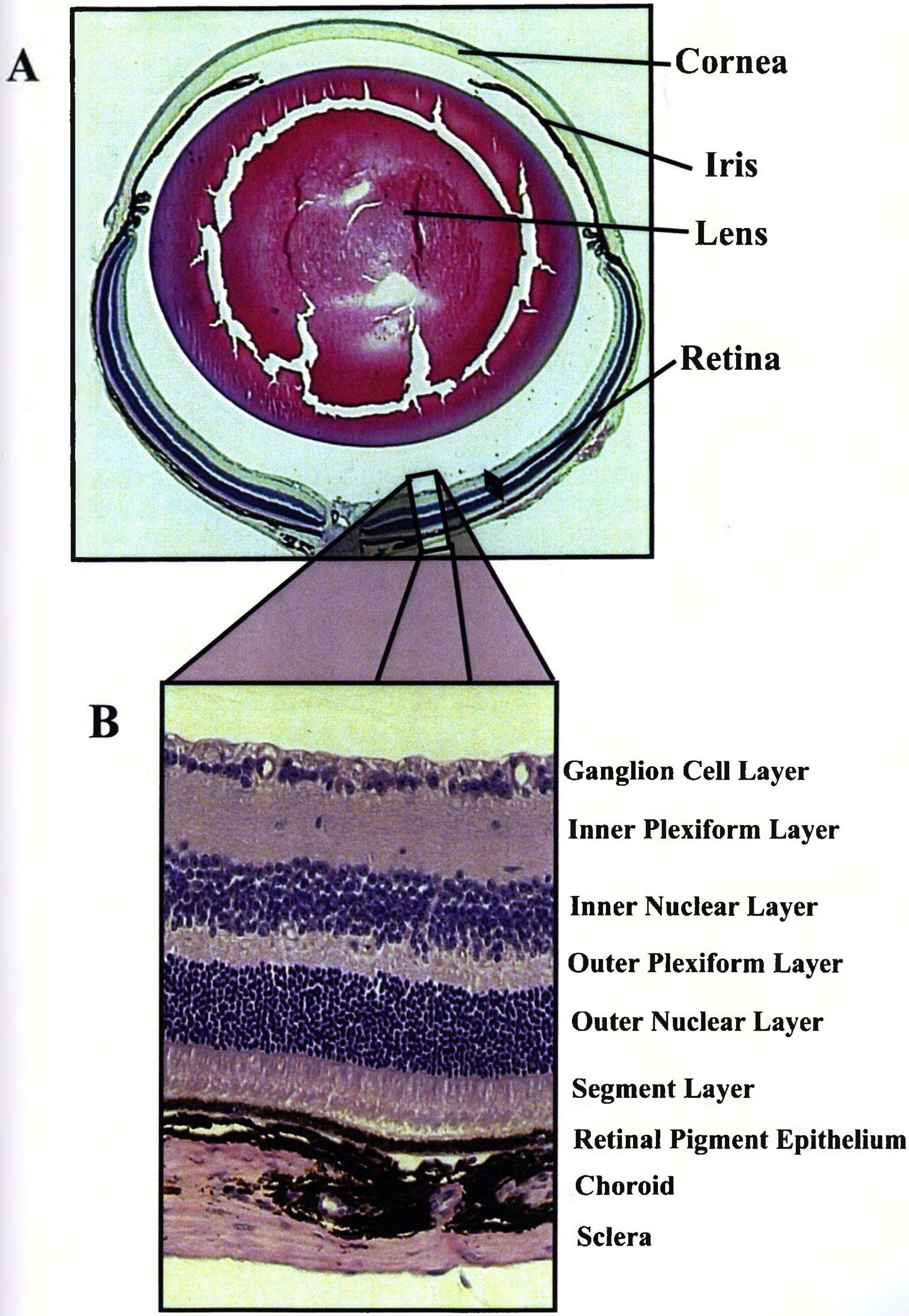
A
Cornea
Iris
Lens
Retina
B
Ganglion Cell Layer
Inner Plexiform Layer
Inner Nuclear Layer
Outer Plexiform Layer
Outer Nuclear Layer
Segment Layer
Retinal Pigment Epithelium
Choroid
Sclera

Figure 1.9 - Chemical Structure of the neuroprotective agent memantine hydrochloride. Memantine is a voltage-dependent moderate affinity uncompetitive NMDA receptor antagonist that reduces excitotoxic insult induced by overstimulation of glutamate receptors. Memantine is currently approved by the food and drug administration (FDA) for use in the treatment of dementia related to moderate and severe Alzheimer's disease due to its effects of moderating excitotoxicity.

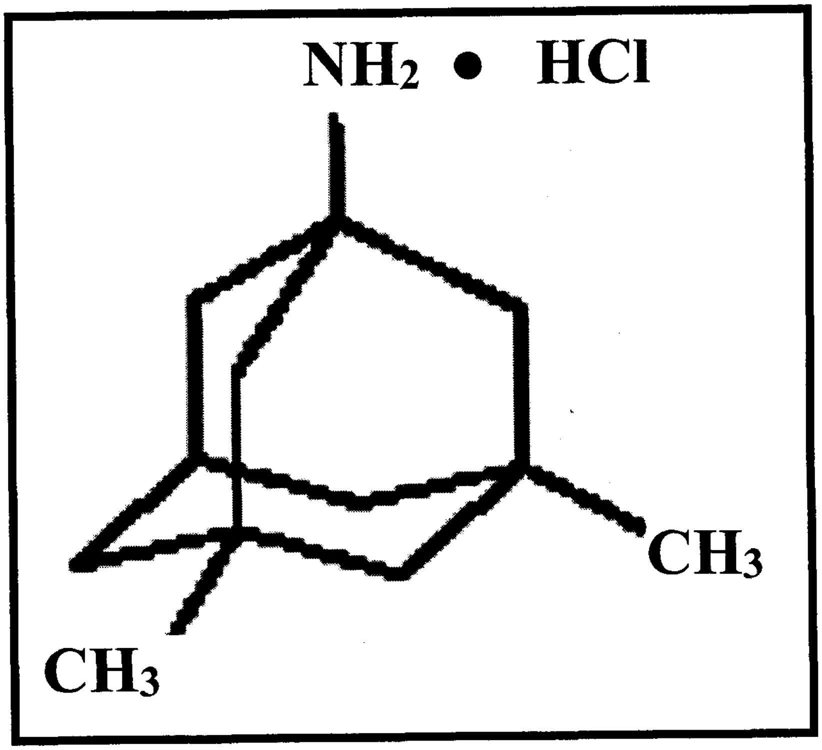
NH2 • HCl
CH3
CH3

Figure 2.1 - Experimental design used to assess retinal degeneration and a potential intervention strategy. The experimental design included 100 mice, 50 male wild type (WT) and 50 male *harlequin* mice. These mice were further divided into five groups of animals consisting of 10 *hq* and 10 WT animals each that were euthanized at two, four, six, eight and ten months of age. The five groups of animals were subdivided into untreated (H_2O) and memantine-treated cohorts of animals (*hq*: n = 5, WT: n = 5). The untreated cohorts of animals received regular drinking water *ad libitum* as a vehicle control. The memantine treated cohorts received drinking water containing dissolved memantine hydrochloride (Sigma-Aldrich, St. Louis, MO) *ad libitum.* Drug-treated mice had a target memantine dosage of 30 mg/kg/day (Minkeviciene et al., 2004). Eye structure and function were assessed *in vivo* using ERG and OCT testing in a longitudinal fashion beginning at two months of age and continuing monthly until date of euthanization. Postmortem histopathology was preformed on all eyes to determine significant changes in eye structure that could be associated with a loss in retinal function.

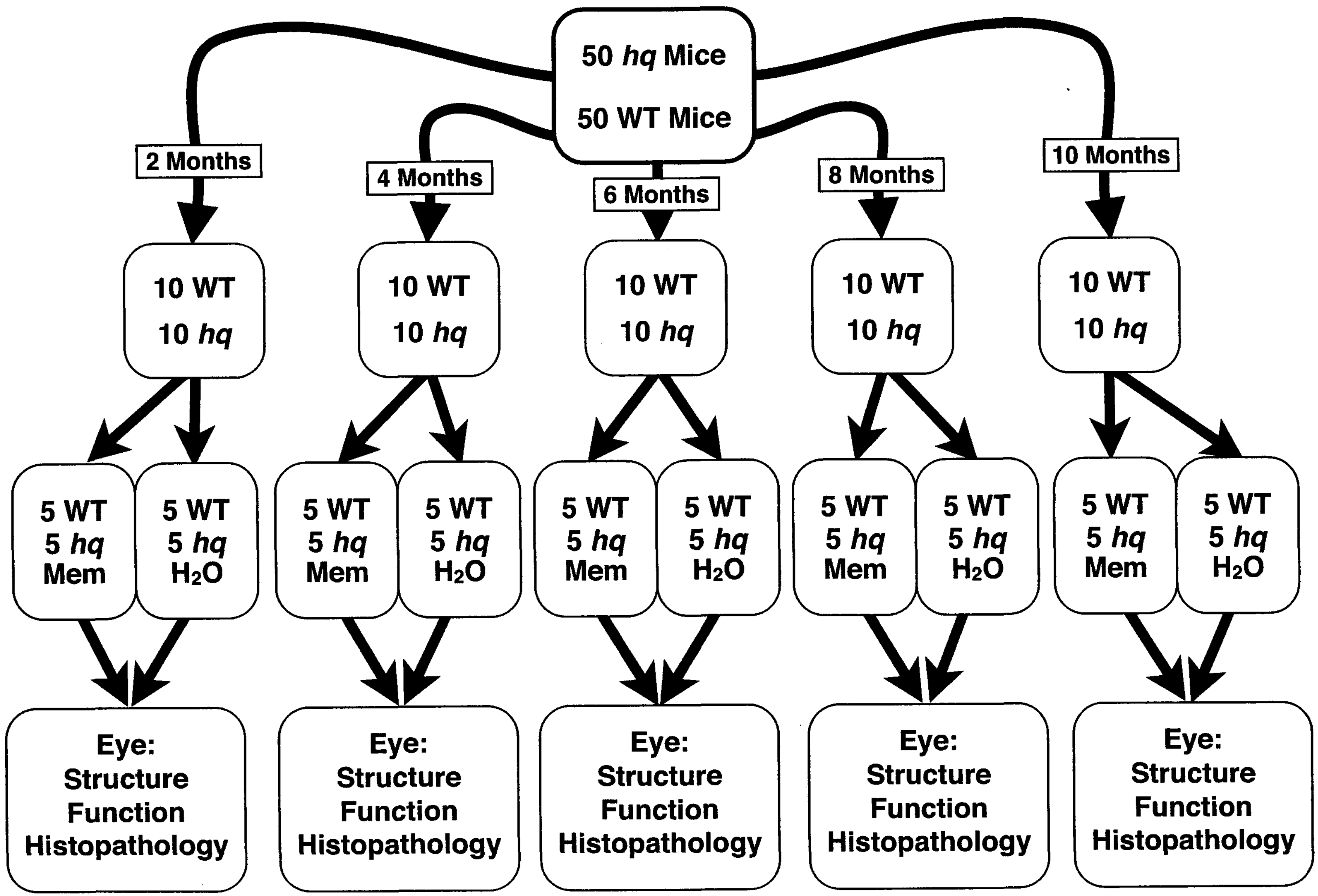
50 *hq* Mice
50 WT Mice
2 Months
4 Months
6 Months
8 Months
10 Months
10 WT
10 *hq*
5 WT
5 *hq*
Mem
5 WT
5 *hq*
H_2O
Eye:
Structure
Function
Histopathology

Figure 2.2 - Electroretinography experimentation began at two months of age and was continued monthly thereafter until date of euthanization. A. Electrical response from the retina was triggered by a series of white light flashes coming from a colordome stimulator (Diagnosys, Lowell, Massachusetts) placed over the animals head. The colordome stimulator can be lowered directly over the head of the anesthetized mouse. **B.** Birds eye view of an anesthetized mouse from the lowered color dome prior to electroretinography testing. A reference lead was placed in the mouth of the anesthetized animal with a gold mini-plate resting on the tongue. A grounding lead was inserted subcutaneously in the tail of the mouse close to the body. Non-invasive electrode were formed by a small wire twisted into a small loop that would fit comfortably on the eye of the animal. In this photo, electrodes are placed beside the animal and not on the cornea to avoid unnecessary corneal insult.

A

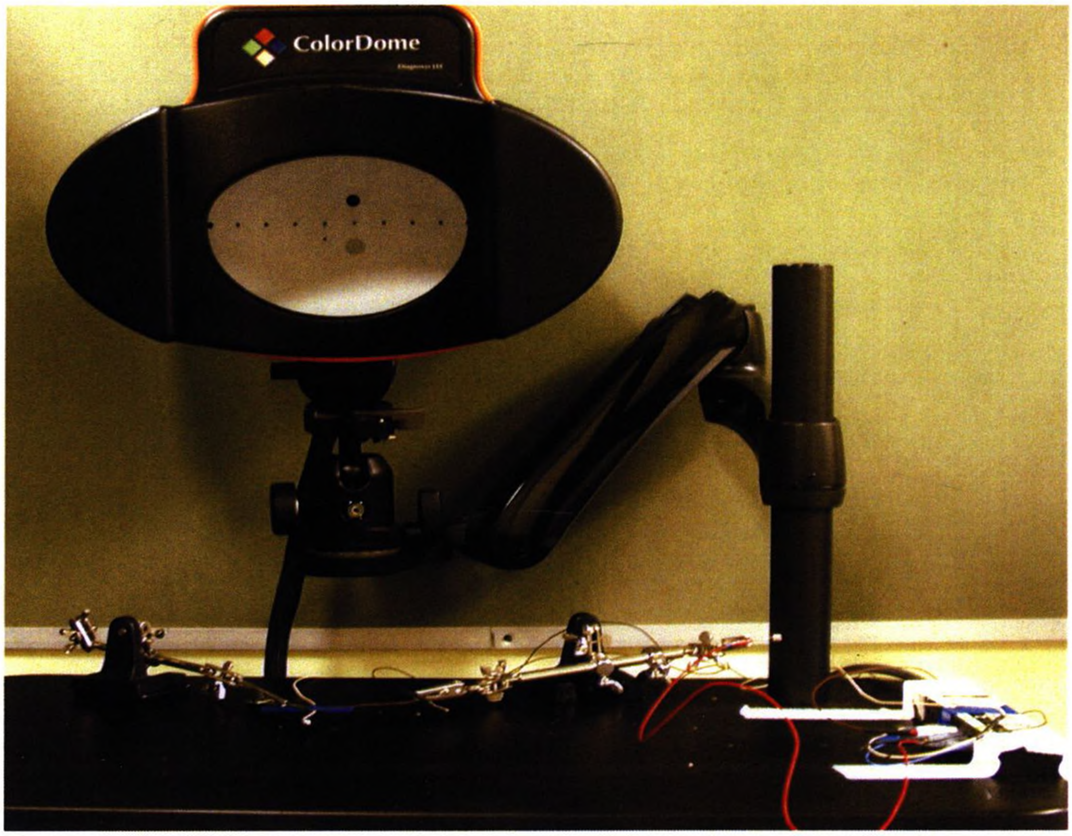

B

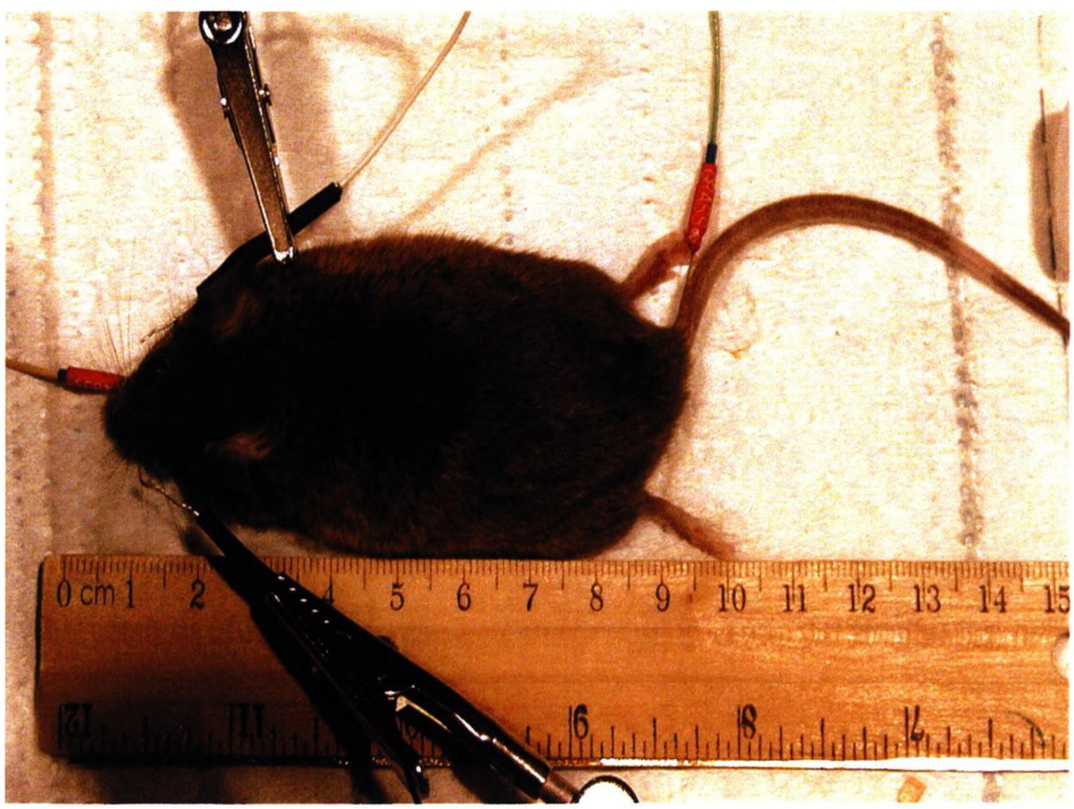

Figure 2.3 - A custom platform designed for OCT imaging by the Engineering department at *The* University *of* Western Ontario. This design allowed for minute manipulation (knobs indicated by solid red boxes) allowing for precise alignment of the mouse eye in front of the OCT machine. **A.** The mouse platform (dotted red box) can be rotated 360° in both the horizontal and vertical plane which allows for a properly oriented mouse in front of the OCT machine leading to reproducible images. **B.** The platform can be vertically raised and lowered (Y plane) and moved in any horizontal planes (X, Z) in order to adjust for animal size and placement on the platform.

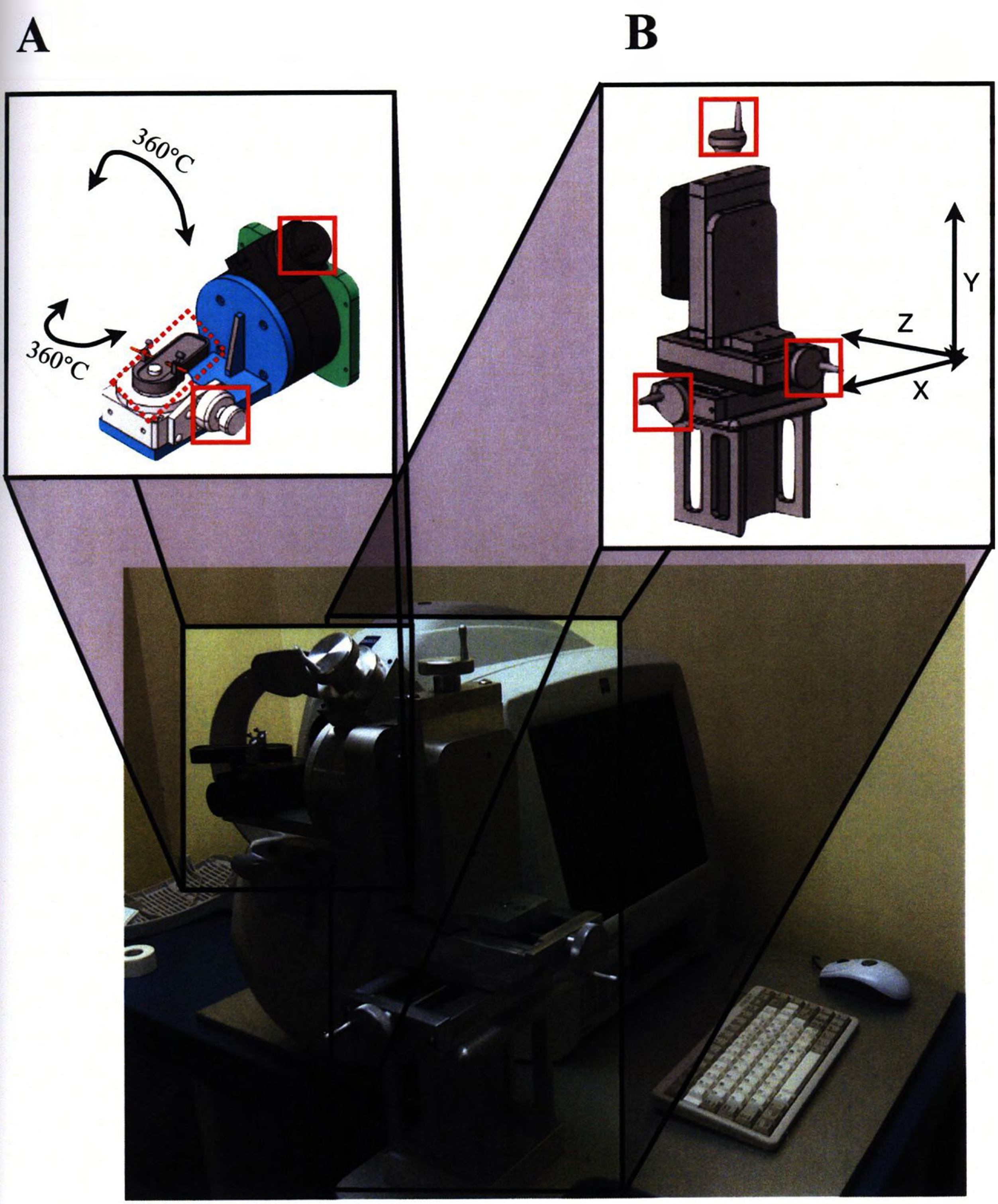
A
B
360°C
360°C
Y
Z
X

Figure 2.4 - *In vivo* measurements of ocular tissues using Ocular Coherence Tomography (OCT). A. Schematic drawing depicting the eye tested and the transverse plane of image capture (OS: left eye; OD: right eye). **B.** Example of an OCT image of the anterior and posterior segments of the mouse eye. Five measurements were captured in the anterior portion of the mouse eye. Three measures of corneal thickness included: central cornea, nasal peripheral cornea and temporal peripheral cornea. A measure of the anterior chamber width was used to determine degrees of microophthalmia. A measure of anterior chamber depth was used to determine abnormal lens placement. Three measures of retinal thickness were obtained from images of the posterior retina. The anterior retina consisted of the neural retina. The posterior retina consisted of the retinal pigment epithelium and choroid. The central whole retinal thickness is combination of the anterior retina and posterior retina measured from the center of the retinal image.

A

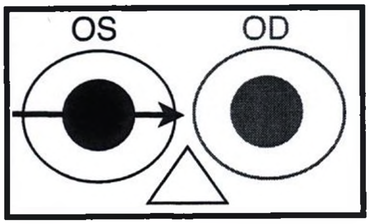
OS
OD

B

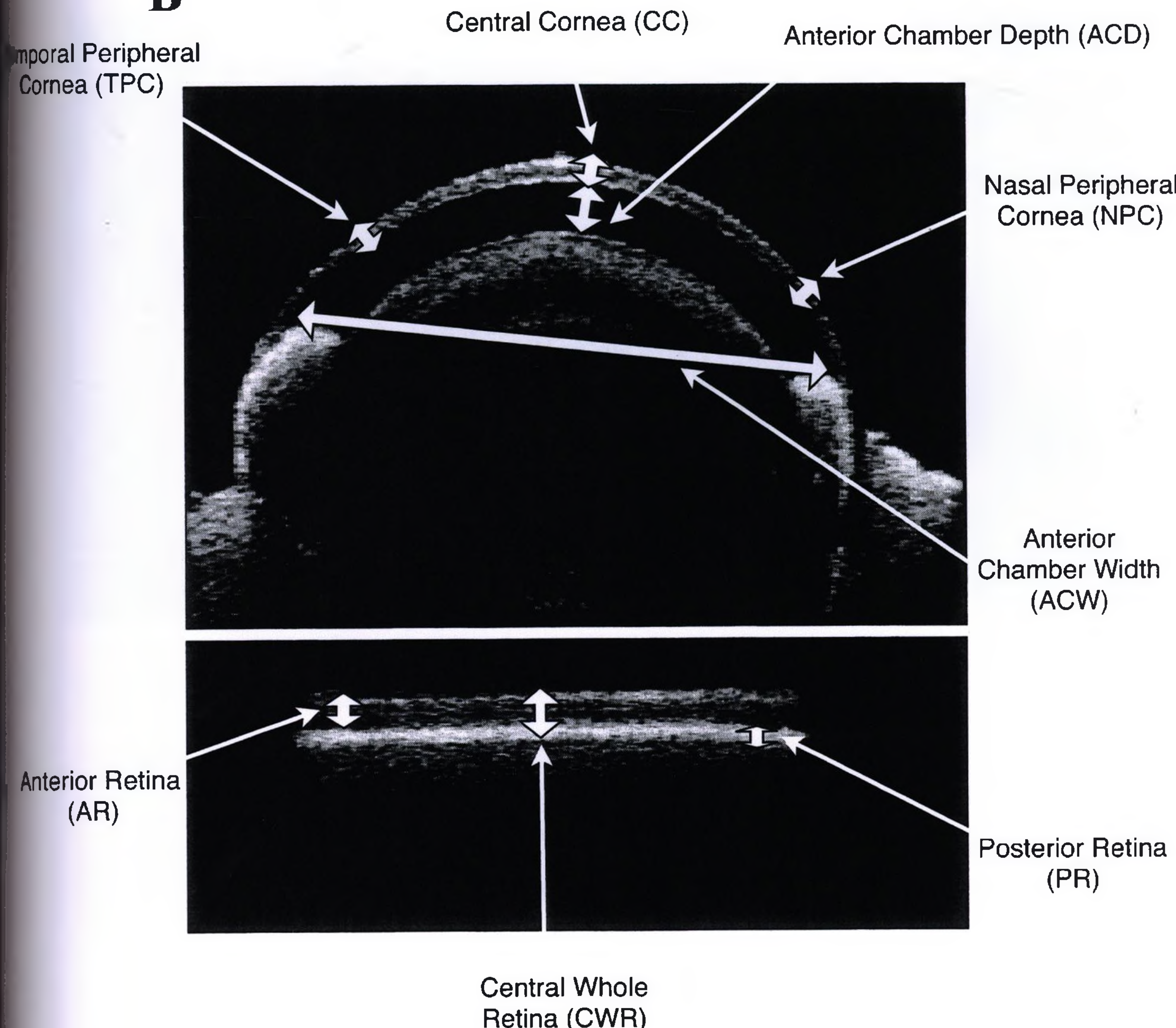
Central Cornea (CC)
Anterior Chamber Depth (ACD)
mporal Peripheral Cornea (TPC)
Nasal Peripheral Cornea (NPC)
Anterior Chamber Width (ACW)
Anterior Retina (AR)
Posterior Retina (PR)
Central Whole Retina (CWR)

Figure 2.5 - Schematic representing tissue section orientation for postmoretem analysis. Step-sectioning levels are indicated by the dotted lines and letters A through E. The solid diagonal line would produce an oblique section. **A.** Section orientation from a human eye. (Image adapted from: Anatomy and Physiology of the eye - Interactive CD-ROM) **B.** Section orientation from a mouse eye. Postmortem analysis was preformed on B-Cut and C-Cut sections of the mouse eye.

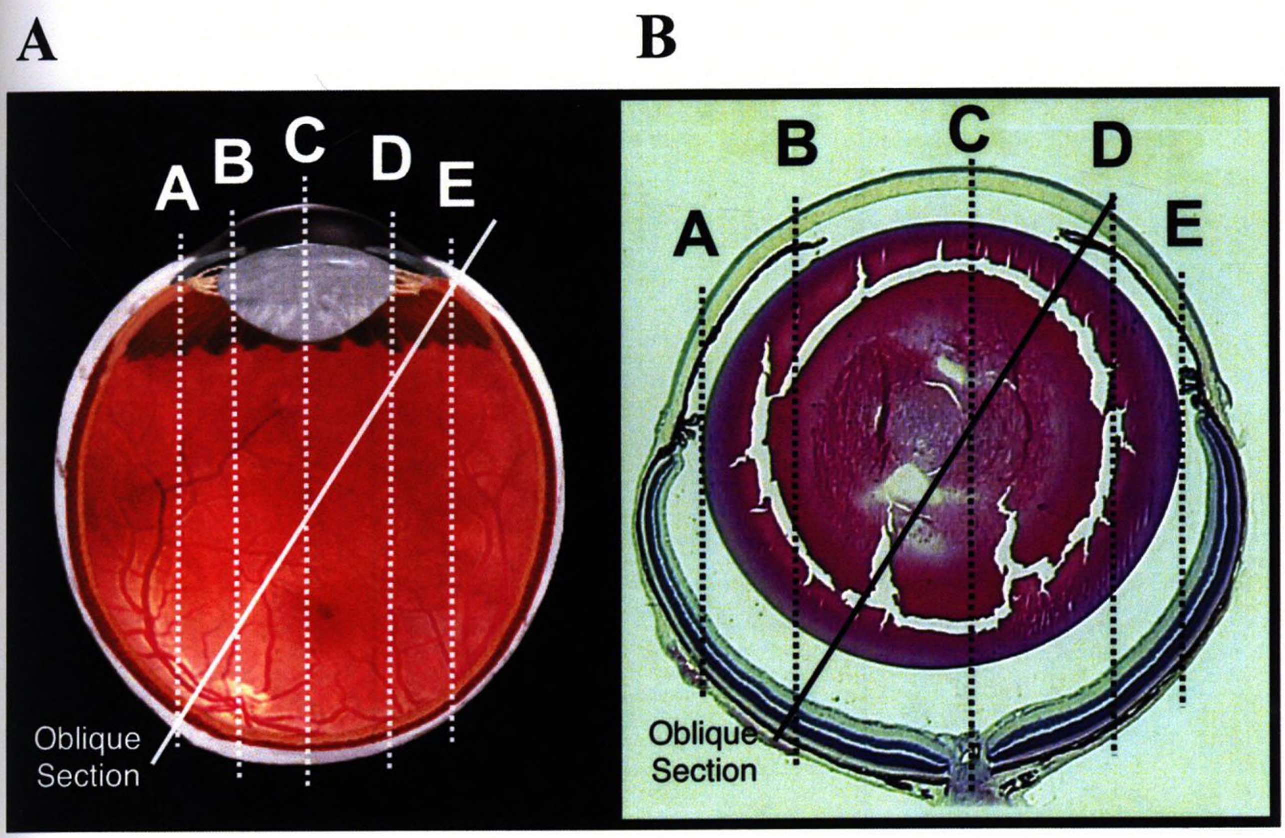
A
B
A
B
C
D
E
Oblique Section
A
B
C
D
E
Oblique Section

Table 2.1 Sample size of experimental cohorts in postmortem assays.

Cohort	2 Months of Age	4 Months of Age	6 Months of age	8 Months of age	10 Months of Age
[1]Untreated WT	n = 5	n = 5	n = 5	n = 5	n = 5
[2]Untreated *hq*	n = 3	n = 4	n = 1	n = 4	n = 3
Memantine-treated WT	n = 5	n = 5	n = 5	n = 4	n = 5
[2]Memantine-treated *hq*	n = 3	n = 5	n = 1	n = 4	n = 5

[1] Cohort obtained desired sample size at all months of age
[2] Sample size of six month cohort is inadequate for statistical analysis

Figure 2.6 - Postmortem tissue analysis from the hematoxylin and eosin stained mouse eye. The C-cut sections of the OD were stained using hematoxylin and eosin stain. A whole eye image was obtained at 2X magnification and was used to determine orientation of the eye. **A.** Three images of the retina were obtained at 20X magnification (boxed). Six measurements of corneal epithelium thickness per image were averaged to determine a mean corneal epithelium thickness for each mouse. Histology of the corneal stroma was assessed at 20X magnification. **B.** Three images were obtained from the retina: ventral, central and dorsal (boxed). Three separate 100 μm horizontal measures were used to determine average ganglion cell nuclei counts. Six measures inner plexiform layer thickness, outer plexiform layer thickness and photoreceptor segment thickness were measured and averaged to determine mean layer thicknesses in the retina. Six vertical cell counts were measured in the inner nuclear layer and outer nuclear layer. These cell counts were averaged to determine a mean thickness for each layer. Six measures of whole retinal thickness were obtained from each image and used to determine the average retinal thickness per mouse at each region imaged.

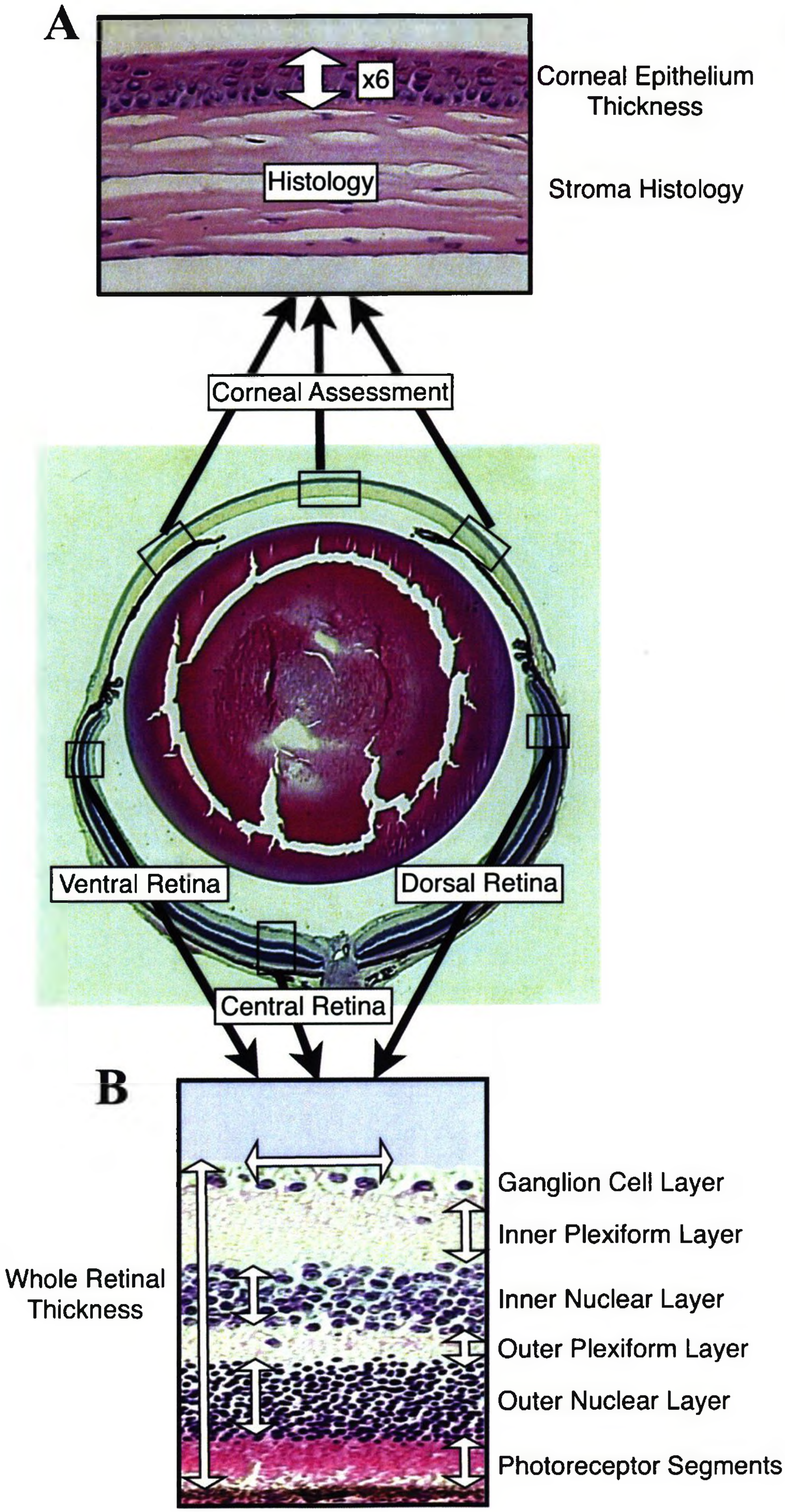
A
x6
Corneal Epithelium Thickness
Histology
Stroma Histology
Corneal Assessment
Ventral Retina
Dorsal Retina
Central Retina
B
Ganglion Cell Layer
Inner Plexiform Layer
Whole Retinal Thickness
Inner Nuclear Layer
Outer Plexiform Layer
Outer Nuclear Layer
Photoreceptor Segments

Appendix C

Comprehensive Tables of Statistically Determined Values

This appendix contains a copy of all statistically determined p-values, correlation coefficients and linear regression analysis.

Abbreviations of Appendix C:

UWT - untreated wild type

U*hq* - untreated *harlequin*

MWT; memantine-treated wild type

M*hq* - memantine-treated *harlequin*;

UWTS - untreated wild type single ERG/OCT

U*hq*S - Untreated *harlequin* single ERG/OCT

Mos - Months of age

p - Correlation coefficient

Table C.1 - P-Values of mean body mass between cohorts using single-factor ANOVA statistical comparisons

	P-Value			
Age	**UWT vs. U*hq***	**UWT vs. MWT**	**U*hq* vs. M*hq***	**MWT vs. M*hq***
Weaning	0.0000	0.1926	0.4113	0.0000
2 Mos	0.0000	0.0000	0.1075	0.0000
3 Mos	0.0000	0.0000	0.8599	0.0000
4 Mos	0.0000	0.0000	0.7092	0.0000
5 Mos	0.0000	0.0017	0.8861	0.0000
6 Mos	0.0000	0.0050	0.7866	0.0000
7 Mos	0.0000	0.0303	0.8288	0.0000
8 Mos	0.0000	0.0064	0.9358	0.0000
9 Mos	0.0018	0.0335	0.4432	0.0149
10 Mos	0.0047	0.1657	0.2827	0.0123

Table C.2 - P-Values of mean water consumption corrected for body mass (ml/g/day) between cohorts using single-factor ANOVA statistical comparisons

	P-Value			
Age	**UWT vs. U*hq***	**UWT vs. MWT**	**U*hq* vs. M*hq***	**MWT vs. M*hq***
2 Mos	0.0236	0.0007	0.9637	0.0099
3 Mos	0.0001	0.0090	0.8736	0.0134
4 Mos	0.0000	0.0144	0.9216	0.0220
5 Mos	0.0000	0.7199	0.1560	0.0393
6 Mos	0.0074	0.5896	0.2067	0.0418
7 Mos	0.0355	0.5309	0.3817	0.0300
8 Mos	0.2944	0.4209	0.2971	0.0022
9 Mos	0.0001	0.1490	0.4963	0.1228
10 Mos	0.3462	0.1472	0.8587	0.8915

Table C.3 - P-Values of mean daily memantine consumption (mg/g/day) between cohorts using single-factor ANOVA statistical comparisons

	P-Value
Age	MWT vs. M*hq*
2 Mos	0.9499
3 Mos	0.7648
4 Mos	0.9599
5 Mos	0.0949
6 Mos	0.2829
7 Mos	0.8319
8 Mos	0.0535
9 Mos	0.1951
10 Mos	0.1533

Table C.4 - P-Values of mean a-wave latency (ms) between OD and OS of experimental cohorts using single-factor ANOVA statistical comparisons

	P-Value			
Age	UWT	U*hq*	MWT	M*hq*
2 Mos	0.6052	0.9284	1.0000	0.5644
3 Mos	0.3140	0.9163	0.4476	0.7073
4 Mos	0.9371	0.7940	0.6730	0.5881
5 Mos	0.8925	0.6506	0.4208	0.6129
6 Mos	0.8664	0.8190	0.4758	0.5849
7 Mos		0.6816	0.3764	0.7791
8 Mos	0.8174	0.6490	0.6540	0.5781
9 Mos	0.9365		0.1890	
10 Mos	0.6122	0.9244	0.4356	0.1121

Table C.5 - P-Values of mean a-wave amplitude (µV) between OD and OS of experimental cohorts using single-factor ANOVA statistical comparisons

	P-Value			
Age	**UWT**	**U*hq***	**MWT**	**M*hq***
2 Mos	0.0157	0.6351	0.5656	0.1918
3 Mos	0.1938	0.4430	0.4698	0.1932
4 Mos	0.1781	0.1071	0.2792	0.3346
5 Mos	0.1144	0.9592	0.6144	0.0997
6 Mos	0.0762	0.8544	0.4858	0.1394
7 Mos		0.9505	0.2974	0.9376
8 Mos	0.0638	0.0698	0.3405	0.9213
9 Mos	0.9452		0.7859	
10 Mos	0.2627	0.1682	0.7417	0.5679

Table C.6 - P-Values of mean b-wave latency (ms) between OD and OS of experimental cohorts using single-factor ANOVA statistical comparisons

	P-Value			
Age	**UWT**	**U*hq***	**MWT**	**M*hq***
2 Mos	0.5945	0.2171	0.8571	0.0616
3 Mos	0.0173	0.7482	0.0961	0.8738
4 Mos	0.2461	0.0701	0.9287	0.3151
5 Mos	0.9409	0.2520	0.5754	0.0431
6 Mos	0.7142	0.8326	0.9647	0.5745
7 Mos		0.5832	0.7559	0.8504
8 Mos	0.5082	0.6241	0.1472	0.6485
9 Mos	0.7460		0.1352	
10 Mos	0.8908	0.9567	0.8548	0.8808

Table C.7 - P-Values of mean b-wave amplitude (μV) between OD and OS of experimental cohorts using single-factor ANOVA statistical comparisons

	P-Value			
Age	**UWT**	**U*hq***	**MWT**	**M*hq***
2 Mos	0.1119	0.9375	0.1329	0.1394
3 Mos	0.2387	0.7080	0.4610	0.0684
4 Mos	0.3538	0.9075	0.1852	0.2382
5 Mos	0.2047	0.2484	0.7114	0.0381
6 Mos	0.5043	0.3515	0.9041	0.1832
7 Mos		0.6689	0.1163	0.6170
8 Mos	0.0361	0.5276	0.3989	0.6574
9 Mos	0.9767		0.6599	
10 Mos	0.5038	0.4086	0.7855	0.5081

Table C.8 - P-Values of mean a-wave latencies (ms) between cohorts using single-factor ANOVA statistical comparisons

	P-Value			
Age	**UWT vs. U*hq***	**UWT vs. MWT**	**U*hq* vs. M*hq***	**MWT vs. M*hq***
2 Mos	0.0004	0.0124	0.1094	0.0051
3 Mos	0.0000	0.0053	0.4640	0.0010
4 Mos	0.0000	0.3102	0.3392	0.0023
5 Mos	0.0000	0.5658	0.6881	0.1520
6 Mos	0.0001	0.0169	0.5565	0.0000
7 Mos			0.7589	0.0004
8 Mos	0.0005	0.6030	0.5181	0.0188
9 Mos		0.6424		
10 Mos	0.0000	0.0108	0.5436	0.0009

Table C.9 - P-Values of mean a-wave amplitudes (μV) between cohorts using single-factor ANOVA statistical comparisons

	P-Value			
Age	**UWT vs. U*hq***	**UWT vs. MWT**	**U*hq* vs. M*hq***	**MWT vs. M*hq***
2 Mos	0.0948	0.8043	0.1027	0.7826
3 Mos	0.0336	0.6598	0.5933	0.0397
4 Mos	0.0012	0.0012	0.5391	0.6794
5 Mos	0.0139	0.1639	0.2866	0.1074
6 Mos	0.0001	0.0870	0.4880	0.0000
7 Mos			0.2323	0.0000
8 Mos	0.0020	0.0422	0.3104	0.0011
9 Mos		0.2584		
10 Mos	0.0515	0.0731	0.0069	0.0020

Table C.10 - Linear regression analysis of a-wave amplitudes with a confidence interval of ± 2 SEM

	Confidence Intervals			
	Y-intercept		Slope	
Cohort	**min**	**max**	**min**	**max**
UWT	185.133	211.563	-1.166	-6.175
U*hq*	196.498	228.856	-10.092	-16.455
MWT	184.334	210.124	-4.979	-9.383
M*hq*	180.926	220.326	-10.91	-18.337

Table C.11 - P-Values of mean b-wave latencies (ms) between cohorts using single-factor ANOVA statistical comparisons

	P-Value			
Age	**UWT vs. U*hq***	**UWT vs. MWT**	**U*hq* vs. M*hq***	**MWT vs. M*hq***
2 Mos	0.6574	0.2267	0.8279	0.8515
3 Mos	0.3844	0.0006	0.5367	0.0347
4 Mos	0.0003	0.2529	0.8813	0.1358
5 Mos	0.9718	0.9090	0.2243	0.1886
6 Mos	0.8558	0.0850	0.7809	0.4311
7 Mos			0.9875	0.8968
8 Mos	0.4541	0.3112	0.0216	0.0016
9 Mos		0.6049		
10 Mos	0.3252	0.0097	0.5400	0.1128

Table C.12 - P-Values of mean b-wave amplitudes (μV) between cohorts using single-factor ANOVA statistical comparisons

	P-Value			
	UWT vs. U*hq*	**UWT vs. MWT**	**U*hq* vs. M*hq***	**MWT vs. M*hq***
2 Mos	0.0266	0.1502	0.0113	0.0020
3 Mos	0.0000	0.0003	0.5276	0.0047
4 Mos	0.0000	0.1495	0.0743	0.0002
5 Mos	0.0114	0.0584	0.4869	0.0056
6 Mos	0.0000	0.0684	0.6714	0.0000
7 Mos			0.7406	0.0000
8 Mos	0.0000	0.0043	0.3472	0.0009
9 Mos		0.0954		
10 Mos	0.0002	0.1410	0.0082	0.0000

Table C.13 - Linear regression analysis of b-wave amplitudes with a confidence interval of ± 2 SEM

	Confidence Intervals			
	Y-intercept		Slope	
Cohort	**min**	**max**	**min**	**max**
UWT	606.365	679.788	-19.617	-33.703
U*hq*	580.475	672.444	-48.969	-66.927
MWT	566.197	646.465	-19.978	-33.55
M*hq*	451.955	561.518	-32.23	-52.797

Table C.14 - P-Values comparing electroretinography data of ten-month-old untreated mice and untreated mice tested a single time using single-factor ANOVA statistical comparisons

Electroretinography	UWTS vs UWT	U*hq*S vs U*hq*	UWTS vs U*hq*S
a-wave latency	0.1401	0.1897	0.0004
a-wave amplitude	0.1577	0.0000	0.0249
b-wave latency	0.1855	0.9777	0.8827
b-wave amplitude	0.1953	0.3943	0.0000

Table C.15 - Body mass correlation (*p*) with electroretinography data in the U*hq* cohort

Age	a-wave latency	b-wave latency	a-wave amplitude	b-wave amplitude
2 Mos	-0.1225	0.0245	0.5416	0.0200
4 Mos	-0.4257	-0.1990	-0.4281	0.2898
6 Mos	-0.5064	-0.0283	0.5961	0.4066

Table C.16 - Body mass correlation (*p*) with electroretinography data in the M*hq* cohort

Age	a-wave latency	b-wave latency	a-wave amplitude	b-wave amplitude
2 Mos	-0.1183	0.0686	0.4184	0.0014
4 Mos	-0.3873	0.1237	-0.6780	0.6238
6 Mos	-0.5725	0.0633	0.8179	0.6727

Table C.17 - Water consumption correlation (*p*) with electroretinography data in the U*hq* cohort

Age	a-wave latency	b-wave latency	a-wave amplitude	b-wave amplitude
2 Mos	-0.23065	0.08240	-0.07810	0.14560
4 Mos	-0.54185	0.14318	0.24819	-0.08544
6 Mos	-0.02000	0.59135	0.22670	-0.12288

Table C.18 - Water consumption correlation (*p*) with electroretinography data in the M*hq* cohort

Age	a-wave latency	b-wave latency	a-wave amplitude	b-wave amplitude
2 Mos	-0.05099	0.14457	0.11135	0.01000
4 Mos	-0.28280	0.06700	0.02449	0.15199
6 Mos	0.05831	-0.32218	0.50318	-0.26019

Table C.19 - Memantine consumption correlation (*p*) with electroretinography data in the MWT cohort

Age	a-wave latency	b-wave latency	a-wave amplitude	b-wave amplitude
2 Mos	0.05385	-0.62880	-0.46430	-0.15620
4 Mos	-0.35143	-0.67630	0.23540	-0.66110
6 Mos	-0.15652	0.08770	0.32202	-0.14390

Table C.20 - Memantine consumption correlation (*p*) with electroretinography data in the M*hq* cohort

Age	a-wave latency	b-wave latency	a-wave amplitude	b-wave amplitude
2 Mos	0.49010	0.46032	0.08190	0.35580
4 Mos	0.00710	-0.58700	0.05740	-0.14730
6 Mos	0.56560	-0.66950	0.40260	-0.10440

Table C.21 - P-Values of mean central corneal thickness (mm) between OD and OS of experimental cohorts using single-factor ANOVA statistical comparisons

	P-Value			
Age	UWT	U*hq*	MWT	M*hq*
2 Mos	0.1114	0.0421	0.4641	0.6161
3 Mos	0.6638	0.4860	0.7571	0.0493
4 Mos	1.0000	0.7245	0.5860	0.0102
5 Mos	0.5528	0.6985	0.7748	0.5983
6 Mos	0.7805	0.6186	0.6690	0.3331
7 Mos	0.2045		0.9047	0.5918
8 Mos	0.2639	0.5672	0.8708	0.5287
9 Mos	0.2256			
10 Mos	0.5610	0.7415	0.3972	0.8128

Table C.22 - P-Values of mean nasal peripheral corneal thickness (mm) between OD and OS of experimental cohorts using single-factor ANOVA statistical comparisons

	P-Value			
Age	**UWT**	**U*hq***	**MWT**	**M*hq***
2 Mos	0.5447	0.5899	0.7332	0.0784
3 Mos	1.0000	0.3319	0.3306	0.1375
4 Mos	0.3239	0.3122	0.5125	0.5447
5 Mos	0.4226	0.5425	1.0000	0.4989
6 Mos	0.2920	0.7016	0.7041	0.2446
7 Mos	0.5995		1.0000	0.3118
8 Mos	0.5085	0.4479	0.1427	0.9561
9 Mos	0.2907		0.2746	
10 Mos	0.0118	1.0000	0.3972	0.8087

Table C.23 - P-Values of mean temporal peripheral corneal thickness (mm) between OD and OS of experimental cohorts using single-factor ANOVA statistical comparisons

	P-Value			
Age	**UWT**	**U*hq***	**MWT**	**M*hq***
2 Mos	0.3972	0.4091	0.2008	0.4653
3 Mos	0.5373	0.6776	0.1748	0.1693
4 Mos	0.5258	0.1321	0.3026	0.1176
5 Mos	0.4226	0.2929	0.5490	0.0734
6 Mos	0.7153	0.5360	0.8990	0.7510
7 Mos			0.6085	1.0000
8 Mos	0.1474	0.1923	0.5586	0.4635
9 Mos	0.6361		0.4418	
10 Mos	0.8465	0.3739	0.2960	0.4021

Table C.24 - P-Values of mean anterior chamber width (mm) between OD and OS of experimental cohorts using single-factor ANOVA statistical comparisons

	P-Value			
Age	**UWT**	**U*hq***	**MWT**	**M*hq***
2 Mos	0.2984	0.5159	0.6661	0.1065
3 Mos	0.5617	0.8574	0.4326	0.1123
4 Mos	0.5852	0.8982	0.5930	0.4736
5 Mos	0.5149	0.9173	0.6726	0.5891
6 Mos	0.1502	0.8802	0.8051	0.2169
7 Mos	0.5624		0.7013	0.7599
8 Mos	0.5081	0.9881	0.6769	0.4689
9 Mos	0.4494		0.7971	
10 Mos	0.8945	0.5026	0.0496	0.3163

Table C.25 - P-Values of mean anterior chamber depth (mm) between OD and OS of experimental cohorts using single-factor ANOVA statistical comparisons

	P-Value			
Age	**UWT**	**U*hq***	**MWT**	**M*hq***
2 Mos	0.7768	0.4908	0.7365	1.0000
3 Mos	1.0000	0.2805	0.9521	0.9829
4 Mos	1.0000	0.2279	0.5919	0.6156
5 Mos	0.5076	0.2137	0.5852	0.3096
6 Mos	0.5539	0.5612	0.8386	0.5413
7 Mos	0.3140		0.1255	0.5528
8 Mos	0.6658	0.9397	0.4483	0.1072
9 Mos	0.9043		0.2840	
10 Mos	0.5796	0.3084	0.2829	0.1104

Table C.26 - P-Values of mean anterior retinal thickness (mm) between OD and OS of experimental cohorts using single-factor ANOVA statistical comparisons

	P-Value			
Age	**UWT**	**U*hq***	**MWT**	**M*hq***
2 Mos	0.6479	0.7119	0.7754	0.6984
3 Mos	0.4384	0.6716	0.0698	0.6044
4 Mos	0.6514	0.0528	0.7856	0.8998
5 Mos	0.3604	0.1056	0.3432	0.3629
6 Mos	0.4460	0.6073	0.3280	0.6972
7 Mos	0.1006		0.6311	0.7706
8 Mos	0.2094	0.5252	1.0000	0.1645
9 Mos	0.2187		1.0000	
10 Mos	0.2237	0.4628	0.8383	0.2026

Table C.27 - P-Values of mean posterior retinal thickness (mm) between OD and OS of experimental cohorts using single-factor ANOVA statistical comparisons

	P-Value			
Age	**UWT**	**U*hq***	**MWT**	**M*hq***
2 Mos	0.6811	0.1788	0.8567	0.0505
3 Mos	0.5586	0.4860	0.8153	0.0667
4 Mos	0.4105	0.6558	0.6145	0.4434
5 Mos	0.6667	0.5918	0.6333	0.4499
6 Mos	0.5634	1.0000	0.0247	0.1487
7 Mos	0.4671		0.1689	0.3333
8 Mos	0.1673	0.8670	0.8232	0.3229
9 Mos	0.8089		0.6433	
10 Mos	0.7641	0.1377	0.8400	1.0000

Table C.28 - P-Values of mean central whole retinal thickness (mm) between OD and OS of experimental cohorts using single-factor ANOVA statistical comparisons

	P-Value			
Age	**UWT**	**U*hq***	**MWT**	**M*hq***
2 Mos	0.2662	0.4202	0.8103	0.8679
3 Mos	0.1515	0.4095	1.0000	0.6874
4 Mos	0.2435	0.8946	0.4903	0.7952
5 Mos	0.4226	0.7519	0.7748	0.4977
6 Mos	0.8797	0.5195	0.8930	0.6776
7 Mos	0.1946		0.1750	0.8995
8 Mos	0.8910	0.7486	1.0000	0.3508
9 Mos	0.8965		0.6087	
10 Mos	0.0350	0.2230	0.2289	0.5471

Table C.29 - P-Values of mean central corneal thickness (mm) between cohorts using single-factor ANOVA statistical comparisons

	P-Value			
Age	**UWT vs. U*hq***	**UWT vs. MWT**	**U*hq* vs. M*hq***	**MWT vs. M*hq***
2 Mos	0.8678	0.2660	0.0115	0.7109
3 Mos	0.8078	0.2677	0.6492	0.2609
4 Mos	0.6593	0.2380	0.5838	0.5582
5 Mos	0.7663	0.6880	0.9543	0.8017
6 Mos	0.2010	0.3155	0.8075	0.2294
7 Mos		0.0687		0.9537
8 Mos	0.3276	0.0049	0.4526	0.0842
9 Mos		0.8430		
10 Mos	0.3308	0.8302	0.0703	0.0121

Table C.30 - P-Values of mean nasal peripheral corneal thickness (mm) between cohorts using single-factor ANOVA statistical comparisons

	P-Value			
Age	**UWT vs. U*hq***	**UWT vs. MWT**	**U*hq* vs. M*hq***	**MWT vs. M*hq***
2 Mos	0.2991	0.6689	0.1147	0.5611
3 Mos	0.8631	0.8100	0.7481	0.6462
4 Mos	0.1017	0.0285	0.6648	0.1522
5 Mos	0.6278	0.0540	0.8530	0.5690
6 Mos	0.2392	0.7521	0.2825	0.7909
7 Mos		0.0025		0.0400
8 Mos	0.0707	0.0028	0.2070	0.0451
9 Mos		0.4125		
10 Mos	0.1077	0.1272	0.2124	0.0263

Table C.31 - P-Values of mean temporal peripheral corneal thickness (mm) between cohorts using single-factor ANOVA statistical comparisons

	P-Value			
Age	**UWT vs. U*hq***	**UWT vs. MWT**	**U*hq* vs. M*hq***	**MWT vs. M*hq***
2 Mos	0.2254	0.5317	0.1110	0.8004
3 Mos	0.2073	0.7659	0.9580	0.5584
4 Mos	0.0065	0.1508	0.0398	0.1366
5 Mos	0.6202	0.3197	1.0000	0.5160
6 Mos	0.2627	0.4550	0.3038	0.3005
7 Mos		0.0009		0.6182
8 Mos	0.4422	0.0136	0.8104	0.2208
9 Mos		0.1271		
10 Mos	0.0358	0.0835	0.7962	0.0021

Table C.32 - P-Values of mean anterior chamber width (mm) between cohorts using single-factor ANOVA statistical comparisons

	P-Value			
Age	UWT vs. U*hq*	UWT vs. MWT	U*hq* vs. M*hq*	MWT vs. M*hq*
2 Mos	0.0024	0.2967	0.0172	0.0007
3 Mos	0.0000	0.0432	0.3760	0.0006
4 Mos	0.0006	0.0010	0.2374	0.0078
5 Mos	0.0379	0.5464	0.4291	0.0313
6 Mos	0.0016	0.8130	0.3904	0.0001
7 Mos		0.4574		0.0418
8 Mos	0.0006	0.0450	0.3716	0.0122
9 Mos		0.0681		
10 Mos	0.2669	0.6529	0.0926	0.0024

Table C.33 - P-Values of mean anterior chamber depth (mm) between cohorts using single-factor ANOVA statistical comparisons

	P-Value			
Age	UWT vs. U*hq*	UWT vs. MWT	U*hq* vs. M*hq*	MWT vs. M*hq*
2 Mos	0.3966	0.7106	0.0130	0.0012
3 Mos	0.1396	0.3972	0.1571	0.0054
4 Mos	0.8320	0.0958	0.5679	0.8739
5 Mos	0.3748	0.3779	0.9884	0.9924
6 Mos	0.0256	0.7980	0.1552	0.3243
7 Mos		0.0055		0.0466
8 Mos	0.3161	0.4940	0.1719	0.1907
9 Mos		0.7414		
10 Mos	0.7849	0.4796	0.3269	0.1608

Table C.34 - P-Values of mean anterior retinal thickness (mm) between cohorts using single-factor ANOVA statistical comparisons

	P-Value			
Age	**UWT vs. U*hq***	**UWT vs. MWT**	**U*hq* vs. M*hq***	**MWT vs. M*hq***
2 Mos	0.2362	0.2387	0.3115	0.2831
3 Mos	0.3109	0.1227	0.3489	0.5881
4 Mos	1.0000	0.0015	0.7877	0.1196
5 Mos	0.7502	0.0572	0.5147	0.0882
6 Mos	0.7382	0.3721	0.5804	0.5494
7 Mos		0.6832		0.3514
8 Mos	0.5155	0.2051	0.2625	0.0066
9 Mos		0.3445		
10 Mos	0.0007	0.0773	0.1802	0.0002

Table C.35 - P-Values of mean posterior retinal thickness (mm) between cohorts using single-factor ANOVA statistical comparisons

	P-Value			
Age	**UWT vs. U*hq***	**UWT vs. MWT**	**U*hq* vs. M*hq***	**MWT vs. M*hq***
2 Mos	0.9196	0.8983	0.1368	0.2472
3 Mos	0.3349	1.0000	0.8498	0.2032
4 Mos	0.8383	0.0243	0.7549	0.0194
5 Mos	0.6988	0.9785	0.2582	0.0725
6 Mos	0.0962	0.0626	0.5022	0.3413
7 Mos		0.0006		0.4327
8 Mos	0.0039	0.0028	0.9180	0.2604
9 Mos		0.0001		
10 Mos	0.1805	0.0073	0.5996	0.7017

Table C.36 - P-Values of mean central whole retinal thickness (mm) between cohorts using single-factor ANOVA statistical comparisons

	P-Value			
Age	**UWT vs. U*hq***	**UWT vs. MWT**	**U*hq* vs. M*hq***	**MWT vs. M*hq***
2 Mos	0.0686	0.3913	0.5507	0.9378
3 Mos	0.0005	0.0436	0.1591	0.5109
4 Mos	0.1654	0.0310	0.0455	0.1114
5 Mos	0.7860	0.6055	0.4118	0.5087
6 Mos	0.8622	0.3223	0.5198	1.0000
7 Mos		0.9403		0.2889
8 Mos	0.7962	0.7440	1.0000	0.7049
9 Mos		0.0917		
10 Mos	0.0075	0.4429	0.6874	0.0034

Table C.37 - P-Values comparing corneal thickness of ten-month-old untreated mice and untreated mice tested a single time using single-factor ANOVA statistical comparisons

Corneal Region	UWTS vs UWT	U*hq*S vs U*hq*	UWTS vs U*hq*S
Central Cornea	0.5728	0.0240	0.1501
Nasal Peripheral Cornea	0.0973	0.0552	0.0378
Temporal Peripheral Cornea	0.0649	0.0000	0.7815

Table C.38 - P-Values comparing the anterior chamber of ten-month-old untreated mice and untreated mice tested a single time using single-factor ANOVA statistical comparisons

Anterior Chamber	UWTS vs UWT	U*hq*S vs U*hq*	UWTS vs U*hq*S
Width	0.2889	0.5742	0.8709
Depth	0.4069	0.9375	0.6201

Table C.39 - P-Values comparing retinal thickness of ten-month-old untreated mice and untreated mice tested a single time using single-factor ANOVA statistical comparisons

Retinal Thickness	UWTS vs UWT	U*hq*S vs U*hq*	UWTS vs U*hq*S
Anterior Retina	0.0004	0.9025	0.1793
Posterior Retina	0.0000	0.0706	0.1801
Central Whole Retina	0.0008	0.1561	0.0297

Table C.40 - P-Values of mean corneal epithelium thickness (mm) between cohorts using single-factor ANOVA statistical comparisons

	P-Value			
Age	UWT vs. U*hq*	UWT vs. MWT	U*hq* vs. M*hq*	MWT vs. M*hq*
2 Mos	0.0468	0.6927	0.7531	0.1009
4 Mos	0.0128	0.1495	0.1126	0.6511
6 Mos		0.5960		
8 Mos	0.4316	0.3405	0.4153	0.3249
10 Mos	0.3521	0.4660	0.7656	0.5632

Table C.41 - P-Values of mean dorsal retinal ganglion cell counts (nuclei) between cohorts using single-factor ANOVA statistical comparisons

	P-Value			
Age	UWT vs. U*hq*	UWT vs. MWT	U*hq* vs. M*hq*	MWT vs. M*hq*
2 Mos	0.9697	0.5028	0.1012	0.0369
4 Mos	0.5718	0.7599	0.2717	0.1347
6 Mos		0.7679		
8 Mos	0.6799	0.5368	0.5801	0.7084
10 Mos	0.8650	0.6802	0.2474	0.5988

Table C.42 - P-Values of mean central retinal ganglion cell counts (nuclei) between cohorts using single-factor ANOVA statistical comparisons

	P-Value			
Age	**UWT vs. U*hq***	**UWT vs. MWT**	**U*hq* vs. M*hq***	**MWT vs. M*hq***
2 Mos	0.4816	0.0393	0.6560	0.0686
4 Mos	0.0085	0.6938	0.0282	0.0438
6 Mos		0.2001		
8 Mos	0.3911	0.2746	0.5801	0.1239
10 Mos	0.3711	0.1097	0.4327	0.0813

Table C.43 - P-Values of mean ventral retinal ganglion cell counts (nuclei) between cohorts using single-factor ANOVA statistical comparisons

	P-Value			
Age	**UWT vs. U*hq***	**UWT vs. MWT**	**U*hq* vs. M*hq***	**MWT vs. M*hq***
2 Mos	0.3574	0.0111	0.6433	0.8056
4 Mos	0.5983	0.2662	0.1633	0.3718
6 Mos		0.3706		
8 Mos	0.4480	0.1903	0.3903	0.8439
10 Mos	0.6622	0.4094	0.3151	0.7541

Table C.44 - P-Values of mean dorsal retinal inner plexiform layer thickness (µm) between cohorts using single-factor ANOVA statistical comparisons

	P-Value			
Age	**UWT vs. U*hq***	**UWT vs. MWT**	**U*hq* vs. M*hq***	**MWT vs. M*hq***
2 Mos	0.7346	0.5277	0.7904	0.6203
4 Mos	0.7398	0.4800	0.5362	0.9313
6 Mos		0.3630		
8 Mos	0.3569	0.0853	0.3947	0.1438
10 Mos	0.0605	0.3802	0.0125	0.0585

Table C.45 - P-Values of mean central retinal inner plexiform layer thickness (µm) between cohorts using single-factor ANOVA statistical comparisons

	P-Value			
Age	UWT vs. U*hq*	UWT vs. MWT	U*hq* vs. M*hq*	MWT vs. M*hq*
2 Mos	0.9687	0.7779	0.2458	0.2647
4 Mos	0.2565	0.2772	0.9764	0.7593
6 Mos		0.5726		
8 Mos	0.1057	0.6468	0.3755	0.3196
10 Mos	0.0734	0.3226	0.3777	0.0638

Table C.46 - P-Values of mean ventral retinal inner plexiform layer thickness (µm) between cohorts using single-factor ANOVA statistical comparisons

	P-Value			
Age	UWT vs. U*hq*	UWT vs. MWT	U*hq* vs. M*hq*	MWT vs. M*hq*
2 Mos	0.6764	0.5353	0.4730	0.4000
4 Mos	0.2465	0.9012	0.4325	0.7075
6 Mos		0.2148		
8 Mos	0.8116	0.0744	0.7776	0.1103
10 Mos	0.1514	0.1895	0.2602	0.3032

Table C.47 - P-Values of mean dorsal retinal inner nuclear layer cell counts (nuclei) between cohorts using single-factor ANOVA statistical comparisons

	P-Value			
Age	UWT vs. U*hq*	UWT vs. MWT	U*hq* vs. M*hq*	MWT vs. M*hq*
2 Mos	0.5370	0.5237	1.0000	0.4763
4 Mos	0.1250	0.1950	0.2924	0.7404
6 Mos		1.0000		
8 Mos	0.3776	0.6517	0.1135	0.1682
10 Mos	0.2199	0.6075	0.0624	0.4071

Table C.48 - P-Values of mean central retinal inner nuclear layer cell counts (nuclei) between cohorts using single-factor ANOVA statistical comparisons

	P-Value			
Age	**UWT vs. U*hq***	**UWT vs. MWT**	**U*hq* vs. M*hq***	**MWT vs. M*hq***
2 Mos	0.7024	0.7245	1.0000	0.5778
4 Mos	0.1013	0.3052	0.0786	1.0000
6 Mos		0.6666		
8 Mos	0.7980	0.1090	0.0972	1.0000
10 Mos	0.0209	0.3466	0.4327	0.0400

Table C.49 - P-Values of mean ventral retinal inner nuclear layer cell counts (nuclei) between cohorts using single-factor ANOVA statistical comparisons

	P-Value			
Age	**UWT vs. U*hq***	**UWT vs. MWT**	**U*hq* vs. M*hq***	**MWT vs. M*hq***
2 Mos	1.0000	0.0650	1.0000	0.1599
4 Mos	0.0892	0.1411	0.0016	0.0353
6 Mos		1.0000		
8 Mos	0.3935	0.0479	1.0000	0.5370
10 Mos	0.2199	0.1053	0.3979	0.3506

Table C.50 - P-Values of mean dorsal retinal outer plexiform layer thickness (µm) between cohorts using single-factor ANOVA statistical comparisons

	P-Value			
Age	**UWT vs. U*hq***	**UWT vs. MWT**	**U*hq* vs. M*hq***	**MWT vs. M*hq***
2 Mos	0.7911	0.8924	0.6271	0.7218
4 Mos	0.7250	0.5377	0.9710	0.9026
6 Mos		0.5532		
8 Mos	0.5631	0.1899	0.1504	0.6959
10 Mos	0.0092	0.5654	0.0920	0.8819

Table C.51 - P-Values of mean central retinal outer plexiform layer thickness (µm) between cohorts using single-factor ANOVA statistical comparisons

	P-Value			
Age	**UWT vs. U*hq***	**UWT vs. MWT**	**U*hq* vs. M*hq***	**MWT vs. M*hq***
2 Mos	0.9635	0.9328	0.0640	0.0425
4 Mos	0.2663	0.6776	0.9328	0.1091
6 Mos		0.9536		
8 Mos	0.0004	0.6450	0.7706	0.0149
10 Mos	0.0044	0.4632	0.0318	0.0022

Table C.52 - P-Values of mean ventral retinal outer plexiform layer thickness (µm) between cohorts using single-factor ANOVA statistical comparisons

	P-Value			
Age	**UWT vs. U*hq***	**UWT vs. MWT**	**U*hq* vs. M*hq***	**MWT vs. M*hq***
2 Mos	0.7629	0.3041	0.4195	0.3084
4 Mos	0.3861	0.7720	0.1066	0.3057
6 Mos		0.3055		
8 Mos	0.7670	0.2904	0.9492	0.1520
10 Mos	0.1285	0.9365	0.3498	0.4228

Table C.53 - P-Values of mean dorsal retinal outer nuclear layer cell counts (nuclei) between cohorts using single-factor ANOVA statistical comparisons

	P-Value			
Age	**UWT vs. U*hq***	**UWT vs. MWT**	**U*hq* vs. M*hq***	**MWT vs. M*hq***
2 Mos	0.4327	0.2707	0.6433	0.7129
4 Mos	0.2381	0.0203	0.2771	0.8535
6 Mos		0.4458		
8 Mos	0.2675	0.0569	0.1655	0.3153
10 Mos	0.1695	0.8028	0.1861	0.4974

Table C.54 - P-Values of mean central retinal outer nuclear layer cell counts (nuclei) between cohorts using single-factor ANOVA statistical comparisons

	P-Value			
Age	UWT vs. U*hq*	UWT vs. MWT	U*hq* vs. M*hq*	MWT vs. M*hq*
2 Mos	0.5317	0.2029	0.7953	0.0845
4 Mos	0.0140	0.4609	0.3912	0.2189
6 Mos		1.0000		
8 Mos	0.2242	0.0460	0.2350	0.0941
10 Mos	0.0007	0.8327	0.2371	0.0221

Table C.55 - P-Values of mean ventral retinal outer nuclear layer cell counts (nuclei) between cohorts using single-factor ANOVA statistical comparisons

	P-Value			
Age	UWT vs. U*hq*	UWT vs. MWT	U*hq* vs. M*hq*	MWT vs. M*hq*
2 Mos	0.1599	0.1005	1.0000	0.4593
4 Mos	0.1455	0.0125	0.0429	0.4554
6 Mos		0.4021		
8 Mos	0.5891	0.0055	0.6269	0.3559
10 Mos	0.0384	0.0203	0.2659	0.3935

Table C.56 - P-Values of mean dorsal retinal photoreceptor segment thickness (μm) between cohorts using single-factor ANOVA statistical comparisons

	P-Value			
Age	UWT vs. U*hq*	UWT vs. MWT	U*hq* vs. M*hq*	MWT vs. M*hq*
2 Mos	0.4889	0.2388	0.6876	0.1485
4 Mos	0.1130	0.2428	0.6290	0.0693
6 Mos		0.0959		
8 Mos	0.1646	0.0077	0.5389	0.9798
10 Mos	0.5665	0.0975	0.3621	0.3855

Table C.57 - P-Values of mean central retinal photoreceptor segment thickness (µm) between cohorts using single-factor ANOVA statistical comparisons

	P-Value			
Age	**UWT vs. U*hq***	**UWT vs. MWT**	**U*hq* vs. M*hq***	**MWT vs. M*hq***
2 Mos	0.4975	0.3736	0.6898	0.0802
4 Mos	0.1090	0.3706	0.9720	0.3577
6 Mos		0.3503		
8 Mos	0.3664	0.2971	0.9220	0.0550
10 Mos	0.0495	0.1666	0.1283	0.1427

Table C.58 - P-Values of mean ventral retinal photoreceptor segment thickness (µm) between cohorts using single-factor ANOVA statistical comparisons

	P-Value			
Age	**UWT vs. U*hq***	**UWT vs. MWT**	**U*hq* vs. M*hq***	**MWT vs. M*hq***
2 Mos	0.6246	0.4161	0.4098	0.0359
4 Mos	0.0248	0.6041	0.3037	0.0593
6 Mos		0.2868		
8 Mos	0.2164	0.0061	0.4469	0.3622
10 Mos	0.1163	0.1720	0.2144	0.7922

Table C.59 - P-Values of mean dorsal retinal thickness (µm) between cohorts using single-factor ANOVA statistical comparisons

	P-Value			
Age	**UWT vs. U*hq***	**UWT vs. MWT**	**U*hq* vs. M*hq***	**MWT vs. M*hq***
2 Mos	0.9478	0.4057	0.8360	0.5733
4 Mos	0.1133	0.1694	0.3553	0.2950
6 Mos		0.5192		
8 Mos	0.5650	0.0139	0.3263	0.9383
10 Mos	0.0474	0.2929	0.1364	0.8443

Table C.60 - P-Values of mean central retinal thickness (µm) between cohorts using single-factor ANOVA statistical comparisons

	P-Value			
Age	UWT vs. U*hq*	UWT vs. MWT	U*hq* vs. M*hq*	MWT vs. M*hq*
2 Mos	0.7319	0.3604	0.2439	0.1106
4 Mos	0.2917	0.7214	0.8399	0.1412
6 Mos		0.9700		
8 Mos	0.2315	0.3033	0.6429	0.3005
10 Mos	0.0162	0.1734	0.1091	0.0354

Table C.61 - P-Values of mean ventral retinal thickness (µm) between cohorts using single-factor ANOVA statistical comparisons

	P-Value			
Age	UWT vs. U*hq*	UWT vs. MWT	U*hq* vs. M*hq*	MWT vs. M*hq*
2 Mos	0.8790	0.3920	0.1166	0.1316
4 Mos	0.0217	0.5122	0.6377	0.0627
6 Mos		0.7186		
8 Mos	0.9968	0.0116	0.2012	0.1571
10 Mos	0.0628	0.0893	0.2292	0.4294

Table C.62 - P-Values of mean dihydroethidium fluorescence in the corneal epithelium between cohorts using single-factor ANOVA statistical comparisons

	P-Value			
Age	UWT vs. U*hq*	UWT vs. MWT	U*hq* vs. M*hq*	MWT vs. M*hq*
2 Mos	0.0874	0.9403	0.6865	0.3362
4 Mos	0.0559	0.8099	0.1575	0.9027
6 Mos		0.3442		
8 Mos	0.3447	0.9128	0.0595	0.1748
10 Mos	0.3847	0.0329	0.2403	0.4969

Table C.63 - P-Values of mean dihydroethidium fluorescence in the dorsal ganglion cell layer between cohorts using single-factor ANOVA statistical comparisons

	P-Value			
Age	UWT vs. U*hq*	UWT vs. MWT	U*hq* vs. M*hq*	MWT vs. M*hq*
2 Mos	0.5912	0.9036	0.8077	0.3123
4 Mos	0.1772	0.7095	0.0867	0.3108
6 Mos		0.2563		
8 Mos	0.7428	0.2170	0.6343	0.8949
10 Mos	0.2871	0.7527	0.6425	0.8668

Table C.64 - P-Values of mean dihydroethidium fluorescence in the dorsal inner nuclear layer between cohorts using single-factor ANOVA statistical comparisons

	P-Value			
Age	UWT vs. U*hq*	UWT vs. MWT	U*hq* vs. M*hq*	MWT vs. M*hq*
2 Mos	0.8610	0.6599	0.2811	0.5416
4 Mos	0.1484	0.6207	0.0365	0.0679
6 Mos		0.7012		
8 Mos	0.1147	0.8472	0.4139	0.9926
10 Mos	0.5873	0.3995	0.6581	0.4567

Table C.65 - P-Values of mean dihydroethidium fluorescence in the dorsal outer nuclear layer between cohorts using single-factor ANOVA statistical comparisons

	P-Value			
Age	UWT vs. U*hq*	UWT vs. MWT	U*hq* vs. M*hq*	MWT vs. M*hq*
2 Mos	0.7350	0.7310	0.4791	0.5071
4 Mos	0.1619	0.3456	0.0300	0.0109
6 Mos		0.7333		
8 Mos	0.0329	0.9649	0.5216	0.8438
10 Mos	0.9317	0.9981	0.9161	0.8413

Table C.66 - P-Values of mean dihydroethidium fluorescence in the central ganglion cell layer between cohorts using single-factor ANOVA statistical comparisons

	P-Value			
Age	UWT vs. U*hq*	UWT vs. MWT	U*hq* vs. M*hq*	MWT vs. M*hq*
2 Mos	0.5622	0.9255	0.7940	0.2709
4 Mos	0.3770	0.7713	0.2490	0.4443
6 Mos		0.6166		
8 Mos	0.2675	0.8602	0.2594	0.3104
10 Mos	0.9074	0.7456	0.9833	0.7961

Table C.67 - P-Values of mean dihydroethidium fluorescence in the central inner nuclear layer between cohorts using single-factor ANOVA statistical comparisons

	P-Value			
Age	UWT vs. U*hq*	UWT vs. MWT	U*hq* vs. M*hq*	MWT vs. M*hq*
2 Mos	0.9417	0.8183	0.3745	0.2156
4 Mos	0.1221	0.2723	0.1201	0.2163
6 Mos		0.5750		
8 Mos	0.0542	0.8068	0.3820	0.8319
10 Mos	0.3211	0.1969	0.7725	0.7281

Table C.68 - P-Values of mean dihydroethidium fluorescence in the central outer nuclear layer between cohorts using single-factor ANOVA statistical comparisons

	P-Value			
Age	UWT vs. U*hq*	UWT vs. MWT	U*hq* vs. M*hq*	MWT vs. M*hq*
2 Mos	0.8975	0.8239	0.2627	0.2388
4 Mos	0.2537	0.9099	0.1316	0.2316
6 Mos		0.8962		
8 Mos	0.0545	0.4682	0.5401	0.8908
10 Mos	0.3922	0.3445	0.9590	0.9812

Table C.69 - P-Values of mean dihydroethidium fluorescence in the ventral ganglion cell layer between cohorts using single-factor ANOVA statistical comparisons

	P-Value			
Age	**UWT vs. U*hq***	**MWT vs. M*hq***	**U*hq* vs. M*hq***	**UWT vs. MWT**
2 Mos	0.6335	0.5898	0.8922	0.8844
4 Mos	0.1302	0.0992	0.0620	0.0200
6 Mos		0.3311		
8 Mos	0.7990	0.9984	0.4353	0.6150
10 Mos	0.0794	0.8866	0.0620	0.7110

Table C.70 - P-Values of mean dihydroethidium fluorescence in the ventral inner nuclear layer between cohorts using single-factor ANOVA statistical comparisons

	P-Value			
Age	**UWT vs. U*hq***	**UWT vs. MWT**	**U*hq* vs. M*hq***	**MWT vs. M*hq***
2 Mos	0.1744	0.4258	0.8567	0.6114
4 Mos	0.1530	0.5272	0.0315	0.0419
6 Mos		0.0888		
8 Mos	0.1400	0.8611	0.3148	0.8057
10 Mos	0.4209	0.8306	0.3419	0.8962

Table C.71 - P-Values of mean dihydroethidium fluorescence in the ventral outer nuclear layer between cohorts using single-factor ANOVA statistical comparisons

	P-Value			
Age	**UWT vs. U*hq***	**UWT vs. MWT**	**U*hq* vs. M*hq***	**MWT vs. M*hq***
2 Mos	0.2358	0.8459	0.8025	0.2543
4 Mos	0.2778	0.3083	0.0272	0.0136
6 Mos		0.1653		
8 Mos	0.0146	0.6120	0.4271	0.6081
10 Mos	0.6264	0.5147	0.5423	0.7190

Table C.72 - P-Values comparing retinal apoptosis profiles over the experimental lifespan of cohorts using a Fisher's exact statistical comparison

	P-Values			
Retinal Position	**UWT vs. U*hq***	**UWT vs. MWT**	**U*hq* vs. M*hq***	**MWT vs. M*hq***
Whole Retina	0.1182	0.6113	0.0496	0.6885
Central Cornea Outer Nuclear Layer	0.1550	0.2437	0.0667	0.8854
Whole Retina vs. Central Corneal Outer Nuclear Layer	0.9576	0.9089	1.0000	1.0000

Table C.73 - P-Values of mean whole retinal apoptosis between cohorts using single-factor ANOVA statistical comparisons

	P-Value			
Age	**UWT vs. U*hq***	**UWT vs. MWT**	**U*hq* vs. M*hq***	**MWT vs. M*hq***
2 Mos	0.2682	0.2443	0.1544	0.0358
4 Mos	0.0089	0.2960	0.1292	0.1102
6 Mos		0.8671		
8 Mos	0.5293	0.5452	0.5536	0.5737
10 Mos	0.7201	0.1991	0.6318	0.2437

Table C.74 - P-Values of mean central retinal outer nuclear layer apoptosis between cohorts using single-factor ANOVA statistical comparisons

	P-Value			
Age	**UWT vs. U*hq***	**UWT vs. MWT**	**U*hq* vs. M*hq***	**MWT vs. M*hq***
2 Mos	0.3692	0.6898	0.0548	0.0142
4 Mos	0.0095	0.3466	0.5753	0.0219
6 Mos		0.4938		
8 Mos	0.4942	0.5498	0.8537	0.8829
10 Mos	0.9486	0.3986	0.9002	0.2872